Magneto-optical properties of semiconductor nanocrystals in glass

Dissertation

presented to the Faculty of Physics of the
TU Dortmund University, Germany,
in partial fulfillment of the requirements
for the degree of

Doktor rer. nat.

by

Gang Qiang

technische universität
dortmund

Dortmund, January, 2022

Accepted by the Faculty of Physics of the TU Dortmund University, Germany.

Day of the oral examination: 10th January 2022

Examination board:
Prof. Dr. Dmitri R. Yakovlev
Prof. Dr. Heinz Hövel
Prof. Dr. Götz S. Uhrig
Dr. Anton Savitsky

Contents

Summary

Understanding of the spin and exciton properties in colloidal nanostructures paves the way for their applications in a variety of fields, such as spintronics and quantum science and technology. Using magneto-optical experimental techniques, the fundamental properties such as polarization, g-factor, spin dynamics in three kind of semiconductor nanocrystals (NCs), i.e. CdSe, CuCl and all-inorganic perovskite ($CsPbBr_3$, $CsPbI_3$) are studied, which help to understand the exciton fine structures and related interactions in each material.

By combining both the experimental and theoretical efforts, the puzzling behavior of the polarized emission of dark excitons in the ensemble of CdSe NCs is explained by considering the nanocrystal size dispersion and phonon effect. The spin coherent dynamics in the pump-probe measurements show two components, i.e. one oscillating and one nonoscillating. The Larmor frequency from the oscillating component is unambiguously assigned to the electron based on the theoretical analysis. While the nonoscillating component is clarified to be contributed by the frozen exciton spin polarization created by the pump pulse in NCs with heavy-light hole splitting determined by the crystal field.

The polarization properties and g-factors in CuCl NCs are investigated comprehensively, where the degree of circular polarization of the Z_3 exciton emission is found to increase linearly with the magnetic field at low temperatures up to 8 T. In the spin-flip Raman scattering measurements, a g-factor about 2 is resolved which can be assigned to the electron.

The magnetic field and temperature dependent recombination dynamics reveal a dark ground state in both $CsPbBr_3$ and $CsPbI_3$ NCs with corresponding bright-dark exciton splitting being 4.2 meV and 6.5 meV, respectively. In $CsPbI_3$ NCs, very interesting anomalous polarization and spin dynamics are observed, which is related to the interaction between the dark exciton state and the bright exciton fine structure. The spin-flip Raman scattering measurements on $CsPbI_3$ NCs also reveal two g-factors, i.e. one is about 2.5 and another one about 1.5.

Zusammenfassung

Das Verständnis der Spin- und Exzitoneneigenschaften in kolloidalen Nanostrukturen ebnet den Weg für ihre Anwendungen in einer Vielzahl von Fachgebieten wie z.B. der Spintronik oder der Quantenwissenschaft und -technologie. Unter Verwendung magneto-optischer experimenteller Techniken werden die grundlegenden Eigenschaften wie Polarisation, g-Faktor und Spindynamik in drei Sorten von Halbleiter-Nanokristallen (NCs), d.h. CdSe, CuCl und anorganischen Perowskiten ($CsPbBr_3$, $CsPbI_3$), untersucht, was zum besseren Verständnis der Exzitonen-Feinstruktur und der damit verbundenen Wechselwirkungen in den einzelnen Materialien beiträgt.

Durch die Kombination der experimentellen und theoretischen Bemühungen ist es gelungen, das ungewöhnliche Phänomen polarisierter Emission von dunklen Exzitonen im Ensemble der CdSe NCs zu erklären, indem die Dispersion der Nanokristallgröße und der Phononeneffekt einbezogen wurden. Die kohärente Spin-Dynamik weist zwei Komponenten auf, nämlich eine oszillierende und eine nicht oszillierende. Die Larmorfrequenz der oszillierenden Komponente wird dem Elektron auf der Grundlage der theoretischen Analyse eindeutig zugewiesen. Die nicht oszillierende Komponente wird durch die eingefrorene Exziton-Spinpolarisation verursacht, die durch den Pump-Puls in NCs mit einer durch das Kristallfeld bedingten Aufspaltung von Schwer- und Leichtlöchern entsteht.

Die Polarisationseigenschaften und g-Faktoren in CuCl NCs werden umfassend untersucht, und es wird herausgestellt, dass der Grad der zirkulären Polarisation der Z_3 Exzitonenemission bei niedrigen Temperaturen bis zu 8 T linear mit dem Magnetfeld zunimmt. In den Messungen der Spin-Flip-Raman-Streuung wird ein g-Faktor von etwa 2 festgestellt, der dem Elektron zugeordnet werden kann.

Die magnetfeld- und temperaturabhängige Rekombinationsdynamik offenbart einen dunklen Grundzustand sowohl in $CsPbBr_3$ als auch in $CsPbI_3$ NCs mit einer entsprechenden Hell-Dunkel-Exzitonenspaltung von 4.2 meV bzw. 6.5 meV. In $CsPbI_3$ NCs werden sehr interessante anomale Polarisations- und Spindynamiken beobachtet, die mit der Wechselwirkung zwischen dem dunklen Exzitonzustand und der hellen Exziton-Feinstruktur zusammenhängen. Die Messungen der Spin-Flip-Raman-Streuung in $CsPbI_3$ NCs ergeben zwei g-Faktoren, von denen einer etwa 2.5 und der andere etwa 1.5 beträgt.

Chapter 1

Motivation

The fast development of semiconductor industry following Moore's law has been continuing since the early 70's of last century, however, this tendency can not sustain anymore due to the fact that the miniaturization of transistors by the long-established technologies is already close to the end. With the availability of 5 nm process tools from Sumsung and TSMC, 5 nm chips are already commercialized by electronic giants like Apple and Huawei for their latest smartphone in October 2020, and it is expected that 3 nm or 2 nm nodes technology will be launched in the coming few years. As transistors are manufactured smaller and smaller, further shrinking of their size will be extremely difficult, and the processing and manufacturing will confront drastic challenges.[1] While as every coin has two sides, the end of Moore's law is supposed to open a new era in information technology as the focus of research and development shifts from miniaturizing transistor size to the coordinated introduction of new devices with novel architectures.[2] It is well known that the electron in semiconductors has three degree of freedom, i.e. charge, spin and valley. Historically, the electronic devices in our daily life are primarily based on the charge property, but it is also possible to build devices that rely on spin and valley properties, i.e. spintronics[3–5] and valleytronics.[6–9] Our researches focus on the spin properties of electrons and holes in semiconductor nanostructures.

In the study of semiconductor spintronics, electron spin is at the very center of interest, and the underlying basis is the intimate connection between the charge and spin degrees of freedom of the electron via the Pauli principle.[10,11] Spin also offers a way to store and manipulate phase coherence over length and time scales which make it as one of the potential candidates for constructing quantum bit (qubit) as the elementary unit for quantum information processing, building spin-based quantum computers, and for quantum internet.[12–14] During the last two decades, researchers have been following the basic criteria formulated by David P. DiVincenzo and Daniel Loss[15,16] to build quantum information processing and computing systems, it states as:

(1) A scalable physical system with well characterized qubits;
(2) The ability to initialize the state of the qubits to a simple fiducial state;
(3) Long relevant decoherence times, much longer than the gate operation time;
(4) A universal set of quantum gates;
(5) A qubit-specific measurement capability;

In order to take the full advantage of current semiconductor manufacture technologies for future quantum devices, a lot of work has been done and more are to be done on silicon, germanium or compound semiconductor nanostructures.[17–25] Many interesting physics have been discovered and lots of progresses have been made, but most of the studies are based on samples prepared by the molecule beam epitaxy technique (MBE) or other very expensive technologies, which sets a very high entry criteria for experimental researchers and could also be a potential problem for further large-scale application of quantum devices based on these materials.

Fortunately, benefiting from the progresses in synthesis techniques during the last few decades, colloidal semiconductor nanocrytals (NCs) gradually catch up with their MBE counterparts,[26] not only from the sample preparation aspect but also from the popularity in the fundamental as well as application researches.[27–34] Nowadays, colloidal NCs can be synthesized with well defined shape, very small size dispersion ($<$ 5%), various of composition and heterostructure, specific surface conditions, and most importantly with very low cost. Their electrical, optical as well as spin properties have been extensively investigated, which paves the way for their applications not only in biology,[35–37] laser,[38–40] light emitting diode,[41–43] solar cell,[44,45] transistors,[46] but also in spintronics and scalable quantum information systems.[34,47–51]

Currently, there are two main methods for synthesizing colloidal NCs, the wet-chemical method and the high-temperature precipitation method. Historically, the research about colloidal semiconductor NCs started in the early 1980s independently by Efros and Ekimov on samples prepared by high-temperature precipitation in glass matrix,[52–55] and by Brus on solution samples prepared by the wet-chemical method.[56–59] Due to its simple technological protocols and flexibility, the wet-chemical method achieved great successes later on, especially in nanocrystal shape control, surface modification, heterostructure and superlattice design. However, it has been frequently reported in the literature that wet-chemically synthesized NCs suffer from degradation and instability due to the direct contacting with oxygen and water in the air, as well as surrounding environment fluctuation, etc. While NCs grown in the glass matrix not only show comparable optical properties, but are also free from these problems thanks to the matrix encapsulation.[60] This is very important for practical applications and is one of the reasons why we choose semiconductor NCs grown in glass matrix for current study. Moreover, NCs synthesized in this way own simpler surface conditions due to the absence of organic ligand passivation, they also have the ideally random orientation of the nanocrystal quantization axis in the ensemble which makes the theoretical modeling easier.

Magnetic fields have been used as a powerful tool in semiconductor NCs research to address spin-dependent phenomena, identify the exciton fine structures, and to explore the mechanisms responsible for recombination of dark excitons which are optically forbidden in the electric dipole approximation. Many important discoveries have been firstly made on wet-chemically synthesized colloidal NCs, e.g. shortening of the dark exciton lifetime,[61–65] circular polarization of photoluminescence (PL),[66–69] exciton fine structure splitting including the Zeeman effect in single NCs,[65,70–74] anisotropic exchange interaction,[75,76] and electron spin coherence.[77,78] All those make the first step for colloidal NCs towards applications in spintronics and quantum information science based on the spin-dependent phenomena. On the contrary, only few magneto-optical studies has been performed on semiconductor NCs in the glass matrix. Here, we studied four nanocrystal samples with different compositions, i.e. CdSe, CuCl, $CsPbBr_3$ and $CsPbI_3$, and focused on their magneto-optical and spin properties.

This thesis is organized in the following way: we describe our research motivation in Chapter 1, and summarize the fundamentals of colloidal semiconductor NCs in Chapter 2 with the main goal to show the establishment and perfection of the bright-dark exciton theory, exciton fine structure and dark exciton recombination mechanisms. Chapter 3 contains the sample information and all experimental techniques that were utilized. In Chapter 4, the study of exciton polarization properties in CdSe NCs is presented. Chapter 5 shows the pump-probe results measured on CdSe NCs, Chapter 6 summarizes the magneto-optics of CuCl NCs, e.g. polarization properties, optical orientation of the Z_3 excitons and spin-flip Raman scattering (SFRS). In Chapter 7 and Chapter 8, we studied the recombination dynamics, polarization properties and spin dynamics in perovskite $CsPbBr_3$ and $CsPbI_3$ NCs, respectively. The spin-flip Raman scattering measurements on $CsPbI_3$ NCs are described in Chapter 9. Finally, we give an outlook for further research in this field in Chapter 10.

Chapter 2

Fundamentals of colloidal semiconductor nanocrystals

During the last few decades, colloidal semiconductor nanocrystals (NCs) as a relative new member of low dimensional quantum systems have experienced a fast development in all aspects such as synthesis, properties characterization and applications. [26] In this chapter, we first introduce some basic concepts in low dimensional semiconductor physics, then move to the bright-dark exciton model and band-edge exciton fine structures in II-VI, III-V and perovskite colloidal semiconductor NCs. Finally, we summarize the recombination mechanisms of dark excitons known in the literature by now.

2.1 Basic concepts

2.1.1 Exciton, trion and biexciton

An exciton is composed of an electron and a hole bound by Coulomb interaction. Excitons are classified into two types based on their size, i.e. an exciton localized to a single lattice site is called Frenkel exciton as schematically shown in Fig. 2.1. If it spans over many lattice sites, it is called Wannier exciton or Wannier-Mott exciton. The Frenkel excitons are usually observed in insulators and molecular crystals, while Wannier-Mott excitons mainly present in semiconductors.

When semiconductors are under photoexcitation, one absorbed photon with energy equal or higher than the band gap will lift an electron from the valence band to the conduction band, and leave a hole (electronic vacancy) in the valence band. Then the Coulomb interaction holds the electron and hole together to create an exciton (X) as

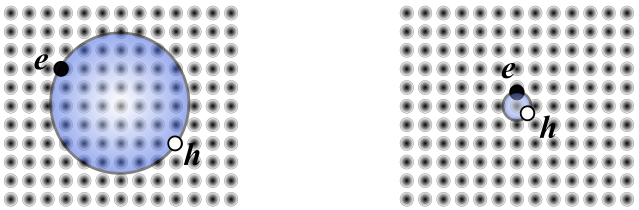

(a) Wannier-Mott exciton (b) Frenkel exciton

Figure 2.1: Schematic diagram of (a) a Wanneir-Mott exciton, and (b) a Frenkel exciton. The black and white circles represent electron (e) and hole (h), respectively. The blue shadow areas indicate the relative size of the exciton.

shown in Fig. 2.2(a). In some cases, when many excitons are excited simultaneously, two excitons may bind together to form an exciton molecule which is also referred as biexciton (M) as presented in Fig. 2.2(b). If there are resident carriers in the material, photoexcited excitons may combine with them to form trions (T), i.e. if an exciton combines with an electron (a hole), it will produce a negative (positive) trion, T^- (T^+) as shown in Fig. 2.2(c) and Fig. 2.2(d). Moreover, excitons and biexcitons can bound to defects or acceptors (A^0) to form bound excitons (A^0,X) and bound biexcitons (A^0,M). Figure 2.2(e) shows the energy diagram of different possible quasiparticles in semiconductor NCs, $E_{b,BM}$, $E_{b,BX}$, $E_{b,M}$ and $E_{b,T^-(T^+)}$ refer to the binding energy of bound biexciton, bound exciton, biexciton and negative(positive) trion, respectively.

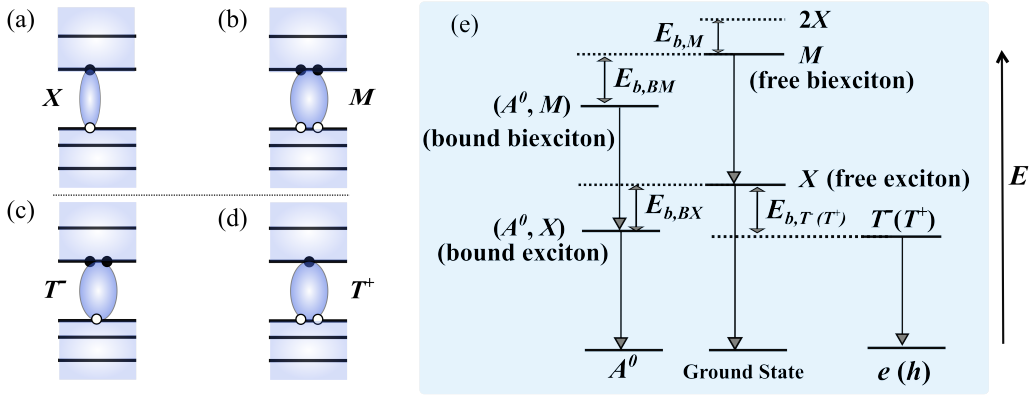

Figure 2.2: Quasiparticles in semiconductor NCs, (a) exciton (X), (b) biexciton (M), (c) negative trion (T^-) and (d) positive trion (T^+). (e) Energy diagram of the the bound states (left-hand side), free states (middle) and charged state (right-hand side), where the free biexciton, free exciton, and neutral acceptor are denoted by M, X, and A^0, the bond biexciton, bond exciton, negative trion and positive trion are marked by (A^0,M), (A^0,X), T^- and T^+, respectively. $E_{b,BM}$, $E_{b,BX}$, $E_{b,M}$ and $E_{b,T^-(T^+)}$ are the binding energy of bound biexciton, bound exciton, biexciton and negative(positive) trion. The vertical upward arrow shows the energy (E) increasing direction.

The biexciton binding energy $E_{b,M}$ is defined as the energy difference between two free excitons ($2X$) and the biexciton (M): $E_{b,M} = 2E_X$ - E_M. It can be determined through observation of the biexciton photoluminescence at energy $\hbar\omega_M$ and information about the remaining excitation in the material, i.e assuming that the radiative decay of the biexciton produces an exciton, then $E_M = \hbar\omega_M + E_X = \hbar\omega_M + \hbar\omega_X$, where $\hbar\omega_X$ denotes the exciton emission energy, therefore the biexciton binding energy $E_{b,M}$ is given by the spectral shift $\hbar\omega_X$ - $\hbar\omega_M$,[79] and similar ideas can be used to get $E_{b,BM}$, $E_{b,BX}$ and $E_{b,T^-(T^+)}$.

2.1.2 Quantum confinement effect

Optical properties of colloidal semiconductor NCs are related to the transitions between quantized levels of electron and hole. For a spherical nanocrystal surrounded by an infinite potential barrier, the energy of the electron and hole quantized levels, characterized by angular momentum quantum number l, can be written in parabolic approximation as:[80]

$$E_{l,n}^{e,h} = \frac{\hbar^2 \phi_{l,n}^2}{2m_{e,h}a^2}. \tag{2.1}$$

where $m_{e,h}$ is the electron and hole effective mass, a is the crystal radius, $\phi_{l,n}$ is the nth root of the spherical Bessel function of order l, $j_l(\phi_{l,n}) = 0$. The energy of the lowest electron and hole quantized levels increase with decreasing nanocrystal size, therefore increases the total energy of the band edge optical transitions. However, the Coulomb interaction between the optically created electron and hole strongly affects the optical properties and must be taken into consideration. Note that the quantization energy increases with decreasing size as $1/a^2$, while the Coulomb energy grows only as $1/a$, so that the later is only a small correction to the quantization energies of electrons and holes in small NCs and reduces transition energies by only a relatively small amount. But, in large NCs, the Coulomb interaction will become more important than the quantization energy. Therefore, for the analysis of experimental data, one needs to consider three different cases: $a \gg a_B$, $a \approx a_B$ and $a \ll a_B$ corresponding to the weak, intermediate and strong confinement regime, respectively. a_B is the Bohr radius of bulk exciton, $a_B = \hbar^2\varepsilon/\mu e^2$, where ε is the dielectric constant, μ is the exciton reduced mass.[81–83] The details about the three confinement Regimes are as following:

Weak Confinement Regime:
In the case of $a \gg a_B$, the binding energy of an exciton E_{ex} owing to the Coulomb interaction between electron and hole is larger than the quantization energy of both the electron and hole, therefore the optical spectra are determined by the quantum confinement of the exciton center of mass, and the exciton ground state energy is:

$$\hbar\omega = E_g - E_{ex} + \frac{\hbar^2\pi^2}{2Ma^2}. \tag{2.2}$$

where E_g is the semiconductor energy gap and $M = m_e + m_h$ is the exciton translation mass. This case is often realized in large crystals.

Intermediate Confinement Regime:
An interesting situation occurs in semiconductors with very different values of the electron and hole effective masses in an intermediate region of sizes $a_e > a > a_h$, where $a_e = \hbar^2\varepsilon/m_e e^2$and $a_h = \hbar^2\varepsilon/m_h e^2$ are the Bohr radii of electrons and holes, respectively. In this case, the hole moves in the average potential of the much faster electron and is localized at the center of the nanocrystal. The region of the hole motion around the crystal center in this case is much smaller than the nanocrystal radius, and the size dependence of the exciton ground state can then be described as the behavior of a donor localized at the nanocrystal center.

Strong Confinement Regime:
This case is realized in the small NCs where $a \ll a_B$. For these NCs, the optical spectra can be considered as spectra of transitions between electron and hole quantized levels and the electron-hole Coulomb interaction only slightly lowers the transition energy. Moreover, the optical transition is allowed only between levels with the same quantum numbers, the absorption spectra can be described by:

$$\hbar\omega = E_g + E_v^h(a) + E_v^e(a) - 1.8\frac{e^2}{\varepsilon a}. \tag{2.3}$$

where the Coulomb correction is calculated in first order perturbation theory.[83]

2.1.3 Dielectric confinement effect

In low-dimensional semiconductor structures, besides the spatial confinement, a difference between the dielectric constants inside (ε_{in}) the nanostructure and dielectric constants of the surrounding media (ε_{out}) leads to a dielectric confinement which affects the electron-hole Coulomb interaction.[84,85] The dielectric confinement effect is usually very small in semiconductor and semiconductor heterostructures due to the very close values of the dielectric constants, i.e. $\varepsilon_{in}/\varepsilon_{out} \approx 1$. But in semiconductor nanostructures, it becomes significant, and the energy spectra of excitons, their selection rules, and their optical polarization properties can be strongly affected.[86–89] It has been shown that in thin semiconductor films, the electric field of the carriers penetrates into the surrounding media with a smaller dielectric constant which leads to an enhancement of the exciton binding energy and a decrease in the exciton effective radius a_{ex}.[84] The smaller a_{ex} in turn increases the exciton oscillator strength and the electron-hole short-range exchange interaction, finally modifies the band-edge optical properties.

Generally, the dielectric confinement not only affects the Coulomb interaction between charges, but also changes the energy of a single particle, electron or hole, localized

inside the nanostructures. This effect can be described as the effective interaction of the electron (hole) with its own image charge that is positioned outside. The respective electron (hole) self-energy potential $V_{self(r_{e(h)})}$ should be added to the spatial confining potential $V_{pot(r_{e(h)})}$ created by the potential profile of the nanostructure. Therefore the final confining potential considering both spatial and dielectric confinement can be written as:

$$V_{conf(r_{e(h)})} = V_{pot(r_{e(h)})} + V_{self(r_{e(h)})}. \tag{2.4}$$

The self-energy potential $V_{self(r_{e(h)})}$ is always proportional to ε_{in} - ε_{out}. It is repulsive when $\varepsilon_{in}/\varepsilon_{out}$ >1 describing an effective surface polarization field pulling the carriers into the nanostructure, which leads to an additional confinement of the carriers.

2.1.4 Phonons in semiconductor nanocrystals

Phonons are quanta of atomic vibrations in crystalline solids. In a monoatomic solid with only one atom per primitive cell, one can have three acoustic phonon branches corresponding to the three degrees of freedom of atomic motion, one of longitudinal polarization and two of transverse polarization. In crystals with two atoms per primitive cell, new phonon features will show up, i.e. each polarization mode develops into two branches known as acoustic and optical branches, therefore we have one longitudinal acoustic phonon (LA), two transverse acoustic phonon (TA), one longitudinal optical phonon (LO) and two transverse optical phonon (TO).[90] In compounds with a greater number of atoms and complex crystal structures, the number of optical phonons is more than three. For example, if the crystal unit cell contains N atoms, then $3N$ degrees of freedom result in 3 acoustic phonons and $3N$ - 3 optical phonons. These phonons propagate in the lattice of a single crystal as a wave and exhibit dispersion depending on their wavelength or equivalently their wavevector in the Brillouin zone. However, phonon propagation will be interrupted when a grain boundary is encountered. This naturally happens in nanocrystals, this refers to the phonon confinement effect which is noticeable when the nanocrytal size is smaller than typically 20 lattice parameters.[91] The infrared absorption/reflectivity or Raman spectroscopy is helpful to probe the phonon spectra, but only the optical phonons close to the zone center can be measured as a consequence of the infinite periodicity of the crystal lattice. However, in the case of nanocrystals, this zone center rule is relaxed, therefore optical phonons away from the Brillouin zone center can contribute to the phonon lines and result in an asymmetric broadening of the phonon lineshape.

The confinement effect also modifies the acoustic phonon properties, Lamb firstly studied confined acoustic phonons in a small sphere in theory.[92] From his theory, two types of vibrational modes are obtained in an elastic sphere, i.e. spheroidal (also called ellipsoidal mode) and torsional modes, they are expressed by the spherical Bessel function. The spherical modes and the torsional modes are characterized by a branch

number n and an angular momentum l, and the frequencies of the lowest-energy spherical and torsional modes specified by $n = 0$ and $l = 2$ are calculated as:[93]

$$\omega_{OS}^2 = \omega_{OT}^2 = \frac{2.36}{D} v_l (n = 0, l = 2). \tag{2.5}$$

where ω_{OS} and ω_{OT} refer to the spherical and torsional mode frequencies, D is the diameter of NCs, v_l is the longitudinal sound velocity. The different vibratinal eigenmodes are shown schematically in Fig. 2.3, Figure 2.3(a) and Fig. 2.3(b) are the torsional and spherical modes.

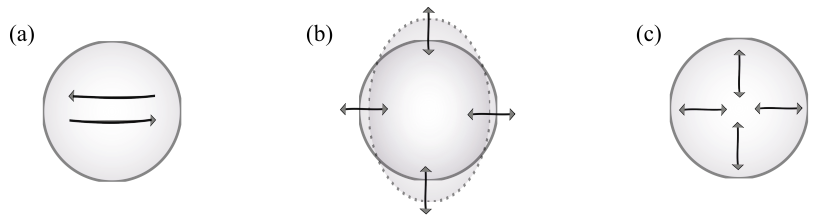

Figure 2.3: Vibratinal eigenmodes of a spherical particle: (a) the torsional mode, (b) the spherical or ellipsoidal mode, and (c) the breathing mode. Adapted from Ref.[93].

It has been reported that the phonon properties of NCs are strongly influenced by their surroundings, i.e. capped ligands, matrix.[93–96] For example, Schnitzenbaumer and Dukovic compared the phonon damping behavior in CdTe quantum dots (QDs), CdTe/CdSe core/shell QDs capped with octadecylphosphonic acid ligands, and CdTe QDs capped with Se^{2-}.[96] They found that the longitudinal optical phonons have similar frequencies and damping behavior in all three samples, however, the longitudinal acoustic phonon mode in the Se^{2-}-capped CdTe QDs is severely damped, much more than in CdTe and CdTe/CdSe QDs capped with the native aliphatic ligands. They attribute these differences to the way how the QD dissipates vibrational energy to its surroundings as a function of ligand identity. Using the spectral hole burning spectroscopy, Okamoto and Masumoto studied the confined acoustic phonons in CuCl NCs in glass and in NaCl matrix, they discovered that the acoustic phonon mode varies depending on the elastic constants of the surrounding matrices.[93] For CuCl NCs in glass, the spherical and torsional modes are observed, while for CuCl NCs embedded in NaCl host crystal, a new breadth modes with $n = 1$ and $l = 0$ was resolved as shown in Fig. 2.3(c) whose frequency is described as:

$$\omega_{OB}^2 = \frac{5.7}{D} v_l (n = 1, l = 0). \tag{2.6}$$

Moreover, the frequencies of different phonon modes are found to be proportional to the inverse of the nanocrystal diameter underlining the importance of quantum confinement in determining the phonon properties.[93] Saviot et al.[97] investigated the size

dependence of the acoustic and optical vibrational modes in CdSe NCs embedded in glass matrix using resonant Raman scattering. In the low-frequency Raman scattering range, they observed a fine structure due to the confinement of acoustic modes, and the Raman line corresponding to the interaction with the optical modes shifts and widens with a decreasing of the particle size. These results can be well explained by a single model in terms of eigenvibrations of spherical nanocrystallites. It is worth noting that both acoustic and optical phonons play an important role in the energy relaxation, exciton recombination and coherence processes. [94,95,98,99]

2.2 Band-edge exciton fine structure

The bright-dark exciton model proposed by Efros et al. in 1996 [62] achieved great success in explaining the optical properties of II-VI and III-V colloidal semiconductor NCs. However, in the first version of the model, they did not take into account the long-range exchange interaction, resulting in the underestimation of the splitting between the upper bright and lower dark exciton states. Later on, they included the long-range exchange interaction and made an additional correction concerning the closeness in energy of the ground ($1S_{3/2}$) and the first excited ($1P_{3/2}$) hole levels in spherical NCs. [100] The effects of image charge connected with the discontinuity of dielectric constants at the nanocrystal surface and the self-interaction of the electron and hole with their own images are also included in the improved model (see 2.1.3). [100,101] Recently, along with the availability of pervoskite NCs and the discovery of novel optical properties, a new theory of exciton fine structures for these novel materials has been developed by additionally including the Rashba effect. [101,102] In this section, we first introduce the model for II-VI and III-V colloidal semiconductor NCs, and then turn to the new model for pervoskite NCs.

2.2.1 Bright-dark exciton model for II-VI and III-V semiconductor nanocrystals

The bright-dark exciton model was firstly proposed and tested on CdSe and CdTe NCs, [62] but actually it can be applied to describe the exciton fine structure in all II-VI and III-V semiconductor NCs. Here, we take CdSe as an example to introduce the latest version of the model. [100]

2.2.1.1 Band-edge $1S_{3/2}$ $1S_e$ exciton fine structure

The band-edge exciton fine structure level diagram is shown in Fig. 2.4. In spherically symmetric CdSe NCs with a cubic lattice structure or quasi-symmetric NCs in which

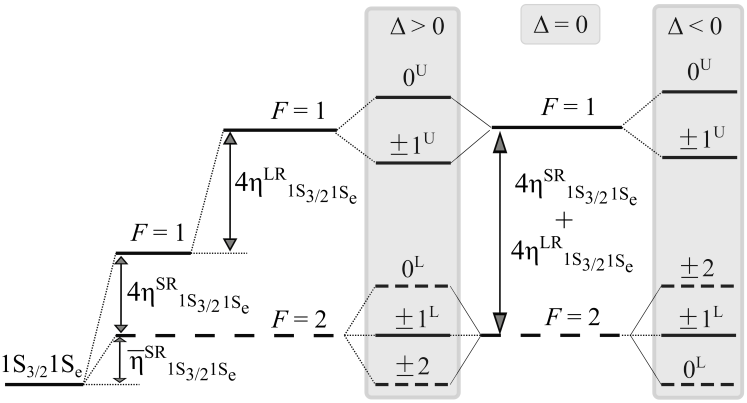

Figure 2.4: Fine structure of the exciton levels within the $1S_{3/2}1S_e$ exciton manifold created by short- and long-range electron-hole exchange interactions ($4\eta^{SR}_{1S_{3/2}1S_e}$, $4\eta^{LR}_{1S_{3/2}1S_e}$) and hole level splitting Δ due to crystal field splitting Δ_{int} as well as shape anisotropy splitting Δ_{sh}, $\Delta = \Delta_{int} + \Delta_{sh}$. The level structures are shown for the cases $\Delta > 0$, $\Delta = 0$, and $\Delta < 0$. The horizontal dash lines correspond to the optically forbidden dark states, solid lines represent the optically active states. Adapted from Ref. [100].

the effect of shape asymmetry on the hole energy spectra is compensated by the effect of the hexagonal crystal field, the electron ground $1S_e$ level is doubly degenerate with respect to its spin projection, $s_z = \pm 1/2$, and the hole ground $1S_{3/2}$ level is 4-fold degenerate with respect to the angular momentum projections $M = 3/2$,1/2, -1/2, and -3/2 on nanocrytal quantization axis. Therefore, the band-edge optical transition is 8 fold degenerated.

The electron-hole exchange interaction, given by:

$$\widehat{H}^{exch}_{1S_{3/2}1S_e} = \eta_{1S_{3/2}1S_e}\left[\frac{3}{2}\| - (\sigma_e \cdot F)\right] + \overline{\eta}_{1S_{3/2}1S_e}\|. \tag{2.7}$$

splits the 8-fold degenerate exciton state in spherical NCs into a ground optically passive (dark) 5-fold degenerate state with a total angular momentum projection of $F = 2$ and an upper optically active 3-fold degenerate state with $F = 1$, leaving a energy gap which is $4\eta_{1S_{3/2}1S_e}$. $\eta_{1S_{3/2}1S_e}$ is the electron-hole exchange constant, $\|$ is the 8 x 8 unit matrix, and σ_e is the electron Pauli matrix. Note that Eq. (2.7) describes the absolute position of the exciton fine structure levels relative to the reference energy of the lowest optical $1S_{3/2}1S_e$ transition in the absence of exchange interaction. The first term describes the asymmetric splitting of the $F = 1$ and $F = 2$ levels, and the second term describes an overall shift of all fine structure levels from the reference energy.

Including the internal hexagonal crystal field and nonspherical ellipsoidal shape of NCs will break the spherical symmetry and split $M = \pm$ 3/2 and $\pm$ 1/2 hole sublevels.

The splitting is described by:[62]

$$\widehat{H}^{an} = (\Delta/2)\left[5/4 - M^2\right]. \tag{2.8}$$

where the total hole level splitting $\Delta = \Delta_{int} + \Delta_{sh}$. Δ_{int} and Δ_{sh} refer to the splitting caused by the hexagonal field and shape anisotropy, respectively. The splitting described by Eq. (2.8) finally results in five band-edge exciton states with total momentum projections $F_z = M + s_z$ on the hexagonal c-axis of the NC. The levels are labeled by F_z: one level with $F_z = \pm 2$, two with $F_z = \pm 1$, and two with $F_z = 0$. Both of the ± 1 states (1^L and 1^U, U, L correspond to the upper and lower states) are optically active bright excitons. For the states with $F_z = 0$, only the upper one, 0^U, is optically active (solid lines), while the lower one, 0^L, is an optically passive dark exciton (dashed lines), as labeled in Fig. 2.4. When $\Delta > 0$ (oblate CdSe NCs), the ground exciton is the optically forbidden dark exciton with $F_z = \pm 2$, and when $\Delta < 0$, it is the dark 0^L exciton level with $F_z = 0$.

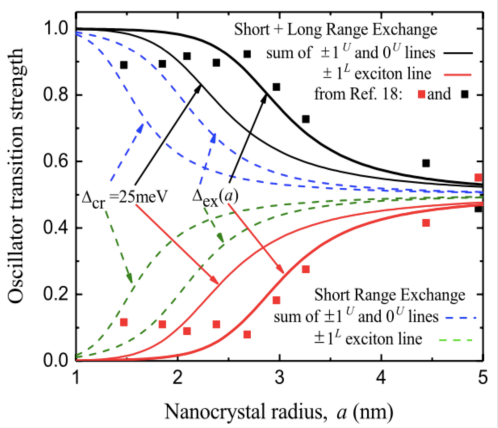

Figure 2.5: The relative oscillator transition strengths calculated with and without the long range exchange interaction for models with various light-heavy hole splitting Δ are compared with the experimental results. Curves labelled $\Delta_{cr} = 25$ meV were calculated for spherical shaped NCs with fixed bulk crystal field splitting parameter $\Delta_{cr} = 25$ meV. The curves labeled Δ_{ex} include, in addition to the bulk crystal field splitting, the splitting connected with the NC shape anisotropyΔ_{sh}. The total experimental splitting $\Delta_{ex} = \Delta_{int} + \Delta_{sh}$ takes into account the experimentally determined size variation of nanocrystal ellipticity, along with the calculated values of Δ_{int} and Δ_{sh}. Adapted from Ref.[100].

In the first version of bright-dark exciton model,[62] the long-range exchange interaction is completely neglected, in order to have a better description of the band-edge exciton fine structure, it must also be included into the theory. The terms "long-range" and "short-range" exchange refer to the nonanalytic and analytic portions of the exchange interaction, respectively, as defined in Ref.[103]. With this definition, the short-range exchange interaction $\eta^{SR}_{1S_{3/2}1S_e}$ within the $1S_{3/2}1S_e$ exciton manifold in the

strong confinement regime can be written as:

$$\eta^{SR}_{1S_{3/2}1S_e} = \hbar\omega_{ST}\chi_{1S_{3/2}1S_e}(\beta)(a_{ex}/a)^3. \tag{2.9}$$

where $\hbar\omega_{ST} = 0.13$ meV is the short-range exchange splitting in bulk CdSe, a_{ex} is the bulk exciton radius, a is the NC radius, and the dimensionless function $\chi_{1S_{3/2}1S_e}(\beta)$, which depends on β, the ratio of light- to heavy-hole effective mass. While the long-range exchange interaction, $\eta^{LR}_{1S_{3/2}1S_e}$ can be written as:

$$\eta^{LR}_{1S_{3/2}1S_e} = \frac{\hbar\omega_{LT}}{4}\left(\frac{a_{ex}}{a}\right)^3\left[\xi_{1S_{3/2}1S_e}(\beta) + \{\frac{\kappa-1}{\kappa+2}\}\frac{2|Q_0^{(1)}(\beta)|^2}{3}\right]. \tag{2.10}$$

where $\hbar\omega_{LT}$ is the bulk exciton longitudinal transverse splitting, which, in CdSe, is equal to 0.95 meV. $\xi_{1S_{3/2}1S_e}(\beta)$ and $Q_0^{(1)}(\beta)$ are dimensionless functions, and κ is the ratio of internal, ε_{in}, to external, ε_{out}, high-frequency dielectric constants.

Goupalov and Ivchenko[104] carefully studied the electron-hole exchange interactions in semiconductors within the framework of empirical tight-binding model. They found that long-range exchange corrections should be included when the band-edge optical transitions are principally interatomic (as in the case of anion- to-cation transitions between the nearest neighbors in many binary semiconductors), while in the case where the band-edge optical transitions are principally intra-atomic in nature, the long-range contribution vanishes in spherical nanocrystals, consistent with the argument of Takagahara.[105] CdSe belongs to the first situation, and the long-range exchange interaction is estimated to be 2.5 times larger than the short-range term. Its strong impact on the optical properties in semiconductor NCs is shown in Fig. 2.5 where the size dependent relative oscillator transition strengths of optically allowed transition change significantly by including additionally long-range exchange interaction.

2.2.1.2 Effect of $1P_{3/2}$ $1S_e$ exciton manifold

The effect of the $1P_{3/2}$ $1S_e$ exciton on the optical properties needs to be paid careful attention, because for example in small CdSe NCs, the ground $1S_{3/2}$ hole level is not energetically far away from the first excited $1P_{3/2}$ level,[106] therefore the crystal field, NC shape anisotropy, and the electron-hole exchange interaction can lead to overlapping between these two exciton manifolds. This effect becomes even more pronounced in NCs made from semiconductors with weak spin-orbit coupling effect, where the $1S_{3/2}$ and $1P_{3/2}$ hole levels can even switch order with decrease of the NC size, resulting in the $1P_{3/2}$ state becoming the ground hole confinement level, lying below the $1S_{3/2}$ hole levels.[107] The fine structure of the exciton levels for the $1P_{3/2}1S_e$ exciton manifold are shown schematically in the Fig. 2.6. Although the $1P_{3/2}1S_e$ states are dipole-forbidden due to parity, they still show a nonzero long-range exchange correction due to the fact

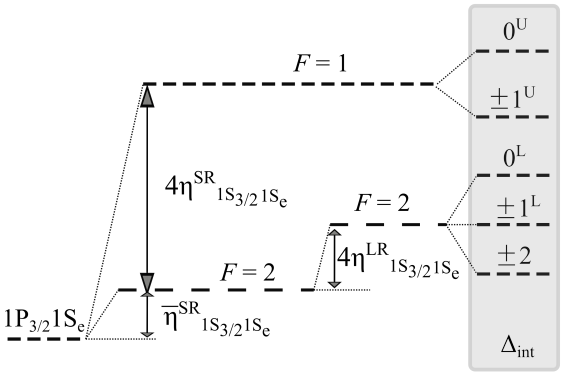

Figure 2.6: Fine structure of the exciton levels within the $1P_{3/2}1S_e$ exciton manifold created by short- and long-range electron-hole exchange interactions ($4\eta^{SR}_{1S_{3/2}1S_e}$, $4\eta^{LR}_{1S_{3/2}1S_e}$) and hole level splitting Δ_{int} due to crystal field splitting only. All states are dark due to parity, therefore all levels are marked by dashed lines. Adapted from Ref. [100].

that the long-range exchange effect in NCs is originated from longitudinal electric field coupling, the selection rules could be different from coupling to propagating transverse electric fields. [100]

As for the $1P_{3/2}1S_e$ state, its effect on the nanocrystal photoluminescence is of most interest for the discussion of the band-edge exciton fine structure based on the temperature dependent photoluminescence decay. Since optical selection rules do not allow transitions between the $1P_{3/2}$ hole and the $1S_e$ electron levels in II-VI and III-V semiconductor spherical NCs due to their different parity of the wave functions, all eight $1P_{3/2}1S_e$ exciton states are dipole-forbidden or dark. This generally increases the total number of optically passive dark excitons at the band edge from 5 to 13 and decreases the radiative decay rate by a factor of 3/16 at high temperatures for which the exciton states from both the $1P_{3/2}1S_e$ and the $1S_{3/2}1S_e$ manifolds are equally populated. The characteristic radiative decay rate $1/\tau_{ex}$ in II-VI and III-V semiconductor spherical nanocrystals is described as:

$$\frac{1}{\tau_{ex}} = \frac{8\omega n E_p}{9 \cdot 137 m_0 c^2} D^2 K. \tag{2.11}$$

where ω is the frequency of emitted light, n is the refractive index of the surrounding medium, E_p is the Kane energy parameter, m_0 is the free electron mass, $D = 3\varepsilon_{out}/(2\varepsilon_{out} + \varepsilon_{in})$ is the depolarization factor, wherein $\varepsilon_{out} = n^2$ and ε_{in} are high-frequency dielectric constants of the medium and semiconductor, respectively.

$$K = |\int d^3_{r_e} d^3_{r_h} \Psi_{ex}(r_e,r_h)\delta(r_e - r_h)|^2. \tag{2.12}$$

K is the square of the overlap integral between the electron and hole within the wave function of a confined exciton $\Psi_{ex}(r_e,r_h)$. For temperatures that populate all 16 band-edge excitons, the decay time can be estimated as $\tau_{rd} = (16/3)\tau_{ex}$. This indicates clearly

that at high temperature, i.e. room temperature, some of the upper optically active exciton states from the $1P_{3/2}1S_e$ manifolds are partially populated and will contribute to photoluminescence (PL), this needs to be paid careful attention when one tries to estimate the bright-dark splitting by analyzing the temperature dependence of PL decay.[108,109]

2.2.2 Exciton fine structure in perovskite nanocrystals

Studies on various materials have found that the lowest exciton sublevel is dark, and its optical transition to the ground state is dipole-forbidden. However, in all-inorganic cesium lead halide perovskites $CsPbX_3$ (X = Cl, Br, I) NCs, the lowest exciton sublevel has been reported to be bright.[102] This anomalous band-edge exciton fine structure has attracted a lot of interests, although it is only reported by now in $CsPbX_3$ NCs and also later reports show some conflicts, i.e. the ground state is still dark, in $CsPbX_3$ or $CsPbX_3$-based NCs.[63,110,111] Recently, Sercel et al.[101] reviewed the effective-mass/electron-hole exchange theory for the exciton fine structure in cubic and tetragonal $CsPbBr_3$ NCs. Their calculation shows that within the exchange model, the ground exciton level is optically inactive, and in tetragonal $CsPbBr_3$ NCs, the level order for the optically active excitons is opposite to what has been reported experimentally by Becker.[102] An explanation for the observed bright exciton level order is offered in terms of the Rashba effect, which supports the existence of a bright ground-state exciton in these NCs. It is also noted that, in small NCs, the bright-dark level inversion caused by the Rashba effect is suppressed by the enhanced electron-hole exchange interaction. In this section, we first discuss the structure of perovskite $CsPbX_3$, then introduce the theory for explaining band-edge exciton fine structure in perovskite NCs.

2.2.2.1 Lattice structure of perovskite $CsPbX_3$

The perovskite material has the general formula of ABX_3, where A is a monovalent cation, B is usually a divalent cation of dissimilar size, and X is a monovalent anion to achieve charge neutrality. The basic structure of perovskite is an octahedron, whereas the final structure of the bulk material can be anything from a high-symmetry cuboid to a low-symmetry monoclinic structure.[113] The materials used in our study are all-inorganic $CsPbX_3$ perovskites with X being Br and I.

Phase transitions in perovskites are very diverse. The undistorted perovskite is normally denoted as α-phase (cubic), the perovskite structure after the first phase transition is marked as β-phase (tetragonal), after the second phase transition is referred as γ-phase (orthorhombic), and the non-perovskite structure is named as δ-phase (orthorhombic).[114] These phase transitions are fully reversible as shown in Fig. 2.7. Taking $CsPbI_3$ as an example,[112] at room temperature, it is stable in the δ-phase

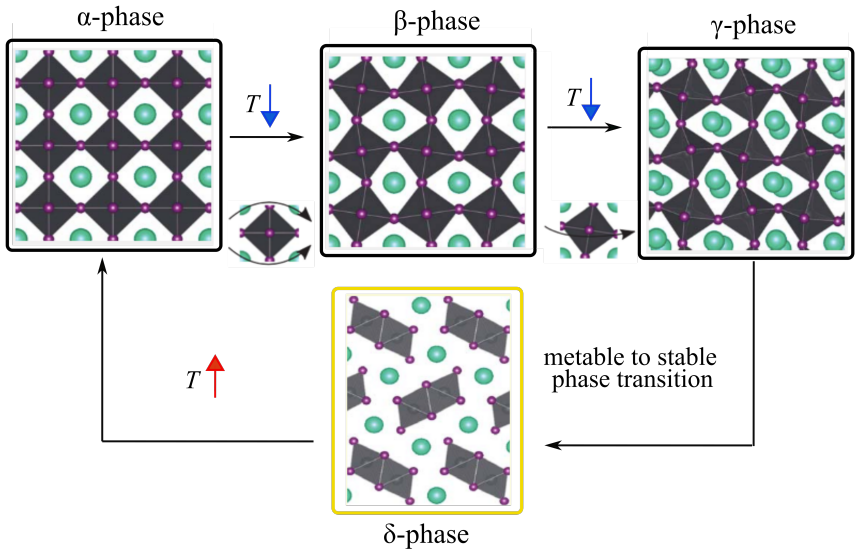

Figure 2.7: Crystal structure of different phases and their relative transitions in perovskite. The transitions between the black phases are governed by the local Pb-centered octahedral distortions, which is depicted using one lead atom at the center and six iodide atoms at the edges (purple) confining the cesium cations (cyan). T with blue (red) arrows indicates decreasing (increasing) temperature. Adapted from Ref. [112].

(yellow) which converts to the black perovskite α-phase once heating above 360 °C. Upon cooling, the perovskite structure remains kinetically stabilized converting to the black perovskite β- and γ-phases at 260 and 175 °C, respectively. [114]

As for $CsPbBr_3$, it crystallizes in the orthorhombic phase at room temperature. The Pb-centered octahedral distortion occurs through two successive phase transitions at 88 and 130 °C transforming the crystal structure to tetragonal and cubic, respectively. [115] However, due to the large surface-to-volume, perovskite NCs are able to be stabilized at certain phase at temperatures deviating from the phase-stable temperature region. [116,117]

2.2.2.2 Bright and dark exciton states: role of Rashba effect

The $CsPbX_3$ perovskite crystals comprise corner-sharing PbX_6 octahedra with Cs^+ ions filling the octahedral voids, the cubic phase structure is shown as an example in Fig. 2.8. The bandgap is located at the R point in the Brillouin zone, near which the valence and conduction bands are well described within the effective-mass model. [102] The top of the valence band arises from a mixture of Pb $6s$ and Br $4p$ atomic orbitals with an overall s symmetry, which is doubly degenerated with respect to the spin freedom with $J_h = 1/2$. The conduction band consists of Pb $6p$ orbitals, due to the large spin-

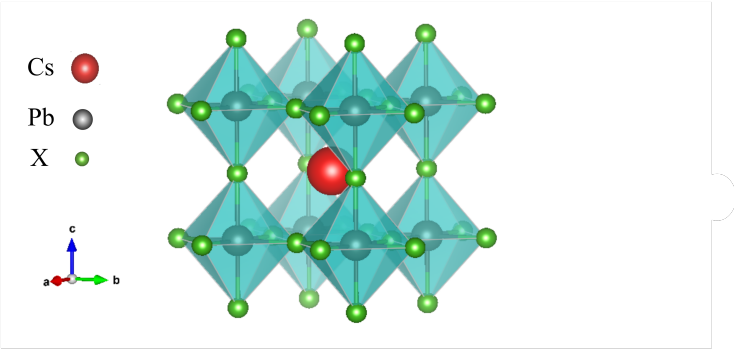

Figure 2.8: Crystal structure of $CsPbX_3$ in cubic phase.

orbit coupling effect, the electron at the bottom of the conduction band becomes also doubly degenerate with $J_e = 1/2$. When the momentum of electron and hole states are combined, the band-edge exciton state splits as a result of electron-hole exchange into a singlet state $J = 0$ and a threefold degenerate triplet state $J = 1$.[102] A complete diagram for the band-edge exciton fine structure is shown in Fig. 2.9. If only electron and hole exchange interaction (both short-range and long-range exchange interaction) is considered, the ground exciton level is dark or optically inactive. The crystal field splits the $J = 1$ level into three sublevels, but will not change the ordering between dark and bright levels. However, the Rashba effect is able to revert exciton levels and makes the triplet bright exciton ground state possible. Although the study of Rashba effect is very tricky, several methods have been applied to tackle this question.[73,118–120] For example, Isarov et al. performed magneto-optical measurements at cryogenic temperatures on $CsPbBr_3$ NCs in various magnetic fields. They observed a nonlinear energy splitting between polarized transitions versus the magnetic field as well as a crossover between the Rashba effect and Zeeman effect at fields above 4 T. They assign the origin of the Rashba effect to the lattice distortion induced by Cs^+ motion degree of freedom or due to a surface effect in nanoscale NCs.[73]

If one focuses on NCs with tetragonal crystal symmetry and takes the inversion symmetry-breaking direction v_z along the z axis as the tetragonal c axis, the Rashba Hamiltonian $H_R^{e(h)}$ for electrons (holes) can be written as:

$$H_R^{e(h)} = \alpha_{e(h)} v_z (\sigma_x^{e(h)} \widehat{P}_y^{e(h)} - \sigma_y^{e(h)} \widehat{P}_x^{e(h)})/\hbar. \tag{2.13}$$

where α_e and α_h are the Rashba coefficients for the electron and hole, $\sigma_x^{e(h)}$ and $\sigma_y^{e(h)}$ are Pauli operators representing the electron (hole) spin components along x and y axes, $\widehat{P}_x^{e(h)}$ and $\widehat{P}_y^{e(h)}$ are momentum operators of the electron (hole) along x and y axes. It is noted that the Rashba terms do not affect the exciton fine structure in the strong confinement limit where electron and hole motion are uncorrelated. However, in the weak confinement limit, they lead to exciton fine structure splitting that can be found in second order perturbation theory.[101] In NCs having tetragonal crystal

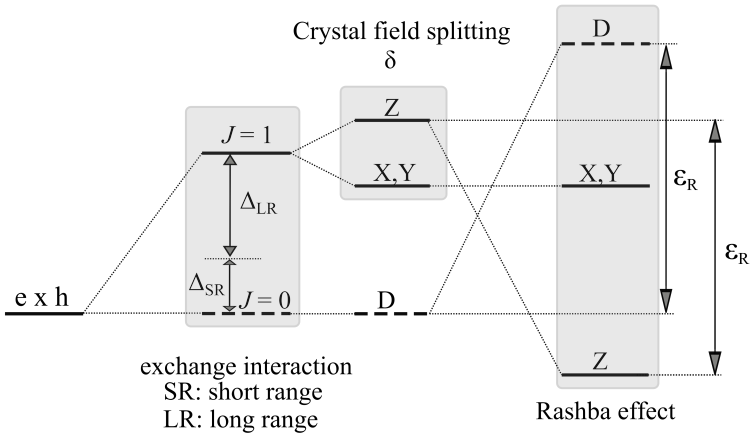

Figure 2.9: The fine structure of the band-edge exciton levels created by the short-range (SR) and long-range (LR) electron-hole exchange interaction, crystal field splitting (δ), and Rashba splitting. The level structures are shown for a cube-shaped nanocrystal with tetragonal crystal structure and positive crystal field ($\delta > 0$). The right-hand side of the figure shows the effect of Rashba splitting with a symmetry breaking axis along the z direction taken as the c crystallographic axis, with splitting energy ε_R. The horizontal dash lines correspond to the optically forbidden dark states, solid lines represent the optically active states. Adapted from Ref. [101].

symmetry, the exciton fine structure correction is described as:

$$\Delta E^R = -2(A_c - A_r)\varepsilon_R(\sigma_x^e\sigma_x^h + \sigma_y^e\sigma_y^h). \tag{2.14}$$

where A_c and A_r are coefficients reflecting the center-of-mass and relative motion of the exciton, $\varepsilon_R = \sigma_e\sigma_h\mu/\hbar^2$ is the exciton Rashba energy.

2.2.3 Effect of Coulomb impurities induced symmetry descent on the exciton fine structure

Doping has been demonstrated to be an efficient tool for modifying the optical properties of semiconductors and their nanostructures. Based on the standard cation-exchange colloidal synthesis procedure, Sahu and colleagues synthesized Ag-doped CdSe NCs with well controlled dopant concentration and studied the optical properties. They observed that at lower doping concentration, the addition of even one impurity per nanocrystal causes a dramatic enhancement in the fluorescence efficiency. [121]

Inspired by these experimental results, Sercel et al. [122] investigated theoretically the effect of symmetry breaking introduced by the doping of semiconductor NCs with Coulomb impurities, where they found that the presence of a Coulomb center breaks the nanocrystal symmetry and affects its optical properties through the mixing of the

hole spin and parity sublevels. The descent of the NC symmetry from spherical to C_s, which is characterized by just one mirror plane symmetry element, leads step by step to the activation of all five $F_z = \pm 2, \pm 1, 0$ excitons. Even the ground exciton becomes optically active, which is expected to be seen in low temperature photoluminescence measurements. Their calculation shows that the symmetry breaking happens by two mechanisms: first, mixing by even parity terms in the Coulomb multipole expansion results in an exciton fine structure consisting of three optically active doublets which are polarized along x, y, and z axes with a ground optically passive dark exciton state; second, odd parity terms which break inversion symmetry significantly and activate optical transitions which are optically forbidden in the unperturbed nanocrystal due to both spin and parity selection rules. Furthermore, in the case of small sized quasi-spherical nanocrystals, the introduction of a single positively charged Coulomb center is shown to result in significant enhancement of the radiative decay rate at room temperatures by up to a factor of 10.

2.3 Recombination mechanisms of the dark exciton

Dark excitons in colloidal semiconductor NCs are in principle optically forbidden based on the electric dipole approximation, however in practice, they do emit photons and can be well resolved by techniques like fluorescence line narrowing (FLN) [61] and single dot photoluminescence (PL) spectra.[108,123] There are several mechanisms that assist their recombination, i.e. temperature-induced bright-dark state repopulation,[108] magnetic field induced bright-dark state mixing,[61,62] dangling bound spin assisted recombination,[124,125] crystal symmetry decent [122] and possible nuclear spin assisted recombination of dark exciton states,[126] which is similar to the case of dangling bond spins but have never been systematically studied in colloidal semiconductor NCs. In this part, we summarize all the mechanisms reported up to now in literature to present a complete picture of dark exciton recombination physics in colloidal semiconductor NCs.

2.3.1 Phonon assisted recombination

The dark exciton transition is optically forbidden because its total angular momentum along the quantization axis is $\pm$ 2, while photon can only carry momentum $\pm$ 1. To meet the conservation law of angular momentum, other particles or quasiparticles need to be introduced into the process. Phonons are naturally the best candidates since they are easily populated or depopulated by increasing or decreasing the temperature. Here, only the lowest dark exciton state and the first close bright exciton state are considered, the possible contribution from the $1P_{3/2}$ $1S_e$ exciton manifold is neglected. The exciton fine structure at zero magnetic field is shown in Fig. 2.10.

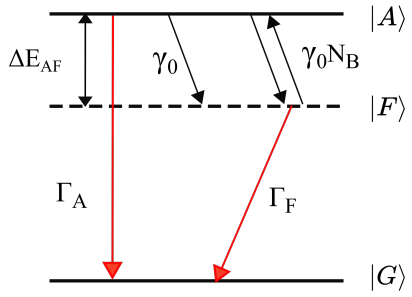

Figure 2.10: Scheme of exciton energy levels. $|A\rangle$, $|F\rangle$, and $|G\rangle$ denote bright and dark exciton states, and crystal ground state, respectively. ΔE_{AF} is the bright-dark splitting. γ_0 is the zero-temperature relaxation rate from the bright to the dark exciton state. $\gamma_0 N_B$ is the thermal activation rate. Γ_A and Γ_F are the recombination rates of the bright and dark excitons.

The recombination rates of the upper lying bright $|A\rangle$ and the lower dark $|F\rangle$ states are Γ_A and Γ_F. The PL intensity in this case can be written as $I(t) = \eta_A \Gamma_A p_A + \eta_F \Gamma_F p_F$, where $\eta_{A,F}$ are the corresponding quantum efficiencies, and $p_{\mathrm{A,F}}$ are the occupation numbers of the corresponding levels. The relaxation rates between these levels are given by γ_0 and γ_{th}, where γ_0 is the zero-temperature relaxation rate from the bright to the dark exciton state, and $\gamma_{th} = \gamma_0 N_B$ corresponds to the thermally-activated relaxation rate between the dark and bright exciton states, $N_B = 1/\left[\exp(\Delta E_{AF}/k_B T) - 1\right]$ is the Bose–Einstein phonon number at temperature T, k_B is the Boltzmann constant. Assuming that γ_0, Γ_A and Γ_F are temperature independent parameters, the system dynamics can be described by the set of rate equations:

$$\begin{aligned} \frac{dp_A}{dt} &= -\left[\Gamma_A + \gamma_0(N_B+1)\right] p_A + \gamma_0 N_B p_F, \\ \frac{dp_F}{dt} &= -\left[\Gamma_F + \gamma_0 N_B\right] p_F + \gamma_0(N_B+1) p_A. \end{aligned} \tag{2.15}$$

The corresponding solutions are:

$$\begin{aligned} p_A &= C_1 e^{-t\Gamma_{short}} + C_2 e^{-t\Gamma_{long}}, \\ p_F &= C_3 e^{-t\Gamma_{short}} + C_4 e^{-t\Gamma_{long}}, \end{aligned} \tag{2.16}$$

with $\Gamma_{short} = \tau_{short}^{-1}$ and $\Gamma_{long} = \tau_{long}^{-1}$ being the rates for the short- and long-lasting PL decays, τ_{long} and τ_{short} are the corresponding time constants:

$$\begin{aligned} \Gamma_{short,long}(T) = \frac{1}{2}\left[\Gamma_A + \Gamma_F + \gamma_0 \coth\left(\frac{\Delta E_{AF}}{2k_B T}\right)\right] \\ \pm \frac{1}{2}\sqrt{(\Gamma_A - \Gamma_F + \gamma_0)^2 + \gamma_0^2 \sinh^{-2}\left(\frac{\Delta E_{AF}}{2k_B T}\right)}, \end{aligned} \tag{2.17}$$

Here the formula with sign '+' in front of the square root corresponds to Γ_{short}, and the formula with sign '−' describes Γ_{long}.

For nonresonant excitation, after the laser pulse absorption, $|A\rangle$ and $|F\rangle$ levels are assumed to be equally populated with $p_{\mathrm{A}}(t=0) = p_{\mathrm{F}}(t=0) = 0.5$, which gives:

$$\begin{aligned} p_A &= C_1 e^{-t\Gamma_{short}} + (0.5 - C_1) e^{-t\Gamma_{long}}, \\ p_F &= C_3 e^{-t\Gamma_{short}} + (0.5 - C_3) e^{-t\Gamma_{long}}. \end{aligned} \tag{2.18}$$

Here C_1 and C_3 are temperature dependent parameters:

$$\begin{aligned} C_1 &= \frac{\gamma_0 + \Gamma_A - \Gamma_{long}}{2(\Gamma_{short} - \Gamma_{long})}, \\ C_3 &= \frac{-\gamma_0 + \Gamma_F - \Gamma_{long}}{2(\Gamma_{short} - \Gamma_{long})}. \end{aligned} \tag{2.19}$$

The PL intensity is then described by:

$$I(t) = \left[\eta_A \Gamma_A C_1 + \eta_F \Gamma_F C_3\right] e^{-t\Gamma_{short}} + \left[\eta_A \Gamma_A (0.5 - C_1) + \eta_F \Gamma_F (0.5 - C_3)\right] e^{-t\Gamma_{long}}. \tag{2.20}$$

This dependence represents a bi-exponential PL decay, as typically observed in colloidal NCs at cryogenic temperatures. Indeed, after nonresonant photoexcitation and energy relaxation of excitons, the bright and dark states at $t = 0$ are equally populated, but only the emission from the bright exciton is observed due to $\Gamma_A \gg \Gamma_F$. In the limit $k_B T = 0$, the excitons relax to the $|F\rangle$ state with a rate γ_0. These two processes, namely, recombination of the bright exciton and relaxation to the dark state, result in a fast initial drop of the time-resolved PL with a rate $\Gamma_{short} = \Gamma_A + \gamma_0(1+2N_B) \approx \gamma_0(1+2N_B)$. At longer delays, the $|A\rangle$ level is empty, and the emission arises from the $|F\rangle$ state with a rate $\Gamma_{long} = \Gamma_F$.

At a temperature of a few Kelvin, when $\Delta E_{AF} \gg k_B T$ the time-resolved PL is also bi-exponential with the decay rates Γ_{short} and Γ_{long} defined by Eq. (2.17). When the temperature is increased, the short-lived (long-lived) component decelerates (accelerates). If $\gamma_0 \gg \Gamma_A$, at elevated temperatures corresponding to $\Delta E_{AF} \leq k_B T$ the decay turns to be mono-exponential with $\Gamma_{long} = (\Gamma_A + \Gamma_F)/2$. Therefore, the temperature dependence of the Γ_{long} can be used as a powerful tool to estimate the ΔE_{AF} value. This has been tested at the single dot level, and the energy splitting obtained by it is in excellent agreement with the energy splitting directly measured from the FLN spectra.[123] The analysis of the temperature dependence of the time-resolved PL decay is routinely used to evaluate ΔE_{AF} in NCs.[70,109,127,128] However, this method is indirect and might be affected by thermal activation of trap states, surface dangling bonds, contributions from higher energy states[129] and $1P_{3/2}\ 1S_e$ exciton manifold.

Generally in colloidal NCs, like CdSe, $\gamma_0 \gg \Gamma_A \gg \Gamma_F$, thus Eq. (2.17) can be simplified:[108]

$$I(t) = \frac{\eta_A \Gamma_A N_B + \eta_F \Gamma_F}{1 + 2N_B} \exp\left(-\frac{t}{\tau_{long}}\right) + \eta_A \Gamma_A \left[N_A(0) - \frac{N_B}{1 + 2N_B}\right] \exp\left(-\frac{t}{\tau_{short}}\right), \tag{2.21}$$

$$\tau_{long}^{-1}(T) = \frac{\Gamma_F + \Gamma_A}{2} - \left(\frac{\Gamma_A - \Gamma_F}{2}\right) \tanh\left(\frac{\Delta E_{AF}}{2k_B T}\right), \tag{2.22}$$

$$\tau_{short}^{-1} = \gamma_0(1 + 2N_B). \tag{2.23}$$

The temperature dependence of the PL decay of excitons in neutral NCs can be described by the Eq. (2.21) - Eq. (2.23). ΔE_{AF} can be evaluated by fitting an experimentally measured temperature dependence of $\tau_{long}^{-1}(T)$ with Eq. (2.22). Note that Eq. (2.21) - Eq. (2.23) are based on the assumption $\gamma_0 \gg \Gamma_A \gg \Gamma_F$ which can not hold in some cases like CdSe NPLs[109] and perovskite NCs.[63] In order to analyze the recombination dynamics in perovskite semiconductor NCs, Chen et al. took the assumption γ_0, $\Gamma_A \gg \Gamma_F$[63] at low temperature ($k_B T \ll \Delta E_{AF}$), therefore Eq. (2.17) is simplified to:

$$\tau_{long}^{-1}(T) = \Gamma_F + \frac{N_B \gamma_0 \Gamma_A}{\Gamma_A + \gamma_0(2N_B + 1)}, \tag{2.24}$$

$$\tau_{short}^{-1} = \Gamma_A + \gamma_0(2N_B + 1). \tag{2.25}$$

However, using the one-acoustic-phonon thermal mixing model described in Fig. 2.10, Fu et al.[130] failed to fit their data, so they proposed a three-level two-LO-phonon thermal mixing model[65,130] to explain the recombination dynamics, and the basic idea is shown in Fig. 2.11. Similar to the one-acoustic-phonon model, the optically forbidden dark state $|F\rangle$ lies below the optically allowed bright state $|A\rangle$, being separated by the bright-dark energy splitting ΔE_{AF}.[65,130] The fast component of the PL decay is assigned to the recombination of bright excitons with recombination rate Γ_A and the rapid thermalization of exciton from $|A\rangle$ to $|F\rangle$ state. The long component corresponds to the dark exciton recombination with the rate Γ_F. The main difference here is that the recombination of dark excitons is assisted by the absorption and emission of LO phonons, e.g. LO_1 and LO_2, whose energy difference matches the bright-dark splitting. The decay rates of the long and the short components of the PL decay, Γ_{long} and Γ_{short}, are given by:

$$\tau_{long,short}^{-1} = \frac{1}{2}\{\Gamma_A + \Gamma_F + \gamma_\uparrow + \gamma_\downarrow \pm \sqrt{[\Gamma_A - \Gamma_F + \gamma_\downarrow - \gamma_\uparrow]^2 + 4\gamma_\uparrow\gamma_\downarrow}\}. \tag{2.26}$$

where Γ_A and Γ_F are decay rates of the bright and dark excitons, $\gamma_\uparrow = \gamma_0 N_{LO_1}(\ \gamma_0 N_{LO_2} + 1)$ and $\gamma_\downarrow = \gamma_0 N_{LO_2}(\ \gamma_0 N_{LO_1} + 1)$, $N_{LO_i} = 1/[exp(E_{LO_i}/k_B T) - 1]$ are the Bose-Einstein phonon numbers (i = 1,2), γ_0 is a characteristic two-phonon mixing rate, and E_{LO_i} is the energy of LO_i phonon.

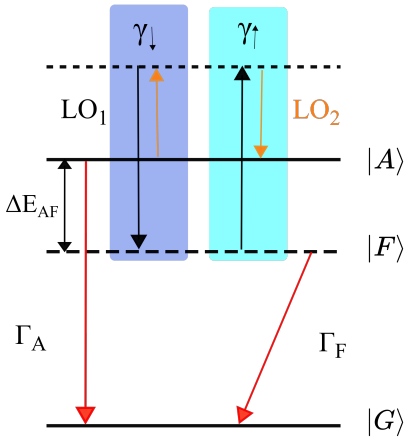

Figure 2.11: Scheme of three-level two-LO-phonon thermal mixing model. $|A\rangle$, $|F\rangle$, and $|G\rangle$ denote the bright and dark exciton states, and the crystal ground state, respectively. ΔE_{AF} is the bright-dark splitting. Γ_A and Γ_F are the recombination rates of the bright and dark excitons. $|A\rangle$ and $|F\rangle$ are thermally mixed with a two-LO-phonon process with rates $\gamma_\uparrow$ (cyan part) and $\gamma_\downarrow$ (blue part), LO_1 and LO_2 (the black and orange arrows) refer to different LO phonons with the energy difference matching ΔE_{AF}.

2.3.2 Magnetic field induced bright-dark state mixing

The dark excitons in colloidal NCs was firstly observed by Bawendi et al.[131] using transient hole burning spectroscopy, however, the determination of their existence through magnetic-optical spectroscopy was only achieved by Nirmal et al.[61] few years later, where they observed the magnetic field dependent emission decays and LO phonon spectra. Later on, Efros and colleagues came up with a complete theoretical desciption of the exciton fine structure.[62]

For NCs in the magnetic field B, if B is not directed along the quantization axis of the nanocrystal, recombination of the dark exciton is allowed. In this case the total angular momentum F is no longer a good quantum number, the ± 2 dark exciton states are mixed with optically active ± 1 bright exciton states leading to the direct optical recombination of the ± 2 excitons. The effect of an external magnetic field B on NCs is well described by the molecular Zeeman effect:

$$\widehat{H}_B = \frac{1}{2} g_e \mu_B \boldsymbol{\sigma} \boldsymbol{B} - g_h \mu_B \mathcal{K} \boldsymbol{B}. \tag{2.27}$$

Here, g_e and g_h are the electron and hole g factors, μ_B is the Bohr magneton, σ is the electron Pauli spin-1/2 matrix, $\mathcal{K} = L + J$ is the hole total angular momentum where L is the orbit angular momentum and J is 3/2 Luttinger spin matrix. The diamagnetic B^2 terms is neglected in Eq. (2.27).

In small NCs, even the influence of the strongest magnetic field need to be considered

as a perturbation. Treating it as a perturbation, one can determine the influence of the magnetic field on the unperturbed exciton state using the perturbation matrix $\widehat{E}'_B = \langle \Psi_{\sigma,M} | \mu_B^{-1} \widehat{H}_B | \Psi_{\sigma',M'} \rangle$, one can refer to Ref.[62] for the details. The calculation shows that once mixing with the optically active $F = 1$ bright exciton states, the recombination rate of the $|F| = 2$ exciton in a magnetic field can be written as:[132]

$$\frac{1}{\tau_2(B)} = \frac{(g_e \mu_B B sin\theta)^2}{48\eta^2} \frac{1}{R\tau_0}. \tag{2.28}$$

$\eta = (a_{ex}/a)^3 \hbar\omega_{ST}\chi(\beta)$ is the exchange interaction, $\chi(\beta)$ is a dimensionless function, here only the short-range exchange interaction is considered. θ is the angle between the magnetic field direction and the c axis. $1/R = D_\perp/D_\parallel$ takes into account the anisotropy of the local field corrections to the probability of the optical transition in nonspherical NCs with $D_\perp = |E^{in}_{x,y}|^2/|E^{out}_{x,y}|^2$, $D_\parallel = |E^{in}_z|^2/|E^{out}_z|^2$, $E^{in}_{x,y,z}$ and $E^{out}_{x,y,z}$ are the electric field components of the photon inside and outside of the NC. The characteristic time τ_0 is the radiative decay time for the upper exciton state with $F = 0$ which does not depend on the crystal radius.

In large crystals, the magnetic field splitting $g_e\mu_B B$ is of the same order as the exchange interaction η and cannot be considered as a perturbation. At the same time, both these energies are much smaller than the splitting due to the crystal asymmetry. If one only considers the mixing of the $|F| = 2$ dark exciton with the lowest $|F| = 1$ exciton, the decay time of the dark exciton in a magnetic field becomes:

$$\frac{1}{\tau_2(B)} = \frac{\sqrt{1+\zeta^2+2\zeta cos\theta} - 1 - \zeta cos\theta}{2\sqrt{1+\zeta^2+2\zeta cos\theta}} \frac{3}{2\tau_0}. \tag{2.29}$$

where $\zeta = \mu_B g_e B/3\eta$, the probability of exciton recombination increases in weak magnetic fields ($\zeta \ll 1$) and saturates in strong magnetic fields ($\zeta \gg 1$). Most importantly, from Eqs. 2.28 and 2.29, one can conclude that the recombination lifetime depends on the angle between the crystal quantization axis and the magnetic field. The recombination time is different for NCs of different orientations, this leads to a nonexponential time decay dependence for an ensemble system.

Note that within the three-level two-LO-phonon thermal mixing models shown in Fig. 2.11, the magnetic field effect on the PL decay can be described by:[65,130]

$$\tau^{-1}_{long,short} = \frac{1}{2}\{\Gamma_A + \Gamma_F + \gamma_\uparrow + \gamma_\downarrow \pm \sqrt{\left[(\Gamma_A - \Gamma_F)\frac{\Delta E_{AF}}{\Delta} + \gamma_\downarrow - \gamma_\uparrow\right]^2 + 4\gamma_\uparrow\gamma_\downarrow}\}. \tag{2.30}$$

where $\Delta = \sqrt{{\Delta E_{AF}}^2 + (\Delta g \mu_B B)^2}$ with ΔE_{AF} being the zero-field bright-dark energy splitting.

2.3.3 Dangling-bond spins assisted recombination

For wet-chemically synthesized NCs, organic or inorganic ligands are used to tailor the synthesis procedures and stabilize the nanocrystal surface by saturating the dangling bonds of surface atoms. However, the complete saturation is hard to achieve in practice, not every dangling bond can be passivated due to steric hindrance and weak interaction of a facet with the ligands. While for colloidal semiconductor NCs grown in a glass matrix, the surface atoms are free from passivation. Importantly, the dangling bond spins (DBSs) on the surface of NCs have been reported to dramatically affect the optical properties of NCs.[124,125]

In most cases, the ground exciton state of semiconductor NCs has momentum projection $F = \pm 2$ and is an optically passive (dark) state. The separation ΔE_{AF} between the ground state and the lowest optically active $F = \pm 1^L$ state increases with decreasing NC radius, and varies, for example, from several meV to 20 meV.[62] Therefore, the low-temperature photoluminescence (PL) in NCs is completely controlled by the optical properties of the ± 2 dark exciton state. Besides the phonon- and magnetic field assisted recombination of dark excitons as discussed in section 2.3.1 and section 2.3.2, DBSs assisted recombination also plays an important role especially at low temperature. The corresponding mechanism is shown in Fig. 2.12.

When cooling the system down to low temperatures where the thermal energy is smaller than the bright-dark splitting, i.e. $k_B T \ll \Delta E_{AF}$, all the excitons are thermalized in the dark ground state. In this case, if the temperature T is also higher than the critical temperature (T_c) of dangling bond magnetic polaron (DBMP) formation as shown in the upper part of Fig. 2.12, all DBSs are randomly oriented. The spin flip-flop virtual process between the DBSs and electron spins in the exciton transforms dark exciton states to bright exciton states which then emit light and contribute to the PL spectrum. Therefore, the emission spectrum shows the dark exciton line (i.e. zero phonon line (ZPL)) shifting from bright exciton line (E_A) by ΔE_{AF} along with the corresponding phonon replica. Their relative intensities depend on the efficiency of the DBS-assisted and LO-phonon-assisted recombination mechanisms.[124] When $T < T_c$, the optical pumping of NCs results in dynamic polarization of DBSs, thus the dark-exciton line and its phonon replica are additionally shifted by $E_p \rho_{db}$ because of the DBMP formation as shown in the lower part of Fig. 2.12. Here, $\rho_{db} = (N^- - N^+)/N$ is the DBS polarization degree, $N = N^- - N^+$ is the total number of DBSs at the nanocrystal surface, $E_p = \alpha N_{db}$ is the DBMP binding energy for complete DBS polarization ($\rho_{db} = 1$) and α is the exchange constant for electron interaction with a single DBS.

Once the DBMP is formed, the mechanism of DBS-assisted dark exciton recombination will be switched off completely, and the ZPL and 1PL intensities will be redistributed in favour of the LO-phonon-assisted transitions when the external magnetic field is absent. Biadala et al.[125] conducted experiments on colloidal CdSe NCs

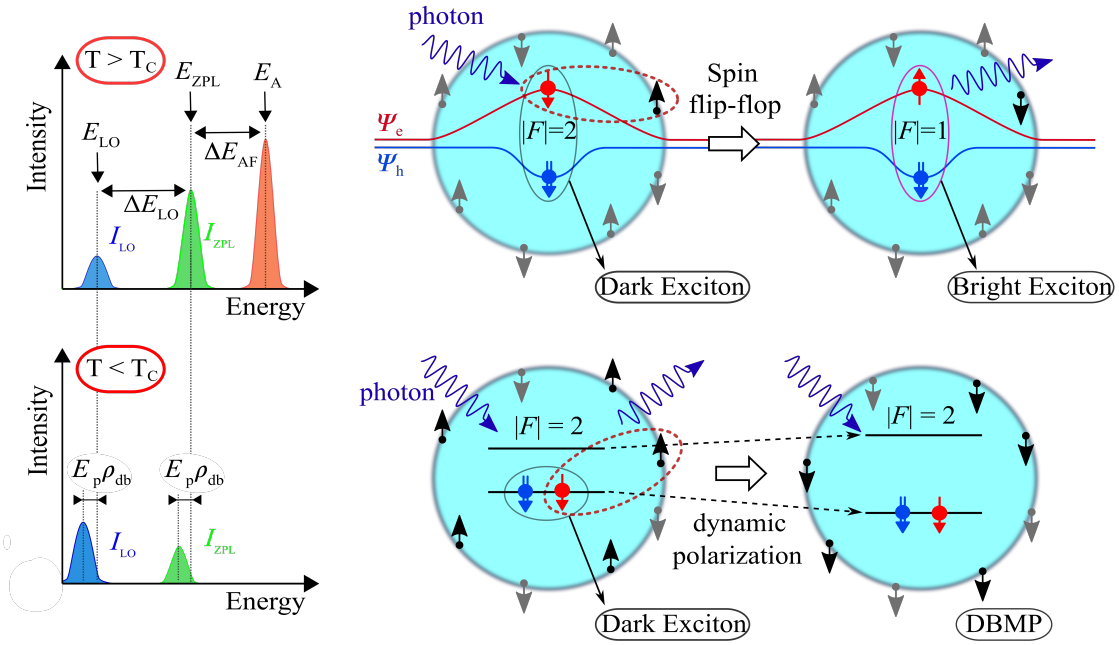

Figure 2.12: The dark exciton radiative decay via dangling bond spin flip-flop assisted recombination (right) and the respective lines in the emission spectra (left) for two temperature regimes when the thermal energy is smaller than the bright-dark splitting, $k_BT < \Delta E_{AF}$. For temperature higher than the critical temperature, T_c, i.e. $T > T_c$, the radiative decay of the dark exciton is triggered by a virtual spin flip-flop transition between the electron in exciton and the dangling bond spin (DBS), subsequently the bright exciton recombines radiatively, in this case the DBSs are not polarized. The PL spectrum is composed of emission from the bright (E_A) and the dark exciton (E_{ZPL}) as well as the phonon replica (E_{LO}). The related energy shifts are described by ΔE_{LO} and ΔE_{AF}. For $T < T_c$, the dangling bond assisted recombination results in the dynamic polarization of DBSs and the accompanying formation of a dangling bond magnetic polaron (DBMP). Due to the polarization of the DBSs, the intensity of the zero phonon line (ZPL) drops, and the ZPL together with the phonon replica shift towards lower energies by $E_p\rho_{db}$ because of DBMP formation. Adapted from Ref. [124,125].

with diameter 2.8 nm at cryogenic temperature and showed the direct evidence for the presence of DBMP. Evaluation of the data shows that the DBMP bonding energy is about 7 meV, and approximately 60 dangling bond spins are involved in the formation of each DBMP.

2.3.4 Possible role of nuclear spins

The nuclear spin physics is an important part of spin physics in semiconductor nanostructures, which has been extensively studied in molecular beam epitaxy grown semiconductor samples like quantum dots and quantum wells. [20,22] The interpaly of electron

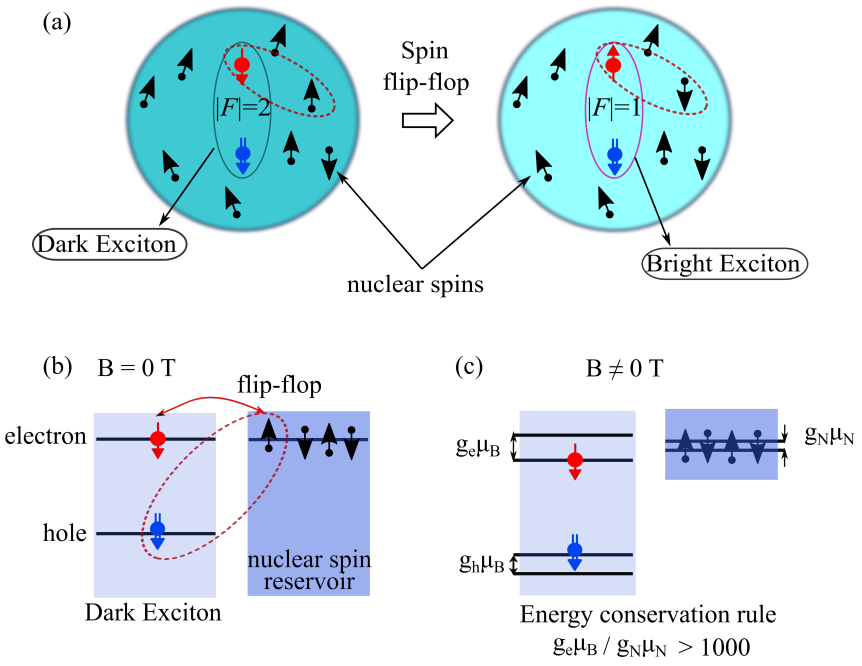

Figure 2.13: (a) Schematics for the nuclear spin assisted recombination of dark excitons. The dark, red and blue arrows represent the nuclei, electron and hole spins. (b) Dark exciton recombination activated by an interaction between electron spin and the nuclear spin reservoir, when the external magnetic field is zero. (c) Large energy mismatch in the Zeeman splitting of electron and nuclei breaks the energy conservation rule and prevents spin-flip mechanisms. Adapted from Ref.[126].

spins and nuclear spins can lead to very interesting phenomena, however, in colloidal semiconductor NCs, the effect of nuclear spin is rarely reported. Recently, Brodu et al.[126] observed magnetic-field-induced lengthening of the dark exciton lifetime in InP-based NCs which is strikingly different from what has been discussed in section 2.3.2. They explain this behavior as a result of the hyperfine interaction between the spin of the electron in dark excitons with the nuclear magnetic moments.

As it is demonstrated in Fig. 2.13 (a) and (b), similar to the mechanism of dangling bond spin assisted dark exciton recombination, the nuclear spins can also help the dark exciton to recombine via the spin flip-flop virtual transition. However, once the external magnetic field is applied, as shown in Fig. 2.13 (c), the spin-flip mechanisms will be prevented due the energy mismatch of the electron and nuclei Zeeman splitting. The nuclear spins and dangling bond spins work in a very similar manner in assisting dark exciton recombination. It is possible to distinguish the two mechanisms by checking the temperature dependence, because the dangling bond spins assisting mechanism works only when the system temperature is higher than the T_c of DBMP, while the nuclear spin is not sensitive to environment temperature fluctuation.

Chapter 3

Experimental techniques and samples

3.1 Experimental techniques

3.1.1 Absorption spectroscopy

The absorption spectra at various temperatures were measured on two setups. For the first setup, we combine an Agilent Cary 6000i UV-Visible-NIR spectrophotometer with a helium flow cryostat which enables temperature from 4.2 K up to 300 K. The second setup consists of a magneto-optical cryostat and a laser-driven white light source (EQ-99X-FC) as shown in Fig. 3.1. During the measurement, a white light beam is sent to the cryostat, right before its optical window, the spot size of the beam is adjusted by a pin hole. The beam travels further through the sample holder where a sample can be installed. The transmitted light is focused by two lenses (L_1, L_2), and selected by a mechanical slit (MS). It propagates further to a spectrometer via a multimode fiber, and dispersed in a SpectraPro-500i monochromator (Acton Research Corporation), finally detected by a CCD camera. To get the absorption spectrum, we firstly measure the transmission spectra of the white light with and without a sample as indicated by the two subgraphs at the right lower part of Fig. 3.1, then calculate the absorption spectrum using formula:

$$\alpha d = ln(I_0/I) \tag{3.1}$$

where α is the absorption coefficient, d is the thickness of the samples, I and I_0 are the intensity of the transmitted light with and without the presence of the sample.

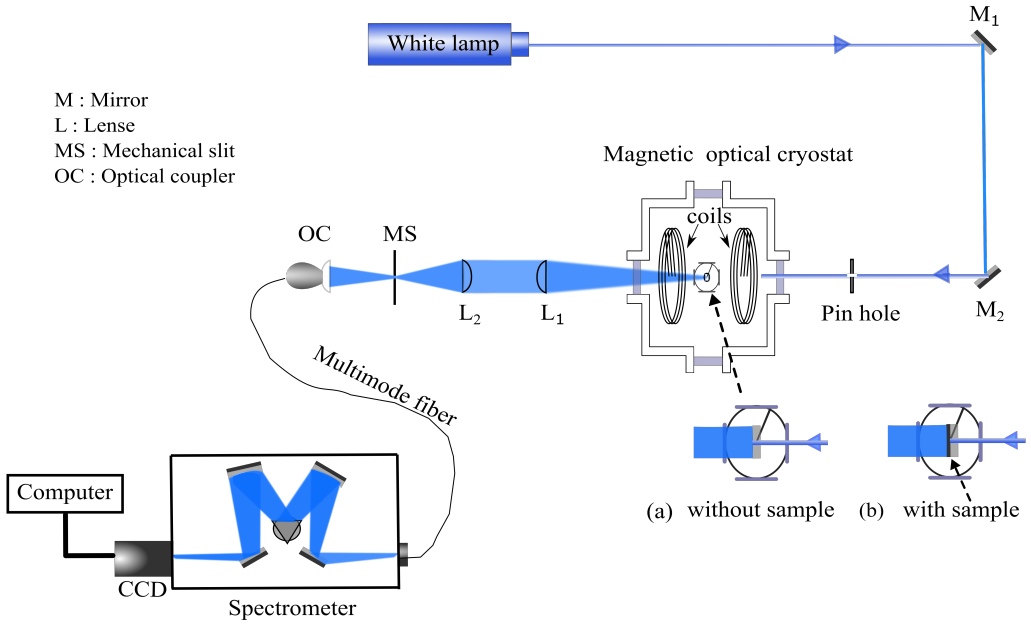

Figure 3.1: Schematic for absorption measurements in magneto-optical croystat. (a) and (b) at the right lower corner show the zoom-in structure of the sample holder without and with a sample which is represented by the black strip as indicated by the dashed arrow.

3.1.2 Polarization-resolved magneto-PL and PL decay technique

The polarization resolved photoluminescence (PL) and PL decay techniques are very powerful tools to obtain the g-factor and spin relaxation information of excitons or trions in semiconductor NCs. By analyzing the degree of the circular polarization P_c^{int}, time-resolved degree of the circular polarization $P_c(t)$ and magnetic field dependent PL decay, one can not only get the g-factor and the spin relaxation time, but also determine the type of the exciton, and even get insight into the energy transfer properties. [133]

For current research, different optical cryostats were used with magnetic fields up to 8 T, 17 T and 30 T. The basic schemes of experimental setups are similar to each other, here the scheme for 17 T setup is shown in Fig. 3.2 as an example. The samples were mounted on a titanium holder in Faraday geometry (external magnetic field B is perpendicular to the sample plate and parallel to the light wave vector) in the core of a superconducting solenoid which generates the magnetic field. The sample chamber was immersed in a liquid helium bath, and the thermal exchange between samples and liquid helium was established via the helium gas. By heating the sample chamber with a resistor, the temperature at the sample position can be adjusted.

For polarization-resolved magneto-PL measurements, the PL was excited using a PicoQuant semiconductor diode laser working in the continuous wave (cw) mode (wave-

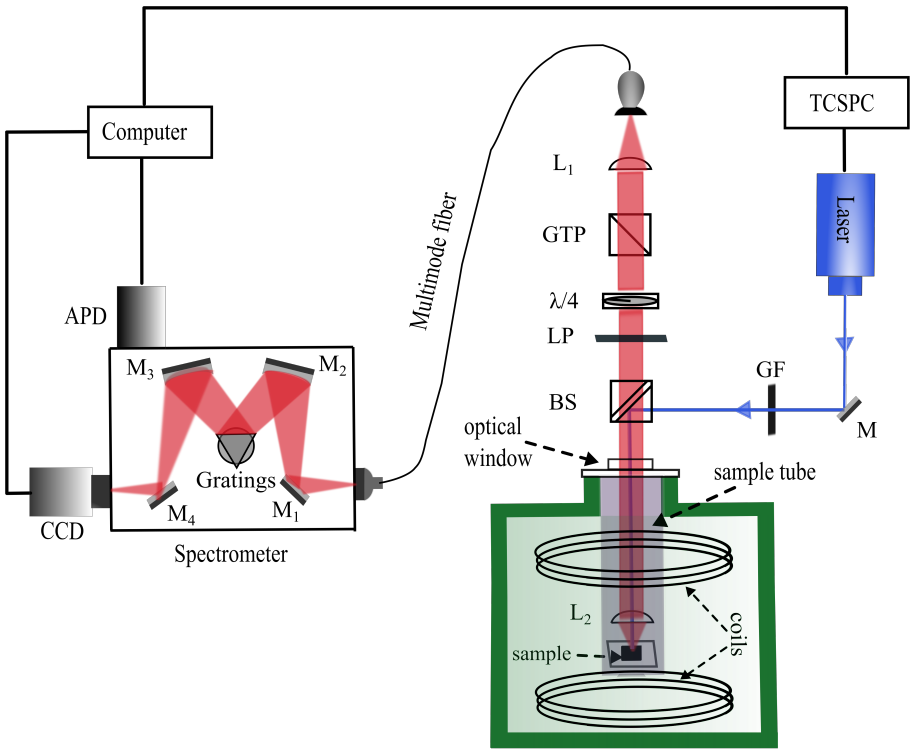

Figure 3.2: Schematics for the measurements of magnetic field dependent PL and PL decay. APD is avalanche photodiode, L represents lens, GTP is the Glan-Taylor prism, TCSPC is the time correlated single photon counter, GF refers to the grey filter which is used to adjust the laser excitation power, BS is a beam splitter, LP is the long pass filter. M_1 to M_4 are mirrors inside the spectrometer, and by flipping M_4, PL signal can be sent either to CCD or to APD.

length 405 nm, photon energy 3.06 eV). The samples were excited nonresonantly, and low excitation power density was used to exclude the effect of multiexciton states. The PL signal was filtered out from the scattered laser light by a long-pass filter and detected in backscattering geometry through a multimode fiber. The PL was dispersed in a 0.55 m spectrometer, and then measured by either a liquid nitrogen-cooled charge-coupled-device (CCD) camera or a silicon CCD camera. A circular polarizer (a combination of Glan-Taylor prism and $\lambda/4$ plate) inserted between the sample and the detection fiber allows us to separate the σ^+ and σ^- polarized PL components by simply changing the angle between the optical axis of $\lambda/4$ and Glan-Taylor prism.

For polarization-resolved magneto-PL decay measurements, the sample was excited using the same PicoQuant diode laser but working in the pulsed mode. The laser internal repetition rate is from 31.25 kHz to 80 MHz, but it can be adjusted down to even smaller ones such as 1 kHz by using external trigger, e.g. DG535 Digital Delay/Pulse generator. The laser is connected to a time-correlated single-photon counting module (TCSPC) which then linked to the computer where the avalanche photodiode (APD)

is connected. The TCSPC can be either PicoHarp 300 with highest time resolution 200 ps manufactured by PicoQuant or MCS6A multiscaler with resolution 100 ps manufactured by FAST ComTec GmbH. When laser pulses are created, its power is firstly adjusted by a grey filter, then it propagates to a beam splitter (BS) where part of the laser beam is directed inside the cryostat and focused onto the sample by a lens (L_2), the same lens is used to collect the PL from samples. The PL then travels though the optical window on the top of the cryostat, passes the BS again, and goes through a long pass filter where the scattered laser light is cut. After that, the σ^+ and σ^- polarized PL components are selected by the circular polarizer, i.e. a combination of a Glan-Taylor prism and a $\lambda/4$ plate, then go to the spectrometer, and finally detected by the APD.

By setting the magnetic field to 0 T and changing the temperature, using the same setup described above, we can measure the temperature dependent PL as well as PL decay, the latter is very important for us to analyze the band-edge exciton fine structure, i.e. bright-dark splitting ΔE_{AF}, see section 2.3.1.

Since, in this thesis, we measured four different materials with different emission ranges, the above description is only applied for CdSe, $CsPbBr_3$, $CsPbI_3$ NCs. For CuCl NCs, the setup is slightly different, as the CuCl NCs emission is in the deep blue range another laser systems are needed for the excitation. For PL measurements, CuCl NCs samples were mounted inside the variable temperature insert of a Oxford magnetic optical cryostat, which provided magnetic fields up to 8 T and temperature from 1.9 K to 300 K, the temperature is monitored additionally by a thermal sensor which is also on the sample holder and slightly above the sample. Samples were excited by either a pulse laser (Laser2000, Laser-Export Co.Ltd, LCS-DTL-374QT) with wavelength of 355 nm (3.49 eV), frequency 1 kHz or a cw laser which combines a tunable single-frequency cw Ti:Sa laser (Matisse DS) with a second harmonic unit, providing efficient and stable second harmonic generation of single-frequency. It is based on a low-loss, ultra compact enhancement cavity using a patented triangle-shaped ring resonator, and a temperature stabilized nonlinear LBO crystal generating the second harmonic of the enhanced fundamental radiation. In order to ensure a stable detection position on the sample surface, each CuCl NCs sample was covered by a mask having a hole of 2 mm diameter and the central part with 300×300 μm^2 size of the illuminated sample area was selected by a cross slit. The PL signal was sent either through a multimode fiber (in pulse excitation measurements) or directly (in cw excitation measurements) to a SpectraPro-500i monochromator (Acton Research Corporation) with 0.55 m focal length, and finally detected by a silicon CCD camera.

3.1.3 Photoluminescence in magnetic fields up to 30 T

The 30 T experiments were performed in the High Magnetic Field Lab, Nijmegen. Samples were mounted inside a liquid helium bath cryostat, which was inserted in a 50 mm bore Florida-Bitter magnet with a maximum dc magnetic field of 32 T. The

emission of a 405 nm cw diode laser was focused onto the sample by a lens (10 mm focal length), and the same lens was used to collect the signal. The polarized PL was dispersed with a 0.55 m spectrometer and measured with a liquid nitrogen-cooled CCD camera, the same scheme is adopted as in Fig. 3.2. The accessibility of this high magnetic field is important for our research, especially for understanding the polarization properties in CdSe and $CsPbI_3$ NCs.

3.1.4 Pump-probe Faraday ellipticity technique

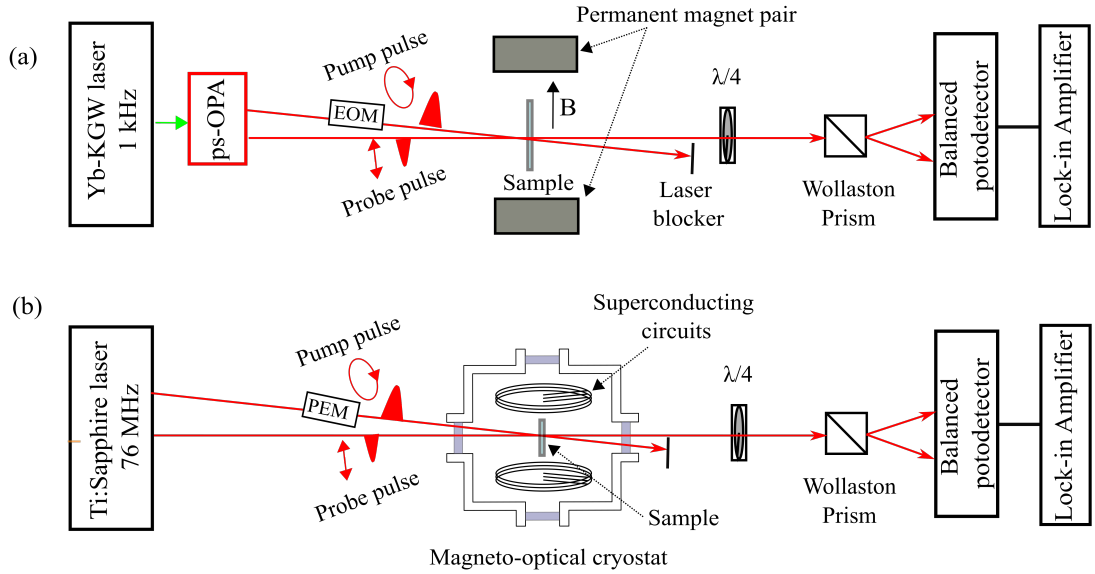

Figure 3.3: Schematics for the pump-probe measurements at (a) room temperature, and (b) low temperature in a magneto-optical cryostat. ps-OPA is the picosecond optical parametric amplifier, EOM refers to the electric optical modulator, PEM is the photoelastic electric modulator.

Pump-probe technique is a very powerful tool to study the coherence properties of electrons and holes in semiconductors. In our experiments, two slightly different setups are employed, one is for room temperature measurements with a static magnetic field applied by a permanent magnet pair, the other one is for low temperature measurements in a magneto-optical cryostat with tunable magnetic field and temperature.

We performed the pump-probe Faraday ellipticity measurements on CdSe NCs embedded in glass matrix firstly at room temperature, the setup configuration is displayed in Fig. 3.3(a). The excitation is based on a regenerative amplifier Yb-KGW (Ytterbium doped potassium gadolinium tungstate) laser system (PHAROS, Light Conversion Ltd.) combined with a narrow band ps-OPA (ORPHEUS-PS, Light Conversion Ltd). The pump and probe pulses are emitted by the ps-OPA and energy-degenerated at a wave-

length corresponding to the first optical transition position of the room-temperature absorption spectra for each sample. The laser duration is 2.5 ps with line width of 0.23 nm, and the OPA repetition rate is set to 1 kHz. The pump pulses are circularly polarized for the generation of spin polarization, while the subsequent dynamics of the spin polarization is monitored using linearly polarized probe pulses by tuning the time delay relative to the pump pulse via a mechanical delay line. The ellipticity signals are recorded using an optical polarization bridge combined with lock-in detection, it is similar to the commonly used Faraday rotation detection scheme but providing stronger spin-dependent signals for laser wavelengths resonant to the charged exciton transitions.[134] In order to eliminate background and nuclear spin effects, the pump beam is modulated between σ^+ and σ^- circular polarization by an electro-optical modulator (EOM). All measurements are performed in a transverse external magnetic field $B =$ 0.43 T applied by the permanent magnet pair.

With the configuration in Fig. 3.3(b), we checked the coherent properties of charge carriers at low temperature in different magnetic fields, the basic principle is the same as in Fig. 3.3(a). In this case, we used a Ti:Sapphire laser which emits a train of 2 ps light pulses with a repetition rate of 76 MHz (repetition period $T_R = 13.2$ ns). The laser output is split into a pump and a probe beam, the polarization of the pump beam is modulated between σ^+ and σ^- by a photoelastic modulator (PEM). The probe beam is linearly polarized, and the rotation of the transmitted probe polarization is analyzed using a quarter-wave plate and a Wollaston prism followed by a balanced photo diode scheme. A lock-in amplifier synchronized to the differential frequency of both pump and probe modulations is used to avoid any contribution of the scattered pump.

3.1.5 Fluorescence line narrowing spectroscopy

The fluorescence line narrowing (FLN) provide an alternative way to determine the bright-dark splitting ΔE_{AF} in the semiconductor NCs.[128] For resonant excitation, we used a ring dye laser with R6G dye and a dye laser with DCM dye for CdSe NCs samples. A tunable single-frequency continuous wave (cw) Ti:Sa laser (Matisse DS) combined with a second harmonic unit was used for CuCl NCs samples. The scattered light was analyzed by a Jobin-Yvon U1000 double monochromator equipped with a cooled GaAs photomultiplier. To record sufficiently strong signals of the dark exciton emission and also to suppress the laser stray light, a spectral slit width of 0.2 cm^{-1} (0.025 meV) was used. The measurements were performed on samples immersed in pumped liquid helium (typically at a temperature of 1.9 K). The FLN signal was collected in backscattering geometry with linearly polarized excitation (H) and subsequent detection of the PL with orthogonal linear polarization (V). For details about the technique, one can refer to Ref. [135].

3.1.6 Spin-flip Raman scattering spectroscopy

Spin-flip Raman scattering (SFRS) spectroscopy provides a powerful tool to address the spin structure and measure the g-factor of charge carriers and exciton. It has been successfully applied to semiconductors of different dimensionality: bulk,[136,137] epitaxially-grown quantum wells[138–140] and quantum dots,[141,142] colloidal CdSe nanoplatelets[143] and colloidal CdS quantum dots embedded in a glass matrix.[144]

In SFRS experiments, the photon energy of the excitation laser is tuned into resonance with the exciton energy, which serves as an intermediate state for light scattering. As the experiments are performed in an external magnetic field, the spin-flip of a charge carrier (in most cases it is an electron) or of an exciton is accompanied by its transition between the Zeeman-split sublevels. Accordingly, the Raman scattered light has components shifted from the laser energy to Stokes or anti-Stokes by the amount of the Zeeman splitting. The Raman shift corresponding to the Zeeman splitting can be used for the evaluation of g-factors and their anisotropy supporting the identification of the type of carriers that are involved in the scattering.[135]

Insight into the spin-flip mechanism can be provided by analyzing the underlying selection rules for the circularly polarized Raman spectra measured in Faraday geometry or linearly polarized Raman spectra measured in Voigt geometry. In Fig. 3.4 and Fig. 3.5, the electric-dipole selection rules are analyzed for SFRS processes involving a neutral exciton, negative and positive trion in an uniaxial system, here we take perovskite $CsPbX_3$ as an example. The basic structure of perovskite has been presented in section 2.2.2, we want to note that the band structure in $CsPbX_3$ is reversed as comparing to the one in CdSe-based NCs.[64] In perovskite the conduction band has Γ_4^- (p-like) symmetry and the valence band Γ_1^+ (s-like) symmetry. Spin-orbit interaction, which in CdSe NCs splits states in the valence band, in perovskite acts on the conduction band splitting it into the 2-fold degenerated Γ_6^- state ($J = 1/2$) and 4- fold degenerated Γ_8^- state ($J = 3/2$), where J is the total angular momentum. The valence band is 2-fold degenerated Γ_6^+ state ($J = 1/2$). When an exciton is formed from Γ_6^+ and Γ_6^- states, the exchange interaction will result in the lowest 2-fold Γ_1^- optically forbidden dark exciton state ($J = 0$) and the energetically higher 6-fold Γ_4^- optically allowed bright exciton state (J= 1).[145] In the following discussion, we mainly refer to the bright exciton.

Figure 3.4 shows the SFRS mechanisms for the Stokes process under resonant σ^+ excitation in Faraday geometry, where the magnetic field is pointing parallel to the light propagation direction. In the electric-dipole approximation, the total change of the photon angular momentum projection amounts to $\Delta l = 0$ or ± 2. When the projection of the total angular momentum of the exciton complex j_z on the z-quantization axis changes by ± 2, the transitions are circularly cross-polarized, while for $\Delta l = 0$ they are either linearly or co-circularly polarized. For resonant probing of the exciton, the optical excitation of states $|j_z\rangle = |s_{z,e}, j_{z,h}\rangle = |+1\rangle = |+1/2, +1/2\rangle$ and $|-1\rangle = |-1/2, -1/2\rangle$

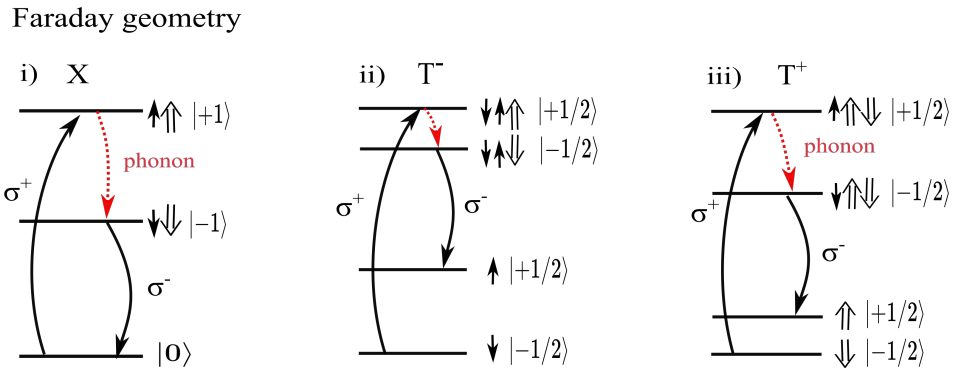

Figure 3.4: Schemes of electric-dipole-allowed SFRS stokes process for the exciton, negative and positive trions. The Faraday geometry is considered for a band edge exciton state. (i) For an exciton, the spin flips of electron and hole are allowed via acoustic phonon scattering. (ii) In the negative trion (T^-), the hole spin is scattered by an acoustic phonon. The incident and scattered photon energy is $\hbar\omega_i - \hbar\omega_s > 0$ in the Stokes process. (iii) In the positive trion (T^+), the unpaired electron spin interacts with an acoustic phonon.

by absorption of σ^+ and σ^- polarized light are allowed. Here, $s_{z,e}$ and $j_{z,h}$ represent the projections of the electron and hole spin angular momentum onto the z axis. For SFRS of exciton shown in Fig. 3.4(i), the incident σ^+ polarized photon creates an exciton in the state $|+1\rangle = |+1/2, +1/2\rangle$. A single spin-flip of either the electron or hole leads to a dark exciton state of $|0\rangle = |-1/2, +1/2\rangle$ or $|0\rangle = |+1/2, -1/2\rangle$. Hence, Raman scattering of a single carrier spin in an exciton is not observable. However, the simultaneous reversal of the electron and hole spins is allowed, and this exciton spin-flip scattering process from $|+1\rangle$ to $|-1\rangle$ is induced by an acoustic phonon, as shown by the red dashed arrow. The exciton annihilation yields a scattered photon having opposite circular polarization to the incident one, i.e., σ^- polarization in the considered example. Therefore, the exciton-SFRS is observable in the ($\sigma^{+\eta}$, $\sigma^{-\eta}$) configuration. The Raman shift is given by the exciton Zeeman splitting: $\Delta E_{SF} = \Delta E_X$.

In the case of negative trions, the σ^+ polarized incident photon can excite a negative singlet trion$|s_{z,e},s_{z,e},j_{z,h}\rangle = |-1/2, +1/2, +1/2\rangle$. Hereby, a resident electron with spin $-1/2$ should be involved, see Fig. 3.4(ii). For T^-, the electron spin-flip (SF) is forbidden by Pauli's exclusion principle. Only the unpaired hole can flip its spin via acoustic phonon scattering, thus the T^- trion is scattered from $|-1/2, +1/2, +1/2\rangle$ to $|-1/2, +1/2, -1/2\rangle$. The T^- annihilation leaves behind a σ^- polarized scattered photon and a spin-up electron. Therefore, the relevant polarization configuration is ($\sigma^{+\eta}$, $\sigma^{-\eta}$) and the Raman shift is equal to $\Delta E_{SF} = \Delta E_e + \Delta E_h$ coinciding with that of the exciton. Note that since the sign of $\Delta E_{e,h}$ depends on the sign of the electron (hole) g-factor, $\Delta E_{e,h}$ can be either positive or negative.

Figure 3.4(iii) shows the situation for positive trions. By making a analogy with the negative trion, the resonant probing of the positive trion $|s_{z,e},j_{z,h},j_{z,h}\rangle = |+1/2, +1/2, -1/2\rangle$

solely yields a SFRS process of the unpaired electron spin. It scatters from $s_{z,e} = +1/2$ to $-1/2$ via an acoustic phonon. The annihilation of the $|-1/2, +1/2, -1/2\rangle$ trion results in a σ^- polarized photon and leaves a $|+1/2\rangle$ hole. The respective selection rule is $(\sigma^{+\eta}, \sigma^{-\eta})$, and the Raman shift is again $\Delta E_{SF} = \Delta E_e + \Delta E_h$.

One notice that all three processes shown in Fig. 3.4 have some common features, i.e. (I) the second-order Raman process which only accounts for incoming (absorption) and outgoing (emission) photons is forbidden. Instead, the SFRS processes involve an intermediate state, therefore the total process is of third order, (II) scattering is provided by an acoustic phonon, (III) the scattered photon has opposite polarization to the incident photon, (IV) for spin-flip processes within trions, the unpaired carrier spin is actively flipped and the resident carrier is left with opposite spin orientation, (V) all processes have the same Raman shift $\Delta E_{SF} = \Delta E_e + \Delta E_h$.

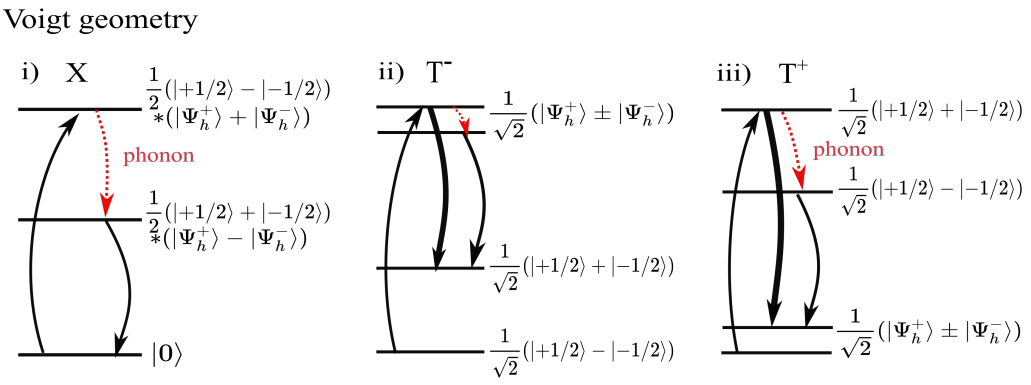

Figure 3.5: Schemes of electric-dipole-allowed SFRS stokes process for the exciton, negative and positive trions in Voigt geometry. The resonant excitation is linearly polarized. Second-order Raman processes are shown by thick arrows in the scattering channel, and thin arrows indicate third-order processes involving phonons. (i) The exciton spin flips via acoustic phonon scattering. (ii) For T^-, a second-order process provides an electron spin flip. (iii) For T^+, a second-order process provides a hole spin flip. Note, for both trions in the singlet state only the wave functions of the unpaired carrier are designated.

In perovskite $CsPbX_3$ with cubic symmetry, the SFRS is governed by the differential scattering cross section being proportional to $|(\hat{e_i} \times \hat{e_s}) \times \hat{B}|^2$. In the backscattering geometry, the cross product of the polarization vectors of the incident $\hat{e_i}$ and scattered light $\hat{e_s}$ with the magnetic field vector $\hat{B}$ differs from zero only if the magnetic field has a nonzero component perpendicular to the light propagation direction. In contrast to the Faraday geometry, in Voigt geometry the external magnetic field is perpendicular to the light wave vector and to the structure z axis, therefore the carriers and exciton complexes cannot be described by spin basis states. As a result, for trions, the second-order Raman processes become allowed. They do not require intermediate phonon scattering and, therefore, have a higher probability in comparison to the third-order processes considered in Faraday geometry. Nevertheless, the third-order processes are

also allowed in Voigt geometry as an additional spin-flip channel for trions and as the main channel for excitons as illustrated in Fig. 3.5. The optical transitions are analyzed in commonly used crossed-linear polarizations. Note that, here, we do not consider the conduction band mixing contrast to the case in semiconductor quantum wells,[140] then the electron wave functions are composed of both spin basis states with equal probability: $1/\sqrt{2}(|{\pm}1/2\rangle \pm |{\mp}1/2\rangle)$, the same goes to hole wave functions: $1/\sqrt{2}(|\Psi_h^+\rangle \pm |\Psi_h^-\rangle)$, with $|\Psi_h^{\pm}\rangle = |{\pm}1/2\rangle$.

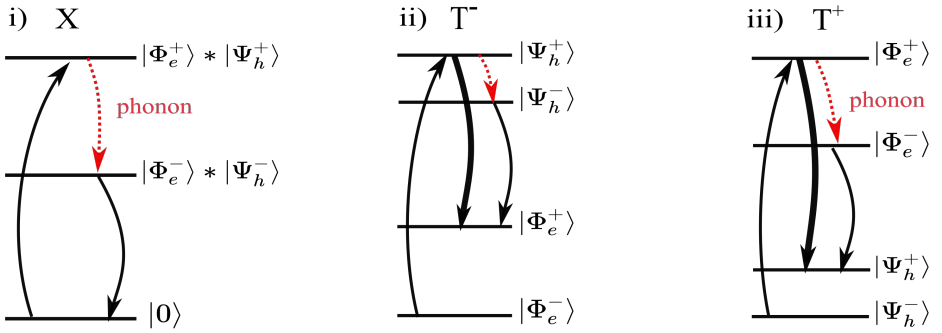

Figure 3.6: Schemes of electric-dipole-allowed SFRS stokes process for the exciton, negative and positive trions in randomly oriented NCs ensemble. The SFRS mechanism is similar to the Voigt geometry for uniaxial systems.

If one reduces perovskite crystal size to nanoscale, and prepares samples containing millions of NCs with random orientation, the scenario will be very different since it is not possible to define a certain quantization axis for the total sample, therefore all the selection rules shown in Fig. 3.4 and Fig. 3.5 will be relaxed. In order to analyze the SFRS mechanism in this case, we need to adopt the scheme shown in Fig. 3.6. It is very similar to Fig. 3.5, but the electron and hole wavefunctions, $|\Phi_e^{\pm}\rangle$ and $|\Psi_h^{\pm}\rangle$, are averaged over the ensemble considering the completely random orientation of NCs. In contrast to uniaxial systems, no anisotropy of the g-factors can be observed, which normally reveals itself in a dependence of the position of the spin-flip line on the orientation of the magnetic field with respect to the crystal axes or the laser beam.

In chapter 6 and chapter 9, we present the high spectral resolution SFRS measurements on CuCl and $CsPbI_3$ NCs samples respectively in magnetic fields up to 8 T at $T = 1.9$ K. The samples were mounted strain-free inside a magnet cryostat. In order to reach 1.9 K, samples were immersed in superfluid helium. The temperature varied among individual measurements by about 60 mK, which corresponds to an energy of 6 μeV. Experiments were performed in either Faraday or Voigt geometry.

In the SFRS measurements, the NCs samples were excited by circularly (Faraday geometry) or linearly (Voigt geometry) polarized laser light. For cw excitation of the $CsPbI_3$ NCs (PL maximum around 594 nm (2.09 eV) at 4.2 K), we used a tunable cw single mode Ti:Sa laser (Matisse DS) equipped with a MixTrain providing a difference

frequency around 532 nm (2.33 eV) by combining the single frequency cw laser beams of a seed laser (1950 nm, 0.64 eV) and the Ti:Sa laser operating at around 835 nm (1.48 eV). High mixing efficiency is achieved by precision temperature control to ensure optimal quasi-phase matching over the entire tuning range of the Matisse. The actual laser wavelength was measured and monitored by a fiber-coupled high resolution wavemeter (HighFinesse WSU). The laser power was generally set to about 50 μW if not specified otherwise. For cw excitation of CuCl NCs (PL maximum around 382 nm (3.25 eV) at 1.9 K), we combined the Ti:Sa laser (Matisse DS) with a second harmonic unit which provides efficient and stable second harmonic generation of single-frequency. The laser power, in this case, was set to about 400 μW.

To study the polarization properties of the backscattered SFRS signal, we use a combination of a $\lambda/4$ (Faraday) or $\lambda/2$ (Voigt) retardation plate and a Glan-Thompson prism in the detection path. The Glan-Thompsen prisms in excitation and detection are crossed to cut the scattered laser light. The SFRS spectra were analyzed by a double monochromator (U1000) equipped with a Peltier-cooled GaAs photomultiplier (PMT) allowing for a spectral resolution as low as 4 picometers. We used the exact same setup as Ref.[135].

3.2 Samples

Four different nanocrystal samples grown in glass matrix are studied, i.e. CdSe, CuCl, $CsPbBr_3$ and $CsPbI_3$.

3.2.1 CdSe nanocrystals

The CdSe NCs embedded in a glass matrix were synthesized by the following method which allows considerably reduce the size dispersion of NCs. The batch composition of 61.5 SiO_2, 15.0 Na_2O, 10.0 ZnO, 2.5 Al_2O_3, 3.0 CdO, 4.1 Se, 2.6 NaF, and 1.3 C (mol.%) was used to synthesize the initial glass suitable for precipitation of the cadmium selenide crystalline phase. The given amount of activated carbon was introduced directly into the batch in order to provide the required redox conditions of the synthesis. The glass batch was melted in a laboratory electric furnace at 1400-1450°C for 3 hours with stirring for 1 hour at the last stage of melting. The glass melt was poured into graphite molds and annealed in an inertial cooling mode. The initial glass was slightly yellowish in color and optically transparent down to light wavelengths in the near ultraviolet. To isolate the nanostructured CdSe phase, small pieces of the initial glass were heat-treated under isothermal conditions in a two-stage treatment mode, which allows preparation of high quality samples with very low size dispersion of the CdSe nanocrystals (standard deviation $< 5\%$ as shown in Ref.[146]). Precipitation of wurtzite modification of CdSe phase was also evidenced there. Using the data on kinetics of CdSe

crystallites growth given in Ref.[146], we determined the heat treatment condition to prepare CdSe nanocrystals with different diameters in the range from 3.3 nm up to 6.1 nm. We label the samples with names starting with D followed by their diameter in nanometer.

The prepared CdSe NCs samples were examined by small angle X-ray scattering (SAXS) with a high primary beam using Ni-filtered CuK_α radiation. The angular dependence of the scattered X-ray intensity is analyzed using Guinier plot[147] to obtain the radius of gyration, R_g, of the CdSe crystallites and evaluate the NC diameters with $D = 2.58R_g$. The basic parameters are given in Table 3.1.

Table 3.1: Parameters of CdSe NCs in glass matrix measured at $T = 4.2$ K.

Sample	D3.3	D4.1	D4.9	D6.1
NC diameter (nm)	3.30 ± 0.17	4.10 ± 0.21	4.9 ± 0.25	6.1 ± 0.31
PL FWHM (meV)	120	99	96	101
PL peak energy (eV)	2.366	2.210	2.111	2.017
Absorption peak energy (eV)	2.455	2.267	2.160	2.039
Stokes shift (meV)	89	57	49	22
Bright-dark splitting from PL decay (meV)	3.9	4.3	2.6	0.9
Bright-dark splitting from FLN (meV)	-	8.4	7.5	3.5

3.2.2 CuCl nanocrystals

Glass of the $NaPO_3$–$Ba(PO_3)_2$–AlF_3 composition was chosen to be a matrix for segregation of CuCl NCs. The glass was synthesized by melt-quenching method in a glassy carbon crucible (placed in a laboratory vertical electric furnace) at a temperature of 1100 °C for 1 h in air. After the synthesis, glasses were subjected to quenching to room temperature. During quenching, a nanocrystalline phase containing copper chloride segregates in the glass matrix. In this work, we measured five samples in total with NCs size being 1.8 nm, 2.9 nm, 4.0 nm, 15.3 nm and 28.0 nm, they are labeled as 18A, 29A, 40A, 153A and 280A, respectively, in the following chapter.

3.2.3 $CsPbX_3$ (X = Br, I) nanocrystals

Sample of the fluorophosphates glass with composition 40 P_2O_5-35 BaO-5 NaF (NaCl)-10 AlF_3-5 Ga_2O_3–2 Cs_2O–2 PbF_2-1 $BaBr(I)_2$, (mol. %) were elaborated using the melt-quench technique. The glass synthesis was performed in closed glassy carbon crucible at temperature $T = 1000$ °C. About 50 g of the batch was melted in a crucible for 20 min. Then the glass melt was cast on a glassy carbon plate and pressed to form a plate with thickness of ∼2 mm. NCs were precipitated by the glass self-crystallization during the cooling of the melt by controlling the residual concentration of bromine,

chlorine or iodineions and the cooling rate of the glass melt. The X-ray diffraction data confirm the formation of $CsPbX_3$ NCs, and $CsPbI_3$ NCs are formed in a cubic phase, $CsPbBr_3$ NCs in the orthorhombic phase.

Chapter 4

Polarized emission of CdSe nanocrystals in magnetic fields

CdSe nanocrystals (NCs) as the test bed for colloidal NCs research have been extensively investigated. Measurements of the circularly polarized PL on CdSe-based NCs in magnetic field[67,68] have revealed a puzzling behavior, i.e. with the increasing of magnetic field, the σ^- polarized PL which is stronger in intensity shifts to higher energy relative to the σ^+ polarized PL. This contradicts with the thermal population of exciton spin sublevels split in the magnetic field. Later on, the same phenomenon was reported for colloidal CdTe NCs.[148] However, this unusual behavior is absent in fluorescence line narrowing (FLN) and single nanocrystal experiments where the inhomogeneous broadening of the PL due to nanocrystal size dispersion in the ensemble is suppressed.[68,70] In Refs.[67,68], the contradiction with respect to the energy shift was tentatively assigned to the interplay between different emission channels of the dark exciton, however, a theoretical model has not been proposed so far.

In this chapter, we studied CdSe NCs in glass matrix with diameter varying from 3.3 nm up to 6.1 nm (see section 3.2 for more information) and investigated the recombination dynamics and spin polarization properties of excitons in strong magnetic fields up to 30 T. We observed not only the same contradiction between intensities and energies of the circularly polarized PL as reported for wet-chemically prepared CdSe NCs, but also a strong spectral dependence of the circular polarization degree. A theoretical model accounting for the contributions of both zero phonon emission (ZPL) and first optical phonon-assisted emission (1PL) of the dark excitons is developed by Dr. Aleksandr A. Golovatenko and Prof. Dr. Anna V. Rodina, which allows us to describe all the experimental signatures.

4.1 Theory of dark exciton polarization in ensemble CdSe nanocrystals

4.1.1 ZPL and 1PL emission

The degree of circular polarization (DCP) is the main parameter for one to get the polarization and spin properties of excitons in semiconductor NCs, it is defined as $P_c = (I^+ - I^-)/(I^+ + I^-)$, where I^+ and I^- are the intensity of σ^+ and σ^- polarized PL. To describe the magnetic field dependence of DCP and the positions of the σ^+ and σ^- polarized PL maxima, we extend the theoretical model of the circularly polarized emission from an ensemble of randomly oriented nanocrystals in Ref. [66]. The extension accounts for the linearly polarized contribution coming from the dark exciton recombination assisted by optical phonons. The model in Ref. [66] accounted for only the zero phonon line (ZPL) emission of the ± 2 dark excitons via the admixture with $\pm 1^L$ bright excitons. This admixture results in the recombination of the ± 2 dark excitons with the emission of photons that are circularly polarized in the plane perpendicular to the c-axis of a nanocrystal (Fig. 4.1). [62,132] The spatial distribution of the PL intensity, in this case, corresponds to the emission of a 2D dipole and has a maximum for the propagation of light along the direction of the c-axis (Fig. 4.1(c), orange curve).

The model in Ref. [66] does not consider the contribution of the optical phonon-assisted recombination of dark excitons. However, it is well known from FLN experiments, that the dark exciton PL has a strong contribution from optical phonon-assisted recombination. [98,149] In the model described below, we consider the recombination of dark excitons with the assistance of one optical phonon, the so-called 1PL emission. The 1PL emission is arranged predominantly via admixture with the 0^U bright exciton. [132] This results in the recombination of ± 2 dark excitons with the emission of photons that are linearly polarized along the c-axis of a nanocrystal. [62,132] The spatial distribution of the PL intensity, in this case, corresponds to the emission of the 1D dipole and has a maximum for the propagation of light in the plane perpendicular to the c-axis (Fig. 4.1(c), green curve). Also, we analyze the impact of the dark exciton recombination via the admixture with the 0^U bright exciton caused by the interaction with acoustic phonons. [132] The inhomogeneous broadening of the PL spectra in the samples under investigation is much larger than the typical energies of the acoustic phonons, for this reason, we neglect the energy shift between the ZPL emission and the acoustic phonon-assisted emission, i.e. we consider the emission at the ZPL energy which includes the contributions coming from the admixture of both 0^U and $\pm 1^L$ bright excitons with the dark exciton.

With the account of the ZPL and 1PL contributions and the random orientation of NCs in an ensemble, the spectral dependence of the $\sigma^{\pm}$ polarized PL intensities in a

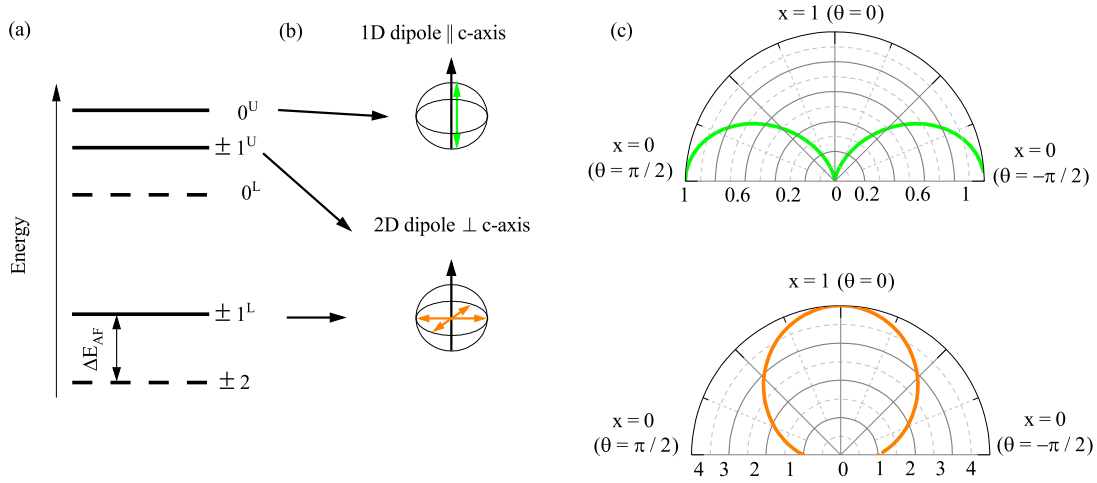

Figure 4.1: (a) Fine structure of the $1S_{3/2}1S_e$ exciton. Dashed lines show the dark excitons ± 2 and 0^L. Solid lines show the bright excitons $\pm 1^L$, $\pm 1^U$ and 0^U. (b) The emission of the 0^U bright exciton has the properties of a 1D dipole, while the emission of the $\pm 1^L$ and $\pm 1^U$ bright excitons has the properties of a 2D dipole. (c) Spatial distribution of the emission intensity for the $\pm 1^L$, $\pm 1^U$ excitons (orange line) and the 0^U exciton (green line) with respect to the direction of the c-axis.[62]

magnetic field are given by:

$$I^{\pm}(E,B) = \int_0^1 dx \sum_{i=\pm 2} \left[I^{\pm}_{i,ZPL}(x,B) f_{ZPL}(E - \delta E_i(B,x)) + I^{\pm}_{i,1PL}(x,B) f_{1PL}(E - \delta E_i(B,x)) \right], \tag{4.1}$$

where $\delta E_{\pm 2}(B,x) = \pm g_F \mu_B B x/2$ are the Zeeman shifts of the ± 2 dark excitons, μ_B is the Bohr magneton, g_F is the dark exciton g-factor, $x = \cos\theta$ with θ being the angle between the c-axis of the nanocrystal and the magnetic field direction. $I^{\pm}_{i,ZPL}(x,B)$ and $I^{\pm}_{i,1PL}(x,B)$ are the intensities of the dark exciton emission with σ^+ (σ^-) polarization in the external magnetic field applied in the Faraday geometry for NCs without and with emission of an optical phonon, respectively.

Using Eq. (4.1) we calculate the spectral dependent degree of integrated DCP as:

$$P_c^{int}(E,B) = \frac{I^+(E,B) - I^-(E,B)}{I^+(E,B) + I^-(E,B)}, \tag{4.2}$$

The functions $f_{ZPL}(E)$ and $f_{1PL}(E)$ determine the inhomogeneous broadening of PL spectra due to nanocrystal size dispersion in an ensemble. We consider the case of a

normal distribution:

$$f_{ZPL}(E-\delta E_i(B,x)) = \frac{1}{w\sqrt{2\pi}} \exp\left(-\frac{(E-\delta E_i(B,x)-E^0_{ZPL})^2}{2w^2}\right), \tag{4.3}$$

$$f_{1PL}(E-\delta E_i(B,x)) = \frac{1}{w\sqrt{2\pi}} \exp\left(-\frac{(E-\delta E_i(B,x)-E^0_{1PL})^2}{2w^2}\right) = f_{ZPL}(E-\delta E_i(B,x)+E_{LO}),$$

here $E_{LO} = 26$ meV is the optical phonon energy in CdSe, E^0_{ZPL} and $E^0_{1PL} = E^0_{ZPL} - E_{LO}$ are the maxima of the ZPL and 1PL emission from the dark excitons, corresponding to the maximum of the size distribution.

The experimental data on the DCP of the emission presented here are measured under continuous-wave laser excitation. Thus, we are interested in the time-integrated PL intensities $I^{\pm}_{i,ZPL}(x,B)$ and $I^{\pm}_{i,1PL}(x,B)$ which are defined as follows:

$$I^{\pm}_{\pm2,ZPL}(x,B) = \Gamma^{\pm}_{\pm2,ZPL}(x,B)N_{ex}(x,B), \quad I^{\pm}_{\pm2,1PL}(x,B) = \Gamma^{\pm}_{\pm2,1PL}(x,B)N_{ex}(x,B), \tag{4.4}$$

$$N_{ex}(x,B) = \frac{G}{\gamma_{tot}(x,B)}, \tag{4.5}$$

where G is the generation rate of excitons, γ_{tot} is the total exciton recombination rate, N_{ex} is the equilibrium population of the excitons.

The external magnetic field not only splits the exciton Zeeman sublevels (by the field component parallel to the c-axis), but also mixes the bright to the dark exciton states (by the field component perpendicular to the c-axis). This mixing results in the additional activation of dark excitons, which can be described within the second order perturbation theory in moderate magnetic fields [62,132] (see section 2.3.2). The resulting magnetic field and angular dependent recombination rates $\Gamma^{\pm}_{\pm2,ZPL}(x,B)$ contributing to the ZPL emission are given by:

$$\Gamma^{\pm}_{-2,ZPL}(x,B) = \frac{1}{2}\gamma_\varepsilon n_{-2}(x,B)\left[\left(\left(\frac{g_e\mu_B B}{2\sqrt{2}\varepsilon}\right)^2(1-x^2)+1\right)(1\mp x)^2+\chi_{ac}(1-x^2)\right], \tag{4.6}$$

$$\Gamma^{\pm}_{+2,ZPL}(x,B) = \frac{1}{2}\gamma_\varepsilon n_{+2}(x,B)\left[\left(\left(\frac{g_e\mu_B B}{2\sqrt{2}\varepsilon}\right)^2(1-x^2)+1\right)(1\pm x)^2+\chi_{ac}(1-x^2)\right], \tag{4.7}$$

$$\gamma_\varepsilon = \frac{\varepsilon^2}{6\eta^2}\frac{1}{\tau_0}, \quad \eta = 0.2\left(\frac{a_B}{a}\right)^3 \text{ meV}. \tag{4.8}$$

where g_e is the electron g-factor, ε is the characteristic energy of interaction that results in the admixture of the dark states to the $\pm1^L$ bright exciton states in zero magnetic field, $\chi_{ac} = \gamma_{ac}/\gamma_\varepsilon$ is the ratio of the linearly and circularly polarized recombination rates of the ZPL emission at $B = 0$ T, τ_0 is the lifetime of the 0^U bright exciton,

$n_{\pm 2}(x,B)$ are the Boltzmann populations of the ± 2 dark exciton states. Note that the angular dependence (x-dependence) arises not only from the perpendicular component of the magnetic field, but is also caused by the spatial profiles of the emission distribution for the 1D and 2D dipoles. For the modeling, we use $\eta = 0.2(a_B/a)^3$ meV which fits ΔE_{AF} values from FLN measurements. The only parameter which depends on η is r_{lin} determining polarization properties of 1PL emission (see below). For $\eta = 0.1(a_B/a)^3$ meV corresponding to short-range exchange interaction between electron and hole, relative change of r_{lin} does not exceed 2% for the whole range of considered NC diameters, and does not affect our conclusions about the role of the 1PL emission of the dark excitons.

The angle-specific recombination rates of dark excitons with the assistance of optical phonons are given by:

$$\Gamma^{\pm}_{-2,1PL}(x,B) = \frac{1}{2}\gamma_\varepsilon \chi(x,B) n_{-2}(x,B) \left[r_{lin}(1-x^2) + (1-r_{lin})(1 \mp x)^2\right], \tag{4.9}$$

$$\Gamma^{\pm}_{+2,1PL}(x,B) = \frac{1}{2}\gamma_\varepsilon \chi(x,B) n_{+2}(x,B) \left[r_{lin}(1-x^2) + (1-r_{lin})(1 \pm x)^2\right], \tag{4.10}$$

$$\chi(x,B) = \chi_0 \left[1 + c_{1PL}\left(\frac{g_e \mu_B B}{2\sqrt{2}\varepsilon}\right)^2 (1-x^2)\right], \tag{4.11}$$

where $\chi_0 = \gamma_{\mathrm{LO}}/\gamma_\varepsilon$ is the ratio of the 1PL recombination rate to the ZPL recombination rate at $B = 0$ T. c_{1PL} is a phenomenological parameter, which determines the increase of the 1PL recombination rate in a magnetic field. The parameter r_{lin} determines the fraction of the optical phonon-assisted recombination rate via the admixture to the 0^U bright exciton. According to Ref.[132], it equals to:

$$r_{lin} = \left(\frac{E_{LO}^2(\Delta + 4\eta + E_{LO})^2}{2(3\Delta\eta + E_{LO}(\Delta + 4\eta) + E_{LO}^2)^2} + 1\right)^{-1}. \tag{4.12}$$

The factor 2 in the denominator instead of 4 in equation (19) from Ref.[132] is used because here we are interested in recombination rates, while in Ref.[132] transition dipole moments were compared. The total recombination rate then equals to:

$$\gamma_{tot}(x,B) = \gamma_\varepsilon \left[\left(\frac{g_e \mu_B B}{2\sqrt{2}\varepsilon}\right)^2 (1-x)^2 + 1 + \chi(x,B) + \chi_{ac}\right]. \tag{4.13}$$

4.1.2 Ensemble-averaged PL decay

As the PL decay is measured from an ensemble of randomly oriented NCs, we need to develop a procedure for averaging the exciton lifetime over the ensemble. In this case, we consider the decay of the normalized PL intensity of the dark excitons at a fixed energy E. The increase of the dark exciton recombination rate depends on the angle

θ between the c-axis of the nanocrystal and the direction of the magnetic field. The total PL decay equals to the sum of decays from NCs having all possible values of the angle θ:

$$I(E,B,t) = A_{\mathrm{L}} \frac{\int_0^1 dx G(x,B) \exp\left[-t\tilde{\gamma}_{tot}(x,B)\right]}{\int_0^1 dx G(x,0)}\,, \tag{4.14}$$

$$\tilde{\gamma}_{tot}(x,B) = \frac{\gamma_{tot}(x,B)}{\gamma_{tot}(x,0)\tau_{B=0}} = \frac{\gamma_{tot}(x,B)}{(\gamma_\varepsilon + \gamma_{LO} + \gamma_{ac})\tau_{B=0}}\,, \tag{4.15}$$

$$G(x,B) = f_{ZPL}(E) \sum_{i=\pm 2} \Gamma^{\pm}_{i,ZPL}(x,B) + f_{1PL}(E) \sum_{i=\pm 2} \Gamma^{\pm}_{i,1PL}(x,B), \tag{4.16}$$

here $I(E,B,0)$ is PL intensity at $t = 0$, A_{L} is the amplitude of the decay component corresponding to the dark exciton recombination. Note that $\gamma_{tot}(x,0) = \gamma_\varepsilon + \gamma_{LO} + \gamma_{ac}$ is the radiative recombination rate of dark excitons in zero magnetic field, $\tau_{B=0}$ is the lifetime of the dark excitons in zero magnetic field. We neglected the contribution of the Zeeman splitting of dark excitons in the functions $f_{ZPL}(E)$ and $f_{1PL}(E)$, as these energies are much smaller than the characteristic PL linewidth. The lifetime characterizing the PL decay of the dark excitons in magnetic field for a randomly oriented ensemble of NCs can be calculated as:

$$\tau_{\mathrm{ens}}(B) = \frac{\int_0^1 dx\, G(x,B)\tilde{\gamma}_{tot}(x,B)^{-1}}{\int_0^1 dx\, G(x,B)}\,, \tag{4.17}$$

which has the meaning of an ensemble-averaged dark exciton lifetime.

4.1.3 Energy of PL maximum in zero magnetic field

In an inhomogeneous ensemble of NCs, the energy of the PL maximum at $B = 0$ T is determined by the relative intensities of the ZPL and 1PL emission of the dark excitons. One can find the energy of the PL maximum using the following consideration. At zero magnetic field, the PL intensity is given by:

$$I^{\pm}(E) = \int_0^1 dx \sum_{i=\pm 2} \left[I^{\pm}_{i,ZPL}(x) f_{ZPL}(E) + I^{\pm}_{i,1PL}(x) f_{1PL}(E) \right]\,, \tag{4.18}$$

the averaging over the random angle distribution of the ensemble results in the same intensity for both circular polarizations $I^+(E) = I^-(E)$, as expected.

We can rewrite Eq. (4.18) as

$$I^{\pm}(E,0) = f_{ZPL}(E) \left\langle I_{ZPL} \right\rangle + f_{1PL}(E) \left\langle I_{1PL} \right\rangle\,, \tag{4.19}$$

where

$$\langle I_{ZPL}\rangle = \int_0^1 dx \sum_{i=\pm 2} I^{\pm}_{i,ZPL}(x,0) = \frac{4+2\chi_{ac}}{3(1+\chi_0)}, \tag{4.20}$$

$$\langle I_{1PL}\rangle = \int_0^1 dx \sum_{i=\pm 2} I^{\pm}_{i,1PL}(x,0) = \frac{2\chi_0(2-r_{lin})}{3(1+\chi_0)}\,. \tag{4.21}$$

Taking the derivative of Eq. (4.19), we get the following condition for the PL maximum $E_{\max}$:

$$E_{\max} = E^0_{ZPL} - \frac{E_{LO}}{1+\beta_0 f(E_{\max})} = E^0_{ZPL} - E_{LO}\tilde{\beta}_0(E_{\max})\,, \tag{4.22}$$

where $\beta_0 = \langle I_{ZPL}\rangle \,/\, \langle I_{1PL}\rangle = (2+\chi_{ac})/\chi_0(2-r_{lin})$, $\tilde{\beta}_0 = (1+\beta_0 f(E_{\max}))^{-1}$ and

$$f(E_{\max}) = \frac{f_{ZPL}(E_{\max})}{f_{1PL}(E_{\max})} = \exp\left[\frac{E^2_{LO}(1-2\tilde{\beta}_0(E_{\max}))}{2w^2}\right]. \tag{4.23}$$

It should be noted that the parameter β_0 allows us to find the relation between χ_{ac} and χ_0 in zero magnetic field, and it can be determined from the comparison of the ZPL and 1PL intensities measured in fluorescence line narrowing experiments.

In Figure 4.2(a), the dependence of $E_{\max}$ on the parameter χ_0 is presented with $\chi_{ac} = 0$, $r_{\text{lin}} = 0.7$ and $w = 30$ meV. One can see that an increase of χ_0, representing the relative intensity of the 1PL emission, results in a shift of $E_{\max}$ towards the maximum of the 1PL emission. For a fixed $\chi_0 = 1.5$, one can see in Fig. 4.2(b) that a sufficiently large inhomogeneous broadening ($w > 15$ meV) results in a constant shift of $E_{\max}$ from E^0_{ZPL}. For $w < 15$ meV, a sharp return of $E_{\max}$ to E^0_{ZPL} is observed. The reason is that the spectra of the ZPL and 1PL emission do not overlap anymore, in this case, one can separate the ZPL and 1PL peaks, as usually observed in FLN experiments.

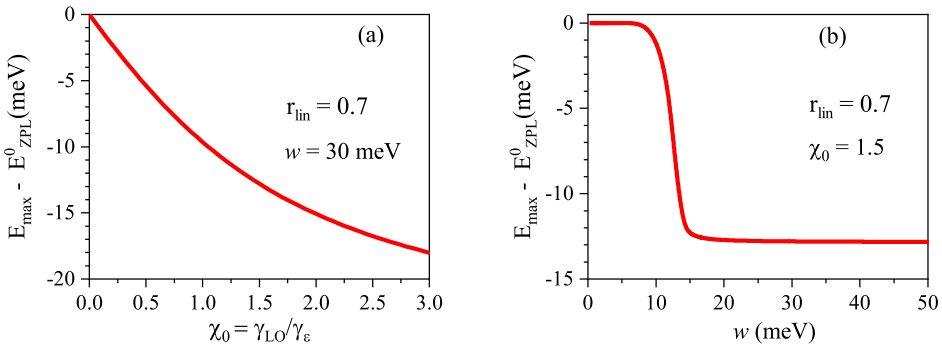

Figure 4.2: Energy of the PL maximum $E_{\max}$ as a function of (a) the LO-assisted recombination rate and (b) the inhomogeneous broadening of PL spectrum.

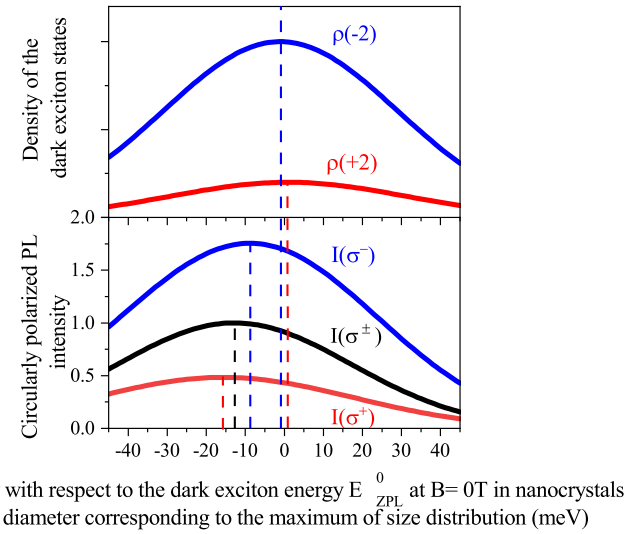

Figure 4.3: Density of the dark exciton states ±2 (upper panel) and spectra of the circularly polarized PL (lower panel). Blue and red curves are plotted for $B = 30$ T. The black curve shows PL spectra at $B = 0$ T. Vertical dash lines show maximum positions. Spectra are plotted for a randomly oriented ensemble of NCs with accounting of size dispersion.

4.1.4 Energy of PL maximum in the magnetic field

To calculate the energies of the σ^+ and σ^- polarized PL maxima, we use the following approach. Taking the derivative of Eq. (4.1), we find a condition for the total maxima of the $\sigma^\pm$ polarized PL in magnetic field, $E^\pm_{\max}(B)$. We assume that the Zeeman energies δE_i and the maximum shifts in magnetic field $\Delta E^\pm_{\max}(B) = E^\pm_{\max}(B) - E_{\max}$ are much smaller than inhomogeneous broadening w and keep only the linear-in-magnetic field corrections to the energy terms and to the distribution functions, to write the following conditions for $\Delta E^\pm_{\max}(B)$:

$$\begin{aligned}\Delta E^\pm_{\max}(B) &= \frac{g_F\mu_B B}{2}\frac{\langle\delta I^\pm_{\rm ZPL}(B)\rangle\, f_0(1-E^2_{LO}\tilde\beta_0^2/w^2)+\langle\delta I^\pm_{1PL}(B)\rangle\,[1-E^2_{\rm LO}(1-\tilde\beta_0)^2/w^2]}{\langle I^\pm_{\rm ZPL}(B)\rangle\, f_0(1-E^2_{LO}\tilde\beta_0^2/w^2)+\langle I^\pm_{1PL}(B)\rangle\,[1-E^2_{LO}(1-\tilde\beta_0)^2/w^2]} \\ &+ E_{LO}\frac{\tilde\beta_0(f_0\beta_\pm(B)+1)-1}{f_0\beta_\pm(B)(1-E^2_{LO}\tilde\beta_0^2/w^2)+[1-E^2_{LO}(1-\tilde\beta_0)^2/w^2]}\,, \end{aligned} \tag{4.24}$$

here,

$$\langle I^\pm_{ZPL}(B)\rangle = \int_0^1 dx \sum_{i=\pm2} I^\pm_{i,ZPL}(x,B)\,, \quad \langle I^\pm_{1PL}(B)\rangle = \int_0^1 dx \sum_{i=\pm2} I^\pm_{i,1PL}(x,B)\,, \tag{4.25}$$

$$\left\langle \delta I^{\pm}_{ZPL}(B) \right\rangle = \int_0^1 dx [I^{\pm}_{+2,ZPL}(x,B) - I^{\pm}_{-2,ZPL}(x,B)] \,, \tag{4.26}$$

$$\left\langle \delta I^{\pm}_{1PL}(B) \right\rangle = \int_0^1 dx [I^{\pm}_{+2,1PL}(x,B) - I^{\pm}_{-2,1PL}(x,B)] \,, \tag{4.27}$$

and $\beta_{\pm}(B) = \left\langle I^{\pm}_{ZPL}(B) \right\rangle / \left\langle I^{\pm}_{1PL}(B) \right\rangle$. The second term in Eq. (4.24) depends on the magnetic field only via $\beta_{\pm}(B)$. Note that $\beta_{\pm}(0) = \beta_0$ and both terms in Eq. (4.24) vanish at $B = 0$.

The diagrams in Fig. 4.3 show the density of dark exciton states ± 2 split in magnetic field (upper panel) for the ensemble of NCs with size dispersion $\sim 5\%$. The energy of the -2 state is lower and its population (density) is higher. When we consider both ZPL and 1PL emission of the dark excitons (lower panel), we find that left- and right-handed polarized PL maxima are shifted to lower energies as compared to that of -2 and +2 state densities in the upper panel. Wherein the maximum of σ^- PL spectrum has higher energy and its intensity is also higher.

4.2 Experimental results

Before going forward, we need to determine the nature of the PL emission in our samples, as it has been mentioned in section 2.1.1, there are several different quasiparticles that can involve in the optical transition in semiconductor NCs, e.g. exciton, trion, biexciton and related bound states. For colloidal CdSe NCs, the bound states are rarely observed, and the effect of biexciton can be safely eliminated since we used small excitation power during the measurements. Therefore, the emission originates from either neutral excitions or trions or both.

It is well documented in the literature that the temperature and magnetic field dependent PL decay measurements are very efficient ways to distinguish exciton emission from trion emission,[150,151] as the PL decay of neutral excitons are sensitive to both magnetic and temperature variations, while PL decay of trion only changes with temperature.

In Figure 4.4(a), we plot the PL spectra of all samples measured at $T = 4.2$ K. Taking sample D6.1 as an example, we show in Fig. 4.4(b) the PL decay at various temperatures. With the increasing of temperature from 2.2 to 20 K, the decay time of the long component, τ_{Long}, shortens from 212 ns down to 58 ns as a result of thermal activation from the dark exciton state to the bright exciton state. A similar behavior is observed when external magnetic field is applied, in Fig. 4.4(c) the long component measured at $T = 2.2$ K decrease from 212 ns down to 119 ns when increasing field up to $B = 17$ T. This is the typical behavior for exciton emission and can be well explained within the diagram in Fig. 2.10 in section 2.3.1. The optically-forbidden dark state $|F\rangle$ with angular momentum projection ± 2 is the exciton ground state.

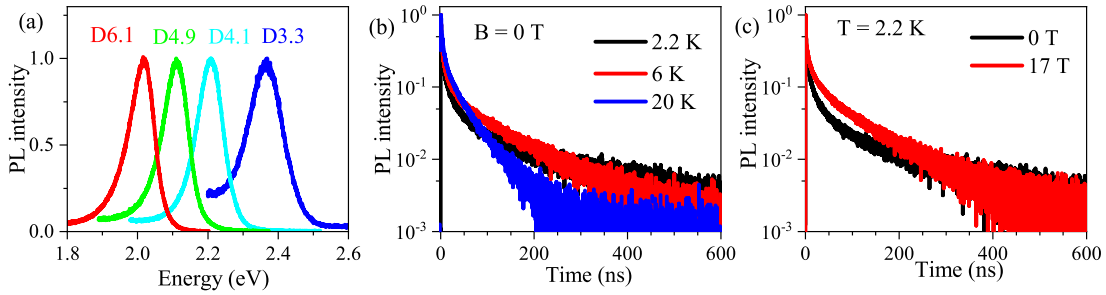

Figure 4.4: Photoluminescence and recombination dynamics. (a) PL spectra of the studied CdSe NCs measured at $T = 4.2$ K. (b) PL decay measured for the sample D6.1 at various temperatures, $B = 0$ T. (c) PL decay measured for the sample D6.1 at $B = 0$ and 17 T, $T = 2.2$ K.

The closest optically-allowed bright state $|A\rangle$ with angular momentum projection ± 1 is shifted to higher energy by the bright-dark splitting ΔE_{AF}.[62] The fast component of the PL decay is contributed by the recombination of bright excitons and their rapid thermalization to the dark state, the long component corresponds to the dark exciton recombination. With the increasing of temperature, dark excitons are lifted to the bright state, accelerating the long tail recombination process. The shortening of the long component in a magnetic field is due to the mixing of bright and dark exciton states by the field component perpendicular to NC quantization axis.[62] These properties allow us to determine the exciton nature of the optical emission and uniquely assign the long decay component τ_{Long} to the recombination of the dark excitons.

4.2.1 Bright-dark splitting ΔE_{AF}: temperature-dependent PL decay and fluorescence line narrowing

The temperature dependence of PL decay is helpful to evaluate the band-edge exciton fine structure, i.e. the bright-dark splitting ΔE_{AF}. Here we firstly measured the PL decay at various temperatures, then got the ΔE_{AF}, and compared it with values from FLN experiments and data in the literature.

Figure 4.5 shows the photoluminescence dynamics for all samples measured at $T = 4.2$ K, $B = 0$ T. The best fits of the decay curves are achieved with four-exponential functions as shown by the black lines, and the corresponding parameters (time and amplitude) are listed in Table 4.1. One can see that the characteristic decay times are about the following values: T_1 is on the order of 0.5 ns, T_2 on the order of 3 ns, T_3 on the order of 25 ns, and T_4 on the order of several hundred ns. For colloidal semiconductor NCs, one may expect the bi-exponential decay as discussed in section 2.3.1. The muliexponential decay is the signature of the inhomogeneity in the ensemble where there are nonradiative processes in some of the NCs which accelerate both the bright

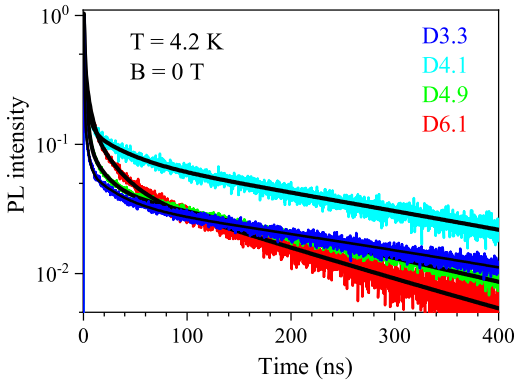

Figure 4.5: Photoluminescence decay in CdSe NCs measured at $T = 4.2$ K for $B = 0$ T. The black lines are fits with four-exponential functions.

Table 4.1: Fitting parameters of the PL decay of the CdSe NCs in glass using four-exponential functions.

Sample	D3.3	D4.1	D4.9	D6.1
NC diameter (nm)	3.3	4.1	4.9	6.1
Time constant T_1 (ns)	0.4	0.5	0.5	0.8
Amplitude A_1	2.1	1.4	1.8	0.9
Time constant T_2 (ns)	2.8	3.3	2.3	4.6
Amplitude A_2	0.2	0.2	0.4	0.3
Time constant T_3 (ns)	27	29	15	23
Amplitude A_3	0.03	0.06	0.07	0.11
Time constant T_4 (ns)	410	315	245	170
Amplitude A_4	0.04	0.08	0.05	0.06

and dark exciton decays. Similar situation was observed in the Ref.[152], where we also observed multiexponential decay for CdSe nanoplatelets at low temperatures, and the corresponding decay curves were successfully fitted with three exponential function with the long decay component being ascribed to dark exciton and the intermediate decay component to the nonradiative recombination of dark excitons. Hence, we assign the two intermediate decay components in our CdSe NCs to the nonradiative decay of the dark excitons, the shortest time T_1 to the bright exciton recombination and its relaxation to the dark exciton state, and the longest time T_4 to the recombination of dark excitons.

Figure 4.6(a) shows a representative example of the PL decay with increasing temperature from 4.2 K to 50 K. It is given for the sample D4.1 at $B = 0$ T. The long tail of the PL decay shortens with increasing temperature, i.e. the recombination rate τ_{Long}^{-1} accelerates. The temperature dependence of τ_{Long} in D4.1 is plotted in Fig. 4.6(b) as an example with the fitting results using Eq. (2.22) shown by the solid line. The evaluated the bright-dark splitting ΔE_{AF} are 3.9, 4.3, 2.6, 0.9 meV in the samples D3.3,

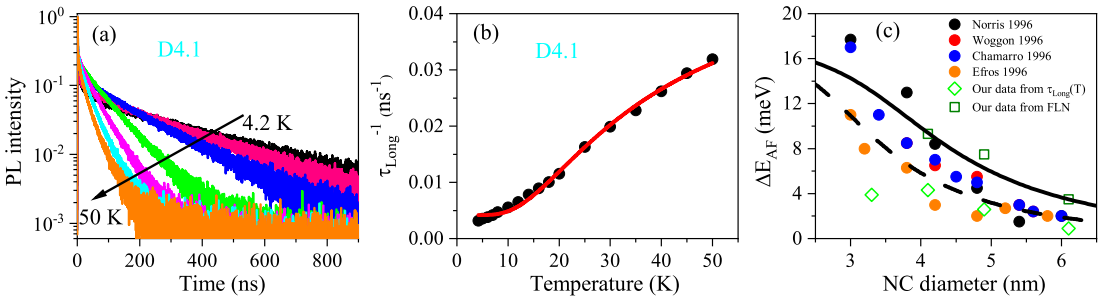

Figure 4.6: (a) PL decay in sample D4.1 at various temperatures increasing from 4.2 K up to 50 K. (b) Temperature dependence of the decay rate for the long component τ_{Long}^{-1} in D4.1. The red line shows a fit with Eq. (2.22) for $\Delta E_{AF} = 4.3$ meV. (c) Size dependence of the bright-dark splitting ΔE_{AF}. The green diamonds are the data from $\tau_{Long}(T)$. The green open squares are the data determined from FLN. Literature data for wet-chemically grown and glass-embedded CdSe NCs are shown by the solid circles.[62,98,149,153] Size dependences of ΔE_{AF} calculated with $\eta = 0.1(a_B/a)^3$ meV and $\eta = 0.2(a_B/a)^3$ meV for spherical wurtzite CdSe NCs are shown by dashed and solid lines, respectively.

D4.1, D4.9 and D6.1, which are shown by the open diamonds in Fig. 4.6(c). They are compared with the literature data available for the wet-chemically grown and glass-embedded CdSe NCs, see the closed circles in Figure 4.6(c). Good agreement is found for ΔE_{AF} in D6.1, D4.9 and D4.1, while for D3.3, ΔE_{AF} deviates from the general tendency, which may point toward a slightly prolate shape of the CdSe NCs.[154]

The solid line in Fig. 4.6(c) show size dependences of ΔE_{AF} calculated as: $\Delta E_{\rm AF} = 2\eta + \Delta/2 - (4\eta^2 + \Delta^2/4 - \eta\Delta)^{1/2}$,[62,155] where $\eta \propto (a_B/a)^3$ is a measure of the electron-hole exchange interaction, $\Delta = 23$ meV is the crystal field spitting in spherical wurtzite CdSe NCs where the hole states are with angular momentum projections $\pm 3/2$ and $\pm 1/2$, $a_B = 5.6$ nm is the exciton Bohr radius in bulk CdSe, a is the NC radius. The dashed line is calculated with accounting for the short-range exchange interaction (but not the long-range) between electron and hole[62] corresponding to $\eta = 0.1(a_B/a)^3$ meV. The solid line fits ΔE_{AF} determined from FLN and it is calculated with $\eta = 0.2(a_B/a)^3$ meV. Note, that the full account of both short-range exchange and long-range exchange interaction[155] would correspond to $\eta = 0.37(a_B/a)^3$ meV.

The fluorescence line narrowing (FLN) provide another way to determine ΔE_{AF}, it also allows us to compare the intensities of the ZPL and 1PL emission lines of the dark exciton as shown in Fig. 4.7. Based on the FLN spectra, we evaluate $\Delta E_{AF} = 3.5$, 7.5 and 8.4 meV in the sample D6.1, D4.9 and D4.1, respectively. The ΔE_{AF} values determined with this method are found to be larger as compared to the values determined from the τ_{Long} temperature dependence, see Fig. 4.6(c). Two explanations for this discrepancy were proposed: (i) the ΔE_{AF} determined from the τ_{Long} temperature dependence correspond to the true values of the bright-dark splitting, while the ΔE_{AF} from FLN can show an additional energy shift due to polaron formation[125], (ii) the

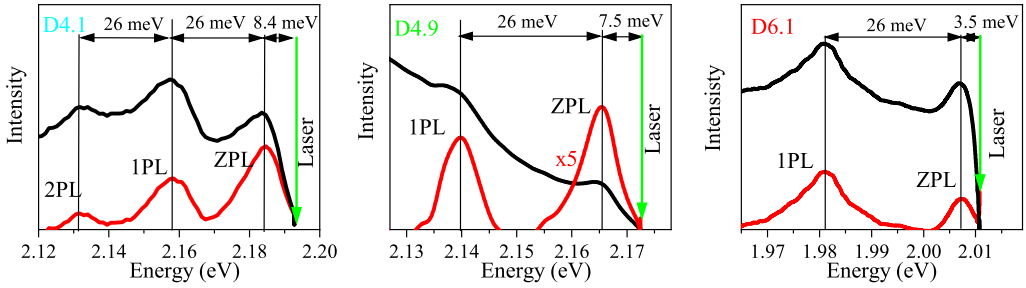

Figure 4.7: Fluorescence line narrowing spectra of sample D4.1, D4.9 and D6.1 measured at $T = 2$ K. The black lines show the FLN spectra as recorded. The red lines show the ZPL and 1PL emission after subtraction of the nonresonant PL background. The black arrows show the energies of the optical phonon $E_{LO} = 26 \pm 0.5$ meV and the bright-dark exciton splittings $\Delta E_{AF}(D4.1) = 8.4$ meV, $\Delta E_{AF}(D4.9) = 7.5$ meV and $\Delta E_{AF}(D6.1) = 3.5$ meV.

ΔE_{AF} determined from the τ_{Long} temperature dependence correspond to the energy of confined acoustic phonons, which provide thermal activation to the bright excitons. [156]

4.2.2 Magnetic field dependence of PL decay

The effect of external magentic field on the reccombination dynamics or PL decay have been shown in Fig. 4.4(c), where the increment of magnetic field results in an acceleration of the dark exciton recombination. The magnetic field dependence of the time constant τ_{Long} is presented in Fig. 4.8. The calculated lifetimes τ_{ens} in a randomly oriented ensemble of NCs (solid lines) using Eq. (4.17) are also shown with parameters ε, χ_0, χ_{ac}, and c_{1PL}. Note that the calculations presented here were achieved by assuming the ZPL emission is governed solely by the admixture of dark exciton to the $\pm 1^L$ bright exciton, this assumption is also applied for the simulations in Fig. 4.9 and Fig. 4.10. All fitting parameters for this scenario are given in Table 4.2.

Table 4.2: Fitting parameters in Fig. 4.8, 4.9 and 4.10.

Sample	D3.3	D4.1	D4.9	D6.1	
g_F	1.6	1.8	1.8	1.6	best fit
g_e	1.42	1.32	1.23	1.1	Refs. [77,78,157]
g_h	-0.06	-0.16	-0.19	-0.16	$g_h = (g_e - g_F)/3$
ε (meV)	0.23	0.24	0.25	0.32	best fit
$\chi_0 = \gamma_{LO}/\gamma_\varepsilon$	0.8	1	1.3	1.5	best fit
$\chi_{ac} = \gamma_{ac}/\gamma_\varepsilon$	0	0	0	0	
c_{1PL}	0.2	0.35	0.45	0.5	best fit
w (meV)	50	36	32	30	PL linewidth

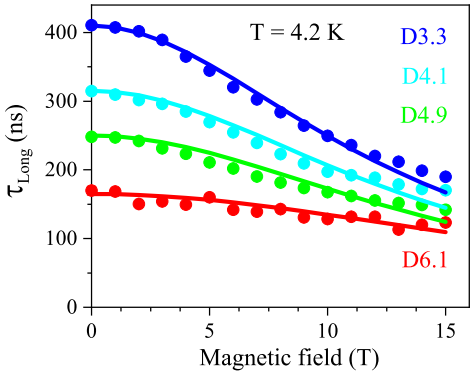

Figure 4.8: Magnetic field dependence of τ_{Long} at $T = 4.2$ K for all CdSe NCs samples. The lines show the averaged lifetime of the dark exciton calculated using Eq. (4.17) for a randomly oriented ensemble of NCs as described in section 4.1.2.

4.2.3 Polarization exciton emission in high magnetic field

Figure 4.9a (left axis) shows circularly-polarized PL spectra for sample D6.1 measured at $T = 4.2$ K and $B = 30$ T. Comparing to the black spectrum at $B = 0$ T, the intensity of the σ^- component (blue) is increased while it is decreased for the σ^+ component (red). The green line in Fig. 4.9a (right axis) shows the spectral dependence of ${P_c}^{int}$, which is larger at the high energy side (-0.63), decreases around the PL peak range, and keeps nearly constant (-0.53) at the low energy side. This is quite unusual as one does not expect to have a considerable spectral dependence of the dark exciton g-factor, g_F, within the emission line. In fact, as we will show below (as summarized in Tables 4.2 and 4.3), g_F is about constant for all studied NCs covering a much larger spectral range.

Figure 4.9b shows the magnetic field dependence of the time-integrated degree of circular polarization, P_c^{int}, collected at the PL maximum. In the ensemble of NCs with randomly oriented c-axis (the case for NCs in glass), theoretically the DCP saturation value should reach -0.75.[66] However, as one can see in Fig. 4.9b, this is obviously not the case, ${P_c}^{int}$ does not reach -0.75 and shows a clear size-dependence. At $B = 30$ T, ${P_c}^{int} = -0.56$ in D6.1 and -0.66 in D3.3. Modeling results for magnetic field dependence of P_c^{int} at the energy of zero magnetic field PL maximum are shown by solid lines. We find that low values of P_c^{int} at B= 30 T are caused by the contribution of predominantly linearly polarized 1PL emission of dark excitons. This contribution is found to be stronger in large nanocrystals resulting in a smaller saturation value of P_c^{int}, which is consistent with the relative intensities of the 1PL and ZPL emission determined from FLN (see Fig. 4.7). Besides the effect on the saturation value in high magnetic fields, the 1PL emission is also responsible for the spectral dependence of P_c^{int} (calculation is shown by orange dash curve in Fig. 4.9(a)). The reason is that the 1PL emission intensity is relatively weaker at the high-energy side of the PL spectrum

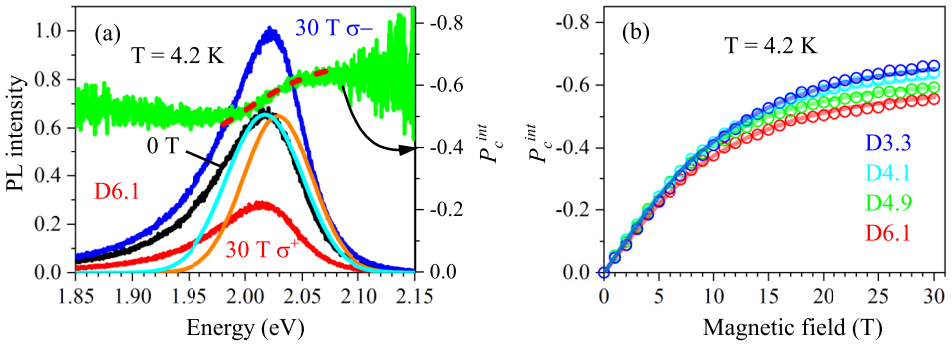

Figure 4.9: Polarized photoluminescence in magnetic field. (a) (left axis) σ^- (blue) and σ^+ (red) circularly polarized emission, measured at $B = 30$ T for the sample D6.1. The black spectrum at $B = 0$ T is shown for comparison. (right axis) Green and red-dashed curves show the experimental and calculated spectral dependence of the time-integrated DCP, respectively. The orange curve is the function $f_{ZPL}(E)$ and the cyan curve is the calculated PL spectrum at $B = 0$ T, which accounts for the ZPL and 1PL contributions. (b) Magnetic field dependence of $P_c^{int}(B)$ measured at the PL maximum in all samples. Lines are fits with Eq. (4.1) and Eq. (4.2).

due to the small number of NCs that can provide this contribution, the pronounced spectral dependence of P_c^{int} in large NCs correlates with its low saturation level owing to the strong 1PL emission.

Figure 4.10(a)-(d) show the magnetic field dependence of the polarized PL intensity. The σ^- polarized component intensity increases monotonously with magnetic field from 0 T to 30 T, while that of the σ^+ polarized component remains almost constant after an initial decrease. The surprise comes from the spectral shifts of the polarized PL components shown in Fig. 4.10(e)-(f). For neutral excitons, it is expected that the PL maximum of the stronger component, i.e. σ^-, shifts in magnetic field to lower energy, since the lower energy spin state of the exciton has the higher thermal population as demonstrated representatively by the dashed lines for sample D6.1 in Fig. 4.10(e), but the experimental shift of the PL maximum reveals a very different behavior. Firstly, for the sample D6.1, D4.9 and D4.1, the σ^+ component shifts to lower energy, secondly, the splitting between σ^+ and σ^- is several times larger than expected. In sample D3.3, both components shift initially to higher energy and the σ^+ lowers its energy for fields above 15 T as shown in Fig. 4.10(h). The calculated magnetic field dependence of the PL intensities in Fig. 4.10(a)-(d) are in a good agreement with the experimental data. Moreover, our calculation shows that in a randomly oriented NCs ensemble, it is the emission of σ^+ polarized photons from the predominantly populated -2 dark exciton state that leads to the saturation of σ^+ PL intensity at a level of 40% of the zero field intensity.

Given the spectrally broad PL bands in our CdSe NCs of about 100 meV width, which is four times the optical phonon energy in CdSe (26 meV in bulk), the PL

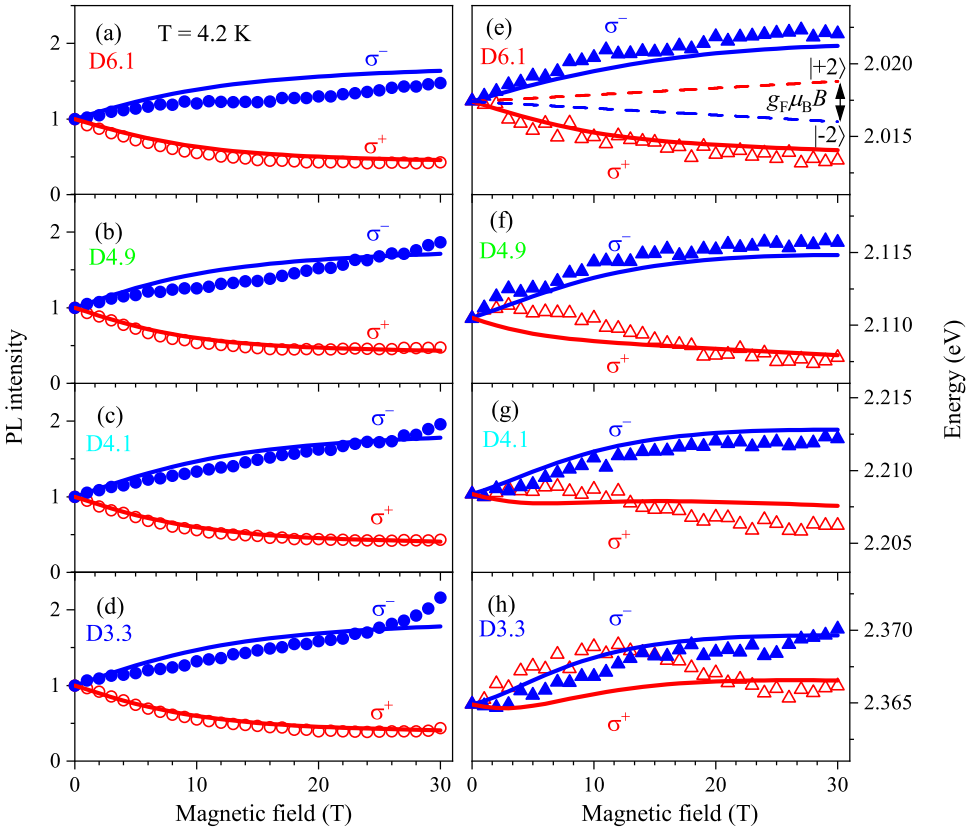

Figure 4.10: Photoluminescence intensity and spectral shifts in magnetic fields. (a-d) PL intensity of the σ^+ (red) and σ^- (blue) polarized PL as a function of magnetic field in the CdSe NCs. (e-h) Magnetic field dependence of the corresponding PL peak energies. For all panels, the symbols correspond to the experimental data, the lines show the modeling results. Dashed lines in panel (e) show the Zeeman splitting of the dark exciton spin sublevels -2 (blue) and $+2$ (red) in a nanocrystal with c-axis parallel to the magnetic field direction. We note that the energy of ± 2 states at $B = 0$ T is taken to be the same as PL maxima position for the sake of demonstrativeness. Relative positions of ± 2 energy states distribution maxima and polarized PL maxima in external magnetic field are shown in Fig. 4.3.

can be composed of the ZPL emission of the dark excitons from NCs of one size and optical phonon-assisted emission of the dark excitons from smaller NCs, as illustrated in Fig. 4.11(a). The contribution of acoustic phonon-assisted recombination of the dark excitons cannot be resolved within the ZPL line, even though it can be observed by single nanocrystal spectroscopy.[158] The ZPL emission usually has properties of a two-dimensional dipole, indicating the activation of the ± 2 dark exciton through admixture with the $\pm 1^{L,U}$ bright excitons (see Fig. 4.1).[159] However, the specific mechanism of the ZPL recombination is still under debate.[132,160,161] It was shown in Ref.[132] that the dark exciton recombination with the assistance of optical or acoustic phonons results in predominantly linearly polarized emission, corresponding to the admixture with the

0^U bright exciton (see Fig. 4.1). Thus, the ZPL and phonon-assisted emission have different spatial distribution profiles, which are determined by the relative orientation between the direction of the light propagation and direction of the anisotropic c-axis of wurtzite CdSe NCs.[62,132,159] In the case of a randomly oriented NCs ensemble, all these factors modify the magnetic field and spectral dependence of P_c^{int}. The ability

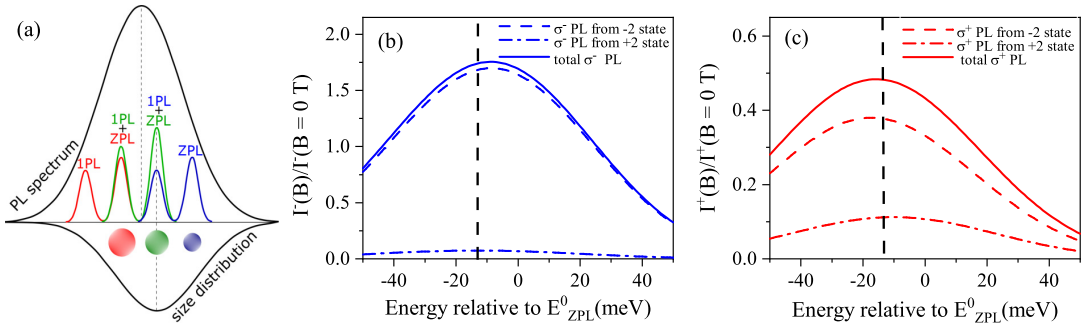

Figure 4.11: (a) Schematics representing the ZPL and 1PL contributions in an inhomogeneous ensemble of NCs. The calculated σ^- (b) and σ^+ (c) polarized PL spectra for sample D6.1 (solid lines) at $T = 4.2$ K and $B = 30$ T. Dashed (dash-dotted) lines refer to the contributions from the -2 ($+2$) dark exciton states. Vertical dashed line shows the position of the PL maximum at $B = 0$ T.

of the dark exciton states to emit both σ^- and σ^+ polarized light explains the energy shifts of the polarized PL maxima in a magnetic field. The spectral maximum of σ^- polarized PL (solid line in Figure 4.11(b)) is determined by the relation between the σ^- polarized emission from the -2 (dashed line) and $+2$ (dash-dotted line) states. In a magnetic field, the ZPL emission from the -2 state dominates, and the PL maximum shifts toward higher energy which is observed in all studied samples (Fig. 4.10(e)-(h)). Similarly in Fig. 4.11(c), the spectral maximum of σ^+ polarized PL is contributed by the emission from the -2 and $+2$ states. In high magnetic fields, the 1PL emission from the -2 state dominates, and the PL maximum shifts to lower energy. Thus, positions of polarized PL maxima to a large extent are controlled by emission of -2 state: ZPL in the case of σ^-, 1PL in the case of σ^+.

Table 4.3: Fitting parameters in Fig. 4.12, 4.13 and 4.14.

Sample	D3.3	D4.1	D4.9	D6.1	
g_F	2.4	2.6	2.6	2.4	best fit
g_e	1.42	1.32	1.23	1.1	Refs.[77,78,157]
g_h	-0.32	-0.42	-0.45	-0.43	$g_h = (g_e - g_F)/3$
ε (meV)	0.18	0.19	0.19	0.25	best fit
$\chi_0 = \gamma_{LO}/\gamma_\varepsilon$	1	1.4	1.75	2.25	best fit
$\chi_{ac} = \gamma_{ac}/\gamma_\varepsilon$	1	1	1	1	
c_{1PL}	0.12	0.18	0.25	0.25	best fit
w (meV)	50	36	32	30	PL linewidth

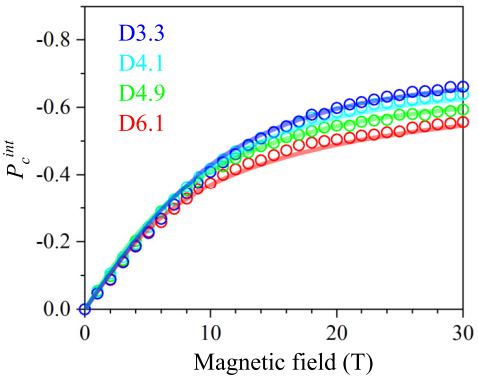

Figure 4.12: Magnetic field dependence of $P_c^{int}(B)$ measured at the PL maximum in all samples under study. Lines are fits with Eq. (4.2). The contributions to the ZPL emission via admixture with both $\pm 1^L$ and 0^U bright exciton are taken into account.

We also have considered the situation where the ZPL emission contains additionally a contribution from the recombination of the dark excitons via mixing with 0^U bright exciton. In this case, we assumed that the recombination rates of the dark excitons through the admixture of the $\pm 1^L$ and 0^U bright excitons are equal, i.e. $\chi_{ac} = \gamma_{ac}/\gamma_\varepsilon = 1$. The fit results are presented in Fig. 4.12 to Fig. 4.14. Within this scenario, we also observe a good agreement with the experimental data, and the main result that we obtain is an increase of the g-factor $g_F \approx 2.5$ which is close to the value reported for single CdSe NCs.[70] The dark exciton g-factors and other fitting parameters are given in Table 4.3.

Figure 4.14 shows the calculated spectrally dependent P_c^{int} (dashed red line) based on the ZPL emission contributed by the admixture of dark excitons with $\pm 1^L$ and 0^U bright states, the fitting parameters are from Table 4.2. From the calculation results, we can draw the conclusion that the increase of the degree of the PL polarization towards higher energies is governed by the decrease of the 1PL emission contribution. This effect is only pronounced in large NCs, while in small NCs, e.g. the sample D3.3, the DCP is almost constant across the PL spectrum.

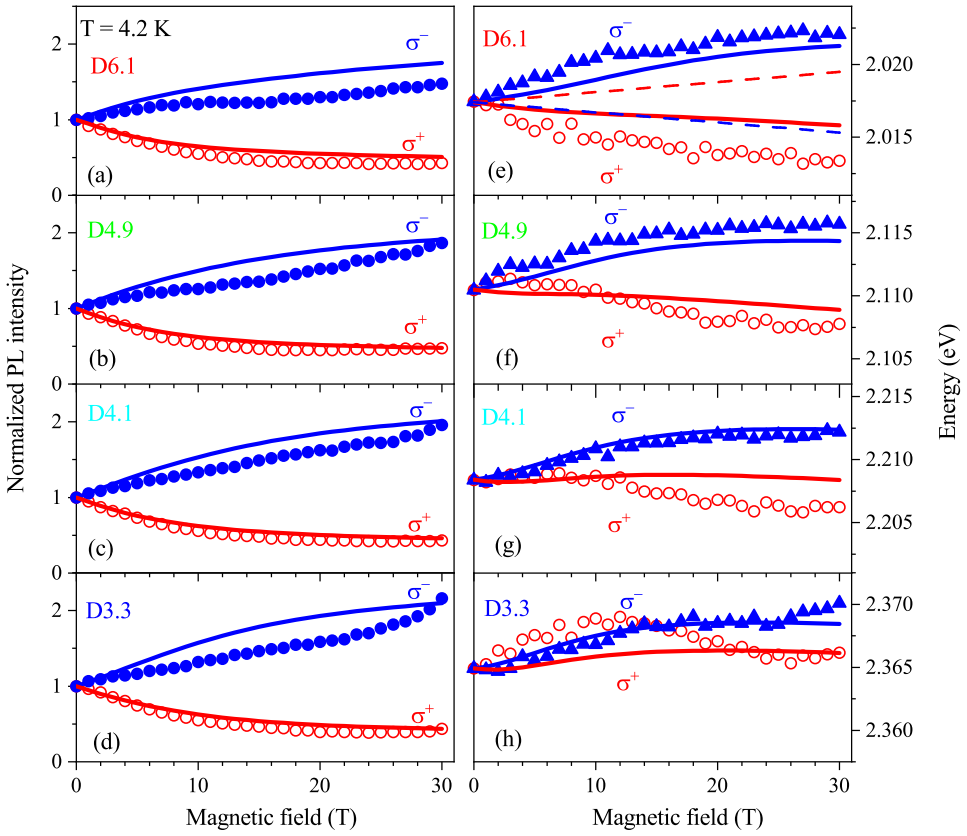

Figure 4.13: PL intensity and spectral shifts in magnetic field. (a-d) Time-integrated intensity of the σ^+ (red) and σ^- (blue) polarized PL as function of the magnetic field in CdSe NCs. (e-h) Corresponding PL peak energies. For all panels, the symbols correspond to the experimental data, while curves show the results of calculations. In the calculations, the contributions to the ZPL emission via the admixture of both $\pm 1^L$ and 0^U bright exciton are taken into account. Dashed lines in panel (e) show the Zeeman splitting of the dark exciton spin sublevels -2 (blue) and $+2$ (red) in a nanocrystal with c-axis parallel to the magnetic field direction and $g_F = 2.4$.

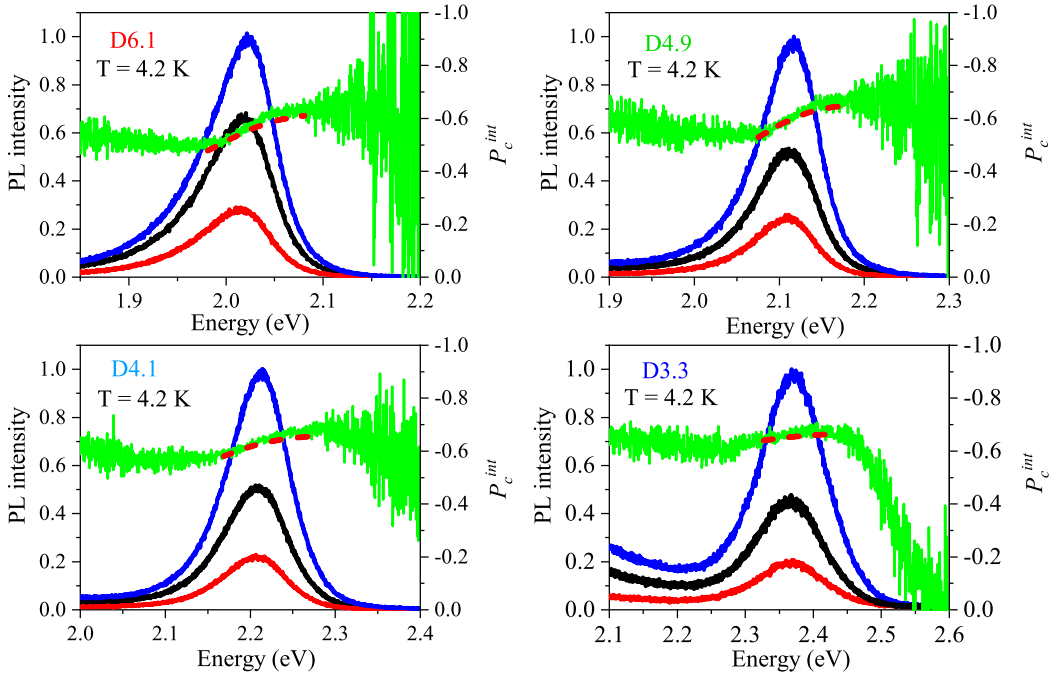

Figure 4.14: PL spectra of the σ^+ (red) and σ^- (blue) polarized components at $B = 30$ T and PL spectrum at $B = 0$ T (black). Green line shows the experimental spectral dependence of the circular polarization degree at $B = 30$ T. Red dash line shows the calculated spectral dependence of the DCP at $B = 30$ T. The emission of the dark excitons at the ZPL energy via the admixture of the 0^U bright exciton is also included.

4.2.4 Spin dynamics from polarization resolved PL decay

The magnetic field induced circular polarization is determined by the exciton population among the Zeeman spin levels split in a magnetic field. The equilibrium DCP, P_c^{eq}, is determined only by the thermal distribution, i.e. by the ratio of the exciton Zeeman splitting to the thermal energy k_BT, while the time-integrated DCP, P_c^{int}, is also affected by the spin-relaxation and recombination processes.[148] When the spin relaxation time is longer than the exciton lifetime, the thermal equilibrium can not be established, then $P_c^{int} < P_c^{eq}$. The relation can be described by $P_c^{int}(B) = d * P_c^{eq}(B)$, where $0 < d \leq 1$ is the so-called dynamical factor. In case of a single exponential decay $d = \tau/(\tau+\tau_s)$, where τ is the exciton lifetime and τ_s is the exciton spin relaxation time. For a multiexponential decay, an averaging should be made accounting for the times and relative amplitudes of each component. For the present study, it is important to ensure that the P_c^{int} measured under cw excitation is close to P_c^{eq}, i.e. that $d \approx 1$.

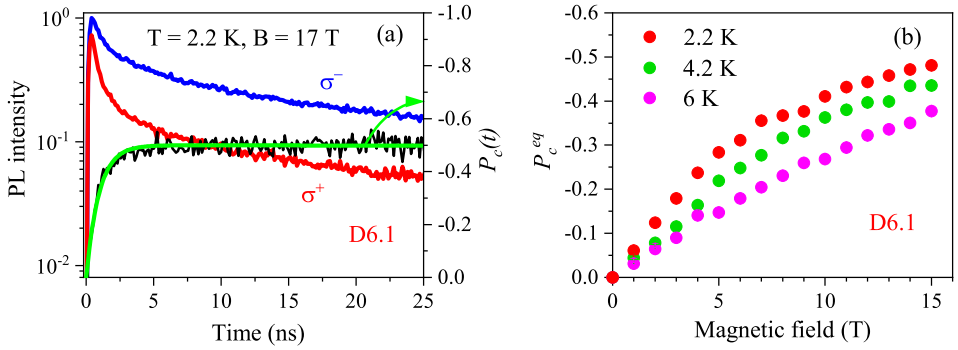

Figure 4.15: (a) Polarized PL decay for sample D6.1 measured at $T = 2.2$ K and $B = 17$ T. Red and blue lines correspond to σ^+ and σ^- polarizations, respectively. Black line shows the time-resolved DCP. (b) Magnetic field dependence of equilibrium DCP (P_c^{eq}) at $T = 2.2$, 4.2 and 6 K for the sample D6.1.

The polarization-resolved PL decay is shown in Fig. 4.15(a) for sample D6.1. The σ^- and σ^+ polarized components are measured at $T = 2.2$ K and $B = 17$ T, and the corresponding time-resolved DCP $P_c(t)$ is shown by the black line. After pulsed laser excitation, the DCP changes rapidly within a nanosecond from 0 to about -0.35, and then slowly evolves until saturating at -0.49, which corresponds to the P_c^{eq}. $P_c(t)$ can be described by the following empirical expression:[150]

$$P_c(B,t) = P_c^{eq}(B)[1 - \exp(-t/\tau_s(B))], \tag{4.28}$$

where τ_s characterize the DCP rise time but is not the true spin relaxation time in general. P_c^{eq} is strongly influenced by the magnetic field and temperature, see Fig. 4.15(b). It increases with increasing magnetic field and is suppressed by elevated temperature. At $T = 2.2$ K, P_c^{eq} varies from 0 up to -0.48 at $B = 15$ T, when the temperature increases, it drops to -0.44 at $T = 4.2$ K and to -0.38 at $T = 6$ K.

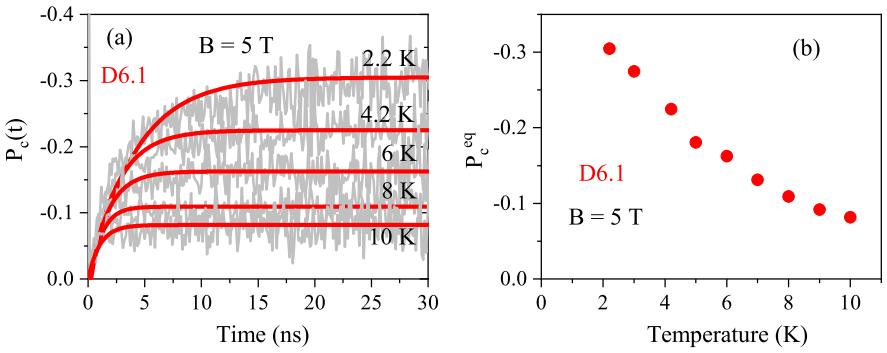

Figure 4.16: (a) Temperature dependence of the time-resolved DCP, $P_c(t)$, at $B = 5$ T, shown by grey curves. Red lines are fits with equation (4.28). (b) Temperature dependence of the equilibrium DCP, P_c^{eq}, at $B = 5$ T for sample D6.1.

Figure 4.16(a) shows the time-resolved DCP measured at $B = 5$ T for various temperatures, which can be well reproduced by equation (4.28), see the solid red lines. With increasing temperature, the DCP rise process accelerates, while P_c^{eq} decreases (-0.30 at $T = 2.2$ K and -0.08 at $T = 10$ K) as shown in Fig. 4.16(b).

The magnetic field dependence of the dynamical factor $d(B) = P_c^{int}(B)/P_c^{eq}(B)$ in all studied samples is shown in Fig. 4.17. At $T = 4.2$ K, it is close to unity, therefore, the time-integrated DCP is close to the value expected for the equilibrium exciton polarization.

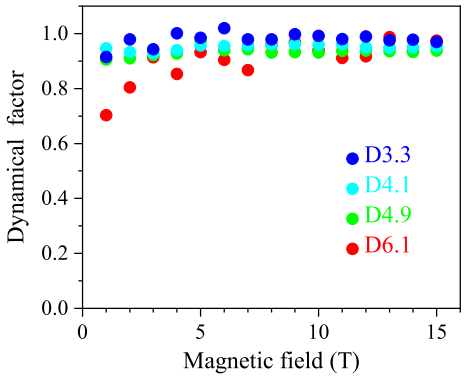

Figure 4.17: Magnetic field dependence of the dynamical factor d measured at $T = 4.2$ K.

4.3 Conclusion

We studied the spin polarization of excitons in CdSe NCs embedded in a glass matrix in strong magnetic fields up to 30 T. Several unusual features in circularly polarized emission spectra have been found: a low saturation of the degree of circular polarization combined with a pronounced spectral dependence, large and inverted spectral shifts between the oppositely polarized PL components. This puzzling behavior is similar to earlier reports on wet-chemically grown CdSe NCs. We have developed a model that takes into account the cumulative contribution of the zero phonon and one optical phonon-assisted emission of dark excitons to the emission spectra, further including the acoustic phonon-assisted emission of dark excitons also gives a good fitting but with a larger dark exciton g-factor. This model describes all experimental findings very well and can be readily extended to other colloidal NCs where inhomogeneous broadening exceeds the optical phonon energy.

Chapter 5

Electron spin coherence in CdSe nanocrystals

Pump-probe Faraday rotation spectroscopy (ppFR) is a powerful tool to study spin phenomena in semiconductors [20] and related nanostructures. [77,78,134,162–164] In the previous more than two decades, spin coherent properties of wet-chemically synthesized colloidal CdSe nanocrystals (NCs) were actively studied. [77,78,165,166] And the results revealed two spin precession frequencies $\Omega_{1,2} = g_{1,2}\mu_B B/\hbar$ with size-dependent g-factors $g_{1,2}$. The g_1 has been unambiguously ascribed to electrons in singly charged NCs, [77] while the origin of g_2 is still under debate and different possibilities were proposed: bright exciton, [77,165] anisotropic electron g-factor, [167] and resident electron localized near the surface of the NC. [78,166] To clarify the origin of g_2, we perform an experimental study of the spin coherent properties and theoretical calculations of the exciton spin precession in CdSe NCs, then compare the results with previously published data.

The theoretical analysis is performed by Dr. Aleksandr A. Golovatenko and Prof. Dr. Anna V. Rodina based on the numerical solution of the time-dependent Schrödinger equation for exciton states with the consideration of the external magnetic field, electron-hole exchange interaction, heavy-light hole splitting caused by the crystal field of wurtzite structure and by the NC shape anisotropy. For a qualitative understanding of the numerical results, the analytical solutions for the precession of spin $S = 1$ is specially considered since it can be thought as an analogue of the bright exciton.

The calculation shows that exciton spin precession in the case of zero heavy-light hole splitting occurs with a twice smaller frequency as it was reported in Ref. [77], which makes problem for the interpretation of g_2 from Ref. [77] as the bright exciton precession frequency. Analysis of the exciton spin precession in NCs with heavy-light hole splitting determined by the crystal field of CdSe wurtzite structure shows that once the pump pulse creates spin polarization of excitons, it will be frozen at its initial value. This

agrees with our experimental data that reveals, besides the Ω_2 precession component, a nonoscillating component in the ellipticity signal at cryogenic temperatures.

5.1 Theoretical consideration of exciton spin ppFR signals

To clear contradictions in the understanding about origin of g_2, here we show the theoretical analysis of the Larmor precession of exciton spin in CdSe NCs performed by Dr. Aleksandr A. Golovatenko and Prof. Dr. Anna V. Rodina. It is assumed that the direction of pump and probe pulses coincides with Z-axis of the laboratory frame and the magnetic field is applied along the X-axis of the laboratory frame, see Fig. 5.1. Direction of nanocrystal c-axis is determined by angles θ,φ as a position of point on the unit sphere. The components B_z,B_-,B_+ in the nanocrystal frame are given by:

$$B_z = B\sin\theta\cos\varphi, \tag{5.1}$$

$$B_+ = B_x + iB_y = B(\cos\theta\cos\varphi + i\sin\varphi), \tag{5.2}$$

$$B_- = B_x - iB_y = B(\cos\theta\cos\varphi - i\sin\varphi) \tag{5.3}$$

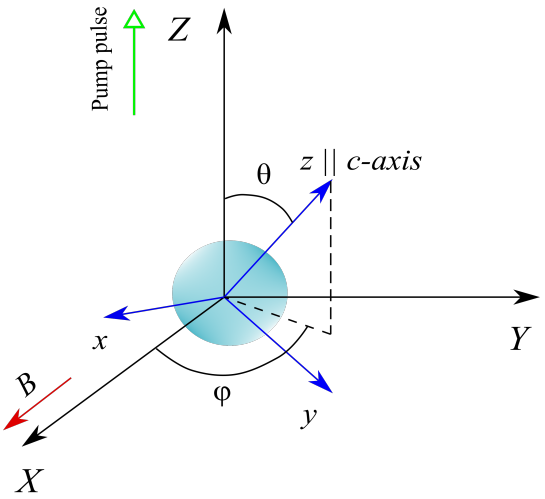

Figure 5.1: Relative positions of laboratory frame with Z-axis coinciding with the pump/probe pulses direction, magnetic field directed along the X-axis of the laboratory frame, and nanocrystal c-axis.

Matrix elements of the magnetic field, exchange interaction and crystal field calculated in the electron-hole basis along the nanocrystal c-axis are given in the following[62](μ_B is omitted in magnetic field matrix elements, the multiplier i is absent in

the off-diagonal terms in contrast to Ref.[62] due to different definition of spherical harmonics in the hole wavefunction):

$$
\begin{array}{c|cccccccc}
 & \uparrow,\frac{3}{2} & \uparrow,\frac{1}{2} & \uparrow,-\frac{1}{2} & \uparrow,-\frac{3}{2} & \downarrow,\frac{3}{2} & \downarrow,\frac{1}{2} & \downarrow,-\frac{1}{2} & \downarrow,-\frac{3}{2} \\
\hline
\uparrow,\frac{3}{2} & E^Z_{\uparrow,3/2} & -\frac{\sqrt{3}}{2}B_-g_h & 0 & 0 & \frac{1}{2}B_-g_e & 0 & 0 & 0 \\
\uparrow,\frac{1}{2} & -\frac{\sqrt{3}}{2}B_+g_h & E^Z_{\uparrow,1/2} & -B_-g_h & 0 & -\sqrt{3}\eta & \frac{1}{2}B_-g_e & 0 & 0 \\
\uparrow,-\frac{1}{2} & 0 & -B_+g_h & E^Z_{\uparrow,-1/2} & -\frac{\sqrt{3}}{2}B_-g_h & 0 & -2\eta & \frac{1}{2}B_-g_e & 0 \\
\uparrow,-\frac{3}{2} & 0 & 0 & -\frac{\sqrt{3}}{2}B_+g_h & E^Z_{\uparrow,-3/2} & 0 & 0 & -\sqrt{3}\eta & \frac{1}{2}B_-g_e \\
\downarrow,\frac{3}{2} & \frac{1}{2}B_+g_e & -\sqrt{3}\eta & 0 & 0 & E^Z_{\downarrow,3/2} & -\frac{\sqrt{3}}{2}B_-g_h & 0 & 0 \\
\downarrow,\frac{1}{2} & 0 & \frac{1}{2}B_+g_e & -2\eta & 0 & -\frac{\sqrt{3}}{2}B_+g_h & E^Z_{\downarrow,1/2} & -B_-g_h & 0 \\
\downarrow,-\frac{1}{2} & 0 & 0 & \frac{1}{2}B_+g_e & -\sqrt{3}\eta & 0 & -B_+g_h & E^Z_{\downarrow,-1/2} & -\frac{\sqrt{3}}{2}B_-g_h \\
\downarrow,-\frac{3}{2} & 0 & 0 & 0 & \frac{1}{2}B_+g_e & 0 & 0 & -\frac{\sqrt{3}}{2}B_+g_h & E^Z_{\downarrow,-3/2}
\end{array}
\tag{5.4}
$$

The diagonal matrix elements are:

$$
\begin{aligned}
E^Z_{\uparrow,3/2} &= \frac{B_z(g_e-3g_h)-\Delta}{2}, \\
E^Z_{\uparrow,1/2} &= \frac{B_z(g_e-g_h)+2\eta+\Delta}{2}, \\
E^Z_{\uparrow,-1/2} &= \frac{B_z(g_e+g_h)+4\eta+\Delta}{2}, \\
E^Z_{\uparrow,-3/2} &= \frac{B_z(g_e+3g_h)+6\eta-\Delta}{2}, \\
E^Z_{\downarrow,3/2} &= \frac{-B_z(g_e+3g_h)+6\eta-\Delta}{2}, \\
E^Z_{\downarrow,1/2} &= \frac{-B_z(g_e+g_h)+4\eta+\Delta}{2}, \\
E^Z_{\downarrow,-1/2} &= \frac{-B_z(g_e-g_h)+2\eta+\Delta}{2}, \\
E^Z_{\downarrow,-3/2} &= \frac{-B_z(g_e-3g_h)-\Delta}{2}.
\end{aligned}
\tag{5.5}
$$

Δ refers to the net splitting of the hole state. The exciton states in the electron-hole

basis in zero magnetic field are given by[168]:

$$
\begin{aligned}
|+1^U\rangle &= -C_+ \left|\uparrow, 1/2\right\rangle + C_- \left|\downarrow, 3/2\right\rangle, \\
|+1^L\rangle &= C_- \left|\uparrow, 1/2\right\rangle + C_+ \left|\downarrow, 3/2\right\rangle, \\
|-1^U\rangle &= C_+ \left|\downarrow, -1/2\right\rangle - C_- \left|\uparrow, -3/2\right\rangle, \\
|-1^L\rangle &= C_- \left|\downarrow, -1/2\right\rangle + C_+ \left|\uparrow, -3/2\right\rangle, \\
|0^U\rangle &= \frac{1}{\sqrt{2}} \left(\left|\downarrow, 1/2\right\rangle - \left|\uparrow, -1/2\right\rangle\right), \\
|0^L\rangle &= \frac{1}{\sqrt{2}} \left(\left|\downarrow, 1/2\right\rangle + \left|\uparrow, -1/2\right\rangle\right), \\
|+2\rangle &= \left|\uparrow, 3/2\right\rangle, \\
|-2\rangle &= \left|\downarrow, -3/2\right\rangle.
\end{aligned}
\tag{5.6}
$$

Electron-hole basis states transformations are described by the following matrix:

$$
\begin{array}{c|cccccccc}
 & \uparrow,\frac{3}{2} & \uparrow,\frac{1}{2} & \uparrow,-\frac{1}{2} & \uparrow,-\frac{3}{2} & \downarrow,\frac{3}{2} & \downarrow,\frac{1}{2} & \downarrow,-\frac{1}{2} & \downarrow,-\frac{3}{2} \\
\uparrow,\frac{3}{2}^* & a^4 & \sqrt{3}a^3c & \sqrt{3}a^2c^2 & ac^3 & a^3c & \sqrt{3}a^2c^2 & \sqrt{3}ac^3 & c^4 \\
\uparrow,\frac{1}{2}^* & \sqrt{3}a^3b & a(a^2d+2abc) & a(bc^2+2acd) & \sqrt{3}ac^2d & \sqrt{3}a^2bc & c(a^2d+2abc) & c(bc^2+2acd) & \sqrt{3}c^3d \\
\uparrow,-\frac{1}{2}^* & \sqrt{3}a^2b^2 & a(b^2c+2abd) & a(ad^2+2bcd) & \sqrt{3}acd^2 & \sqrt{3}ab^2c & c(b^2c+2abd) & c(ad^2+2bcd) & \sqrt{3}c^2d^2 \\
\uparrow,-\frac{3}{2}^* & ab^3 & \sqrt{3}ab^2d & \sqrt{3}abd^2 & ad^3 & b^3c & \sqrt{3}b^2cd & \sqrt{3}bcd^2 & cd^3 \\
\downarrow,\frac{3}{2}^* & a^3b & \sqrt{3}a^2bc & \sqrt{3}abc^2 & bc^3 & a^3d & \sqrt{3}a^2cd & \sqrt{3}ac^2d & c^3d \\
\downarrow,\frac{1}{2}^* & \sqrt{3}a^2b^2 & b(a^2d+2abc) & b(bc^2+2acd) & \sqrt{3}bc^2d & \sqrt{3}a^2bd & d(a^2d+2abc) & d(bc^2+2acd) & \sqrt{3}c^2d^2 \\
\downarrow,-\frac{1}{2}^* & \sqrt{3}ab^3 & b(b^2c+2abd) & b(ad^2+2bcd) & \sqrt{3}bcd^2 & \sqrt{3}ab^2d & d(b^2c+2abd) & d(ad^2+2bcd) & \sqrt{3}cd^3 \\
\downarrow,-\frac{3}{2}^* & b^4 & \sqrt{3}b^3d & \sqrt{3}b^2d^2 & bd^3 & b^3d & \sqrt{3}b^2d^2 & \sqrt{3}bd^3 & d^4
\end{array}
\tag{5.7}
$$

Here $a = \cos\theta'/2$,$b = -\sin\theta'/2$,$c = \sin\theta'/2$,$d = \cos\theta'/2$ for counterclockwise rotation at the angle θ' around the y-axis of nanocrystal frame. And $a = \exp(i\varphi'/2)$,$b = 0$,$c = 0$,$d = \exp(-i\varphi'/2)$ for counterclockwise rotation at the angle φ' around the z-axis of nanocrystal frame. Basis states with index * correspond to transformed coordinate system.

In order to transform from the nanocrystal frame to the laboratory frame, angles $\theta' = -\theta$ and $\varphi' = -\varphi$ are chosen, where φ and θ are angles determining direction of NC c-axis in the laboratory frame. The transformation is realized in two steps: i) rotation around the y-axis of the NC frame by angle $-\theta$; ii) rotation around the z-axis of the NC frame by angle $-\varphi$.

The precession of spin in a single NC is calculated using $\langle S_Z \rangle = \langle \Psi^* | S_Z^{\sigma,J} | \Psi \rangle$, Ψ is the wave function of the system, $S_Z^{\sigma,J}$ is the Z-component of full electron-hole spin matrix. In the electron-hole basis, along the Z-axis of the laboratory frame, $|\Psi\rangle$ equals:

$$|\Psi\rangle = \sum_{k=1}^{8}\sum_{n=1}^{8}\sum_{j=1}^{8}\sum_{i=1}^{8} C_{n,k}^{\text{bas}} C_{j,n}^{\text{c-axis}} C_{i,j}^{\text{eig}} C_i^{t=0} \exp\left[-\frac{\mathrm{i}E_{\text{eig}}t}{\hbar}\right] \tag{5.8}$$

where $C_i^{t=0}$ are amplitudes of initial state in the electron-hole basis along the NC c-axis, $C_{i,j}^{\text{eig}}$ are amplitudes of transition from the electron-hole basis to the eigenvectors basis of matrix 5.4, $C_{j,n}^{\text{c-axis}}$ are amplitudes of reverse transformation from the eigenvectors basis to the electron-hole basis along c-axis of NC, $C_{n,k}^{\text{probe}}$ are amplitudes of transition from the electron-hole basis along c-axis of NC to electron-hole basis along the probe pulse (Z-axis), E_{eig} are eigenvalues of Hamiltonian $\hat{H}$ [62]:

$$\hat{H} = \frac{1}{2} g_e \mu_B \boldsymbol{\sigma B} - g_h \mu_B \boldsymbol{JB} - \eta \boldsymbol{\sigma J} - \frac{\Delta}{2}\left(J_z^2 - \frac{5}{4}\right), \tag{5.9}$$

where the first two terms describe Zeeman splitting of electron and hole states in the applied magnetic field with g_e, g_h being the electron and hole g-factors, respectively, $\boldsymbol{\sigma} = [\sigma_x,\sigma_y,\sigma_z]$ being the electron spin operator composed from Pauli matrices, $\boldsymbol{J} = [J_x,J_y,J_z]$ being the hole spin operator composed from spin 3/2 matrices. The third term is the effective exchange interaction between electron and hole including both short-range and long-range parts [100,155,169]. The last term describes the joint splitting of heavy and light hole subbands by the crystal field of wz-CdSe and shape anisotropy of nanocrystal [62], Δ refers to the net splitting of the hole state.

Matrix $S_Z^{\sigma,J}$ equals:

	$\uparrow,\frac{3}{2}$	$\uparrow,\frac{1}{2}$	$\uparrow,-\frac{1}{2}$	$\uparrow,-\frac{3}{2}$	$\downarrow,\frac{3}{2}$	$\downarrow,\frac{1}{2}$	$\downarrow,-\frac{1}{2}$	$\downarrow,-\frac{3}{2}$
$\uparrow,\frac{3}{2}$	2	0	0	0	0	0	0	0
$\uparrow,\frac{1}{2}$	0	1	0	0	0	0	0	0
$\uparrow,-\frac{1}{2}$	0	0	0	0	0	0	0	0
$\uparrow,-\frac{3}{2}$	0	0	0	−1	0	0	0	0
$\downarrow,\frac{3}{2}$	0	0	0	0	1	0	0	0
$\downarrow,\frac{1}{2}$	0	0	0	0	0	0	0	0
$\downarrow,-\frac{1}{2}$	0	0	0	0	0	0	−1	0
$\downarrow,-\frac{3}{2}$	0	0	0	0	0	0	0	−2

(5.10)

The average spin of excitons in the ensemble of wz-CdSe NCs is calculated as:

$$\langle S_Z^{\text{ens}} \rangle = A \sum_{\varphi=0}^{2\pi} \sum_{\theta=0}^{\pi/2} \sin\theta \, \langle S_Z \rangle \,, \tag{5.11}$$

$$A = 1/ \sum_{\varphi=0}^{2\pi} \sum_{\theta=0}^{\pi/2} \sin\theta$$

summation is performed with a uniform 2^o step for φ,θ, and the statistical weight $\sin\theta$ describes the random orientation of c-axis in an ensemble of NCs.

5.2 Size-dependent spin coherent dynamics at room temperature

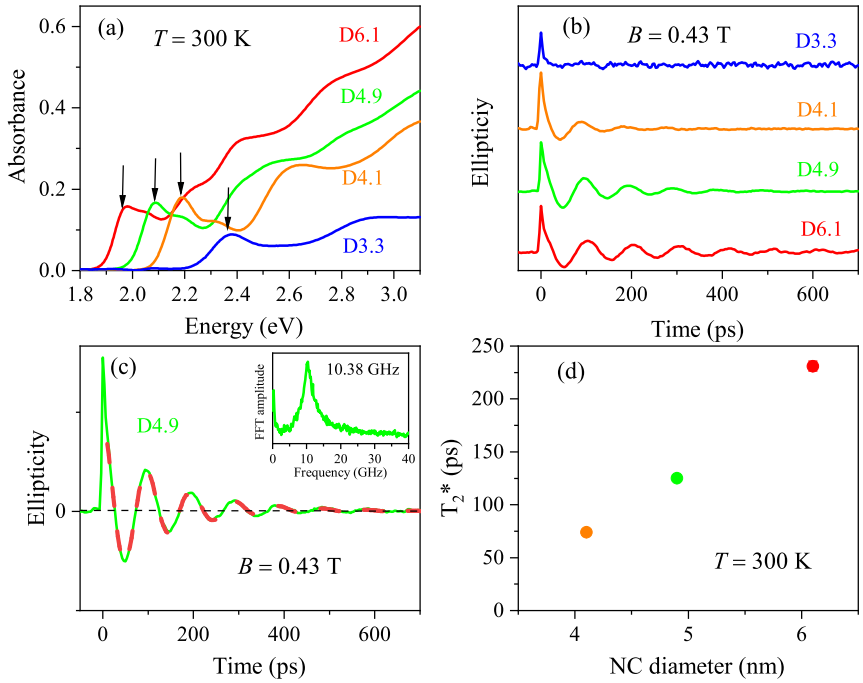

Figure 5.2: Room temperature spin coherence of CdSe NCs in glass matrix. (a) Absorption spectra, black arrows mark the laser energy for pump-probe experiment. (b) Pump-probe Faraday ellipticity measured at $B = 0.43$ T. (c) Faraday ellipticity signal of sample D4.9 (green line) with fit (red dashed line) using only oscillating term of Eq. (5.12), i.e. $A_{\text{no}} = 0$ and $|g| = 1.71$, $T_2^* = 125$ ps. Inset shows the Fast Fourier transform spectrum with a peak at $\omega_L/2\pi = 10.38$ GHz. (d) Size dependence of the spin dephasing time T_2^*.

To start, we first investigate the spin coherent properties of CdSe NCs at room temperature, detailed information about the samples can be found in chapter 3, they

are labeled as D3.3, D4.1, D4.9 and D6.1 respectively, which are D plus the nanocrystal diameter in nanometer. Figure 5.2(a) shows the room temperature absorption spectra, one can see that as the size of NCs decreases, optical transition shifts to the higher energy due to the increase of the electron and hole quantum confinement energies. Figure 5.2(b) shows the pump probe Faraday ellipticity (ppFE) dynamics measured at $B = 0.43$ T at the exciton resonances. Characteristic signals precessing in time domain are found for samples D4.1, D4.9 and D6.1 but no spin coherent signal was detected for sample D3.3. In Fig. 5.2(c), the fitting result of the spin dynamics in sample D4.9 is shown as an example with function [20]:

$$A(t) = A_{\mathrm{o}} \cos(\omega_L t) \exp(-t/T_2^*) + A_{\mathrm{no}} \exp(-t/\tau_s), \tag{5.12}$$

where A_{o} is the amplitude of the oscillating part of the Faraday ellipticity, $\omega_L = |g|\mu_B B/\hbar$ is the Larmor precession frequency, μ_B is the Bohr magneton and $\hbar$ is the reduced Plank constant. The ensemble spin coherence is lost during the spin dephasing time T_2^*. The second term represents the nonoscillating component with amplitude A_{no} and spin lifetime τ_s. We can fit the spin dynamics very well with just the oscillating part, and obtain the g-factor of 1.71 and spin dephasing time of 125 ps. Note that the ppFE experiments do not give direct information about the sign of the g-factors, but it is known for CdSe NCs that the electron g-factor is positive. The existence of only one frequency in the ppFE signal can be also well seen in the Fast Fourier transform (FFT) spectrum plotted as function of $\omega_L/2\pi$ in the inset of Fig. 5.2(c), where a peak at the frequency of 10.38 GHz is clearly seen. The evaluated g-factors for all samples are summarized in Table 5.1. Note that it has been commonly reported in the literature that the surface states play a key role in the appearance of the spin signals, [78,165] since samples used by different groups differ from each other, it is unavoidable that, in some cases for example in our case, to observe only one Larmor frequency. [30,163,165,166,170].

Figure 5.2(d) shows the size dependence of spin dephasing time T_2^* which shortens with decreasing NC size from 230 ps in sample D6.2 to 74 ps in sample D4.1. In finite magnetic fields exceeding the effective field induced for the electrons by the nuclear spin fluctuations, the spin dephasing time of the inhomogeneous spin ensemble is controlled by the g-factor dispersion, Δg. Larger inhomogeneity, therefore, larger Δg is expected for smaller NCs, which explains the observed size dependence of T_2^*.

Table 5.1: Optical parameters of CdSe NCs in glass matrix and measured g-factors. The $E_{1S_{3/2}1S_e}$ is obtained from room temperature absorption spectra.

Sample	NC diameter (nm)	$E_{1S_{3/2}1S_e}$(eV)	g-factor $T = 300$ K	g-factor $T = 6$ K
D3.3	3.30 ± 0.17	2.375	–	–
D4.1	4.10 ± 0.21	2.191	1.77	–
D4.9	4.90 ± 0.25	2.087	1.71	1.89
D6.1	6.10 ± 0.31	1.977	1.62	–

To have a basic understanding about our data, we compare the g-factors from our

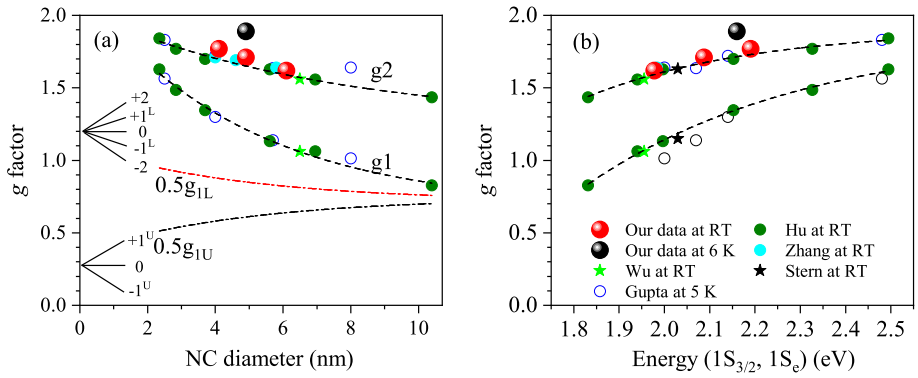

Figure 5.3: (a) Size and (b) first optical transition energy ($1S_{3/2}1S_e$) dependence of g-factors in CdSe NCs. The red (measured at room temperature (RT)) and black (6 K) data points are our results for CdSe NCs in glass matrix. The open circles are data from Ref.[77] measured at $T = 5$ K, dark green (Ref.[78]), cyan (Ref.[163]) data points, green (Ref.[166]) and black (Ref.[165]) stars are room temperature (RT) data. The small and large g-factors are referred as g_1 and g_2. Dashed lines are guide for eyes. Dash-dot lines in the panel (a) show the calculated g-factor corresponding to transitions between equidistant exciton spin states in quasispherical CdSe NCs as shown in the panel (a). To calculate the size dependence of electron g-factor corresponding to $g1$, the hole g-factor $g_h = -0.73$ from Ref.[77] is used.

work with those in the literature. Figure 5.3(a) shows the size dependence of the g-factor. One can see that the g_1 and g_2 from the literature increase with decreasing NCs size, and our data, big red dots (at room temperature, RT), black one (at $T = 6$ K, will be shown later), belong to the g_2 group and matches quite well with the general tendency. Fig. 5.3(b) shows the band-edge transition energy ($1S_{3/2}1S_e$) dependence of the g factors, this way of presentation is instructive at least by two reasons. First, it avoids the uncertainty caused by using various model approaches in evaluating the NC size from the spectral position of the exciton resonance in absorption or emission spectra. Second, it illustrates the main trend in size dependence of electron g-factors in quantum confinement structures originated from the increase of the band gap and respective changes of the spin-orbit coupling.

It is actually surprising for us to observe the g_2 for CdSe NC in glass matrix, because in wet-chemistry grown NCs, g_2 has been assigned to the resident electrons localized inside the nanocrystal but in vicinity of nanocrystal surface. The NCs in glass matrix are expected to have very different surface states comparing to its wet-chemically synthesized counterpart whose surfaces are passivated by organic ligands. Instead of g_2, actually g_1 corresponding to the resident electron in the NC center is expected to be observed in our samples.

5.3 Spin coherent dynamics at cryogenic temperature

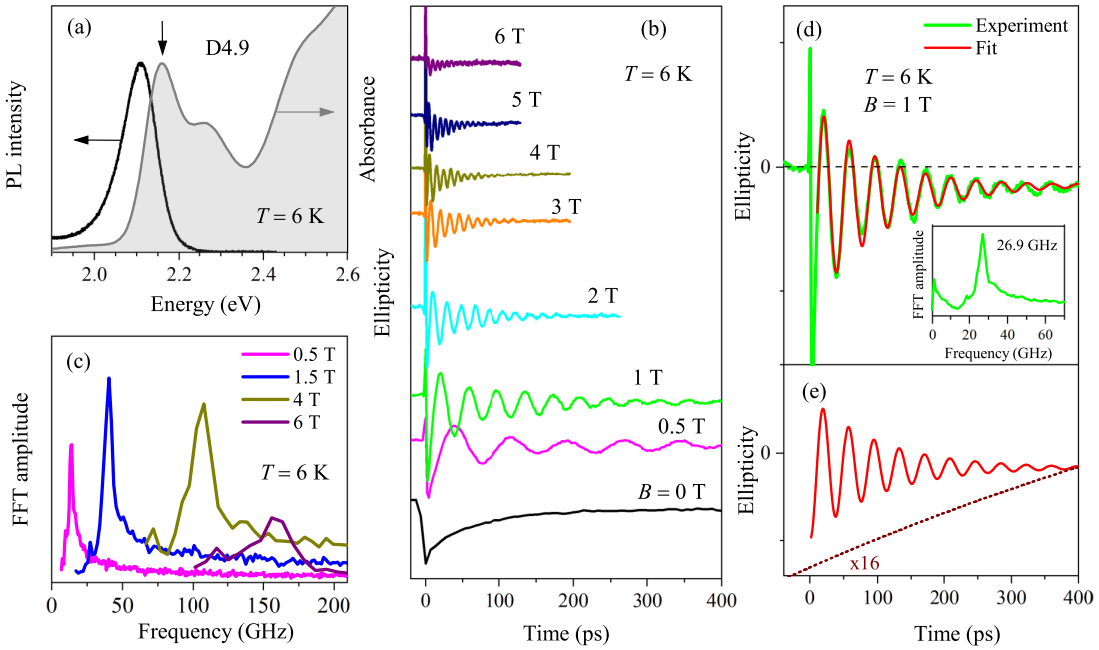

Figure 5.4: (a) Absorption (grey) and photoluminescence (PL) spectra (black) at $T = 6$ K. The vertical arrow indicated the energy position of pump and probe laser beams. (b) Magnetic field dependent ellipticity signal at $T = 6$ K with the pump and probe laser energy at 2.116 eV. (c) Magnetic field dependence of the FFT spectrum based on data in (b). (d) The spectrum measured at $B = 1$ T is replotted (green line) with the fit (red line) using Eq. (5.12). The horizontal dash line indicates the zero level of the signal. Inset shows the FFT spectrum with a peak at 26.9 GHz. (e) Comparison of the oscillating (solid line) and nonoscillating components (dotted line) for the ppFE spectrum in (d). The non-oscillating is multiplied by 16 for clarity.

To further understand the spin coherent dynamics and g-factor in our samples, we performed low temperature ppFE measurement on one of the samples, sample D4.9, the results are shown in Fig. 5.4. Figure 5.4(a) shows the absorption (grey shadowed area) and photoluminescence (PL) (black) spectra at $T = 6$ K. The first optical transition in the absorption spectrum corresponds to the exciton resonance at 2.160 eV and the maximum of the PL spectrum is at 2.105 eV, therefore giving a Stokes shift of 55 meV.

The ppFE signals measured at $T = 6$ K in different magnetic fields up to 6 T are shown in Fig. 5.4(b). The zero-field dynamics show a monotonic decay with two characteristic times 48 ps and 710 ps. In finite magnetic fields, the ppFE signals show characteristic Larmor precession with the frequency increasing in larger magnetic fields where the spin dephasing time also shortens. As one can see in FFT spectra in Fig. 5.4(c) and inset of Fig. 5.4(d), the spin dynamics in the magnetic field is characterized by a single frequency. The more detailed analysis displayed in Fig. 5.4(d) and

Fig. 5.4(e) for $B = 1$ T shows the existence of another nonoscillating component which was absent in the room temperature ppFE spectra.

The magnetic field dependence of ω_L is plotted in Fig. 5.5(a) (left axis), the right axis shows the corresponding Zeeman splitting. Red line is the linear fit using $\omega_L = |g|\mu_B B/\hbar$ from which we get $|g| = 1.89$. It is worthy of noting that the $\omega_L(B)$ dependence does not show any deviation from the linear dependence down to magnetic field of 0.5 T.

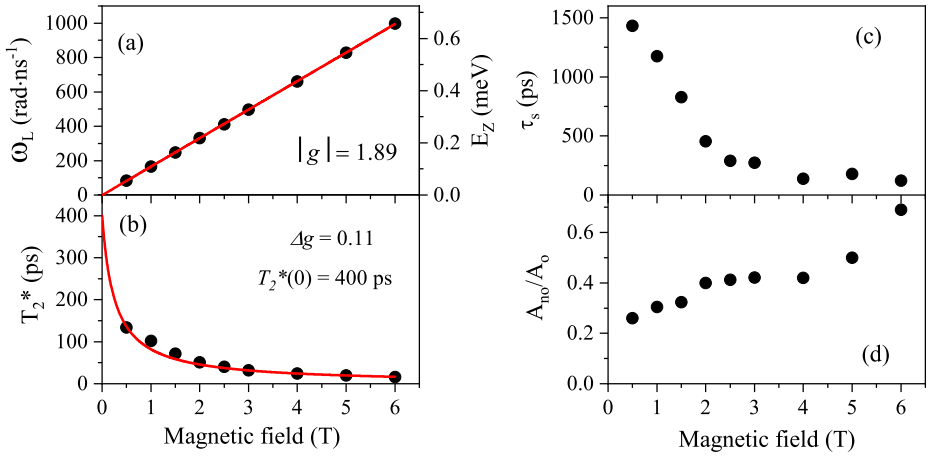

Figure 5.5: (a) Magnetic field dependence of the Larmor precession frequency ω_L and corresponding Zeeman energy (E_Z, right scale) based on the results in Fig. 5.4, red line is the fit with $\omega_L = |g|\mu_B B/\hbar$, which gives $|g| = 1.89$. (b) The magnetic field dependence of corresponding dephasing time T_2^*, red line is the fit using Eq. (5.13), where we get $\Delta g = 0.11$ and $T_2^*(0) = 400$ ps. (c) Magnetic field dependence of the decay time for nonoscillation component. (d) Magnetic field dependence of the amplitude ratio between the nonoscillating (A_{no}) and oscillating (A_{o}) components.

The magnetic field dependence of T_2^* is shown in Fig. 5.5(b), when increasing magnetic field from 0.5 to 6 T, T_2^* decreased drastically from 134 ps to 16 ps, which can be described by:[166]

$$\frac{1}{T_2^*(B)} = \frac{1}{T_2^*(0)} + \frac{\Delta g \mu_B B}{\hbar}, \tag{5.13}$$

where Δg is the dispersion of g factor for the optically excited spin ensemble. The fit (red line) gives $\Delta g = 0.11$, spin dephasing time at zero field $T_2^*(0) = 400$ ps. The magnetic field effect on the nonoscillating component is displayed in Fig. 5.5(c) and Fig. 5.5(d). The spin lifetime of the nonoscillating component (τ_s) decreases from 1430 ps down to 122 ps with the increasing field from 0.5 to 6 T, while the amplitude ratio between the nonoscillating and oscillating components ($A_{\mathrm{no}}/A_{\mathrm{o}}$) increases from 0.26 to 0.70.

The nonoscillating component in the Faraday ellipticity or rotation signal is commonly observed and reported in other publications, however, its origin is still not clear. In the earlier studies, several mechanisms have been proposed to explained it, for instance, the decay of hole spins pinned along the growth axis,[171] the leakage of the longitudinal spin-relaxation signal,[77] surface carrier trapping,[162,165] or the decay of nonoscillating exciton populations.[165,172] In the next section, we will show that the nonoscillating component is actually from the frozen exciton spin polarization created by the pump pulse in NCs with heavy-light hole splitting determined by the crystal field.

5.4 Larmor precession of the exciton spin

To figure out the contradictions of the origin of g_2 precession component, we theoretically consider the Larmor precession of exciton spin in CdSe NCs. In our calculation, we do not consider the radiate decay and spin relaxation of excitons, and assume that in the applied magnetic field, a circularly polarized photon moving along the Z-axis of laboratory frame at $t = 0$ creates a superposition of exciton states $|+1\rangle, |-1\rangle, |0\rangle$, which would be created in the absence of magnetic field meaning that the magnetic field does not affect the exciton state being created. In the case of nanocrystal with zero net splitting of the hole state, i.e. $\Delta = 0$ meV, there is no anisotropy axis, and circularly polarized photon $\sigma^{\pm}$ excites the pure eigenstates $|\pm 1^{U,L}\rangle$ with spin aligned along the Z-axis. For $\Delta \neq 0$ meV, the superposition state $(1 \pm \cos\theta)\,|+1^{U,L}\rangle + (1 \mp \cos\theta)\,|-1^{U,L}\rangle$ is excited by the pump pulse, where θ is the angle between z-axis of NC frame and Z-axis of the laboratory frame.[173]

Calculation of the time evolution of $\langle S_Z\rangle = \langle\Psi^*|S_{\sigma,J}|\Psi\rangle$ (Ψ is the wave function of the system, $S_Z^{\sigma,J}$ is the Z-component of full electron-hole spin matrix given in section 5.1) is realized by expansion of the initially excited state over the eigenstates of Hamiltonian (5.9) and subsequent transformation to the basis along the Z-axis. Results of calculation for spin precession in nanocrystal with $\Delta = 0$ meV is shown in Fig. 5.6(a) by red and black curves for $|1^L\rangle$ and $|1^U\rangle$ excitons, respectively. These curves are described by the $\cos\Omega_{L,U}t$ with $\Omega_{L,U} = 0.5 g_{1^{L,U}}\mu_B B/\hbar$ where $g_{1^{L,U}}$ determines the Zeeman splitting of exciton states $\Delta E_{\pm 1^{L,U}} = g_{1^{L,U}}\mu_B B$. One can see, that for excitons, unlike the electron, the Zeeman splitting equals to doubled energy of $\Omega_{L,U}\hbar$, because Larmor precession is based on transitions between the neighboring spin states, i.e. $+1/2 \leftrightarrow -1/2$ for electron and $-1 \leftrightarrow 0 \leftrightarrow +1$ for exciton. The calculated exciton Larmor frequency is twice smaller compared to the results reported in Ref.[77] where wrong relation between exciton g-factor and exciton Larmor frequency was used. As a result, keeping all the physical assumptions from Ref.[77], one can describe the size dependence of g_2 as a Larmor precession of $|1^L\rangle$ exciton in quasispherical CdSe NCs using $g_h \approx -1.8$ instead of -0.73 obtained in Ref.[77]. The value $g_h \approx -1.8$ is much larger comparing to theoretical estimations[62,174] and experimental results re-

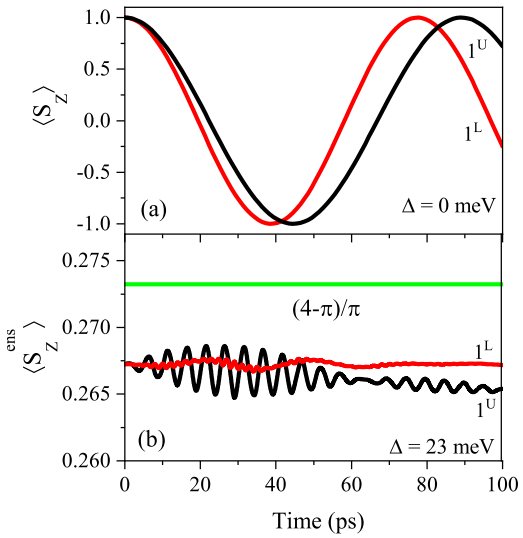

Figure 5.6: Calculated time dependence of the mean exciton spin $\langle S_Z \rangle$ in CdSe NCs with $D = 6$ nm, $g_e = 1.1$, $g_h = -0.86$, $B = 1$ T in (a) ensemble of quasispherical NCs with $\Delta = 0$ meV; (b) randomly oriented ensemble of NCs with $\Delta = 23$ meV. Red and black curves correspond to precession of $|1^L\rangle$ and $|1^U\rangle$ excitons created by σ^+ polarized pump pulse. The green line in the panel (b) is the mean spin value for ensemble of randomly oriented spins $S = 1$ (see Eq. (5.17).

ported previously, making doubtful interpretation of g_2 as the g-factor of $|1^L\rangle$ exciton in quasispherical NCs.

To obtain the evolution of mean spin $\langle S_Z^{\rm ens} \rangle$ in the randomly oriented ensemble of wz-CdSe NCs with $\Delta = 23$ meV, we calculate the time evolution of exciton spin in single nanocrystal with subsequent averaging over the random orientation of NCs (see section 5.1). The results are shown by the black and red lines in the Fig. 5.6(b), one can see that spin precession is suppressed and $\langle S_Z^{\rm ens} \rangle$ only slightly deviates from its initial value. Therefore, for the ensemble of randomly oriented wz-CdSe NCs, pump pulse should create nonoscillating spin polarization of excitons, which will be lost during the time of longitudinal exciton spin relaxation. The microscopic mechanism of Faraday rotation by polarized excitons was considered in Ref. [175], it is based on the exchange interaction between polarized excitons created by pump pulse in NC and virtual excitons created by probe pulse.

To provide a qualitative understanding of the results shown above, we consider the Larmor precession of spin $S = 1$ since it can be thought of as a simplified version of the bright exciton. The Hamiltonian in this case reads as:

$$\hat{H} = \hbar \boldsymbol{\Omega} \boldsymbol{S} - \frac{\Delta}{2}(S_z^2 - 1) + C(S_x^2 - S_y^2) \tag{5.14}$$

where $\boldsymbol{\Omega} = g\mu_B \boldsymbol{B}/\hbar$, $S_{x,y,z}$ are 3×3 spin matrices. The second term is an analogue

of exciton states split by the crystal field of wz-CdSe. The third term mimics the anisotropic exchange interaction resulting in mixing of $|+1\rangle$ and $|-1\rangle$ bright exciton states[169]. In the exciton Hamiltonian (5.9), we skip the anisotropic exchange term considering the spherical shape of NCs, however, it can be included as it was done in Ref.[169]. Imagine at $t = 0$, we excite superposition $A_+ |+1\rangle + A_- |-1\rangle$, as it was the bright exciton in wz-CdSe NCs[62], where $A_\pm = (1 \pm \cos\theta)/(1 + \cos^2\theta)^{1/2}$. In the case of transverse magnetic field ($\boldsymbol{B} \perp \boldsymbol{z}$), spin precession can be described analytically. The mean spin value $\langle S_z(\theta)\rangle$ for arbitrary Ω,Δ,C is:

$$\langle S_z(\theta)\rangle = \frac{4\cos\theta}{3+\cos 2\theta}\left(\cos\omega_+ t \cos\sqrt{\Omega^2+\omega_-^2}\, t + \frac{\omega_-}{\sqrt{\Omega^2+\omega_-^2}} \sin\omega_+ t \sin\sqrt{\Omega^2+\omega_-^2}\, t \right) \tag{5.15}$$

where $\omega_+ = (3C + \Delta)/2\hbar$ and $\omega_- = (\Delta - C)/2\hbar$. Time evolution of the mean spin along the Z-axis of the laboratory frame is given by $\langle S_Z(\theta)\rangle = \langle S_z(\theta)\rangle \cos\theta$.

There are several limiting cases of precession for $\langle S_z(0)\rangle$:

$$\begin{array}{lll} \text{(i)} & \omega_- = \omega_+ = 0 & \cos\Omega t \\ \text{(ii)} & \omega_- = 0 & \cos(2Ct/\hbar)\cos\Omega t \\ \text{(iii)} & \omega_+ = 0 & \cos\sqrt{\Omega^2 + (2C/\hbar)^2}\, t \\ \text{(iv)} & \Omega \ll \omega_-, C \neq 0 & \cos(2Ct/\hbar) \\ \text{(v)} & \Omega \ll \omega_-, C = 0 & 1 - (\Omega\hbar/\Delta)^2(1 - \cos\Delta t/\hbar) \end{array} \tag{5.16}$$

The regime (i) corresponds to the Larmor precession of isotropic spin $S = 1$. The regimes (ii,iii) corresponds to slightly perturbed precession of spin $S = 1$ which is modulated by the anisotropy-related precession $\cos\omega_+ t$ (ii) or have the nonzero cut-off at zero magnetic field (iii). These regimes are realized if conditions $\Delta = C$ or $3C = \Delta$ are satisfied. The cases (iv,v) correspond to large anisotropic distortion which results in the precession at frequency $2C/\hbar$ (iv) or strongly supressed precession (v) for $C = 0$. Note that regime (v) is similar to the result obtained in Ref.[176] for spin precession of heavy hole excitons in the case of large splitting between bright $|\pm 1\rangle$ and dark $|\pm 2\rangle$ exciton states. The regime (v) corresponds to the situation for wz-CdSe NCs. In this case, the initial value of $\langle S_Z\rangle$ remains unchanged during the time of spin coherence. For the randomly oriented ensemble of spins $S = 1$, it is:

$$\langle S_Z\rangle \approx \langle S_Z^{t=0}\rangle = \frac{2}{\pi}\int_0^{\pi/2} \frac{4\cos^2\theta\sin\theta}{3+\cos 2\theta} d\theta = \frac{4-\pi}{\pi} \tag{5.17}$$

As one can see in Fig. 5.6(b), this analytical result show a good agreement with numerical calculations for precession of $|1^{U,L}\rangle$ exciton spin in wz-CdSe NCs. Thus, we

conclude that the exciton Larmor precession in wz-CdSe NCs is suppressed due to large splitting of exciton states originating from the crystal field splitting of light and heavy hole subbands.

5.5 Conclusion

We performed comprehensive study of the coherence property in CdSe NCs in glass matrix. Experimental results show that at room temperature, one Larmor frequency can be resolved from the pump probe Faraday ellipticity spectra, while at low temperature, besides the Larmor precession component, we also resolved another nonoscillating process which is related to the frozen exciton spin polarization created by the pump pulse in NCs with heavy-light hole splitting based on the theoretical analysis. The obtained g-factors belong to the g_2 group in the literature, and our calculation clearly shows that it is related to electrons and its possible exciton origin can be excluded.

Chapter 6

Magneto-optics of CuCl nanocrystals

Due to the special electronic but relative simple crystal structure of CuCl,[177] a lot of effort have been put into its research and many magneto-optical experiments have been performed on the bulk single crystal or films.[178–184] Khan calculated the g-factor of 2.03 for the conduction band and g-factor of -1.44 for the upper valence band Γ_7^+ at the center of the Brillouin Zone.[178] Later on, A. Goltzene and C. Schwab observed the conduction band g-factor of 1.998±0.002 using the electron spin resonance method.[179] Moreover, by measuring the magnetic field dependent reflection spectra, Stande obtained the g-factor of Z_3 exciton and $Z_{1,2}$ exciton which are 0.3 and -0.3 (0.33 and -0.42 for calculation), respectively.[181] While Suga et al.[182] resolved a slightly different value of 0.56 for Z_3 exciton using Faraday rotation spectroscopy.

With the availability of CuCl nanocrystals (NCs) and the discovery of the quantum confinement effect,[52,54,185] relevant magneto-optical experimental results are also reported. For example, Nomura et al.[186] performed magnetic circular dichroism measurements on CuCl microcrystallites embedded in a polymer matrix, and got the effective Z_3 and $Z_{1,2}$ exciton g factor of 0.447 and -0.18, respectively, the former is sitting between the values in bulk crystals reported by Stande[181] and Suga et al.[182] while the later is much smaller. However, as far as we know, no experiments such as polarization and optical orientation, fluorescence line narrowing (FLN) or spin-flip Raman scattering have been reported by now on CuCl NCs.

So in this chapter, we investigated the polarization and optical orientation properties of CuCl NCs in glass matrix, and conducted the FLN and SFRS experiments. The chapter is organized as following: first, we describe the band structure of the CuCl crystal, then present the temperature dependent photoluminescence (PL) and absorption results together with polarization propertie and optical orientation measurement

results. Finally, the FLN and SRFS measurements are discussed.

6.1 Band structure of CuCl

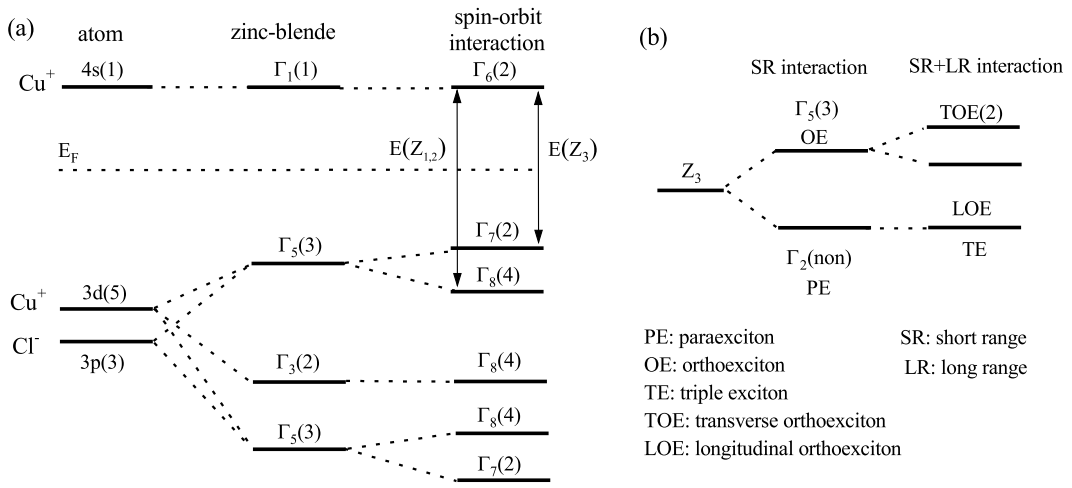

Figure 6.1: Schematic of the conduction and valence bands at the Γ point in CuCl. (a) The first column shows the atomic levels of copper and chlorine, the second column represents partial lifting of the degeneracy of the d levels and hybridization in a cubic crystal field, and the third column demonstrates the spin-orbit splitting effect on the band structure. (b) Scheme describing the effect of short- and long-range exchange interaction on the Z_3 exciton state.

Cuprous halides have zinc blende structure below the transition temperature of about 660 K and wurtzite structure above it.[187] In zinc blende CuCl, the spin-orbit splitting is reversed as compared to all other direct gap zinc-blende semiconductors. As illustrated in Fig. 6.1(a), the uppermost valence band is twofold degenerate having Γ_7 symmetry, while the next lower, fourfold degenerate valence band exhibits Γ_8 symmetry due to the p-d mixing of the atomic orbitals.

The relevant atomic states of copper and chlorine are shown in the first column of Fig. 6.1(a). When subjected to a crystal field of T_d symmetry, the orbital copper d levels split into two Γ_5 and one Γ_3 levels. The former hybridize with the chlorine p levels having the same symmetry resulting in two threefold degenerate Γ_5 levels see second column in Fig. 6.1(a). This hybridization raises the top of the valence band relative to the anion (Cl) p level. Cu d levels are very important for the band structure given the fact that, although the p levels of the isoelectronic anions Cl, Br, and I differ by about 2 eV, the band gaps of the copper halides differ by less than 0.3 eV, i.e. the anion levels have only a small influence on the band gap.[188] Taking the spin-orbit interaction into account results in a splitting of the p-d mixed Γ_5 states into levels of Γ_7 and Γ_8 symmetry see third column in Fig. 6.1(a). The order of the uppermost valence states

in CuCl is reversed, i.e. the Γ_7 states are higher in energy than the Γ_8 states because the d states contribute to the spin-orbit splitting with opposite sign as compared to p orbitals.

The exciton states which originate from Γ_7 (j= 1/2) and Γ_8 (j= 3/2) with the common conduction band Γ_6 are denoted as Z_3 and $Z_{1,2}$, respectively, by Cardona.[177,189] It is worth noting that Z_3 ($Z_{1,2}$) exciton corresponds to the split-off-hole exciton (the degenerate heavy-hole and light-hole excitons), and the Z_3 exciton is the lowest-energy excitonic state.[190] In this work, we mainly focus on the Z_3 exciton state.

If one includes further the short-range exchange interaction, the Z_3 exciton will be split into ortho- and paraexcitons (OE and PE) having Γ_5 (threefold degenerate) and Γ_2 (nondegenerate) symmetry as shown in the first column in Fig. 6.1(b). Optical transitions to the orthoexciton are one-photon allowed, while to the first order, the paraexciton is one-photon transition forbidden. Moreover, the long-range exchange interaction can split the Γ_5 states into transverse and longitudinal orthoexcitons (TOE and LOE), see the second column in Fig. 6.1(b). The Γ_2 state is of the lowest state and strictly dipole-forbidden due to the pure spin triplet nature unless an external field is applied, which is therefore called "triplet exciton" (TE).[184,191]

6.2 Optical properties under pulsed laser excitation

6.2.1 Temperature dependence of the PL and absorption spectra

In order to have a basic understanding about the optical properties of our CuCl NCs, the photoluminescence (PL) (black) and absorption spectra (red) were measured first at T = 4.2 K as shown in Fig. 6.2(a)-(e). In all samples, the absorption spectrum shows two clear peaks corresponding respectively to the Z_3 and $Z_{1,2}$ exciton states.[177,192] Former reports have revealed several emission peaks in the PL spectrum of CuCl NCs, e.g. free-Z_3 exciton (X), bound exciton (BX), biexciton (M) and bound biexciton (BM), etc.[193–195] The PL peak close to the Z_3-exciton absorption band is ascribed to the X emission, the strongest peak at the lower energy is assigned to the M emission. Taking sample 18A in Fig. 6.2(a) as an example, the X and M emission peaks are at 3.25 and 3.18 eV, respectively. The bound exciton state BX is between X and M, and is only resolved in samples with smaller size, i.e. 18A, 29A and 40A, in Fig. 6.2(a)-(c) as marked by vertical arrows. While the bound biexciton state BM which is at the lower energy side of M state, is only present in larger NCs see Fig. 6.2(c)-(e). The BX or BM emission may be associated with impurities such as a Cu^+ vacancies.[194,196] For the smallest sample 18A, in Fig. 6.2(a), at the higher energy side of X, there is another component labeled as X* about 22 meV above X state. It could presumably be attributed to an exciton bound to a higher-lying defect state within the conduction band like Br vacancy defects in $CsPbBr_3$.[197]

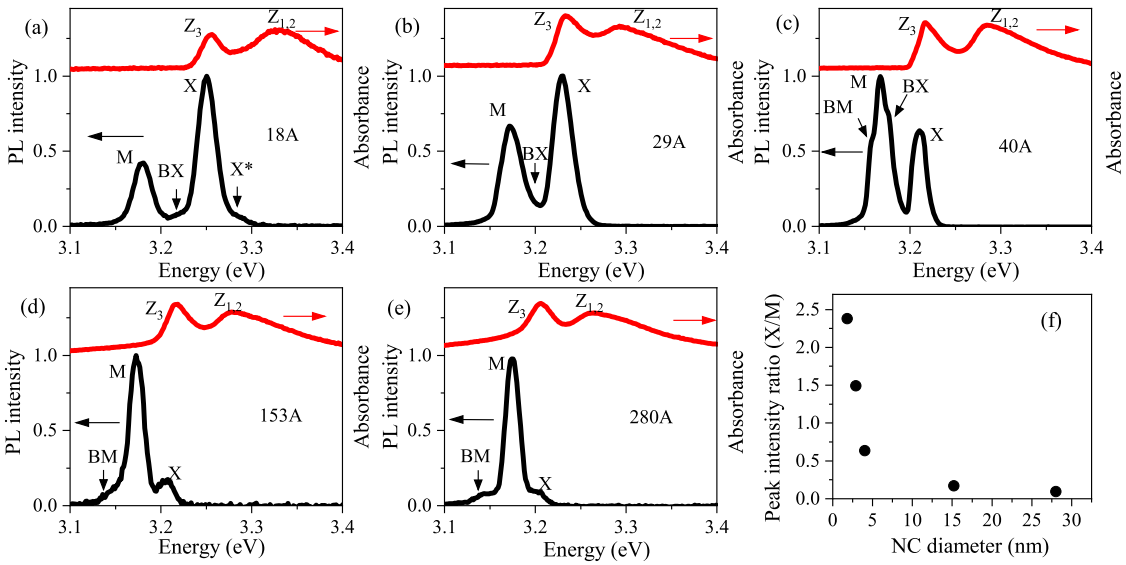

Figure 6.2: Photoluminescence (black) and absorption (red) spectra measured at $T = 4.2$ K for sample (a) 18A, (b) 29A, (c) 40A, (d) 153A, (e) 280A with nanocrystal size 1.8 nm, 2.9 nm, 4.0 nm, 15.3 nm and 28.0 nm, respectively. (f) Size dependence of intensity ratio between X and M peaks.

As the nanocrystal size increases, the intensity of X decreases but that of M increases, the size-dependent intensity ratio is plotted in Fig. 6.2(f). In sample 18A, the intensity ratio is 2.4, while in 280A, it is only 0.1. The similar behavior was also observed earlier in CuCl films.[192,194]

The temperature dependent PL and absorption spectra are shown in Fig. 6.3, the results for sample 18A and 280A are shown as representatives. One can see that the PL intensity in both samples decreases with increasing temperature. The PL spectra are fitted by multi-Gaussian functions, e.g. the PL spectra of sample 18A are fitted with five Gaussian components (see in Fig. 6.3(a2), which are marked as G_X, G_{X*}, G_{BX}, G_M and G_{bkg} respectively referring to X, BX, M, MX, and the broad background emission which maybe comes from the bound states of transverse and longitudinal excitons or biexcitons.[192] The linear absorption spectra are analyzed based on the theory proposed by Norris et al.[198] The well resolved optical transitions are described using multi-Gaussian components while the unresolved continuum-like optical transitions are represented by a polynomial background term. The general mathematical formula for modeling is:[199]

$$A(w) = \sum_{i=1}^{3} \alpha_i exp\left\{ -\left(\frac{w - w_i}{\gamma_i}\right)^2 \right\} + p_1 + p_2 w + p_3 w^2. \tag{6.1}$$

α_i are the weighted coefficients, w_i are the center of the Gaussian peaks, γ_i are the factors determining the Gaussian widths and p_1 , p_2 and p_3 are the polynomial coefficients

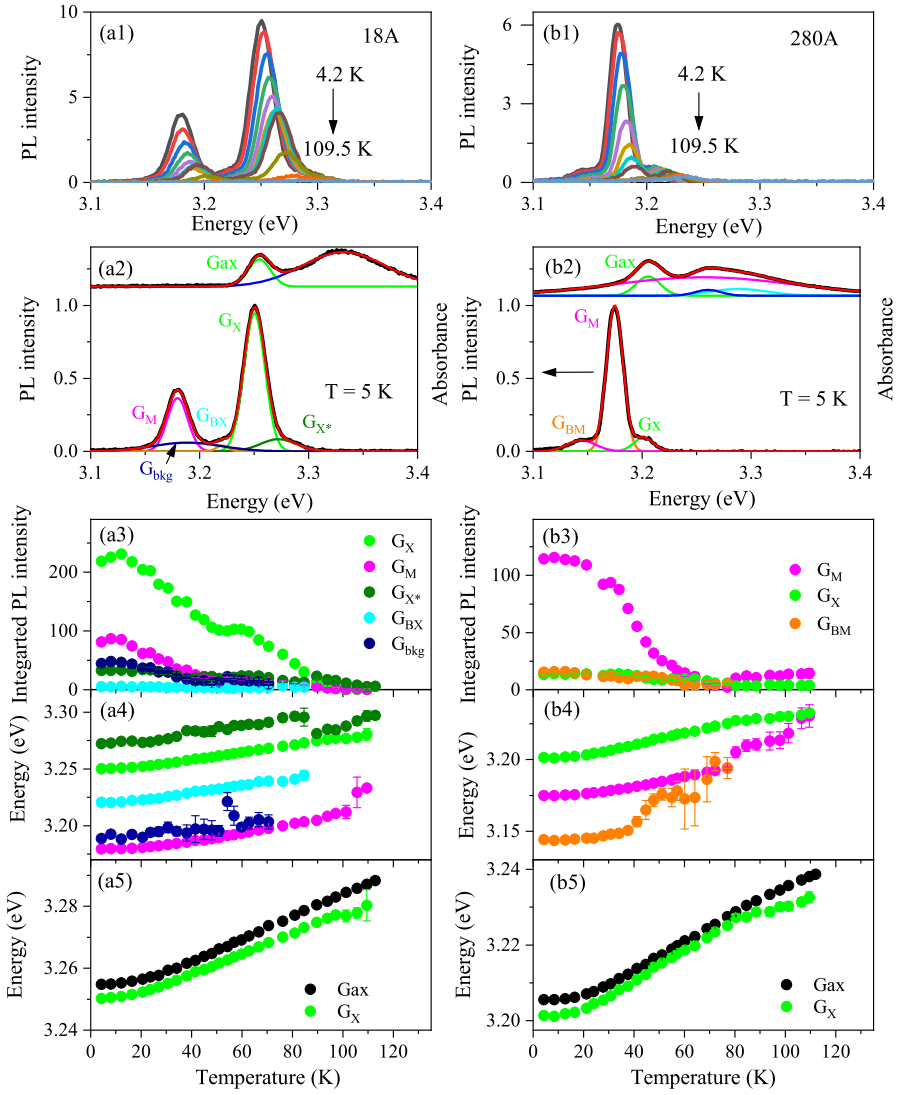

Figure 6.3: Temperature dependent photoluminescence (PL) of CuCl NCs in glass, data for sample 18A ((a1)-(a5)) and sample 280A ((b1)-(b5)) are shown as examples. (a1), (b1) PL spectra at various temperatures. (a2), (b2) PL and absorption spectra measured at $T = 4.2$ K with corresponding simulations, G_X, G_{BX}, G_{X*}, G_M, G_{BM} and G_{bkg} are Gaussian components for the PL fitting referring to the emission from X, BX, X*, M, MX, and the broad background emission. The Gaussian component related to the first optical transition from the absorption spectra is labeled as Gax. (a3), (b3) Temperature dependence of the integrated PL intensity of the Gaussian components in the PL spectra. (a4), (b4) Temperature dependence of the energy position of Gaussian components, for each component the same color is used as in (a3), (b3). (a5), (b5) temperature dependence of energy position for G_X (PL) and Gax (absorption) components.

used to model the background part. The absorption spectra are shown without the background part, and the Gaussian component for the first optical transition is labeled as Gxa.

The fitting results are summarized in Fig. 6.3(a2)-(a5) for 18A and Fig. 6.3(b2)-(b5) for 280A. As it is shown in Fig. 6.3(a3) and Fig. 6.3(b3), the integrated PL intensity of all Gaussian components decreases with increasing temperature, which is presumably due to the thermally activated nonradiative trap states on the surface or inner defects of NCs.[200] Interestingly, their energy positions are blue-shifted with increasing temperature. This is contradictory to the normal situation in GaAs, GaP, Si, CdSe, etc, where the temperature-induced band gap renormalization can be well described by the Varshini equation.[201–203] The observation here is, however, very similar to the situation in perovskite NCs,[204–207] where the blue shift has been ascribed to the stabilization of the valence band maximum with the lattice expansion.[208]

It is also interesting to notice that for sample 18A in Fig. 6.3(a4), within the current temperature range, the energy of Gaussian components shifts basically in parallel. However, for sample 280A shown in Fig. 6.3(b4), the three Gaussian components tend to emerge into the G_X peak with increasing temperature, which underlines the clear difference between samples with small and large nanocrystal size. Moreover, the biexciton emission quenches much faster in larger NCs than that in smaller ones due to the relatively smaller biexciton binding energy in the former case.

We compared the temperature dependence of the G_X and Gax energy position in Fig. 6.3(a5) and (b5). In the low temperature range (< 20 K), the energy position tends to be flat in both samples, and follows a positive linear-dependence above 20 K. This feature has been referred to as the anomalous behavior of bandgap in the literature, not only for CuCl NCs[209] but also for PbS NCs[210] and perovskite NCs.[205] Generally, the temperature induced band gap renormalization can be understood from the interplay of three factors, i.e. (i) first- and second-order electron-phonon interactions that contribute to the energy of the conduction and valence bands, (ii) thermal lattice expansion, and (iii) changes in the phonon occupation number.[205,211] For the case of CuCl, Göbel et al.[209] developed a two-oscillator model to explain it. The idea of their model is as following, considering the relatively large mass difference between Cu and Cl, the acoustic-mode eigenvectors are dominated by copper displacements while those of the optical modes mostly involve chlorine displacements. Therefore, it is efficient to approximate the lattice dynamics of CuCl by two effective harmonic oscillators: one oscillator with an energy of w_{Cu} represents an average acoustic phonon which is purely Cu-like, and a second oscillator with an energy of w_{Cl} represents an average optical phonon which is purely Cl-like. Its mathematical expression is as following:

$$E_0(T) = E_0 + \frac{A_{Cu}}{w_{Cu}M_{Cu}}\left(n\left(w_{Cu},T\right) + \frac{1}{2}\right) + \frac{A_{Cl}}{w_{Cl}M_{Cl}}\left(n\left(w_{Cl},T\right) + \frac{1}{2}\right) \tag{6.2}$$

where E_0 is the band gap at zero temperature, and A_{Cu}, A_{Cl} are effective electron-phonon interaction parameters.

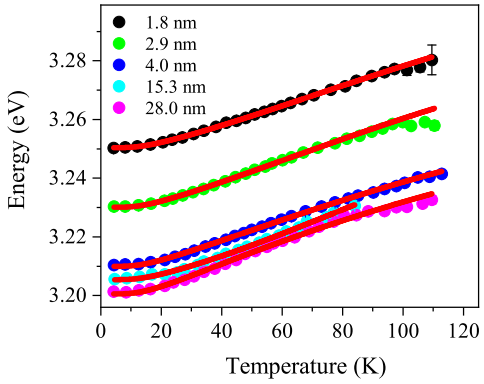

Figure 6.4: Temperature dependence of the peak position of G_X component based on PL spectrum analysis for all the samples. The red solid lines are fits using the two-oscillator model with Eq. (6.2).

The temperature dependence of the G_X component from PL fitting are collected in Fig. 6.4, the red solid lines are simulations using the two-oscillator model. Natural copper and chlorine have two stable isotopes each (relative abundances: ^{63}Cu, 69.2%; ^{65}Cu, 30.8%; ^{35}Cl, 75.8%; and ^{37}Cl, 24.2%), one can set M_{Cu} and M_{Cl} to be the weighted average value, 63.616 and 35.484. w_{Cu} = 1.05 THz and w_{Cl} = 4.0 THz are taken from Ref.[209]. The fitting parameters are listed in Table 6.2.1. With the decreasing of CuCl nanocrystal size, band energy becomes lager due to the quantum confinement effect. Following the principle proposed by Efros et al.,[81,212] depending on the relationship between the nanocrystal size (a), Bohr radius of electron (a_e) and hole (a_h), quantum confinement can be classified into three regimes, i.e. weak confinement ($a > a_e$,a_h), intermediate confinement ($a_{e,(h)} > a > a_{h,(e)}$) and strong confinement (a_e,$a_h > a$).[81,82,212] The exciton Bohr radius in CuCl is 0.7 nm,[213,214] which is smaller than the smallest nanocrystal radius in our samples (0.9 nm), therefore samples studies in this work cross the intermediate and weak confinement regimes up to no confinement effect (bulk, 15.3 nm and 28.0 nm NCs). The fitting parameters A_{Cu} and A_{Cl} show different size dependence, i.e. A_{Cu} increases in larger NCs while A_{Cl} decreases. Since A_{Cu} and A_{Cl} represent the contribution of Cu atoms (acoustic phonon) and Cl atoms (optical phonon) in the electron-phonon interaction process, this maybe related to the size dependent polarization properties which will be discussed later.

As we have discussed in CdSe NCs in chapter 4, the LO phonon is very important in determining the polarization properties of dark excitons, so before turning to the polarization results, we firstly analyze the possible role of opticl phonons in determining the population distribution of X, BX, M, BM and X* states based on the temperature dependent PL spectra as examplified in Fig. 6.3. The energy distance between X and other peaks, i.e. the energy of other peaks minus the energy of X peak, are calculated using the multi-Gaussian fitting results. At low temperature, the energy separations between different peaks are almost constant. The deviation at higher temperature is

Table 6.1: Two-oscillator model fitting parameters for temperature dependent Z_3 exciton (G_X) energy. E_0 is the band gap energy at zero temperature, A_{Cu} and A_{Cl} are effective electron-phonon interaction parameters.

Sample	NC's size (nm)	E_0 (eV)	A_{Cu}	A_{Cl}
18A	1.8	3.25	1.43	8.33
29A	2.9	3.23	1.64	8.03
40A	4.0	3.21	1.70	5.95
153A	15.3	3.20	1.49	11.38
280A	28.0	3.20	2.00	4.86

partially due to the quenched and therefore weak PL intensity which may cause larger errors. Note that the hypothesis of phonon replica should be carefully considered.[195]

Exciton-LO phonon replicas have been previously reported in CuCl crystal at the low temperature,[215] however, in the CuCl films, even though PL spectra similar to ours are observed, solid evidence is found which does not support the phonon replica explanations for the presence of so many peaks.[195] As it is shown in Fig. 6.5, the energy distance between X and M (magenta) in sample 153A and 280A at 4.2 K are 31.8 meV (Fig. 6.5(d)) and 26.5 meV (Fig. 6.5(e)), which agrees very well with the biexciton binding energy (32 meV) in literature.[213,214] While the energy distance increases with decreasing nanocrystal size from 49.9 meV (40A), 57.7 meV (29A) to 70.5 meV (18A) as shown in Fig. 6.2(c)-(a) due to the quantum confinement effect. This indirectly confirms our assignment of X and M peaks. Commonly, the energy distance between exciton and biexciton peak can be regarded as biexciton binding energy,[79,216] but this is only true when the radiative decay of the biexciton produces an exciton, i.e. Z_3 biexciton decays with a Z_3 exciton left. However, Hasuo et al.[217] reported that the radiative decay of a biexciton leaves a $Z_{1,2}$ exciton behind in CuCl crystals, so further experiments are actually needed to clarify if the energy difference between X and M is biexciton binding energy or not.

The energy difference between BX and X (cyan) keeps constant about 38.3 meV throughout the temperature range in sample 29A and 40A see Fig. 6.5(b) and (c). In sample 18A in Fig. 6.5(a), it is also independent of temperature but gives a smaller value of 29.5 meV, the reason for the decrement is not clear but the effect of LO phonons can be eliminated since the LO phonon energy in CuCl is 26 meV which is much smaller comparing to the energy distance between X and BX. Moreover, if LO phonons are involved, the increased LO phonon-exciton interaction at higher temperature should lead to the increasing of the intensity ratio between the LO phonon line and the zero-phonon line. However, as it is shown in Fig. 6.5(f), this is not the case, i.e. with the increasing of temperature, the ratio of the integrated intensity between BX and X in sample 18A is near constant, and decreases in 29A and 40A. The energy difference between X* and X in sample 18A also stays constant at 22 meV up to 80 K in

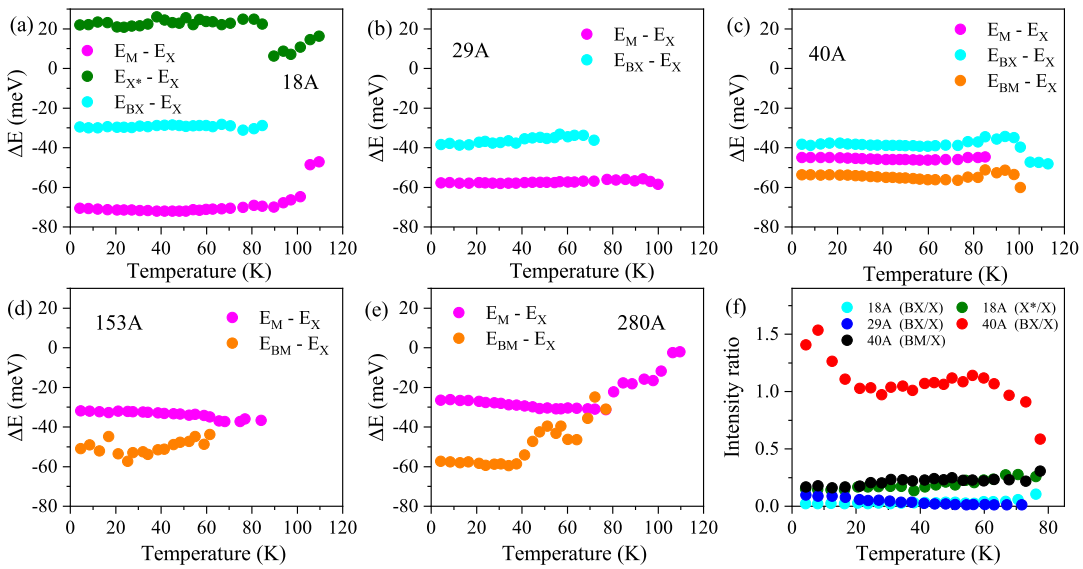

Figure 6.5: Temperature dependence of energy distance of Gaussian components from PL fitting for sample (a) 18A, (b) 29A (c) 40A, (d) 153A and (e) 280A. (f) Temperature dependence of the intensity ratio between X and BX (BX/X) for 18A, 29A, 40A. The intensity ratio between X and X* (X*/X) for 18A, between BM and X (BM/X) for 40A are also shown.

Fig. 6.5(a), the ratio of integrated intensity of X* and X slightly increases in Fig. 6.5(f) (oliver) indicating the possible role of LO phonon for this emission process. The energy distance between X and BM (orange) is 53.6 meV in sample 40A, 50.9 meV in sample 153A and 57.3 meV in sample 280A. One can see that below 40 K, it is more or less constant. These energy distances are close to the double LO phonon energy, however, the temperature dependent PL intensity ratio does not increase from 30 K up to 80 K, therefore the role of LO phonon in BM emission can be also eliminated. Based on the above analysis, we are able to draw the conclusion that the role of LO phonons is negligible for the PL emission in our samples, but the acoustic phonon may play a significant role.

6.2.2 Polarization properties of Z_3 exciton

Figure 6.6(a)-(e) shows the polarization-resolved PL spectra measured at $T = 1.9$ K, $B = 6$ T. External magnetic field polarizes the PL with σ^- component (blue) having larger intensity than σ^+ (red) component. The time-integrated degree of circular polarization (DCP), $P_c{}^{int}$, is calculated using the following equation:

$$P_c^{int} = \frac{I^+ - I^-}{I^+ + I^-}. \tag{6.3}$$

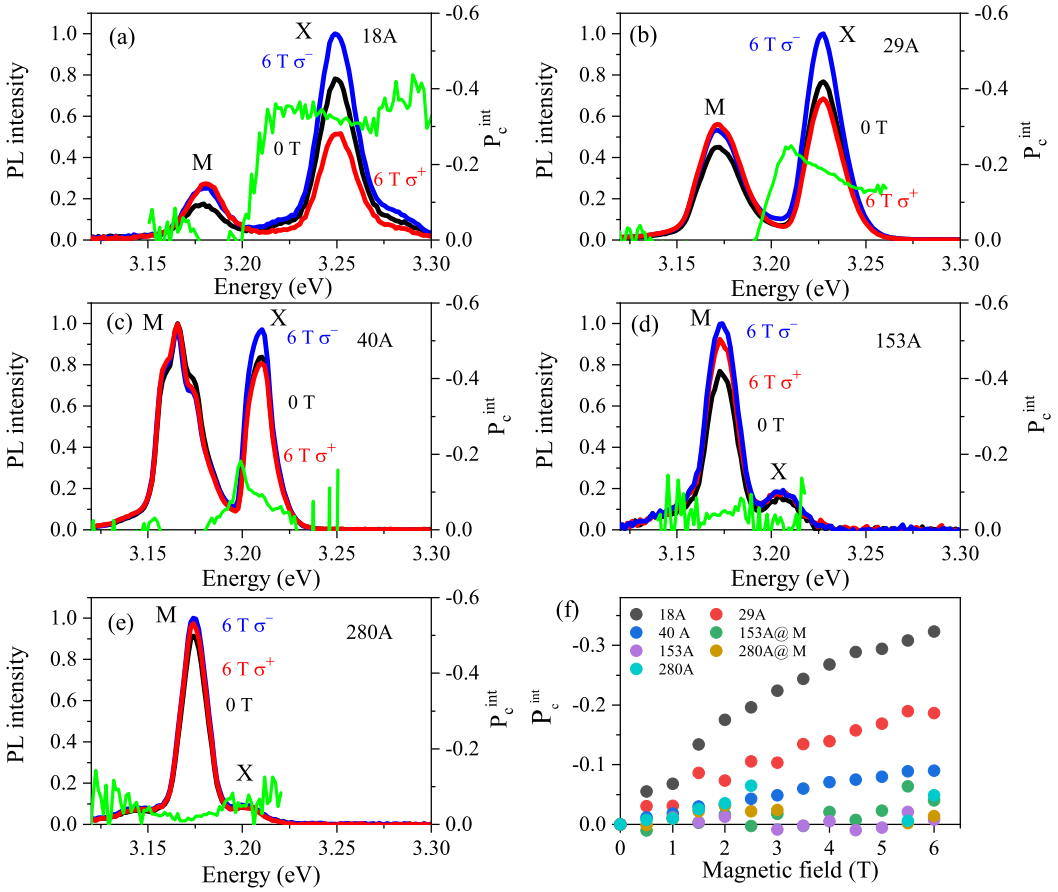

Figure 6.6: Polarized PL spectra at $T = 1.9$ K, $B = 6$ T, the red lines are σ^+ components and blue lines are σ^- components, the black spectra are unpolarized PL at 0 T for comparison. Green lines are the calculated degree of circular polarization (DCP), P_c^{int}, using Eq. 6.3 for sample (a) 18A, (b) 29A, (c) 40A, (d) 153A, (e) 280A. (f) Magnetic field dependence of P_c^{int} at energy position of free Z_3 exciton, X. P_c^{int} at peak position of biexciton M for sample 153A and 280A are also plotted.

Here I^+ and I^- are the intensity of σ^+ and σ^- polarized PL. The green curves are spectrally dependent DCP showing a clear energy dependence. In small NCs, Fig. 6.6(a)-(c), $P_c{}^{int}$ is large in the energy range close to X peak and becomes very small in the range close to M peak, the maximum $P_c{}^{int}$ is between the two regions. On the contrary, in large NCs, Fig. 6.6(d)-(e), the polarization is negligible through the whole spectral range. The magnetic field dependence of $P_c{}^{int}$ at the energy position of X are plotted for all samples, additionally for sample 153A and 280A, the magnetic field dependence of $P_c{}^{int}$ at M energy position are also plotted. One can see that $P_c{}^{int}$ shows a very clear size dependence, the small NCs samples have large DCP. For instance, at 6 T, $P_c{}^{int}$ is -0.32 in sample 18A, -0.19 in sample 29A, -0.09 in sample 40A, -0.05 in sample 153A and 280A.This is quite different from the situation in CdSe NCs [128] where due

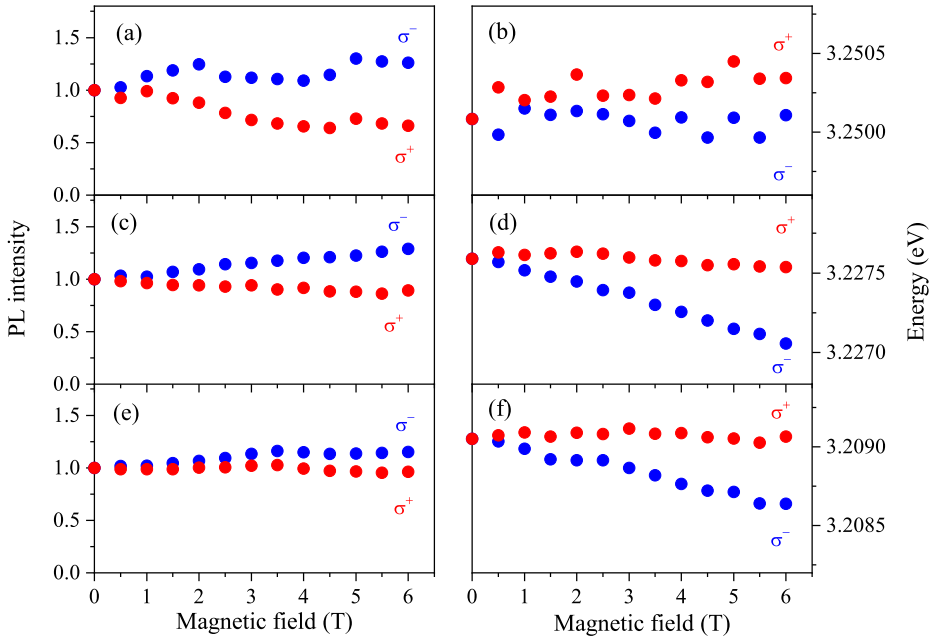

Figure 6.7: Magnetic field dependent intensity and energy position of X peak in polarized PL spectra for sample 18A (a)-(b), 29A (c)-(d) and 40A (e)-(f).

to the effect of LO phonon nearly no size difference is observed in the magnetic field dependent DCP up to 10 T at 4.2 K. Note that in sample 153A and 280A, there is nearly no polarization.

The corresponding magnetic field dependence of X peak energy position as well as their intensity on polarized PL spectra are shown in Fig. 6.7, only data for sample 18A Fig. 6.7(a)-(b), 29A Fig. 6.7(c)-(d) and 40A Fig. 6.7(e)-(f) are present since in large NCs (153A, 280A) there is nearly no polarization. We see that the intensity of σ^- polarized component increases with magnetic field while that of the σ^+ polarized component decrease slightly. Being different from CdSe NCs in glass matrix,[128] the σ^- component owns the stronger intensity and is also at the lower energy comparing to the σ^+ component. Moreover, the σ^- component shifts more pronounced in magnetic field to lower energy which is especially clear in Fig. 6.7(d) and Fig. 6.7(f) probably due to the absence of small inhomogenity and absence of LO phonons in the population distribution among exciton Zeeman levels.[128]

6.3 Polarization and optical orientation under cw laser excitation

In this section, we will show the polarization and optical orientation measurements under cw laser excitation. The degree of circular polarization of Z_3 exciton increases with the decreasing of nanocrystal size, i.e. at $T = 1.9$ K, $B = 8$ T, the DCP is about 30% in sample 18A, 25% in sample 29A and 12% in sample 40A which is comparable with the results from pulsed laser excitation measurements in section 6.2.2. For the optical orientation, when we excite far away from the PL, the degree of optical orientation (P_{oo}) is zero, once shifting the excitation laser energy close to the PL maxmium, P_{oo} increases, and in sample 29A, at $T = 1.9$ K and $B = 8$ T, we get maximum P_{oo} of 5%.

6.3.1 Off-resonance excitation

Figure 6.8(a)-(c) show the polarized PL spectra and spectrally-dependent degree of circular polarization (P_c^{int}, green) for sample 18A, 29A and 40A. The strongest peak in the PL spectra comes from Z_3 exciton, X, emission. P_c^{int} is calculated using Eq. (6.4) based on the polarized PL under linearly polarized laser excitation, $I^{\pm}$ is the intensity of the $\sigma^{\pm}$ spectra. Note that P_c^{int} can be also obtained by the method described in Eq. (6.5) to Eq. (6.7). In sample 18A, 29A and 40A, P_c^{int} increases from higher spectra energy to the lower spectra energy through the PL range, which is different from what we saw under pulsed laser excitation in Fig. 6.6(a)-(d). More importantly, we get a quite different PL spectra, here, the M peak is completely disappearing. This is quite understandable since the pulsed and cw lasers give very different power density, in the literature, PL spectra of different shape are also reported under different type of laser excitation.[194] And generally with pulsed laser excitation, it is easy to see the M and BM peaks.

Figure 6.8(d)-(f) show the magnetic field dependence of P_c^{int} and P_{oo}, P_{oo} is calculated using Eq. (6.5), Eq. (6.6) and Eq. (6.8), where $P_c^{\sigma^{\pm}}$ is the degree of circular polarization under $\sigma^{\pm}$ polarized laser excitation, $I^{\pm}$ is the intensity of the $\sigma^{\pm}$ polarized PL. In all samples, P_{oo} does not change with magnetic field and remains at zero, this is because the excitation energy $E = 3.2887$ eV is far away from the PL, all the information from circularly polarized light are lost during the thermalization process. However, P_c^{int} changes linearly with magnetic field and is also dependent on nanocrystal size, i.e. in sample 18A, P_c^{int} increase from 0 at 0 T to about 30% at 8 T, for sample 29A and 40A, P_c^{int} is 25% and 12%, respectively at 8 T.

Then we analyzed the Zeeman splitting as shown in Fig. 6.8(g)-(i). By fitting with equation $\Delta E = g\mu_B B + offset$, we get g-factor of 0.95, 0.85 and 0.84, which are larger than the Z_3 exciton g-factor 0.3, 0.56 reported by Stande[181] and Suga et al.[182] for CuCl bulk crystal, and 0.447 reported by Nomura et al.[186] for CuCl microcrystallites

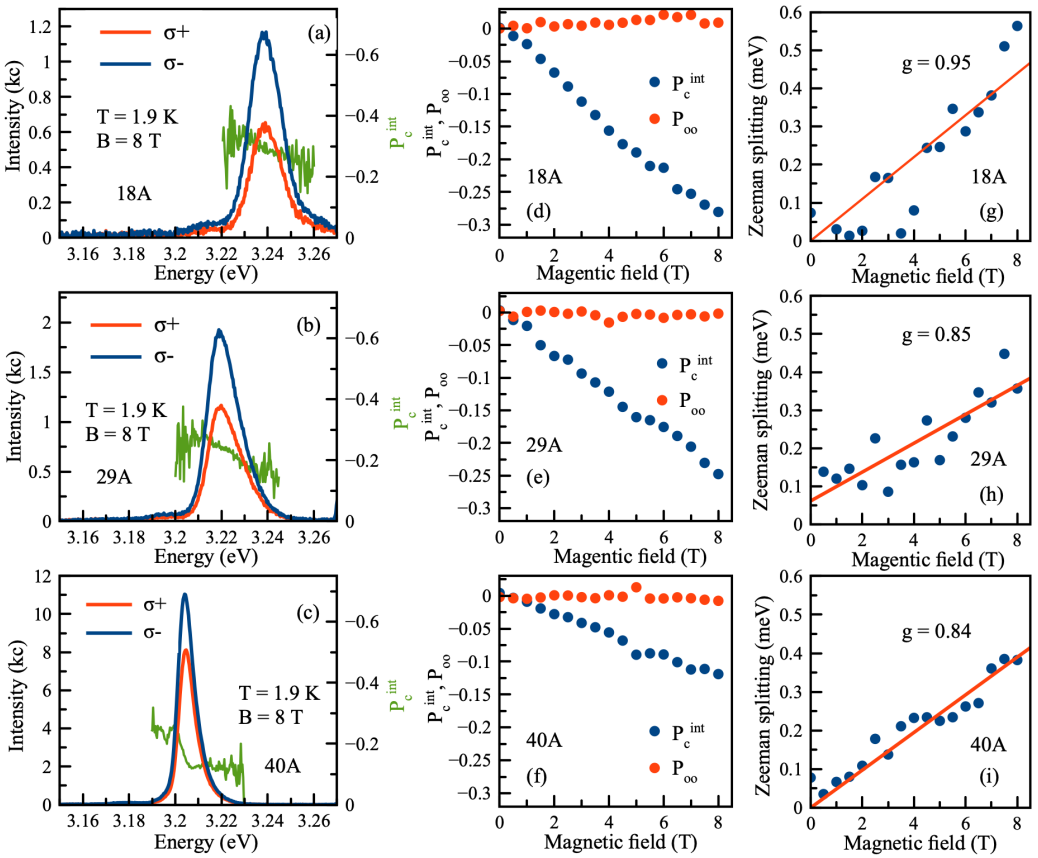

Figure 6.8: (a)-(c) show the polarized PL spectra (σ^+ red, σ^- blue), and spectrally-dependent degree of circular polarization (P_c^{int}, green) for sample 18A, 29A, 40A at $T = 1.9\ K$ with excitation energy $E = 3.2887$ eV. The corresponding magnetic field dependence of P_c^{int}, and the degree of optical orientation (P_{oo}) are shown in (d)-(f). (g)-(i) Magnetic field dependence of the Zeeman splitting calculated based on the energy difference between σ^+ and σ^- polarized PL peak energy. Solid lines are fitting using equation $\Delta E = g\mu_B B + offset$.

embedded in polymer matrix.

Interestingly, under the same excitation condition, we observed the M peak in large NCs as shown in Fig. 6.9(a) and (d) for the polarized PL spectra of sample 153A and 280A. The intensity of M peak is stronger than X peak, but P_c^{int} is still negligible throughout the whole spectral range.

The magnetic field dependence of P_c^{int} in sample 135A in Fig. 6.9(b) seems to increase with magnetic field for both X and M positions, however, in sample 280A in Fig. 6.9(e), it fluctuates randomly. The analysis of the Zeeman splitting gives us two g-factors, one for M, another for X., i.e. in sample 135A, the g-factor is about 1.8 for X and 0.7 for M, in sample 280A, they are 1.5 and 0.18.

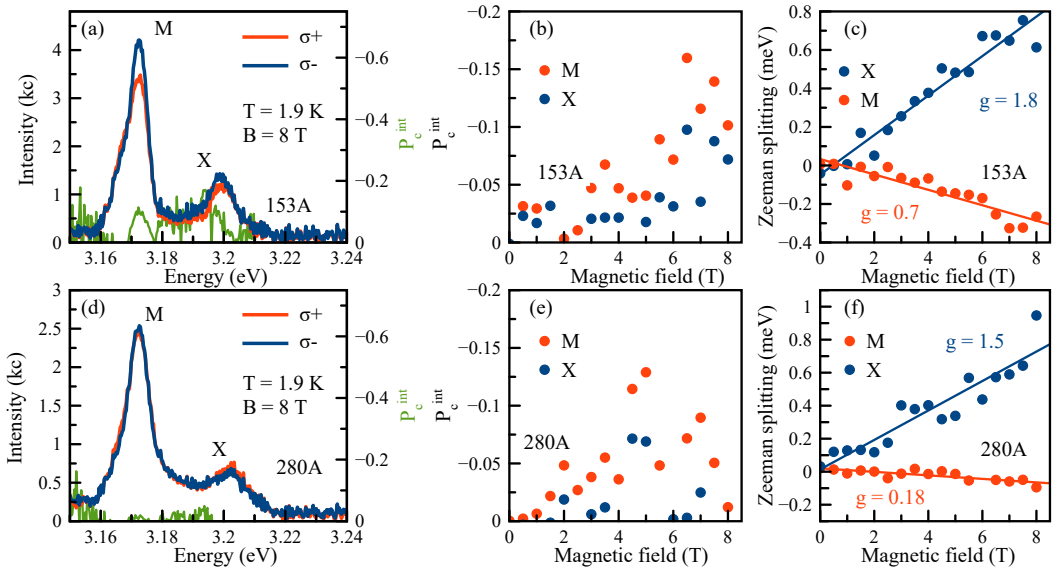

Figure 6.9: (a) and (b) The polarized PL spectra (σ^+ red, σ^- blue), and spectrally-dependent degree of circular polarization (P_c^{int}, green) for sample 153A and sample 280A at $T = 1.9\ K$ with excitation energy $E = 3.2887$ eV. The corresponding magnetic field dependence of P_c^{int} are shown in (b) and (e). (c) and (f) Magnetic field dependence of the Zeeman splitting calculated based on the energy difference between σ^+ and σ^- polarized PL peak energy. Solid lines are fits using Zeeman equation.

$$P_c = \frac{I^+ - I^-}{I^+ + I^-}. \tag{6.4}$$

$$P_c^{\sigma^+} = \frac{I^+ - I^-}{I^+ + I^-}. \tag{6.5}$$

$$P_c^{\sigma^-} = \frac{I^+ - I^-}{I^+ + I^-}. \tag{6.6}$$

$$P_c^{int} = \frac{P_c^{\sigma^+} + P_c^{\sigma^-}}{2}. \tag{6.7}$$

$$P_{oo} = \frac{P_c^{\sigma^+} - P_c^{\sigma^-}}{2}. \tag{6.8}$$

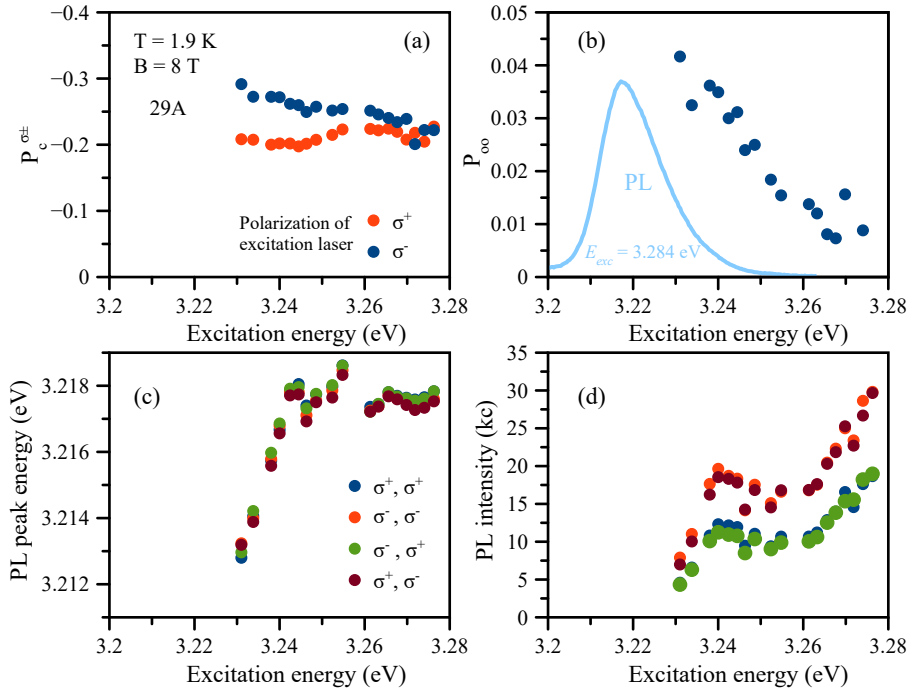

Figure 6.10: (a) Excitation energy dependence of the degree of circular polarization, $P_c^{\sigma\pm}$, under circularly polarized cw laser (σ^+ red, σ^- blue). (b) Excitation energy dependence of the degree of optical orientation, P_{oo}. The blue spectrum is the PL spectrum measured with excitation energy $E_{exc} = 3.284$ eV. (c), (d) Excitation energy dependence of the PL peak energy and PL intensity under different excitation and detection polarization configurations. All measurements are done on sample 29A at $T = 1.9$ K, $B = 8$ T.

6.3.2 Quasi-resonance excitation

Since we excite the samples too far away from optical resonance in Fig. 6.8(d), Fig. 6.8(e) and Fig. 6.8(f), we were not able to observe any optical orientation. In Fig. 6.10, we investigate carefully the excitation energy dependence of this property on sample 29A at $T = 1.9$ K, $B = 8$ T. Firstly, we show in Fig. 6.10(a) the excitation energy dependence of the degree of circular polarization, $P_c^{\sigma\pm}$, under circularly polarized cw laser (σ^+ red, σ^- blue). One see that as the energy gets close to the PL maximum, $P_c^{\sigma-}$ increases linearly from low to high energy, while $P_c^{\sigma+}$ increases first slightly and then gradually decreases. Fig. 6.10(b) shows the excitation energy dependence of P_{oo}, as the excitation energy gets close to the PL peak energy, P_{oo} increases linearly on the whole up to about 4% in the current excitation range. The variation of the PL peak energy under different excitation and detection polarization configuration is plotted in Fig. 6.10(c). From about 3.28 eV down to about 3.24 eV, the PL spectra do not shift. When the excitation energy is smaller than 3.24 eV, it starts to shift to lower energy, and the shifting is about 5 meV till 3.23 eV. Note that polarization configuration does

not play a role in this process. The corresponding PL intensity is shown in Fig. 6.10(d), it first decreases with the excitation energy from about 3.28 eV to 3.26 eV, then slowly increases to 3.24 eV therefore forms a valley. After that, the PL intensity continues to decreases. It does not depend on the polarization of the excitation polarization but can be clearly affected by the detection polarization, i.e. the σ^- polarized PL (red, brown) generally has larger intensity than the σ^- polarized ones.

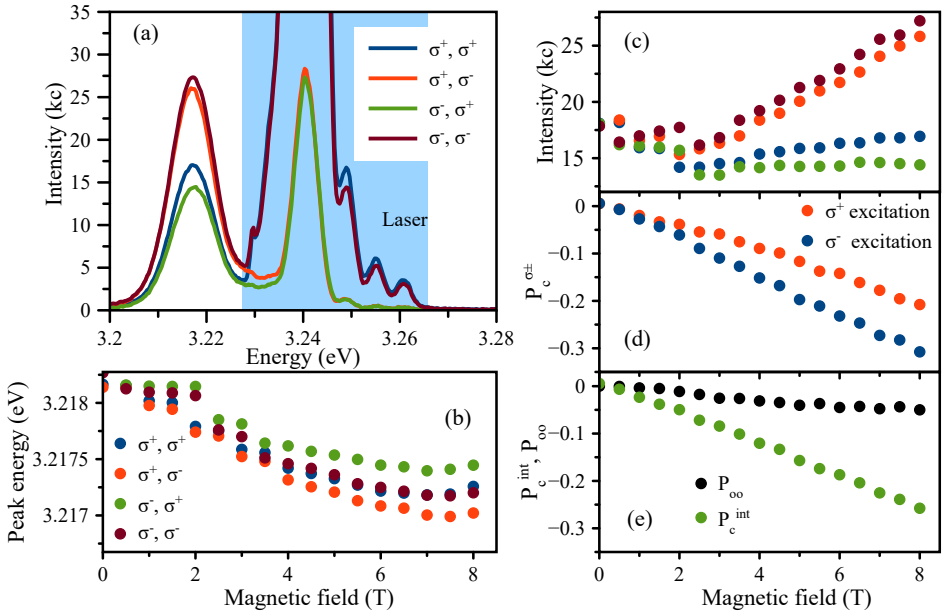

Figure 6.11: Optical orientation measurements on sample 29A at $T = 1.9$ K under quasi-resonant excitation. (a) The PL spectra measured with different excitation and detection polarization configurations at $B = 8$ T. The light blue shadow area corresponds to the excitation laser. (b)-(e) Magnetic field dependence of the PL peak energy, the PL intensity, the degree of circular polarization under circularly polarized laser excitation $P_c^{\sigma\pm}$, and the degree of optical orientation (P_{oo}) and circular polarization (P_c^{int}), here the P_c^{int} is calculated from the average value of $P_c^{\sigma\pm}$.

Figure 6.10(b) has shown that the optical orientation is larger when the excitation energy is closer to the PL maximum, so we studied the optical orientation on sample 29A at $T = 1.9$ K with quasi-resonant excitation as shown in Fig. 6.11. Fig. 6.11(a) are the PL spectra measured with different excitation and detection polarization configurations at $B = 8$ T. The blue shadow area belongs to the laser line. The PL intensity is strongly affected by the detection polarization, and only weakly modified by the excitation polarization also see Fig. 6.11(c). Magnetic field dependence of the PL peak energy is plotted in Fig. 6.11(b), PL shifts to the red with increasing magnetic field in general, and the shifting is 1 to 1.5 meV at 8 T relative to 0 T PL for different polarization configurations. The magnetic field dependence of the PL intensity is shown in Fig. 6.11(c). Below 2 T, PL intensity does not change drastically, once the field

strength is larger than 2 T, it increases linearly with increasing magnetic field, and the σ^- polarized PL has higher intensity than the σ^- polarized component. Fig. 6.11(d) shows the magnetic field dependence of the degree of circular polarization, $P_c^{\sigma\pm}$, under circularly polarized laser excitation. $P_c^{\sigma\pm}$ increases linearly with magnetic field (note here we care about the absolute value), and the value is higher for σ^- excitation, i.e. at $B = 8$ T, $P_c^{\sigma-}$ is 30%, $P_c^{\sigma+}$ is about 20%. The calculated P_{oo} and P_c^{int} are shown in Fig. 6.11(e), the P_c^{int} is calculated from the average value of $P_c^{\sigma\pm}$ which reaches 26% at $B = 8$ T, and the accompanying P_{oo} is about 5%.

6.4 Fluorescence line narrowing (FLN) and spin-flip Raman scattering (SFRS)

In this section, the fluoresence line narrowing (FLN) and spin-flip Raman scattering (SFRS) measurement results are shown. From FLN spectra, a peak close to the laser line in sample 18A, 29A and 40A is seen with the energy distance decreasing with increasing nanocrystal size from 3.4 meV in sample 18A to 1.1 meV in sample 40A. In sample 280A, some phonon lines are observed but since the sample itself is already in the bulk regime, there is no comparability with the data from the other three samples. The SFRS measurements give us a g-factor about 2 which is assigned to the electron based on the literature.[178,179]

6.4.1 FLN spectra from CuCl NCs

Figure 6.12(a_1)-(d_1) show the PL spectra for sample 18A, 29A, 40A and 280A measured under non-resonant excitation with the excitation energy $E_{exc} = 3.306$ eV. Each PL spectrum is normalized to its peak intensity, and the position of the exciton (X), bound exciton (BX), and biexciton (M) are highlighted. With the increasing of the nanocrystal size, PL spectra shift to the lower energy due to the quantum confinement effect. The corresponding FLN spectra in Fig. 6.12(a_2)-(d_2) are measured under resonant excitation at the respective exciton position in all samples and also biexciton position in sample 280A as indicated by vertical arrows in Fig. 6.12(a_1)-(d_1) and denoted in each FLN spectrum. Several peaks, i.e. P_1 to P_3, have been observed. In samples with small NCs (18A, 29A, 40A), a peak (P_1) close to the laser line can be clearly resolved with the Raman shift decreasing with increasing nanocrystal size from 3.4 meV in sample 18A to 1.1 meV in sample 40A. One notices that, in sample 18A, only one peak is apparent, while in sample 29A, another two peaks, P_2 and P_3, with respective Raman shift 9.8 meV and 20.2 meV are observed. P_2 is also observed in sample 40A with relative Raman shift 7 meV. As for sample 280A, we do not observe any FLN signal with resonant excitation at M position. However, when exciting at X position, we observed the FLN spectrum, in which P_1 has Raman shift of 2.6 meV and P_3 has a

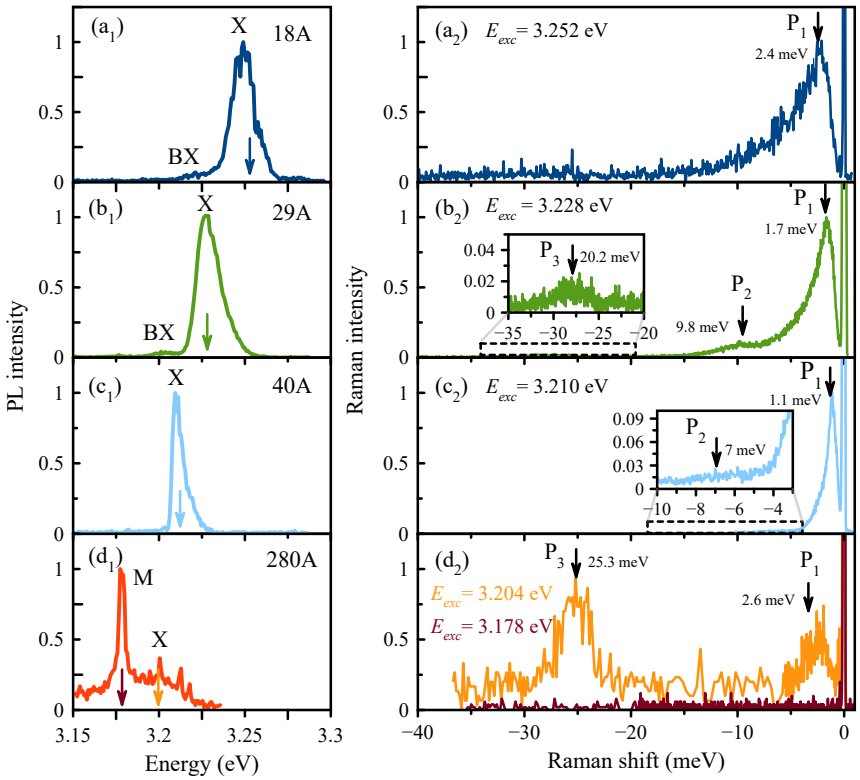

Figure 6.12: Photoluminescence (PL) and fluorescence line narrowing (FLN) spectra for CuCl NCs sample ($a_{1,2}$) 18A, ($b_{1,2}$) 29A, ($c_{1,2}$) 40A, and ($d_{1,2}$) 280A measured at $T = 1.9$ K and $B = 0$ T.

Raman shift 25.3 meV. In Table 6.2, we summarize all peak positions from both PL and FLN spectra.

Table 6.2: Exciton (X), bound exciton (BX), and bi-exciton (M) energies in PL spectra, and energy positions of P_1 to P_3 in FLN spectra in CuCl NCs samples 18A, 29A, 40A and 280A. The PL was excited non-resonantly with excitation energy $E_{exc} = 3.306$ eV, while the excitation in FLN experiments was tuned into resonance with the respective exciton or biexciton positions. Results are in accordance with the figures shown in Fig. 6.12. Data shown in red color are from PL measurements under pulsed laser excitation at $T = 4.2$ K, $E_{exc} = 3.493$ eV in Fig. 6.2.

Sample	PL (eV)			FLN (meV)		
	X	BX	M	P1	P2	P3
18A	3.2491	3.2204	3.1782	2.4		
29A	3.2279	3.2012	3.1713	1.7	9.8	20.2
40A	3.2095		3.1672	1.1	7.0	
280A	3.1988		3.1783	2.6		25.3

6.4.2 SFRS and evaluation of g-factors

The Raman spectra of CuCl NCs with diameter 1.8 nm (sample 18A) under resonant excitation at the exciton position $E_{exc} = 3.252$ eV, are shown in Fig. 6.13 (a). Each spectrum consists of a single Raman line (indicated by the vertical arrows) sitting on a resonant PL background. The Raman lines shift linearly with the magnetic field, which can be reproduced by the Zeeman equation $\Delta E = |g|\mu_B B + \delta_{off}$, where μ_B is the Bohr magneton, δ_{off} is an energy offset, and we obtain a g-factor of 2.15 ± 0.1 as shown in Fig. 6.13 (b). Note that since the peak intensity is very small, a certain measurement uncertainty must be taken into account when determining the g-factor. The interpolation of the Raman shift to zero magnetic field reveals a minor offset of $\delta_{off} = 38.5$ μeV, we will demonstrate later that this offset varies depending on the NC size. A summary of g-factors and zero field offsets obtained from different samples is given in Table 6.3. The Raman intensity increases with the magnetic field as shown in Fig. 6.13 (c), from $B = 4$ to 8 T, it raises by almost one order of magnitude. While the width keeps almost constant at approximately 0.1 meV, see Fig. 6.13 (d).

Due to the extremely weak SFRS signal, the evaluation of the data is very difficult, therefore it is not easy to determine the optical selection rules. However, the situation changes in sample 29A, which will be discussed next.

In comparison to sample 18A, the PL spectrum of sample 29A is red-shifted with the PL maximum located at 3.2279 eV, see Table 6.2 and Fig. 6.12(b_1). In Fig. 6.14(a), the PL spectra measured at T =1.9 K are plotted and the SFRS at three different energy positions as indicated by the vertical arrows are checked. At the BX position, we are not able to monitor any Raman signal and there is also no resonant photoluminesence. But once the excitation energy is shifted into resonance with the exciton line (indicated by the brown arrow in Fig. 6.14(a), it is able to monitor the SFRS signals from both Stokes and anti-Stokes, see Fig. 6.14(c)-(d). When tuning the excitation laser to the

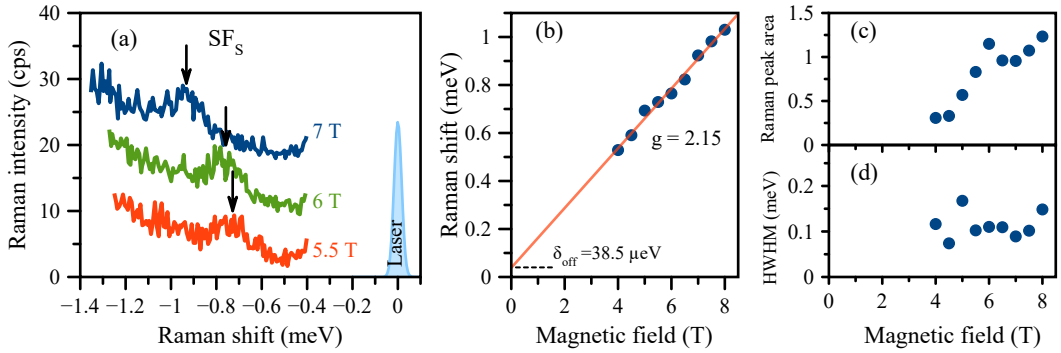

Figure 6.13: (a) Spin-flip Raman scattering spectra at $B = 5.5$, 6.0, and 7.0 T in co-circular polarization configuration (σ^+, σ^+) at $T = 1.9$ K with $E_{exc} = 3.252$ eV. For better visibility, the spectra are shown with different vertical offsets, the spin-flip Raman peaks (SF_s) on Stokes are highlighted by vertical arrows. The excitation laser is represented by the cyan line at zero Raman shift. (b) Magnetic field dependence of the Raman shift. Red line shows a linear fit to the data using Zeeman equation $\Delta E = |g|\mu_B B + \delta_{off}$. The resulting g-factor and zero field offset (δ_{off}) are $g = 2.15$ and $\delta_{off} = 38.5$ μeV. (c-d) Magnetic field dependence of the evaluated Raman peak area and half width at half maximum (HWHM) of the Raman peaks.

higher energy side of the PL (3.241 eV), we observe minor differences as it is shown in Fig. 6.14(b), where the intensity of the Raman line marked by the black arrow is much higher for the resonant excitation of X.

Figure 6.14(c)-(d) show the polarization dependence of the SFRS spectra at $B = 5$ T and 7.5 T, respectively, with $T = 1.9$ K, $E_{exc} = 3.228$ eV. For better visibility, the spectra on anti-Stokes are multiplied by 5. At $B = 5$ T, the SFRS peaks are clearly separated from the PL background, and the spectra vary in the intensity depending on the excitation and detection polarization configurations. However, when increasing the magnetic field up to $B = 7.5$ T, the SFRS peaks are nearly buried by the PL background due to the magnetic field enhanced optical oscillation strength. The data measured with (σ^+, σ^+) polarization configuration under resonant excitation at E_{exc} = 3.228 eV and $E_{exc} = 3.241$ eV are analyzed, and the corresponding magnetic field dependence of the Raman shift is plotted in Fig. 6.14(e) and Fig. 6.14(f). Red lines show the linear fit using Zeeman equation from which we obtain a g-factor of 2.07 with zero field offset of $\delta_{\text{off}} = 32$ μeV as shown in Fig. 6.14(e), and $g = 2.16$ with $\delta_{\text{off}} = 16$ μeV in Fig. 6.14(f).

As it has been demonstrated in FLN spectroscopy in Fig. 6.12, the sample 280A shows quite different properties, therefore we also check the SFRS on it carefully as shown in Fig. 6.15. The inset in Fig. 6.15(a) shows the PL spectrum which is composed of a very sharp M emission peak and a broad X emission shoulder at the higher energy side. We tried to measure the SFRS at both positions, but only got signal from X position. Figure 6.15(a) shows the polarization dependent SFRS spectra at $B = 7.5$ T,

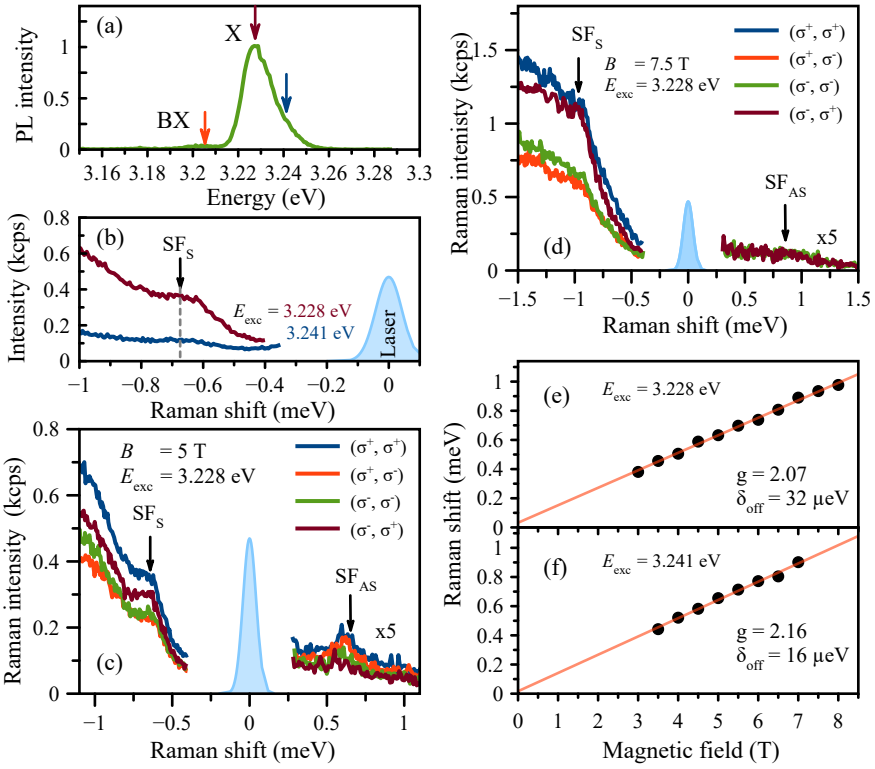

Figure 6.14: (a) PL spectrum of sample 29A measured at $T = 1.9$ K and $B = 0$ T. The position of the exciton (X) and bound exciton (BX) are highlighted. The excitation laser energies are indicated by vertical arrows. (b) SFRS spectra at $T = 1.9$ K and $B = 5$ T for resonant excitation at the PL maximum ($E_{exc} = 3.228$ eV), brown line, and at the higher energy flank of the exciton PL ($E_{exc} = 3.241$ eV), dark blue line. The SF_s together with the black arrow and dash line indicate the position of the Raman peak. The laser at zero Raman shift is represented by the cyan line. (c)-(d) Polarization dependence of the SFRS spectra at $B = 5$ T, 7.5 T with $T = 1.9$ K, $E_{exc} = 3.228$ eV. For better visibility in (d) the spectrum in anti-Stokes is shown enhanced by 5 times. (e)-(f) Magnetic field dependence of the Raman shift in co-polarized configuration (σ^+, σ^+) with excitation energy $E_{exc} = 3.228$ eV and $E_{exc} = 3.241$ eV. Red lines show the linear fit to the data, from which we obtain a g-factor of 2.07 with zero field offset of $\delta_{\text{off}} = 32$ μeV and $g = 2.16$ with $\delta_{\text{off}} = 16$ μeV.

$T = 1.9$ K, interestingly nearly no PL background except a very pronounced Raman peak is seen. However, the SFRS spectra shows no sensitivity to selection rules, as the Raman line can be detected in cross- and co- polarized configurations without visible difference. From the analysis of the linear shift of the Raman peak in the magnetic field, a g-factor of $g = 2.16$ and a zero field offset of $\delta_{\text{off}} = (-33 \pm 20)$ μeV is obtained as shown in Fig. 6.15(b). Similar to sample 18A, the intensity of the Raman peak increases with the magnetic field while the width HWHM does not change evidently.

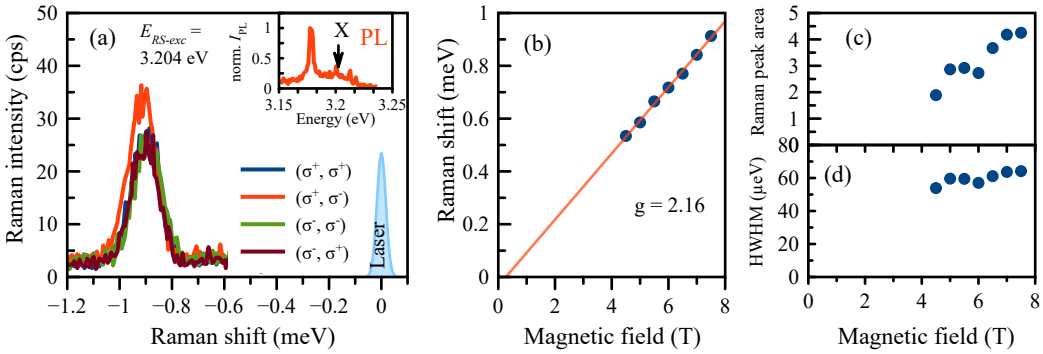

Figure 6.15: (a) Raman spectra of sample 280A in cross- and co- polarized configuration at $B = 7.5$ T, $T = 1.9$ K with $E_{exc} = 3.204$ eV. Laser at zero Raman shift is represented by the cyan line. The insert shows the PL spectrum at $B = 0$ T, wherein the position of the M and X are highlighted, the laser excitation energy is indicated by a vertical arrow. (b) Magnetic field dependence of the Raman shift on Stokes. Red line is the linear fit based on the Zeeman equation through which we obtain the g-factor of $g = 2.16$ and the zero field offset $\delta_{\text{off}} = (-33 \pm 20)$ μeV. (c-d) Raman peak area (c) and half width at half maximum (HWHM) (d) as function of the magnetic field.

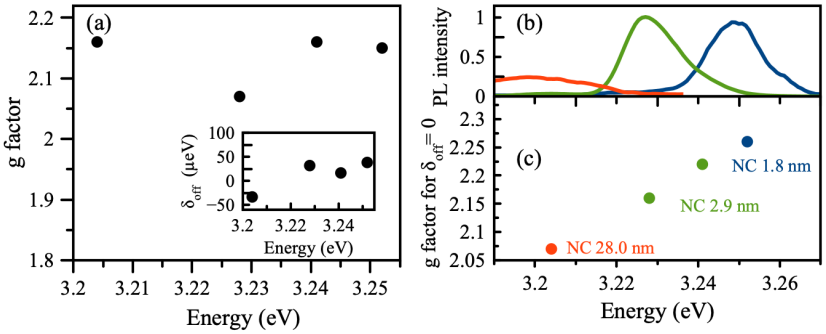

Figure 6.16: Excitation energy dependence of g-factors obtained from Raman scattering measurements on CuCl samples with nanocrystal sizes ranging from 1.9 to 28 nm. The g-factor is presented for not fixed zero field offset (a) and fixed zero field offset to 0 μeV (c). Inset in (a) shows the energy dependence of the corresponding offset. In panel (b), the normalized PL spectra of the three investigated samples 18A, 29A, and 280A at $T = 1.9$ K and $B = 0$ T are shown.

We compare the g-factors obtained in all CuCl NCs samples in Fig. 6.16. Figure 6.16(a) shows the energy dependence of the g-factor obtained, the corresponding offset δ_{off} are plotted in the insert. In this case, the g-factor does not depend on the spectral energy, and δ_{off} is fluctuating between -50 to 50 μeV. Once fixing δ_{off} to be zero for fitting, we get g-factor as shown in Fig. 6.16(c), which is clearly spectral energy dependent and increases from 2.07 to 2.26 with corresponding energy from 3.204

to 3.252 eV. Figure 6.16(b) shows the corresponding PL spectra, one g-factor is getting from sample 18A (blue dot), one from sample 280A (red dot) and two g-factors from sample 29A (green dots). All the data can be found in Table 6.3. The g-factors for electron and $Z_{1,2}$, Z_3 excitons in CuCl are very different,[179,181,182], and the g-factor of about 2 can be assigned to the electron.

Table 6.3: Summary of g-factor in CuCl NCs. The g-factor is obtained from the evaluation of magnetic field dependent Raman shifts on Stokes at $T = 1.9$ K. The energy depicts the excitation laser energy. For better comparison, the g-factor ($g_{\delta_{off}=0}$) with a fixed energy offset of zero was also calculated.

Sample	NC's size (nm)	Energy (eV)	SFRS		
			g-factor	δ_{off} μeV	$g_{\delta_{off}=0}$
18A	1.8	3.252	2.15	38.5	2.26
29A	2.9	3.241	2.16	16.7	2.22
29A	2.9	3.228	2.07	32.0	2.16
280A	28.0	3.204	2.16	33.2	2.07

6.4.3 Impact of excitation power on the Raman scattering

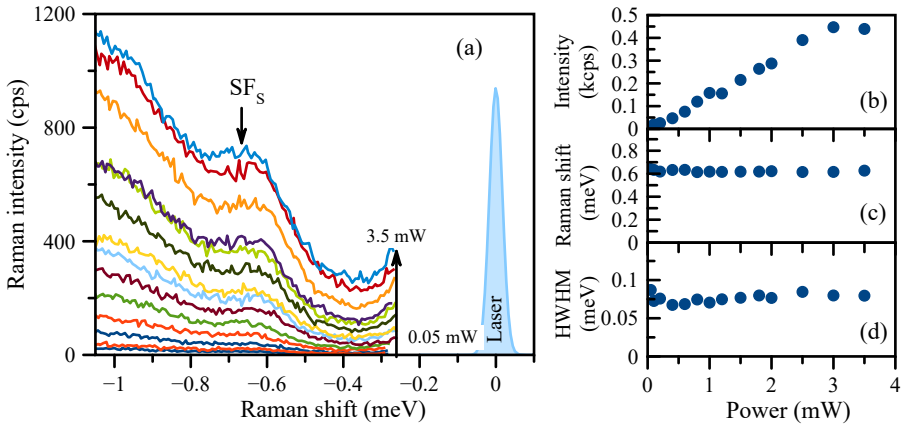

Figure 6.17: The effect of excitation power on spin-flip Raman scattering at $T = 1.9$ K,$B = 5$ T with $E_{exc} = 3.228$ eV. (a) Raman spectra under different laser excitation powers in co-polarized configuration (σ^+, σ^+). The laser power was varied from 0.05 mW to 3.5 mW. The laser is depicted by the cyan line. (b)-(d) Excitation power dependence of the Raman intensity (b), Raman shift (c) and half line width at half maximum (HWHM) (d).

The excitation power density is a crucial factor in SFRS measurement. Strong laser power may lead to an increase of the local lattice temperature, thus, a reduction in the exciton lifetime as well as delocalization of resident electrons. Moreover, laser-induced heating enhances the density of thermal phonons which can violate spin-flip processes.

We investigated the impact of laser power P_{exc} on the resonant Raman scattering on sample 29A, to illustrate briefly how an increment of the excitation power affects the Raman process, SFRS spectra on Stokes are presented in Fig. 6.17(a) exemplarily under various excitation densities. The spectra are measured in co-polarized configuration (σ^+, σ^+) at $T = 1.9$ K and $B = 5$ T for resonant excitation at the PL maximum at $E_{exc} = 3.228$ eV. With increasing excitation power, the scattering intensity as well as the resonant PL background rises. The corresponding Raman peak intensity, Raman shift and half width at half maximum (HWHM) are presented in Figs. 6.17(b)-(d) as a function of the excitation power. One see that the peak intensity increases from 25 cps at $P_{exc} = 0.2$ mW to 440 cps at $P_{exc} = 3.5$ mW, while the Gaussian shape and the HWHM of the Raman peak remain unaltered. The absolute Raman shift remains unchanged at about 633 μeV. The SFRS intensity reveals a linear dependence on P_{exc}, and only for very high excitation powers ($P_{exc} > 3$mW), it turns to saturate.

6.5 Conclusion

We studied the magneto-optical properties of CuCl NCs in glass matrix using different techniques. The polarization measurements show that under the pulsed and cw laser excitation, although the PL spectra are very different in shape, the degree of circular polarization P_c^{int} at the exciton peak position is the same. The optical orientation properties depend heavily on the excitation energy, i.e. for excitation far away from the PL, the degree of optical orientation (P_{oo}) is zero, once shifting laser energy close to the PL maximum, P_{oo} increases clearly. From the spin-flip Raman scattering measurement, we obtain a g-factor of about 2 which can be related to the electron.

Chapter 7

Recombination and spin dynamics in $CsPbBr_3$ nanocrystals

Perovskite-type materials have been studied for quite long time,[218–221] the recent renaissance started a decade ago being inspired by the work on organometal halide perovskite solar cell by Kojima et al.[222] and later continuously improving power conversion efficiency of perovskite solar cells. From the physics point of view, one of the basic questions is to understand the origin of the excellent optical properties of this kind of material, especially the extremely large photon-emission rates which is about 20 and 1000 times of that in any other semiconductor nanocrystals (NCs) at room and cryogenic temperatures, respectively.[102] To reach this purpose, we need to direct our attention to the band edge exciton fine structures. The triplet bright state reported by Becker et al. in all-inorganic perovskite ($CsPbX_3$, X = Cl, Br, I) NCs due to the Rashba effect has inspired a lot of discussion about this topic, since it is in sharp contrast to the situation normally seen in III-V and II-VI semiconductor NCs. However, later studies show that in $CsPbX_3$ or $CsPbX_3$-based NCs, the ground state of band edge exciton is actually still dark.[63,110,111] Even more interestingly, a partially-bright triplet exciton state is observed by Liu et al.[223] using multidimensional coherent spectroscopy where the dark state is positioned energetically within the bright triplet manifold. To have a better understanding about the exciton fine structure and controversy mentioned above, we investigate the $CsPbX_3$ NCs grown in phosphate glass matrix using different techniques. The data of $CsPbBr_3$ NCs are presented in this chapter, and results for $CsPbI_3$ NCs will be shown in the next two chapters. The contents in this chapter are organized in the following way: firstly, we show the temperature dependent PL spectra, secondly, we talk about the exciton fine structure based on the temperature and magnetic field dependence of the recombination dynamics measurements, thirdly,

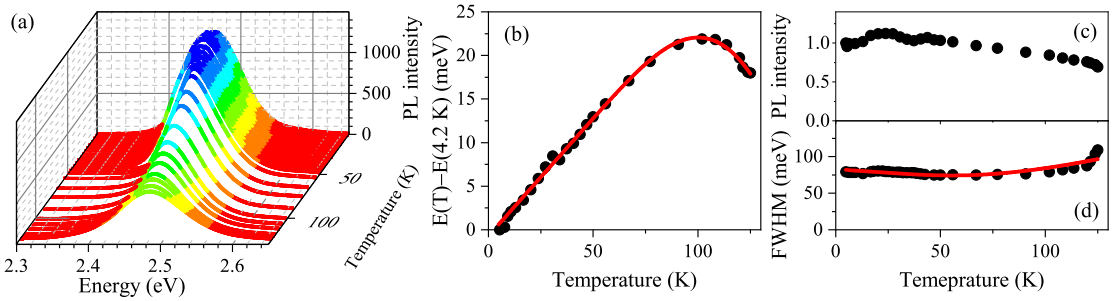

Figure 7.1: (a) Photoluminescence (PL) spectra collected from T = 4.2 K to 125 K. (b) Temperature dependence of the PL peak energy shift relative to that at T = 4.2 K. Temperature dependence of (c) PL intensity, (d) PL full width at half maximum (FWHM).

the polarization results from the high magnetic field measurements are discussed, and finally we show the spin relaxation dynamics.

7.1 Temperature induced bandgap renormalization

It is well-known that temperature impose a strong impact on the semiconductor bandgap, and the thermally induced bandgap renormalization can be understood from the interplay of electron-phonon interactions (EP) and thermal lattice expansion (TE).[205,211] We measured the temperature dependence of photoluminescence (PL) spectra from T = 4.2 K up to 125 K as shown in Fig. 7.1(a). The detailed evolution of the bandgap energy with temperature is presented in Fig. 7.1(b), when increasing temperature from 4.2 K to ∼100 K, PL spectra are blue-shifted and the shift relative to PL spectrum at 4.2 K reaches the maximum (22 meV) at ∼100 K. Further rising of temperature moves the spectra backward to the lower energy.

At constant pressure, the temperature-dependence of the bandgap is generally estimated by the following expression under a quasi-harmonic approximation[205]:

$$\frac{\partial E_g}{\partial T} = \frac{\partial E_g}{\partial V}\frac{\partial V}{\partial T} + \sum_{j,\vec{q}} \left(\frac{\partial E_g}{\partial n_{j,\vec{q}}}\right)\left(n_{j,\vec{q}} + \frac{1}{2}\right), \tag{7.1}$$

where $n_{j,\vec{q}}$ is the number of phonons at j branch with wave vector of $\vec{q}$, and it follows the Bose–Einstein distribution $n_{j,\vec{q}} = \frac{1}{exp(\hbar w_{j,\vec{q}}/k_B T)-1}$, $w_{j,\vec{q}}$ is the angular frequency of the phonon mode.

The first part of Eq. (7.1) describes the contribution of the thermal expansion of the lattice. The coefficient $\frac{\partial E_g}{\partial V}$ depends weakly on temperature and can be regarded as a constant. Its value can be either positive or negative depending on the specifics of the bonding parameters as well as the detailed structure of the bandgap.[205] As

we have mentioned in section 2.2.2.2, the valence band maximum of $CsPbBr_3$ is the hybridization between the p orbit of Br and s orbit of Pb. With increased temperature, TE of the lattice will decrease the interaction between these two orbits, resulting in a decrease of the valance bandwidth and an increase of the bandgap.[224] Therefore, the $\frac{\partial E_g}{\partial V}$ is determined to be positive.

The second part of Eq. (7.1) is attributed to the electron-phonon interaction. Since it is very challenging to calculate all possible phonon modes in the entire Brillouin zone, many models have been developed to interpret the experimental data, such as the one- and two-oscillator models, the latter has been used in the interpolation of temperature induced bandgap renormalization in CuCl NCs in chapter 6. The two-oscillator models are usually used to fit the nonmonotonic temperature-dependent band gap, which usually shows a nonlinear temperature dependence at low temperature and a linear one at high temperature as shown in Fig. 6.4. However, in $CsPbBr_3$ NCs, the linear increase followed by a roughly constant value of the bandgap does not conform with the two-oscillator model,[224] so the one-oscillator model is considered in this case. Combined with the TE, Eq. (7.1) can be simplified to the following expression by assuming a linear relationship between lattice constant and temperature:

$$E_g(T) = E_0 + A_{TE}T + A_{EP}\left(\frac{2}{exp(\hbar\omega/k_BT) - 1} + 1\right), \tag{7.2}$$

where E_0 is the unrenormalized bandgap, A_{TE} and A_{EP} are the weight of the TE and EP interaction, respectively, and $\hbar\omega$ is the average optical phonon energy. The red line in Fig. 7.1(b) shows the fitting result using Eq. (7.2) with parameters: E_0 = 2.46±0.00 eV, A_{TE} = 0.27±0.00 meV/K, A_{EP} = -1.22±0.38 eV, and $\hbar\omega$ = 54.8±3.6 meV. We note that effect of phase transition can be ignored since the transition temperature (340 to 380 K)[224] is much higher than current maximum value.

The variation of PL intensity is shown in Fig. 7.1(c), from 4.2 K to 25 K, it slightly increases and then starts to decrease continuously. At 125 K, the PL intensity is ∼30% less than that at 4.2 K due to the thermally assisted trapping at surface/interface sites and increased fraction of nonemissive processes.[225] The dependence of PL full width at half maximum (FWHM) with temperature is shown in Fig. 7.1(d), from low temperature up to ∼100 K, FWHM keeps nearly constant at ∼80 meV, then gradually increases and gets close to 110 meV at 125 K. The red line is the fitting using:[65,226]

$$\Theta(T) = \Theta_0 + \sigma_{AC}T + \frac{\Theta_{LO}}{exp(E_{LO}/k_BT) - 1}, \tag{7.3}$$

where $\Theta(T)$ is the ZPL linewidth at temperature T, and Θ_0 is its value at zero temperature, k_B is the Boltzmann constant, σ_{AC} and Θ_{LO} are the exciton-acoustic phonon and the exciton-longitudinal optical (LO) phonon coupling coefficients, respectively. E_{LO} is an effective optical phonon energy representing the carrier-LO phonon interaction. The fit yields Θ_0 = 82.7±1.7 meV, σ_{AC} = -0.19±0.05 meVK^{-1}, Θ_{LO} = 30.0±0.46 meV and E_{LO} = 23.6 meV. These parameters are comparable to the values from Ref.[224].

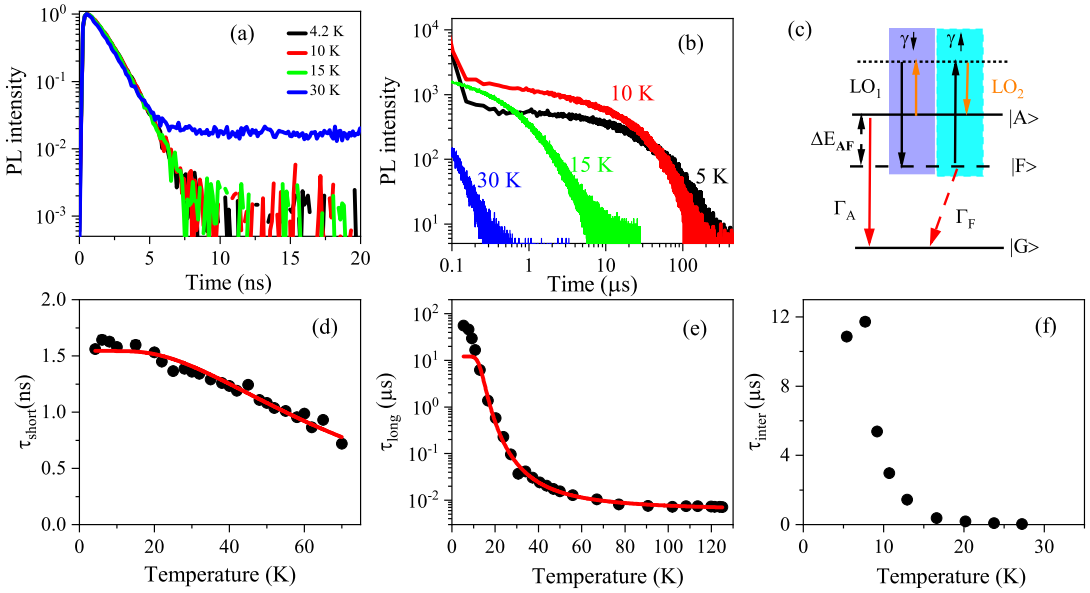

Figure 7.2: Temperature dependence of the recombination dynamics in $CsPbBr_3$ NCs in glass matrix. PL decay measured (a) with laser frequency 2.5 MHz, resolution 200 ps to resolve the initial fast component, and (b) with laser frequency 2 kHz, resolution 102.4 ns to resolve the long component. (c) Scheme of two-LO-phonon thermal mixing model. $|A\rangle$, $|F\rangle$, and $|G\rangle$ denote bright and dark exciton states, and crystal ground state, respectively. ΔE_{AF} is the bright-dark splitting. Γ_A and Γ_F are the recombination rates of the bright and dark excitons. $|A\rangle$ and $|F\rangle$ are thermally mixed via a two-LO-phonon process with rates $\gamma_\uparrow$ (cyan part) and $\gamma_\downarrow$ (blue part), LO_1 and LO_2 (the black and orange arrows) refer to different LO phonons whose energy difference matches ΔE_{AF}. (d)-(f) Temperature dependence of time constants τ_{short}, τ_{long} and τ_{inter} corresponding respectively to the fast, intermediate and long component of the decay curves. The solid red lines in (d) and (e) are the simulations using Eq. 2.26. $\Gamma_A = 0.65$ ns_{-1}, $\Gamma_F = 0.00008$ ns_{-1}, $\gamma_0 = 1.46$ ns_{-1} , $E_{LO_1} = 8.3$ meV, $E_{LO_2} = 14.6$ meV are taking for τ_{short} in figure (d), and $\Gamma_A = 0.36$ ns_{-1}, $\Gamma_F = 0.00008$ ns_{-1}, $\gamma_0 = 1.46$ ns_{-1}, $E_{LO_1} = 7.8$ meV, $E_{LO_2} = 11.3$ meV are taking for τ_{long} in figure (e), the bright-dark splitting $\Delta E_{AF} = 4.2$ meV.

7.2 Fine structure of excitons

In this section, we used the temperature and magnetic field dependent recombination dynamics to study the band edge exciton fine structures. Firstly, we measured the temperature dependence of the recombination dynamics as displayed in Fig. 7.2. At low temperature, three components can be resolved, the fast component with time constant τ_{short}, the intermediate component with time constant τ_{inter} and the long component with time constant τ_{long}. Since τ_{long} at low temperature is very large ~50 μs while τ_{short} is very small ~1 ns, it is not possible for us to have good resolution and proper laser pulse frequency at the same time to resolve them all perfectly, so we employed the following measurement strategy, i.e. to measure PL decay twice, once with low frequency and bad resolution to resolve the long component, another time with high

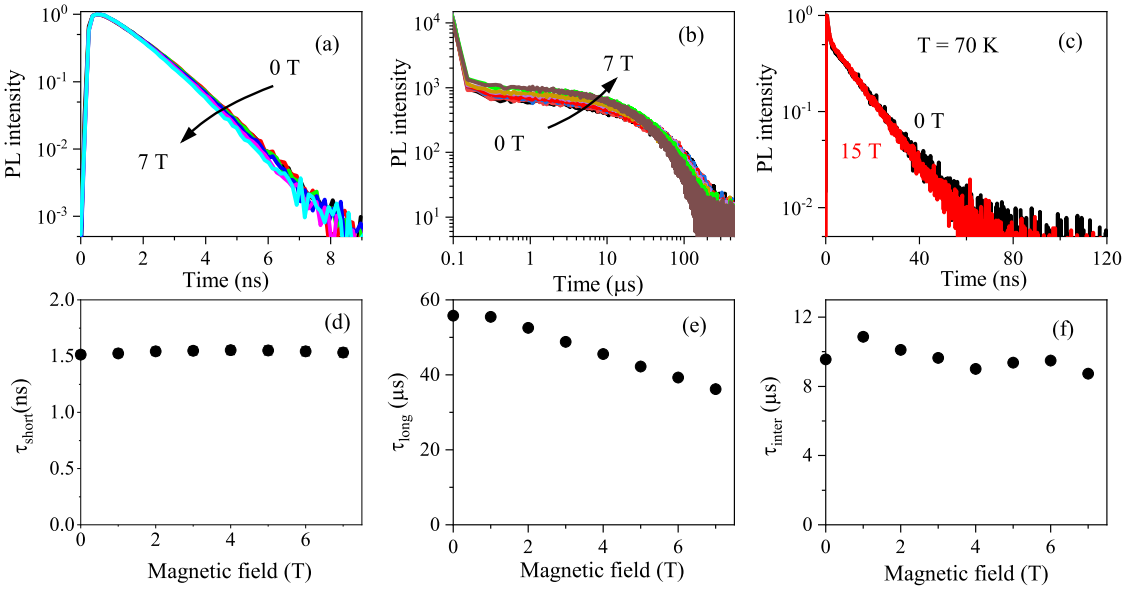

Figure 7.3: Magnetic field effect on the recombination dynamics. (a) Magnetic field dependence of PL decay at $T = 4.2$ K measured with frequency 2.5 MHz and resolution 200 ps to resolve the fast initial decay. (b) Magnetic field dependence of PL decay at $T = 5$ K measured with frequency 2 kHz and resolution 102.4 ns to monitor the long component. (c) Comparison of PL decay at 0 T and 15 T with temperature fixed at 70 K. (d)-(f) Magnetic field dependence of τ_{short}, τ_{long} and τ_{inter}.

frequency and good resolution to resolve the fast component. For instance, at $T = 5$ K, we used laser pulse frequency 2 kHz and resolution 102.4 ns to measure the long component, and used laser frequency 2.5 MHz and resolution 200 ps to measure the short component as shown in Fig. 7.2(a) and (b). The recombination dynamics are found to be very sensitive to temperature, therefore for measurement in Fig. 7.2(b), the pulse frequencies and resolutions are adjusted to optimize the measurement time, e.g. 2 kHz, 102.4 ns at 5 K, 1 MHz, 200 ps at 60 K.

The temperature dependence of τ_{short}, τ_{inter}, τ_{long} extracted from Fig. 7.2(a) and (b) are shown in Fig. 7.2(d)-(f). At low temperature, although the PL decay curves exhibit two-component-like shape, actually three-exponential function is needed to make a satisfactory simulation, because the long tail in Fig. 7.2(b) needs to be fitted by two-exponential function. However, when increasing temperature above ∼30 K, one-exponential function is able to give a good simulation. Moreover, if the temperature is higher than 70 K, the fast and long component are well mixed, and one exponential function is enough to fit the whole decay curve. As it is shown in Fig. 7.2(d)-(f), all the time constants decrease with increasing temperature. The τ_{short} decreases from 1.6 ns at 4.2 K to 0.8 ns at 70 K, τ_{inter} decreases from 11 μs at 5 K to 0.037 μs at 27 K till can not be resolved, and τ_{long} reduces dramatically from ∼56 μs at 5 K to 0.007 μs at 125 K.

It is documented in the literature that temperature and magnetic field dependent PL decay technique is an efficient way to distinguish quasi-particle emission in colloidal NCs.[61,62,128,150] To understand the origin of the PL emission in our sample, we also performed the magnetic field dependent PL decay as shown in Fig. 7.3. It turns out that the magnetic field has nearly no effect on the fast decay component see Fig. 7.3(a) and (d) where τ_{short} keeps almost constant at 1.6 ns up to 7 T. While the long component is obviously accelerated and τ_{long} decreases from ∼56 μs at 0 T to 36 μs at 7 T as displayed in Fig. 7.3(e). The τ_{inter} fluctuates around 10 μs with magnetic field but shows no clear change in Fig. 7.3(f). We also compare the PL decay at 0 T (black) and 15 T (red) with the temperature setting at 70 K in Fig. 7.3(c), one can see that the magnetic field has negligible influence on the recombination process underlining the dominant role of temperature in determining the dynamics.

Based on the results in Fig. 7.2 and Fig. 7.3, we can safely assign the long component of PL decay to dark excitons since its recombination can be accelerated by both temperature and magnetic field.[61,62] The dark exciton emission in perovskite NCs have been well explained within the three-level two-LO-phonon model,[65,130] and the basic idea is described in Fig. 7.2(c). The optically forbidden dark state $|F\rangle$ lies below the optically allowed bright state $|A\rangle$ being separated by the bright-dark energy splitting ΔE_{AF}.[65,130] The fast component of the PL decay is assigned to the recombination of bright excitons with recombination rate Γ_A and the rapid thermalization of exciton from $|A\rangle$ to $|F\rangle$ state, the long component corresponds to the dark exciton recombination with a rate Γ_F. The absorption and emission of LO phonons, named LO_1 and LO_2 with energy difference matching ΔE_{AF} assist the recombination of dark excitons. The solid red lines in Fig. 7.2(d) and Fig. 7.2(e) are the fits using Eq. 2.26. The simulation of τ_{long} gives us $\Gamma_A = 0.65$ ns^{-1}, $\Gamma_F = 0.00008$ ns^{-1}, $\gamma_0 = 1.46$ ns$_{-1}$, $E_{LO_1} = 8.3$ meV, $E_{LO_2} = 14.6$ meV and $\Delta E_{AF} = 4.2$ meV. By fixing ΔE_{AF} as 4.2 meV, $\Gamma_F = 0.00008$ ns^{-1} and $\gamma_0 = 1.46$ ns^{-1}, we reproduced the τ_{short} in Fig. 7.2(d) and got $\Gamma_A = 0.36$ ns^{-1}, $E_{LO_1} = 7.8$ meV and $E_{LO_2} = 11.3$ meV.

The time constant for the intermediate component, τ_{inter}, it is of μs magnitude and changes with temperature but not with magnetic field, so is probably related with trion or trap state. In the literature, different origins for τ_{short} have been proposed, e.g. the bright exciton[102], trion[64] or nonradiative trapping process.[225] Kozlov et al. also studied the $CsPbBr_3$ perovskite NCs in glass matrix, they observed that when rising temperature from 20 to 300 K, the fast decay time decrease from ∼1.3 to 0.4 ns, which is similar to what we observed in this work regarding the tendency as well as time constant values. However, the recombination dynamics in their work are completely different from ours, i.e. there is no clear separation between the fast and long decay components. In wet-chemically prepared $CsPbBr_3$ NCs, the typical lifetime of bright exciton at 5 K is reported to be ∼380 ps[102,111], which is four times smaller than our value. Hu and colleagues[227] studied the single $CsPbBr_3$ perovskite NCs, and observed biexponential PL decay at 4.2 K with time constant ∼355 ps and ∼5.75 ns, while at room temperature the PL decay becomes monoexponential with time constant of

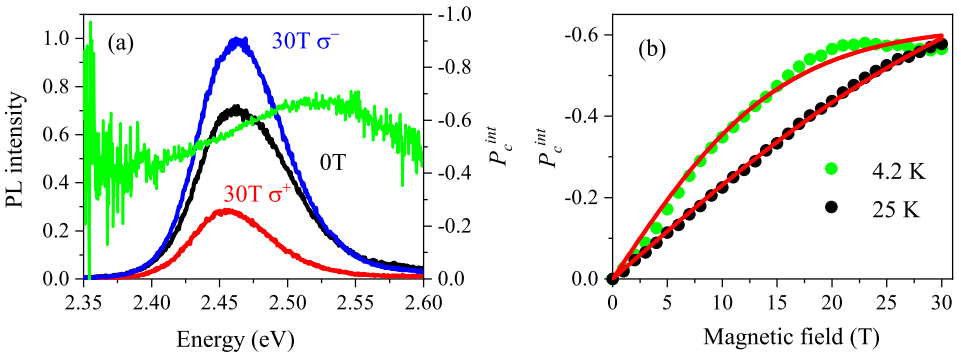

Figure 7.4: (a) Polarized PL spectra at $T = 4.2$ K, $B = 30$ T, the red and blue lines are σ^+ and σ^- components, the black one is unpolarized PL at 0 T for comparison. The green line is the calculated integrated degree of circular polarization P_c^{int}. (b) Magnetic field dependence of P_c^{int} at PL peak position at 0 T with $T = 4.2$ K (green dots) and 25 K (black dots), respectively. Red solid lines are fittings using Eq. 7.4.

~6.44 ns. Similar results were also reported by Canneson et al.,[64] they observed a significant lengthening of fast component from 300 ps to 5 ns when the temperature is increased from 4.2 K to 300 K, which is ascribed to the negative trion.

From our fitting of τ_{long}^{-1} in Fig. 7.2(e) and τ_{short}^{-1} in Fig. 7.2(d), the bright exciton life time turns out to be 1.5 ns and 2.8 ns, respectively, which are between the reported lifetimes for trion and bright exciton,[64,227] so the fast component of PL decay in our case is probably contributed by both of the trion emission and bright exciton emission. Note that the effect of the $1P_{3/2}$ $1S_e$ exciton manifold need to be include into the consideration when the measurements go to high temperature range as discussed in section 2.2.1.2.

7.3 Magneto-optics of dark excitons

7.3.1 Polarization properties

Polarization spectroscopy is a good tool to extract information about the system such as g-factors. Figure 7.4(a) shows the polarization-resolved PL spectra measured at $T = 4.2$ K, $B = 30$ T. The σ^- polarized PL (blue) is enhanced in the external magnetic field while the σ^+ component (red) is suppressed. The time-integrated degree of circular polarization (DCP), P_c^{int}, is calculated by $P_c^{int} = (I^+ - I^-)/(I^+ + I^-)$, where I^+ and I^- are the intensity of σ^+ and σ^- polarized PL. The green curve shows the spectral dependence of P_c^{int}, one can see that for the spectral range close to the PL peak position, P_c^{int} is large at the high energy side and small at the low energy side, for example, at energy position 2.4 eV, P_c^{int} is about 42%, and increases linearly when

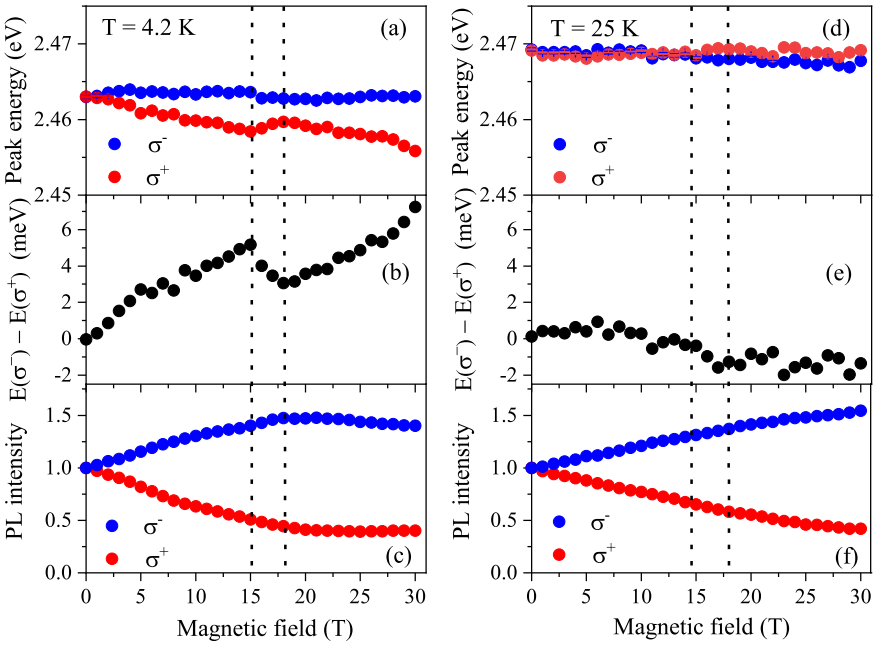

Figure 7.5: Magnetic field dependence of (a) PL peak energy, (b) energy gap between polarized PL, E(σ^-) - E(σ^+) and (c) PL intensity at T = 4.2 K. Corresponding data measured at T = 25 K are shown in (d)-(f). The vertical dashed lines are guide for eyes.

moving to higher energy side of the spectra, at 2.53 eV it reaches the maximum 68%. After that P_c^{int} tends to decrease slightly when moving further to the blue, at 2.6 eV it becomes 49%.

The magnetic field dependence of P_c^{int} is shown in Fig. 7.4(b), two sets of data measured at $T = 4.2$ K and 25 K are presented. At $T = 4.2$ K, P_c^{int} increases smoothly with increasing magnetic field, and saturates around -0.58 after reaching 23 T. While at $T = 25$ K, it increases linearly from 0 T up to 25 T and then continuously rises but with slower rate, and does not saturate up to 30 T. The Red lines show the fitting results with the following equation: [64]

$$P_c(t) = P_c^{sat}[\tau/(\tau + \tau_s)]tanh(g\mu_B B/2k_B T), \tag{7.4}$$

P_c^{sat} is the DCP saturation value, τ is the lifetime of the exciton, τ_s is the spin relaxation time, and k_B is the Boltzmann constant. We get g factor of 0.8 at 4.2 K and 1.9 at 25 K, respectively. Such strong temperature dependence of g-factor is unexpected and most probably due to some mechanisms which contribute to the DCP.

The effect of magnetic field on the PL peak energy, energy gap between polarized PL as well as their intensity are shown in Fig. 7.5. At $T = 4.2$ K, the σ^- PL component not only has a higher energy than σ^+ component, but also owns higher intensity. With the increasing of magnetic field, the energy gap between σ^- and σ^+ polarized PL increase

almost linearly up to 15 T, which is similar to what was observed in wet-chemically synthesized $CsPbBr_3$ NCs.[64] However, it drops suddenly at 15 T till 18 T. Starting from 18 T, it increases again up to 30 T. One can see, from Fig. 7.5(a), this change is mainly contributed by the σ^+ component, its peak energy demonstrates a inverted Z shape with magnetic field. The magnetic field dependence of PL intensity at 4.2 K is shown in Fig. 7.5(c). From 0 T to 18 T, the intensity of σ^+ component decreases monotonously while that of σ^- component increases. When the field is higher than 18 T, σ^+ component intensity reaches a constant level about 40% of the starting value at 0 T. In contrast, the σ^- component intensity slowly decreases up to 30 T.

At $T = 25$ K, the peak energy difference between σ^+ and σ^- polarized PL components is negligible. The σ^+ component even tends to occupy the higher energy position when the magnetic field is larger that 10 T see Fig. 7.5(d) and Fig. 7.5(e), the energy gap decreases on the whole with increasing magnetic field. The PL intensity of σ^+ polarized PL component decreases but that of σ^- component increases monotonously up to 30 T without saturation.

The effect of the magnetic field on exciton energy can be described by:[228]

$$E = E_0 \pm \frac{1}{2} g \mu_B B + c_0 B^2, \tag{7.5}$$

where E_0 is the energy at $B = 0$, μ_B is the Bohr magneton, and c_0 is the diamagnetic coefficient. In principle, we are supposed to get a linear dependence of the energy difference between σ^- and σ^+ polarized PL since $E(\sigma^-) - E(\sigma^+) = g\mu_B B$. The behavior we observed here at 4.2 K is probably related to the magnetic field induced mixing or crossing of exciton sublevels, which is much more evident in $CsPbI_3$ NCs and we are go to talk about in section 8.3 in next chapter.

7.3.2 Spin relaxation dynamics

Quite often, ${P_c}^{int}$ can significantly deviate from the thermal equilibrium value P_c^{eq} which is equals to $P_c^{sat} * tanh(g\mu_B B/2k_B T)$ and is only determined by the thermal populations of the two emitting spin sublevels as long as the effect of inhomogenous broading and phonon effect in ensemble NCs do not need to be considered as discussed in chapter 4, interestingly this condition is possible to be met in $CsPbBr_3$ NCs as reported by swarnkar et al.[229]. The P_c^{eq} in many cases cannot be reached due to the competition between spin relaxation and radiative decay processes. A convenient way to study that is to measure the temporal dependence of the degree of PL polarization, and the basic idea of the experiment is illustrated in Fig. 7.6 where the decay of the σ^+ and σ^- polarized PL measured at $T = 4.2$ K, $B = 15$ T are shown as an example, the corresponding time-resolved DCP, $P_c(t)$, is calculated according to Eq. (7.6) and plotted in Fig. 7.6(b):

$$P_c(t) = \frac{I^+(t) - I^-(t)}{I^+(t) + I^-(t)}, \tag{7.6}$$

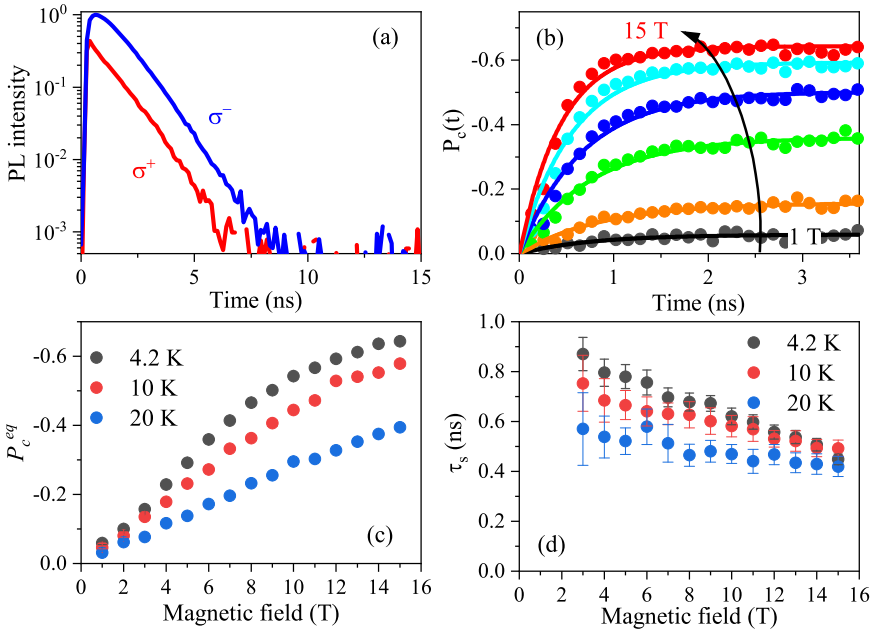

Figure 7.6: (a) Polarized PL decay at $T = 4.2$ K, $B = 15$ T. Red and blue curves correspond to σ^+ and σ^- component, respectively. (b) Time-resolved DCP at $T = 4.2$ K, dots are experimental data, the solid lines are fitting using Eq. (7.7). (c) Magnetic field dependence of equilibrium DCP (P_c^{eq}), and (d) magnetic field dependence of the spin relaxation time, τ_s, at $T = 4.2$, 10 and 20 K.

where $I^+(t)$ and $I^-(t)$ are the intensity of σ^+ and σ^- polarized PL measured at time delay t after pulsed excitation. Note that in the case of cw laser excitation, the calculated DCP corresponds to P_c^{int}. Right after pulsed laser excitation, $P_c(t)$ increases rapidly from 0 to, for example, about 60% at 15 T within 1.5 ns, and saturates at this level which corresponds to the P_c^{eq}. $P_c(t)$ can be described by the following phenomenological expression:

$$P_c(B,t) = P_c^{eq}(B)[1 - \exp(-t/\tau_s(B))], \tag{7.7}$$

where τ_s is the spin relaxation time. P_c^{eq} is strongly influenced by external magnetic field and temperature as shown in Fig. 7.6(c). It increases with increasing magnetic field and is suppressed by higher temperature, for instance, at T =4.2 K, P_c^{eq} increases from 0 up to 64% at 15 T, but decreases to 58% at 10 K and to 39% at 20 K. τ_s, in general, becomes smaller at both higher magnetic field and temperature, but the change is quiet small, it stays between 0.4 ns and 1 ns in current magnetic field and temperature range which is comparable to the τ_{short}.

7.4 Conclusion

To summarize, we have measured the polarization-resolved PL and PL decay on colloidal $CsPbBr_3$ NCs with various temperature up to 125 K and magnetic field up to 30 T. By comparing the temperature and magnetic field dependence of the recombination dynamics, we demonstrate that the ground state of band-edge exciton is dark, and the analysis of the temperature dependent PL decay gives a bright dark splitting about 4.2 meV. We also report the g-factors 0.8, 1.9 at 4.2 and 25 K, respectively, based on the magnetic field dependent polarization data. The spin relaxation time is found to be about 1 ns and changes only slightly with magnetic field and temperature.

Chapter 8

Anomalous polarization and spin dynamics in $CsPbI_3$ nanocrystals

The halide composition strongly affect the properties of perovskite semiconductor nanocrystals (NCs).[63,230–238] In this chapter, we investigate the recombination dynamics, polarization properties and spin dynamics in $CsPbI_3$ perovskite NCs using time- and polarization-resolved spectroscopy at various temperatures and magnetic fields up to 30 T. We found that the lowest energy level of the band-edge exciton is occupied by the dark state. Similar to $CsPbBr_3$ NCs, besides the long tail in the PL decay, another two decay components are also resolved, i.e. the fast and intermediate ones. At low temperature, the fast component dominates the PL emission with a intensity more than two orders of magnitude larger than that of the long component relating to dark excitons. Different from $CsPbBr_3$ NCs, here, we observed an anomalous polarization at low temperature, i.e. with the increasing of magnetic field, the integrated degree of circular polarization (DCP), P_c^{int}, increases and forms a *hump* around 21 T. The spin dynamics at low temperature (e.g. 4.2 K) and high magnetic field (e.g. > 8 T) show that the time resolved DCP, $P_c(t)$, after reaching the maximum, tends to decrease and slowly relaxes to another constant level, which is quite different from the observations in III-V and II-VI semiconductor and also in $CsPbBr_3$ NCs. We propose a mechanism, i.e. the two-LO-phonon assisted spin relaxation among the bright exciton sublevels, to explain this phenomenon.

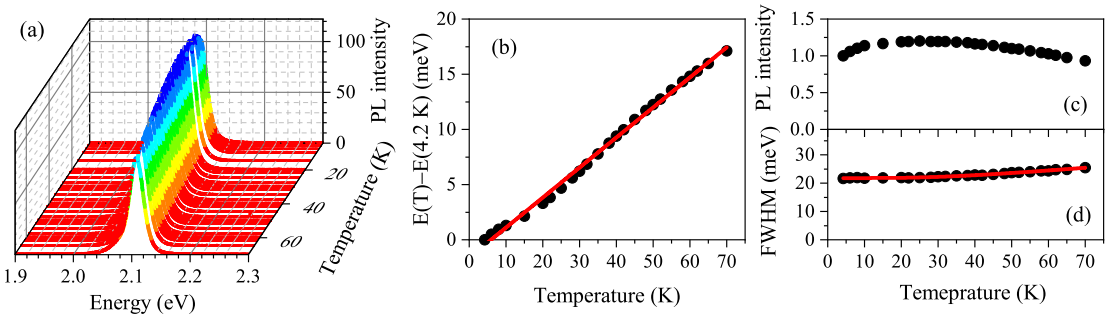

Figure 8.1: (a) Photoluminescence (PL) spectra measured from $T = 4.2$ K to 70 K. (b) PL peak energy shift relative to that at 4.2 K, red line is the fit using Eq. (8.1). Temperature dependence of the (c) PL intensity, and (d) PL full width of maximum (FWHM), the red line is the simulation using Eq. (7.3).

8.1 Exciton-phonon coupling

Before going to the recombination and spin dynamics as well as polarization properties, we characterized the $CsPbI_3$ NCs using temperature dependent PL spectroscopy as shown in Fig. 8.1. Figure 8.1(a) shows the temperature dependence of photoluminescence (PL) spectra from 4.2 K to 70 K. With the increasing of temperature, PL spectra experience a blue-shift, the shifting relative to the PL peak energy at 4.2 K reaches 17 meV at 70 K as it is shown in Fig. 8.1(b). As we have discussed in section 7.1 in chapter 7, under a quasi-harmonic approximation,[205] the thermally induced bandgap renormalization can be understood from the interplay of thermal lattice expansion (TE) and electron-phonon interactions (EP). The contribution of TE depends linearly on temperature as indicated in Eq. (7.2), while the contribution of EP is nonlinear. Since the PL peak energy shift almost perfectly in linear with the temperature as shown in Fig. 8.1(b), we neglect the nonlinear term in Eq. (7.2) and use it as Eq. (8.1) to fit the data, this is also consistent with the literature where the temperature induced PL spectra shift is assigned to the stabilization of the valence band maximum with the lattice expansion.[208,239]

$$E_g(T) = E_0 + A'_{TE}T, \tag{8.1}$$

where E_0 is the unrenormalized bandgap, A'_{TE} is a constant relating to the TE interaction. The fitting gives $E_0 = 2.09\pm0.00$ eV and $A'_{TE} = 0.272\pm0.003$ meV/K.

The PL intensity in Fig. 8.1(c) increases slightly from 4.2 K to 30 K, then turns to decrease continuously. The PL full width at half maximum (FWHM) increases only slightly from 22 meV to 25 meV within current temperature range. The spectral broadening can be reproduced by Eq. (7.3), $\Theta(T) = \Theta_0 + \sigma_{AC}T + \Theta_{LO}/[exp(E_{LO}/k_BT) - 1]$,[65,226] where $\Theta(T)$ is the ZPL linewidth at temperature T, and Θ_0 is its value at zero temperature, k_B is the Boltzmann constant, σ_{AC} and Θ_{LO} are the exciton-acoustic phonon and the exciton-longitudinal optical (LO) phonon coupling coefficients, respec-

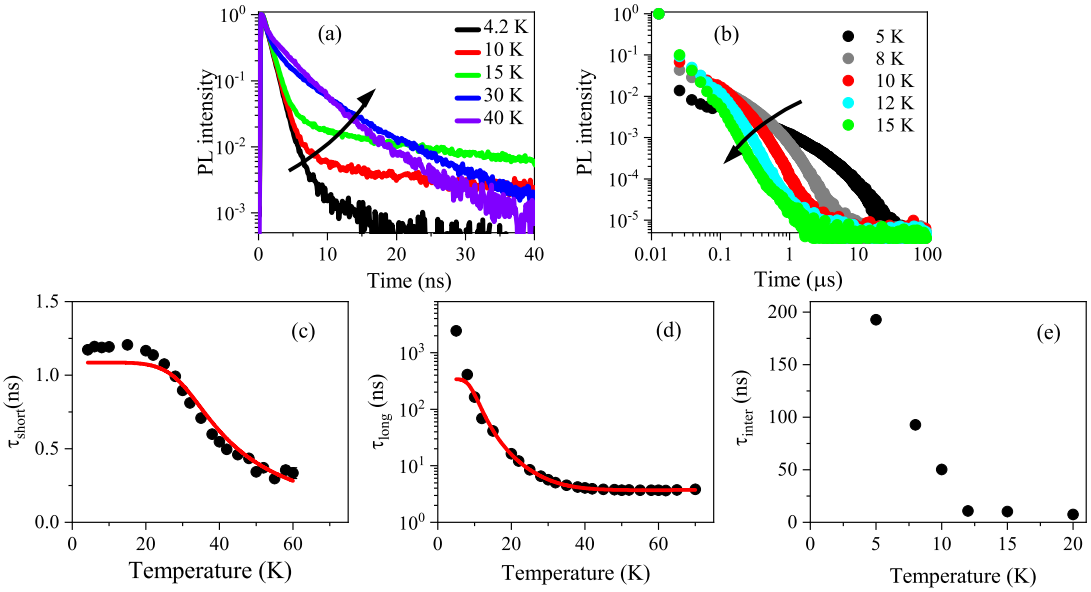

Figure 8.2: Temperature dependence of recombination dynamics in $CsPbI_3$ NCs in glass matrix. PL decay measured (a) with laser frequency 2.5 MHz, resolution 200 ps to resolve the initial fast component, and (b) with laser frequency 10 kHz, resolution 12.8 ns to resolve the long component. (c)-(e) Temperature dependence of time constants τ_{short}, τ_{long} and τ_{inter} corresponding to the fast, intermediate and long component of the recombination dynamics. The red lines in (c) and (d) are fits using Eq. (2.26) based on the two-LO-phonon thermal mixing model, where we take $\Gamma_A = 0.9$ ns^{-1}, $\Gamma_F = 0.003$ ns^{-1}, $\gamma_0 = 3.8$ ns^{-1}, $E_{LO_1} = 10.7$ meV, $E_{LO_2} = 5.4$ meV and $\Gamma_A = 0.4$ ns^{-1}, $\Gamma_F = 0.003$ ns^{-1}, $\gamma_0 = 1.3$ ns^{-1}, $E_{LO_1} = 10.7$ meV, $E_{LO_2} = 5.4$ meV, respectively for the fitting of τ_{short} in (d) and τ_{long} in (e), which gives bright-dark splitting $\Delta E_{AF} = 6.5$ meV.

tively. E_{LO} is an effective optical phonon energy representing the carrier-LO phonon interaction. The fitting, red line in Fig. 8.1(d), yields $\Theta_0 = 21.8 \pm 0.07$ meV, $\sigma_{AC} = 1.6 \pm 5.7$ μeVK^{-1}, $\Theta_{LO} = 12.3 \pm 1.7$ meV and $E_{LO} = 9.1 \pm 1.0$ meV. One notices that the exciton-acoustic phonon coupling coefficient, σ_{AC}, is extremely small indicating that the effect of acoustic phonons on the PL emission is very weak. But the interaction between exciton and longitudinal optical (LO) phonon is quite strong. This supports the availability of the two-phonon thermal mixing model [130] which will be talked about later.

8.2 Fine structure of excitons

A comprehensive knowledge of the fine structure of excitons in semiconductor NCs is required for many applications such as spintronics, single photon source and other aspects of quantum optics. In previous studies, it has been demonstrated that the

temperature and magnetic field dependence of the PL decay measurements help to determine relevant parameters.

The temperature and magnetic field dependence of PL decay are shown in Fig. 8.2 and Fig. 8.3. At low temperature, three components can be resolved from the decay curves, the fast, intermediate and long components with corresponding time constants τ_{short}, τ_{inter} and τ_{long}. Using the same scheme as discussed in chapter 7, we measured the PL decay. Once with high frequency and good resolution to resolve the fast component, another time with low frequency and bad resolution to resolve the long component. For instance, at $T = 5$ K, we set laser pulse with frequency 2.5 MHz and resolution 200 ps to study the fast initial component, and take frequency 10 kHz and resolution 12.8 ns to measure the long component, as shown in Fig. 8.2(a), Fig. 8.3(a) and Fig. 8.2(b), Fig. 8.3(b), respectively.

The long component of PL decay is accelerated rapidly by increasing the temperature as shown in Fig. 8.2(b). At low temperature, the PL decay curves can be well reproduced using three-exponential function, i.e. one exponential function to fit the initial fast component in Fig. 8.2(a), which gives τ_{short}, and two exponential functions for the fitting of the long tail in Fig. 8.2(b), which gives τ_{inter} and τ_{long}. When the temperature is higher than about 20 K, one exponential function is enough for the long tail fitting. If increasing the temperature further higher than 60 K, the fast and long components are well mixed, only one exponential function is needed to fit the whole decay curve. Figure 8.2(c)-(e) show the temperature dependence of time constants, τ_{short}, τ_{inter}, τ_{long}. With the increasing of temperature, all the time constants tend to decrease, i.e. τ_{short} declines from 1.2 ns at 4.2 K to 0.3 ns (which is close the resolution limit of our devices) at 60 K, τ_{inter} decreases from 192 ns at 5 K to 7 ns at 20 K till can not be distinguished anymore, τ_{long} reduces dramatically from 2425 ns at 5 K to only 4 ns at 70 K.

The magnetic field effect on the recombination dynamics is investigated in Fig. 8.3. It is clear that magnetic field has tiny effect on the initial fast decay component as shown in Fig. 8.3(a) and (c), the time constant τ_{short} keeps almost constant at 1.1 ns up to 7 T. However, the time constants τ_{long} and τ_{inter} decrease clearly. At 5 K and 0 T, they are 2425 ns, 192 ns and shortens to 120 ns, 31 ns when increasing magnetic field to 7 T.

The temperature and magnetic field dependent PL decay measurements shown above unambiguously confirm the dark nature of the band-edge exciton ground state, and τ_{long} is assigned to dark excitons.[61,62,128] Therefore, we can apply the two-LO-phonon thermal mixing model described in section 2.3 to analyze the data. The fitting results for temperature dependent τ_{long} is shown by the red line in Fig. 8.2(e) using Eq. (2.26), which gives $\Gamma_A = 0.9$ ns^{-1}, $\Gamma_F = 0.003$ ns^{-1}, $\gamma_0 = 3.8$ ns^{-1} , $E_{LO_1} = 10.7$ meV, $E_{LO_2} = 5.4$ meV and bright-dark splitting $\Delta E_{AF} = 6.5$ meV. By fixing $\Gamma_F = 0.003$ ns^{-1}, $E_{LO_1} = 10.7$ meV, $E_{LO_2} = 5.4$ meV, $\Delta E_{AF} = 6.5$ meV, we fit the τ_{short}

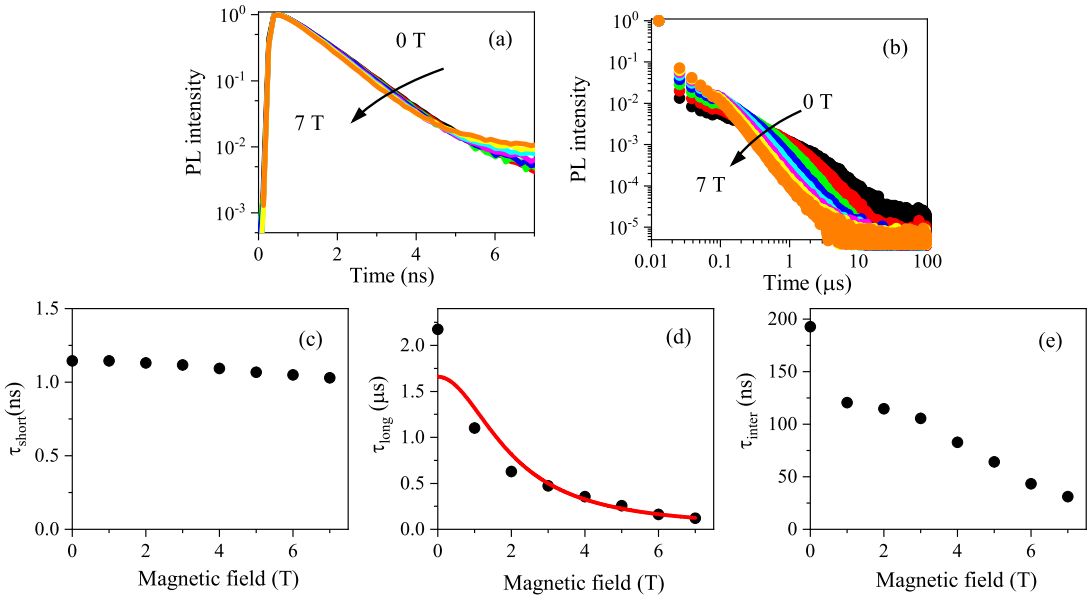

Figure 8.3: Magnetic field dependence of the PL decay at $T = 5$ K. (a) Magnetic field dependence of the initial part of decay curves measured with laser frequency 2.5 MHz and resolution 200 ps. (b) Magnetic field dependence of the long tail of the decay curves measured with laser frequency 10 kHz and resolution 12.8 ns. (c)-(e) Magnetic field dependence of the time constants τ_{short}, τ_{long} and τ_{inter}. The red line in (d) is the fit using Eq. (2.30) by setting $\gamma_0 = 1.3$ ns^{-1} , $E_{LO_1} = 10.7$ meV, $E_{LO_2} = 5.4$ meV, $\Delta g = 3.2$, $\Delta E_{AF} = 6.5$ meV, we get $\Gamma_A = 0.8$ ns^{-1}, $\Gamma_F = 0.0006$ ns^{-1}.

in Fig. 8.2(d) and get $\Gamma_A = 0.4$ ns^{-1} and $\gamma_0 = 1.3$ ns^{-1}, respectively. The magnetic field dependence of τ_{long} measured at 4.2 K is also reproduced quite well as shown in Fig. 8.3(d) using Eq. (2.30), where by setting $\gamma_0 = 1.3$ ns^{-1}, $E_{LO_1} = 10.7$ meV, $E_{LO_2} = 5.4$ meV, $\Delta g = 3.2$, $\Delta E_{AF} = 6.5$ meV, we get $\Gamma_A = 0.8$ ns^{-1}, $\Gamma_F = 0.0006$ ns^{-1}, the parameter Δg= 3.2 is taken from Ref. [65].

By now, it is clear that the dark exciton is responsible for the long component of PL decay. As for the intermediate component, since the corresponding time constant τ_{inter} decreases with increasing temperature and magnetic field as shown in Fig. 8.2(f) and Fig. 8.3(e), and it can not be resolved at higher temperature (>20 K), therefore we ascribe it to the charged dark states or trap states related to dark excitons. [152]

As for the initial fast component of PL decay, three different explanations have been reported, i.e. bright exciton, [102] trion [64] and nonradiative trapping process. [225] Kozlov et al. observed a decreasing of fast decay time from 1.3 to 0.4 ns when rising temperature from 20 to 300 K in $CsPbBr_3$ perovskite NCs, which is similar to our results, however their recombination dynamics are completely different. Therefore, their assignment of the fast decay component to the nonradiative trapping process can not be applied to our case. In wet-chemically prepared $CsPbI_3$ NCs, the typical lifetime

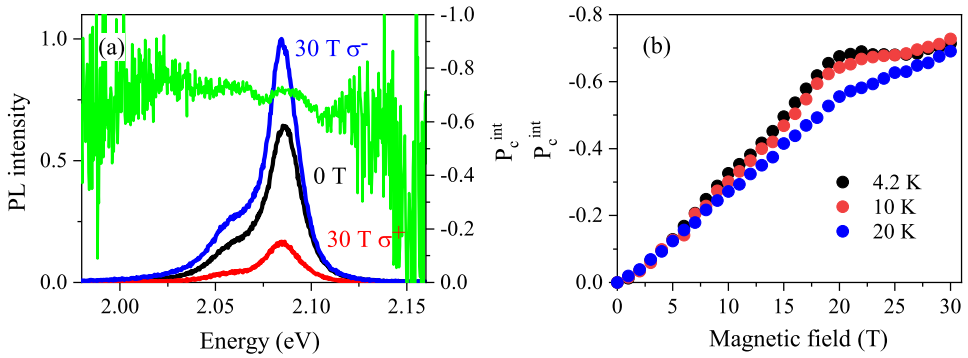

Figure 8.4: (a) Polarized PL spectra at $T = 4.2$ K, $B = 30$ T. The red spectrum is σ^+, blue is σ^- component of the polarized PL, black line is the unpolarized PL spectrum at 0 T for comparison. The green line is the calculated integrated degree of circular polarization P_c^{int}. (b) Magnetic field dependence of P_c^{int} at PL peak position at 4.2 K, 10 K and 20 K.

of bright exciton in individual nanocrytsal is reported to be 0.85 ns at 5 K[102], and ~1 ns at 4 K[240,241]. Benefiting from the suppression of both the PL blinking and spectral diffusion effects in single perovskite $CsPbI_3$ NCs, Yin et al.[242] studied the bright-exciton fine-structure splitting (FSS) in single $CsPbI_3$ nanocrystal and reported similar lifetimes for bright exciton FSS doublet, ~ 0.93 and ~1.02 ns. These bright exciton lifetime values are very close to ours, 1.1 ns at 4.2 K. In the same work, Hu et al.[240] and Yin et al.[242] also report the lifetime for trion, 0.42 ns and 0.83 ns, which are quite deviated and smaller than the bright exciton lifetime. Therefore, we assign the initial fast decay component in our measurements to the bright exciton.

8.3 Polarization properties: possible role of exciton sublevel crossing

As it is already demonstrated that polarization property study is able to provide valuable information about the exciton fine structures, therefore we conducted the experiments and measured the polarization-resolved PL spectra at three different temperatures up to 30 T. Figure 8.4(a) shows the typical polarized PL spectra measured at $T = 4.2$ K, $B = 30$ T. When the magnetic field is applied, PL signal is polarized with σ^- component (blue) being enhanced and σ^+ (red) component being suppressed relative to the spectrum at 0 T (black). The degree of circular polarization (DCP), P_c^{int}, is calculated using $P_c^{int} = (I^+ - I^-)/(I^+ + I^-)$, where I^+ and I^- are the intensity of σ^+ and σ^- polarized PL under cw laser excitation. The green curve in Fig. 8.4(a) shows the spectral dependence of P_c^{int}. It decreases from lower to higher energy side of the spectra in general, for example, at 2.04 eV P_c^{int} is close to -0.8, at 2.12 eV it is only -0.6, and around the peak position P_c^{int} slightly perturbs. This is very different from

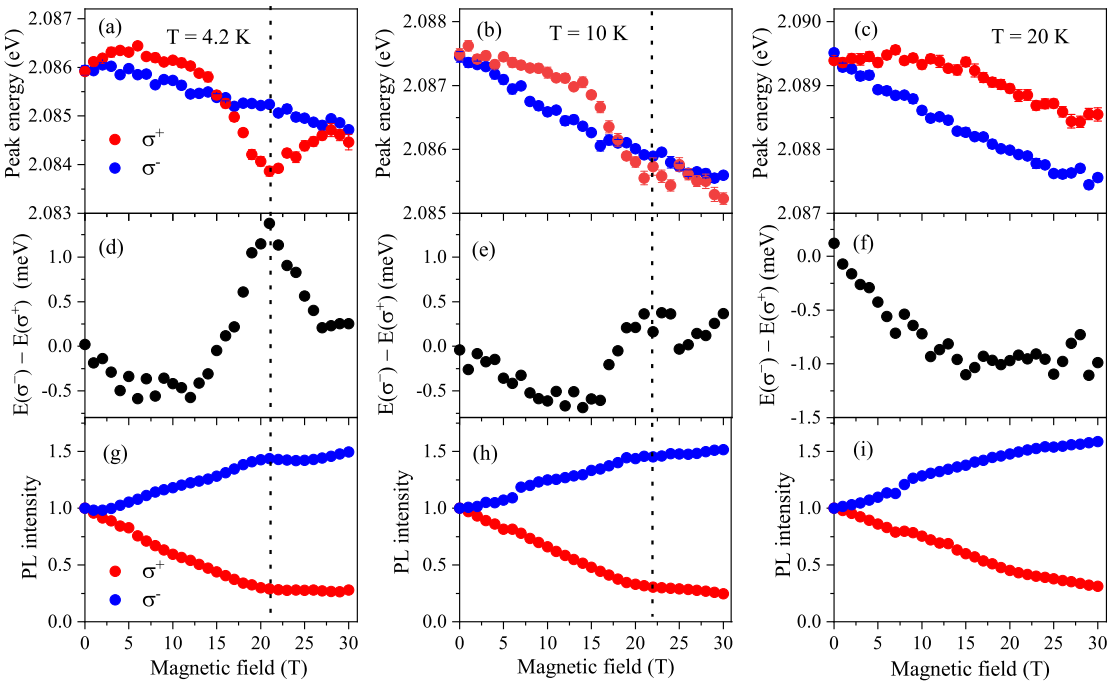

Figure 8.5: Magnetic field dependence of peak position, relative energy shift E(σ^-) - E(σ^+) and intensity of σ^- polarized and σ^+ polarized PL , (a) (d) (g) at T = 4.2 K, (b) (e) (h) at T = 10 K, and (c) (f) (i) at T = 20 K.

our observations in CdSe NCs,[128] where the opposite tendency is observed, i.e. P_c^{int} decreases from high energy side to lower energy side due to the effect of nanocrystal size dispersion and LO phonon replica.

The magnetic field dependence of P_c^{int} (collected at 0 T PL peak position) is shown in Fig. 8.4(b) with temperature setting to 4.2 K, 10 K and 20 K, respectively. P_c^{int} increases with magnetic field and decreases with temperature in general. However, at around 21 T, a *hump* shows up. Taking data measured at 4.2 K as an example, P_c^{int} increases from 0 to -0.69 when magnetic field rise up from 0 T to 21 T, then it keeps almost constant up to 26 T, after that continues increasing up to 30 T and reaches -0.71 without saturation. Increasing of temperature blurs the DCP *hump*, at 20 K only small trace can be resolved.

In order to have a better understanding about this anomalous magnetic field dependent polarization property, we analyzed the variations of the PL peak position, relative energy shift between σ^- and σ^+ polarized PL as well as their intensity as shown in Fig. 8.5. At T = 4.2 K in Fig. 8.5(a), the peak energy of σ^- polarized PL shifts linearly to the lower energy with increasing magnetic field, while that of σ^+ polarized PL displays a complicated behavior, i.e. from 0 T to 4 T, it slightly increases, then slowly decreases till 14 T. And starting from 14 T, it decreases again but with a large rate

to 21 T, after that moves to the higher energy. But once the magnetic field is higher than 28 T, it declines again and tends to be in parallel with the σ^- polarized PL peak energy. As a result, a valley-like shape is formed between 14 T and 28 T. This change is also very clearly seen in Fig. 8.5(d) by the relative energy shift, $E(\sigma^-) - E(\sigma^+)$, where a peak at 21 T pumps out, E(σ^-) and E(σ^+) are the peak energy of polarized PL.

The magnetic field dependence of the polarized PL intensity is plotted in Fig. 8.5(g). When the magnetic field increases from 0 T to 21 T, the intensity of σ^+ polarized PL decreases continuously and finally saturates at 28% of the original level at 0 T. On the contrary, the intensity of σ^- polarized PL increases from 0 T up to 21 T, then stay constant between 21 and 26 T, after that it slowly rises again. This complicated magnetic field dependent σ^+ polarized PL intensity is directly responsible for the magnetic field dependent ${P_c}^{int}$ in Fig. 8.5(b).

At $T = 10$ K, the changes shown in Fig. 8.5(a), Fig. 8.5(d), Fig. 8.5(g) are blurred, the valley observed in Fig. 8.5(a) is not resolvable anymore in Fig. 8.5(b). The corresponding peak in Fig. 8.5(e), although still can be resolved, becomes much vague. In Fig. 8.5(h), the intensity of σ^+ polarized PL continuously decreases and the saturation above 21 T observed in Fig. 8.5(g) is disappeared. By contrast, that of σ^- component increases in the whole field range. It is noted that the increasing rate of σ^+ or σ^- polarized PL intensity becomes a little bit smaller when the magnetic field is higher than 21 T.

At $T = 20$ K, the magnetic field dependence of peak position, relative energy shift and intensity is completely different from that at 4.2 K. As one can see in Fig. 8.5(c), the peak energy of σ^+ polarized PL is always larger than that of σ^- polarized component, while its intensity is smaller as shown in Fig. 8.5(i), this is consistent with the thermal population of exciton state among Zeeman levels. The relative energy shift in Fig. 8.5(f) decreases from 0 T to 14 T, and then keeps constant up to 30 T at -1 meV.

In ensemble colloidal semiconductor NCs with randomly oriented quantization axis, the maximum degree of circular polarization has been predicted to be 75% by considering the relative orientation of nanocrystal quantization axis to the magnetic field direction,[66] however, this value is never achieved in experiments.[66–68,128,148] The reason has been explained recently by us, see chapter 4, by including the size-dispersion-induced inhomogeneous broadening of the PL spectrum, the cumulative contribution of the zero phonon and one optical phonon-assisted emission of dark excitons to the emission spectra into consideration. However, this model is not suitable for current case. Firstly, ${P_c}^{int}$ at 30 T, reaches 71% at 4.2 K which is very close to the theoretical limit. Moreover, it does not saturate up to 30 T as shown in Fig. 8.4(b) and seems to continue to increase at higher field. Secondly, the magnetic field dependence of the PL peak shift for σ^+ and σ^- is too complicated for that model. Therefore, a new theory is expected to explain these observations, which may includes the Zeeman effect, Rasha effect, polaronic effect, divergence of band-edge fine structure in NCs with

different crystal structure and shape, and the contribution of bright exciton sublevels, etc. [65,74,102,130,241]

8.4 Spin relaxation dynamics

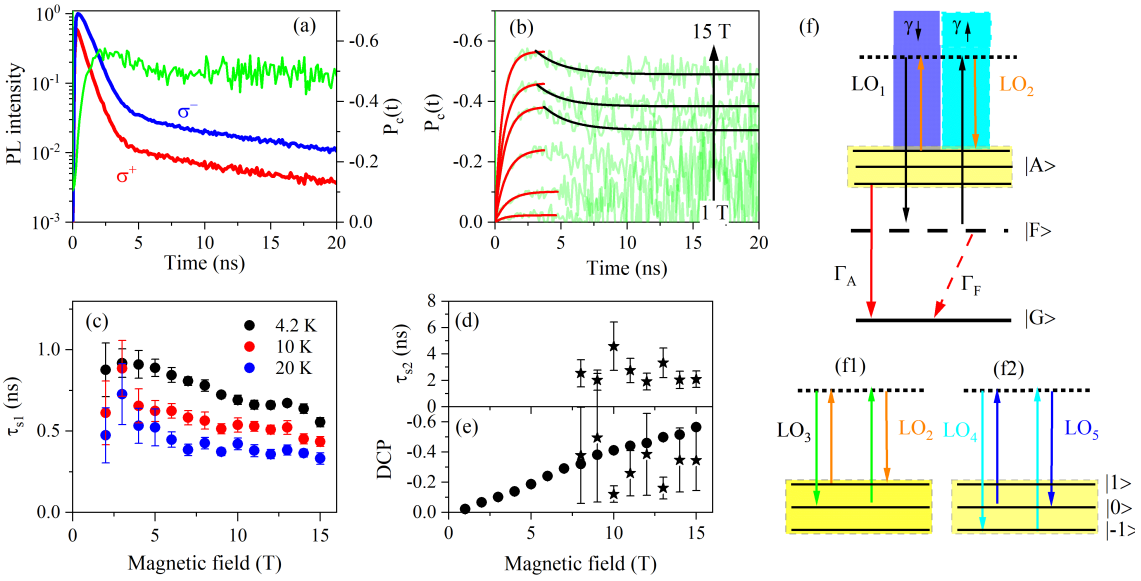

Figure 8.6: (a) Polarized PL decay at $T = 4.2$ K, $B = 15$ T. Red and blue curve correspond to σ^+ and σ^- PL decay component, respectively. The green line is calculated time-resolved DCP, $P_c(t)$. (b) $P_c(t)$ measured at $T = 4.2$ K under various magnetic fields. The red solid lines are fitting with Eq. (8.2) for the rising part of $P_c(t)$, the black lines are fits for the decreasing part using Eq. (8.3). (c) Magnetic field dependence of initial spin relaxation time τ_{s1} at $T = 4.2$, 10 and 20 K. (d) Magnetic field dependence of spin rise time, τ_{s2}, for the decreasing part. (e) Magnetic field dependence of P_{c1}^{eq} (dots) and P_{c2}^{eq} (stars). (f) Schemes of band-edge exciton energy levels in the magnetic field, where triplet bright exciton level $|A\rangle$ splits into three sublevels as marked by the yellow box. $|A\rangle$, $|F\rangle$, and $|G\rangle$ denote bright and dark exciton states, and crystal ground state. Γ_A and Γ_F are the recombination rates of the bright and dark excitons. $|A\rangle$ and $|F\rangle$ are thermally mixed via a two-LO-phonon process with rates $\gamma_\uparrow$ (cyan part) and $\gamma_\downarrow$ (blue part), LO_1 and LO_2 (the black and orange arrows) refer to different LO phonons, their energy difference matches the gap between bright and dark levels. (f1) and (f2) shows the possible mechanisms of the two-LO-phonon assisted relaxation between bright exciton sublevels, $|1\rangle$, $|0\rangle$ and $|-1\rangle$. LO_3, LO_4, LO_5 (green, cyan,blue arrows) are different LO phonons. The energy difference between LO_2 and LO_3, LO_4 and LO_5 matches the Zeeman splitting between $|1\rangle$ and $|0\rangle$, $|0\rangle$ and $|-1\rangle$, respectively.

Understanding the spin dynamics in perovskite is very important for their applications in spintronics. [243] The spin relaxation dynamics in $CsPbI_3$ NCs are investigated in Fig. 8.6. The σ^- and σ^+ polarized PL decay at $T = 4.2$ K, $B = 15$ T are shown in

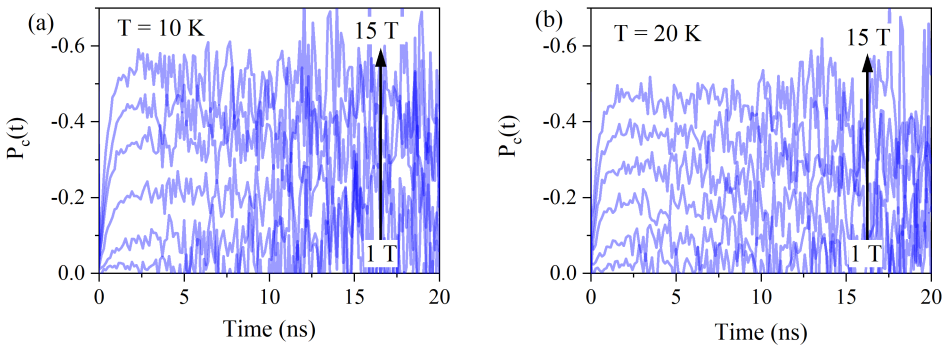

Figure 8.7: Time-resolved DCP, $P_c(t)$, up to 15 T at (a) 10 K and 20 K.

Fig. 8.6(a) as a representative, the corresponding time-resolved DCP, $P_c(t)$, is calculated with $P_c(t) = (I^+(t) - I^-(t))/(I^+(t) + I^-(t))$ and is represented by the green line. Figure 8.6(b) shows $P_c(t)$ measured at 4.2 K under different magnetic fields. One can see that right after the pulsed laser excitation, $P_c(t)$ increases rapidly and saturated at a constant level, P_{c1}^{eq}, within 4 ns at low magnetic field. While, at high magnetic field, e.g. 15 T, after reaching the maximum (P_{c1}^{eq} = -0.57) at 3 ns after laser excitation, $P_c(t)$ starts to decrease exponentially, the red and black lines are the simulation for the initial increasing and later decreasing parts with Eq. (8.2) and Eq. (8.3), respectively.

$$P_c(B,t) = P_{c1}^{eq}(B)[1 - \exp(-t/\tau_{s1}(B))], \tag{8.2}$$

$$P_c(B,t) = P_{c2}^{eq}(B)\exp(-t/\tau_{s2}(B)) + P_0, \tag{8.3}$$

where τ_{s1} and τ_{s2} are time constants, P_{c1}^{eq} and P_{c2}^{eq} are the quasiequilibrium DCP for the initial rise and later decreasing part, P_0 is a constant. However, the decreasing of $P_c(t)$, after arriving the maximum, is only observed at low temperatures and high magnetic fields. For example, at $T = 4.2$ K, only when the magnetic field is not smaller than 8 T, the decrement can be observed. It is interesting to note that in Fig. 8.6(e), the P_{c1}^{eq} from the initial part fitting overlaps with P_{c2}^{eq} obtained from the fitting of the decreasing part at 8 T which is the critical magnetic field for the observation of $P_c(t)$ decline at 4.2 K in current condition. When increasing the temperature from 4.2 K to 10 K and 20 K, as shown in Fig. 8.7, the $P_c(t)$ declining can not be observed even up to 15 T.

Figure 8.6(c) shows the magnetic field dependence of τ_{s1} at various temperatures. We see that τ_{s1} decreases with higher magnetic field or temperature, but only changes slightly within 0.4 ns to 1 ns. The magnetic field does not have a strong impact on τ_{s2} as shown in Fig. 8.6(d), and it only fluctuates slightly around 2.5 ns. The magnetic field dependence of P_{c1}^{eq} and P_{c2}^{eq} at 4.2 K are collected in Fig. 8.6(e), P_{c1}^{eq} increases from 0 to -0.57 monotonously from 0 T to 15 T, and crosses with P_{c2}^{eq} at 8 T.

The spin relaxation dynamics shown in Fig. 8.6(b) is very different from the observations in traditional II-VI and III-V colloidal NCs [128,148,150,244] where right after

pulse laser excitation, $P_c(t)$ increases rapidly and saturates at a constant level without further decline. Due to the electron-hole exchange interaction, the band-edge exciton state in perovskite splits into a singlet state $J = 0$ (dark state) and a threefold degenerate triplet state $J = 1$ (bright state), as it is shown in Fig. 8.6(f). Once the magnetic field is applied, the triplet bright exciton level splits into three sublevels $|1\rangle$, $|0\rangle$ and $|-1\rangle$,[65,130,241] while the dark exciton can not be split due to its singlet feature. As we have discussed above, the recombination dynamics can be reproduced very well by the two-LO-phonon thermal mixing model, the similar idea actually can be applied to understand the spin relaxation processes in Fig. 8.6(b). Note that the declination of $P_c(t)$ after reaching the maximum only shows up at high magnetic field (8 T at 4.2 K), it is reasonable to relate it with the change of the bright exciton sublevels. In the meanwhile, it is only observed at 4.2 K, no traces observed at 10 K and 20 K even up to 15 T, so we suppose that LO phonons are deeply involved in this phenomenon. The initial spin rise part of the spin dynamics can be described as the relaxation between bright and dark exciton levels, and the later decreasing part are supposed to be assigned to processes related to the spin relaxation among bright exciton sublevels, both of them are two-LO-phonon assisted. The assignment depends on the population of available LO phonons for each relaxation process.

In Fig. 8.6(f1) and (f2), we propose two possible processes for the spin relaxation between $|1\rangle$ and $|0\rangle$, $|0\rangle$ and $|-1\rangle$. The energy gaps between them are matched by the energy difference between LO_2 and LO_3, LO_4 and LO_5 phonons, respectively. Taking measurement at 4.2 K as an example, at low magnetic field, the Zeeman splitting is very small meaning a small energy gaps among bright exciton sublevels, due to the energy conservation law, no LO phonons can activate the spin relaxation processes resulting in a 'phonon bottleneck' effect. But when the external magnetic field is larger that 8 T, the increased Zeeman splitting enables a large density of phonon modes to activate the spin relaxation process,[245] therefore leads to the $P_c(t)$ decline after reaching the maximum. There are two possible reasons which can make this phenomena absent at higher temperature in Fig. 8.7. First, at higher temperatures, the energy of LO phonons in the NCs becomes too large, the population of available phonons is reduced extremely.[245] Secondly, the relaxation from bright to dark exciton are rapidly enhanced due to thermal repopulation of the bright and dark excitons, so it becomes dominant in the spin relaxation processes.

8.5 Conclusion

We present a detailed study of band edge exciton fine structures in $CsPbI_3$ nanocrystals grown in glass matrix using time-resolved and polarization-resolved PL spectroscopy. We demonstrate that dark singlet exciton state is located below the bright triplet, which addresses the debate concerning the relative ordering of dark and bright sublevels in all-inorganic halide perovskites in the literature. We applied the two-LO-phonon model

to understand the recombination dynamics, which is found to be more suitable since the exciton-acoustic phonon interaction is extremely weak as demonstrated by the temperature dependent PL spectra data. The simulation with two-LO-phonon model gives a bright-dark splitting about 6.5 meV. A very interesting anomalous polarization is observed at low temperature and high magnetic field. Moreover, for the spin relaxation dynamics, we found that at low temperature (e.g. 4.2 K) and high magnetic field (above 8 T), the time resolved DCP tends to decreases after reaching the maximum, which is never reported in other colloidal semiconductor NCs, and we proposed a two-LO-phonon assisted spin relaxation among the bright exciton sublevels model to explain this unusual spin relaxation process.

Chapter 9

Spin-flip Raman scattering spectroscopy on $CsPbI_3$ nanocrystals

Several different experimental techniques have been applied to study the exciton and spin properties in $CsPbX_3$ NCs, for example, the time-resolved photoluminescence spectroscopy,[63,246,247] multidimensional coherent spectroscopy,[223] single dot spectroscopy,[102,242,248–250] and circular polarized transient absorption spectroscopy.[237,246,251,252] Comparing with the other techniques, the single dot spectroscopy has uncomparable advantages in investigating the band-edge exciton fine structures, e.g. the singlet–triplet sublevel ordering and zero filed splittings.[102,242,248,249] When the magnetic field is switched on, the shifting, splitting, and coupling of sublevels can help to determine the diamagnetic coefficient, exciton g-factor and its anisotropic character.[72] However, this technique is only available in very few situations, for instance, for samples grown by the wet-chemical method where NCs are dispersed in solutions and therefore can be diluted to single NC level. In most of cases like NCs grown in glass matrix, it is not applicable. Fortunately, the spin-flip Raman scattering (SFRS) technique provides an alternative powerful tool to address the spin structure, and measure carrier and exciton g-factors.[136–144]

In this chapter, we employ the spin-flip Raman scattering (SFRS) technique to study the spin properties of colloidal $CsPbI_3$ NCs grown in a glass matrix. By measuring the NCs ensemble in both Faraday and Voigt geometries and analyzing the polarization properties of the Raman spectra, we extract two g-factors, one is about 2.5 which seems to be related to electrons or excitons, another g-factor around 1.5 is probably assigned to holes.

9.1 Transmission and PL spectra, SFRS resonant profile

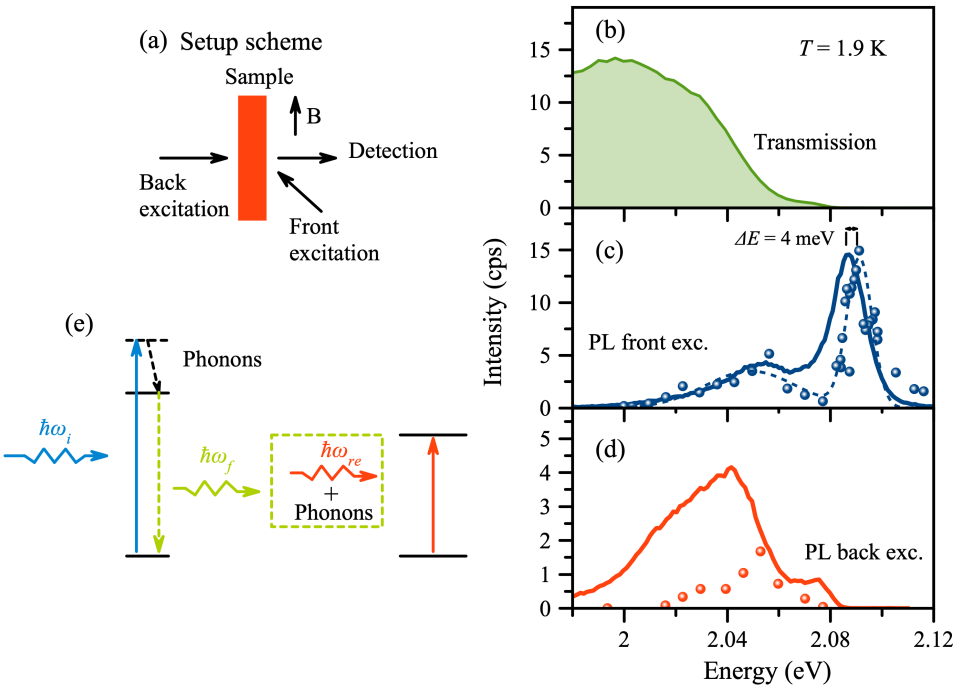

Figure 9.1: (a) Measurement scheme. Our sample is represented by the red rectangular. The magnetic field B is applied either perpendicular (Voigt geometry) or parallel (Faraday geometry) to the excitation laser propagation direction. (b) Transmission spectrum. (c) PL spectrum measured under front excitation. Blue dots represent the SFRS resonance profile (RP) measured at $B = 6$ T, dashed line is the fit with two Guassian functions. The peak energy shift, ΔE, between PL and RP is about 4 meV. (d) PL spectra measured under back excitation. Red dots represent the SFRS RP. All measurements are done at $T = 1.9$ K. (e) Scheme showing the reabsorption process under back excitation. $\hbar\omega_i$, $\hbar\omega_f$, $\hbar\omega_{re}$ are the photon energies of excitation laser, PL emission and reaborption with $\hbar\omega_i > \hbar\omega_f > \hbar\omega_{re}$.

Figure 9.1(a) shows the measurement scheme. The red rectangular represents our sample which is excited either from the backside or frontside, the magnetic field B is applied either perpendicular (Vogit geometry) or parallel (Faraday geometry) to the laser propagation direction. Figure 9.1(b) shows the transmission spectrum at $T = 1.9$ K, the transmission intensity increases from 2.08 eV to the lower energy indicating a strong absorption in the energy range higher than 2.08 eV. The photoluminescence (PL) spectra measured under back- (red) and front-excitation (blue) are shown in Fig. 9.1(c) and Fig. 9.1(d), respectively. One notice that the two spectra differ significantly, i.e. the high energy part of the front-excitation PL spectrum is absent in the back-excitation spectrum due to a reabsorption process, which is consistent with the transmission spectrum and is explained by Fig. 9.1(e). The detailed process can be understood as following: the incoming laser (blue curly arrow) nonresonantly excites small NCs, i.e.

large band gap, and creates hot excitons inside the system. The hot excitons then move to the band-edge and dissipate the extra energy via phonon emission as indicated by the black dashed arrow. Finally, the thermalized excitons recombine and emit light (green curly arrow) which can be reabsorbed by large NCs with smaller band gap. Since the band edge energy of large NCs is probably not in resonance with the emitted light, phonons are expected to be involved.

The red and blue data points in Fig. 9.1(c) and (d) show the SFRS resonance profile (RP). They have similar shape with the respective PL spectra but slightly shift to the higher energy. The blue dashed line in Fig. 9.1(c) is the fit using two Guassian functions, and the energy distance ΔE between PL and RP maximum is 4 meV. The RP describes the intensity of SFRS lines as a function of the excitation energy across the inhomogeneously broadened NCs ensemble, which is mainly affected by three parameters: the orientation of the magnetic field with respect to the nanocrystal quantization axis, the magnetic field strength and nanocrystal size.[253]

9.2 Polarization dependence of SFRS and selection rules

Figure 9.2(a) and (b) show the SFRS spectra measured for different combination of the excitation and detection polarizations, e.g. (σ^η, σ^η) in Faraday geometry and, (π_ν, π_ν) in Voigt geometry at $T = 1.9$ K, $B = 7.5$ T. Both experiments are done under back excitation. In Faraday geometry, we observed a very strong SFRS signal on Stokes for (σ^-, σ^+) polarization configuration, while under the inverted polarization configuration (σ^+, σ^-), the SFRS intensity is dramatically suppressed. For co-polarization configurations (σ^-, σ^-) and (σ^+, σ^+), the SFRS intensity is intermediate. It is also noticed that under the (σ^+, σ^-) configuration, there is a SFRS peak on anti-Stokes, see the inset in Fig. 9.2(a), the g-factors evaluated from the Stokes and anti-Stokes Raman shifts are the same as shown in Fig. 9.3(a). In Voigt geometry, the situation is slightly different. Although we also observed very strong SFRS signal under one of the polarization configuration (π_V, π_V), and very weak signal under the inverted one (π_H, π_H). In the other two configurations, we are able to resolve two SFRS peaks, $S1$ and $S2$, with similar intensity at $T = 1.9$ K, as labeled in Fig. 9.2(b). No SFRS peak is observed at the anti-Stokes.

As we have discussed in section 3.1.6, for a completely randomly oriented NCs ensemble, in principle, one is expected to see more or less same SFRS intensity in all cases regardless of the measurement geometries and polarization configurations[144] since all the selection rules are relaxed. It is quite to surprising to see the extremely strong signal in one of the polarization configurations, however, this is understandable in the current situation. By using the X-ray diffraction spectroscopy, our $CsPbI_3$ NCs have been confirmed to have a cubic structure.[254] Because of the high symmetry, there is possibility to find a general quantization axis even for the ensemble, which makes

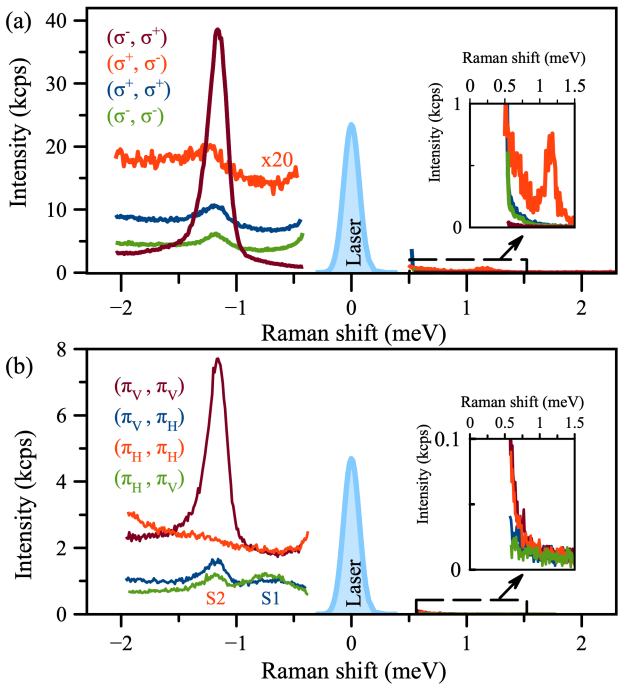

Figure 9.2: Polarization dependence of SFRS spectra under resonant excitation from the back side with $E_{exc} = 2.049$ eV, $B = 7.5$ T, and $T = 1.9$ K. SFRS measured (a) in Voigt geometry, and (b) in Faraday geometry. Laser is represented by the cyan lines at zero Raman shift. Insets show the zoom-in signal on anti-Stokes, where in (a) one peak is clearly resolved in (σ^+,σ^-) polarization configuration.

the clear selection rules possible.

9.3 Magnetic field dependence of Raman shift and g factors

The SFRS in the magnetic field is closely related to the Zeeman splitting. In order to determine the g-factors, we analyzed the magnetic field dependence of the Raman shifts. Figure 9.3(a) shows the data measured in Faraday geometry with polarization configuration (σ^+, σ^-) on anti-Stokes (black dots) and (σ^-, σ^+) on Stokes (dark-red dots). Red lines are linear fittings using Zeeman equation $\Delta E = g_{(AS,S)}\mu_B B + \delta_{off}$, where μ_B is the Bohr magneton, B is the magnetic field, $g_{(AS,S)}$ are the g-factors for SFRS on anti-Stokes and Stokes, δ_{off} is the zero field energy offset contributed by the exchange interaction.[248,255] We obtain $g_{AS} = 2.48$, $g_S = 2.46$ with respective δ_{off} being 0.069 meV and -0.139 meV.

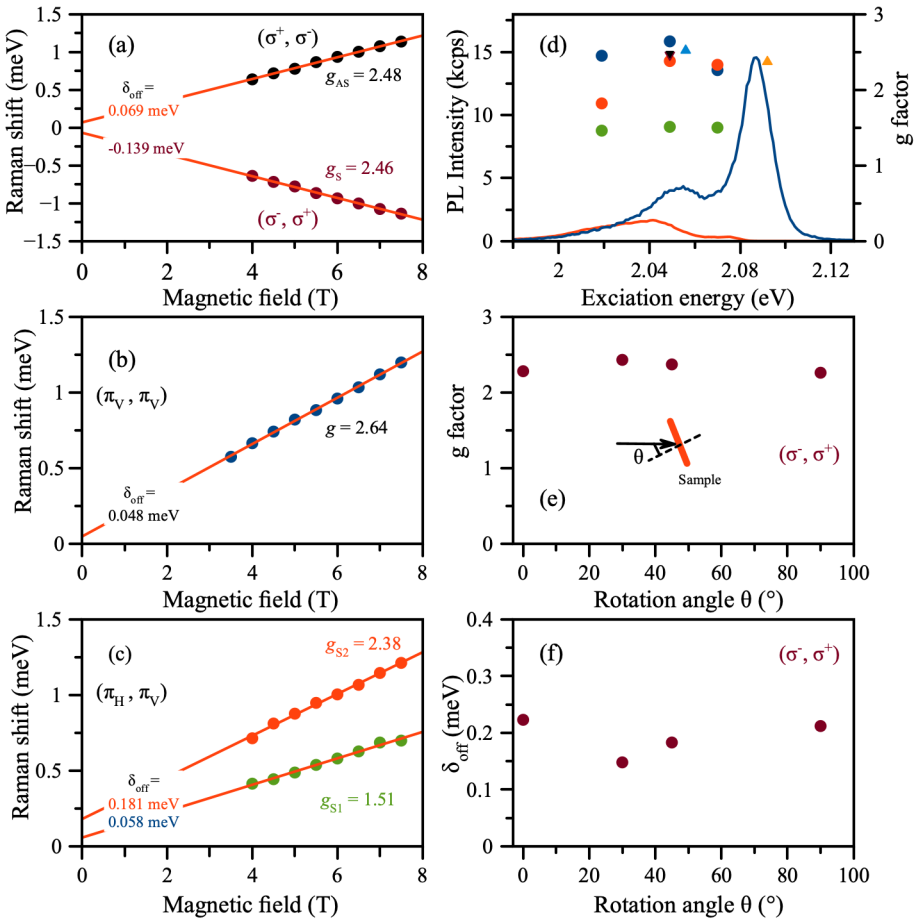

Figure 9.3: (a) Magnetic-field dependence of the Raman shift in Faraday geometry with polarization configuration (σ^+, σ^-) on anti-Stokes (black dots, $g_{AS} = 2.48$) and (σ^-, σ^+) on Stokes (dark-red dots, $g_s = 2.46$). Red lines represent linear fits to the data with respective g-factors and energy offsets δ_{off}. Magnetic-field dependence of the Raman shift in Voigt geometry with polarization configuration (b) (π_V, π_V), $g = 2.64$ and (c) (π_H, π_V), $g_{S1} = 1.51$, $g_{S2} = 2.38$. (d) Summary of g factors as a function of the excitation energy. PL spectra are plotted as a guide for eye (red, blue measured under back, front excitation). The green, red and blue dots are measured in Voigt geometry under back excitation with polarization configuration (π_V, π_V) and (π_H, π_V). The triangle points are measured in Faraday geometry, the downward black and dark-red (overlapped) data points are measured under back excitation corresponding to (a), upward light-blue and orange triangle data points are measured under front excitation. The dependence of (e) g-factor and (f) corresponding energy offset on the angle θ between magnetic field and normal direction of the sample plane, starting from $\theta = 0$ (Faraday geometry) to Voigt geometry $\theta = 90$, see the scheme in (e). The sample is excited from the backside and the polarization configuration is set to be (σ^-, σ^+). All measurements are done at $T = 1.9$ K in positive magnetic field.

Figure 9.3(b) and (c) show the magnetic field dependence of the Raman shifts in Voigt geometry with polarization configuration (π_V, π_V) and (π_H, π_V). The linear

fit in Fig. 9.3(b) gives a g-factor of 2.64 with $\delta_{off} = 0.048$ meV, while in Fig. 9.3(c), we obtain two g-factors, i.e. $g_{S1} = 1.51$ and $g_{S2} = 2.38$ with δ_{off} being 0.181 and 0.058 meV, respectively.

We also checked g-factors at different spectral positions by measuring the magnetic field dependence of the Raman shift under different excitation laser energies as summarized in Fig. 9.3(d). The blue data points are measured in Voigt geometry with polarization configuration (π_V, π_V), see Fig. 9.3(b). The green and red dots are also measured in Voigt geometry but with polarization configuration (π_H, π_V) relating to Fig. 9.3(c). The triangle points are measured in Faraday geometry, the downward black and dark-red (overlapped) data are obtained under back excitation based on Fig. 9.3(a), upward light-blue and orange triangle data points are measured under front excitation. One can see that there are two groups of g-factors, one is about 1.5, another one is around 2.5.

To have more understanding about the g-factors, we performed the angular dependence of SFRS with the basic scheme shown in Fig. 9.3(e), where θ is the angle between the magnetic field direction and the normal direction of sample surface. Starting from Faraday geometry $\theta = 0$, we rotate the sample gradually to $\theta = 90$ (Voigt geometry). The sample is excited from the backside, and the polarization configuration is set to (σ^-, σ^+). It turns out that the g-factor does not change with θ and remains around 2.5 as shown in Fig. 9.3(e). In the meanwhile, the corresponding energy offset δ_{off} also does not display any clear variation as shown in Fig. 9.3(f) and Table 9.1. This seems to support the assignment of g-factor of 2.5 to electrons, the same technique has been applied earlier to characterize the electron g-factor in CdTe/(Cd,Mg)Te quantum wells[140] and indirect band gap (In,Al)As/AlAs quantum dots[142]. The g-factor obtained from Raman shift can be decomposed into the longitudinal and transverse g-factor components, and the dependence of the g-factor on the tilting angle θ is described by:

$$g(\theta) = \sqrt{(g^{\parallel} cos\theta)^2 + (g^{\perp} sin\theta)^2} \tag{9.1}$$

since the electron g-factor is isotropic, it does not change with tilting angle even there is a general quantization axis.[140,142]

However, it is still hard by now for us to determine where the g-factors, i.e. 2.5 and 1.5, come from. More information need to be obtained, and the possibility of excitons and holes should be also carefully considered.

Table 9.1: Parameters of the analysis for the angle dependent SFRS measurements on $CsPbI_3$ NCs at $T = 1.9$ K under back excitation with (σ^-, σ^+) polarization configuration.

Rotation angle (°)	0	30	60	90
g factor	2.28	2.43	2.37	2.26
offset (meV)	0.223	0.148	0.183	0.212

9.4 SFRS in negative magnetic field

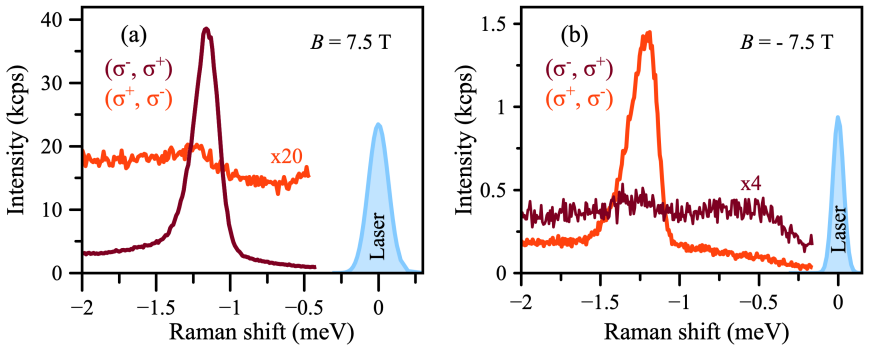

Figure 9.4: Comparison of the polarization dependence of SFRS spectra in positive and negative magnetic field at $T = 1.9\ K$ in Faraday geometry, two polarization configurations (σ^+, σ^-) and (σ^-, σ^+) are displayed. SFRS spectra measured (a) at $B = 7.5$ T under back excitation with excitation energy $E_{exc} = 2.049$ eV, (b) at $B = -7.5$ T under front excitation with excitation energy $E_{exc} = 2.090$ eV. Laser is represented by the cyan lines at zero Raman shift. The signals for (σ^+, σ^-) polarization configuration in (a) and for (σ^-, σ^+) polarization configuration in (b) are zoomed-in for better visibility.

Since the spin-flip Raman scattering is closely related to the Zeeman effect, in order to confirm that the signals which we observed really originate from SFRS instead of other Raman processes, we perform measurements in both positive and negative magnetic fields and compare the SFRS spectra. In Fig. 9.4, the polarization dependence of SFRS spectra for $B = \pm$ 7.5 T at $T = 1.9$ K in Faraday geometry are shown. Figure 9.4(a) shows the SFRS spectra under back excitation with excitation energy $E_{exc} = 2.049$ eV, and Fig. 9.4(b) shows the spectra collected under front excitation with excitation energy $E_{exc} = 2.090$ eV. We know from Fig. 9.3(d) that the g-factors are independent of the excitation energy and does not depend on the front- or backside excitation, therefore comparison between Fig. 9.4(a) and (b) can still give us valuable conclusion even thought they are measured under slightly different conditions. In positive magnetic field, very strong SFRS signal in (σ^-, σ^+) polarization configuration is observed but in (σ^+, σ^-) configuration the signal is very weak. Once the magnetic field is switched to negative, we get the inverted situation, namely, the SFRS signal in (σ^-, σ^+) configuration becomes very weak, while the signal measured in (σ^+, σ^-) configuration becomes very strong.

The cyan lines at zero Raman shift in Fig. 9.4 represent the excitation lasers. It is worth noting that generally the width of electron spin flip Raman line is limited by the width of excitation laser.[139] In Fig. 9.4(b), a narrower laser is used for the excitation as indicated by the narrower cyan line, but we get a more or less same width for the strongest SFRS peak in both measurements, which proofs that the width of lasers used in both cases is proper to resolve the intrinsic SFRS signal.

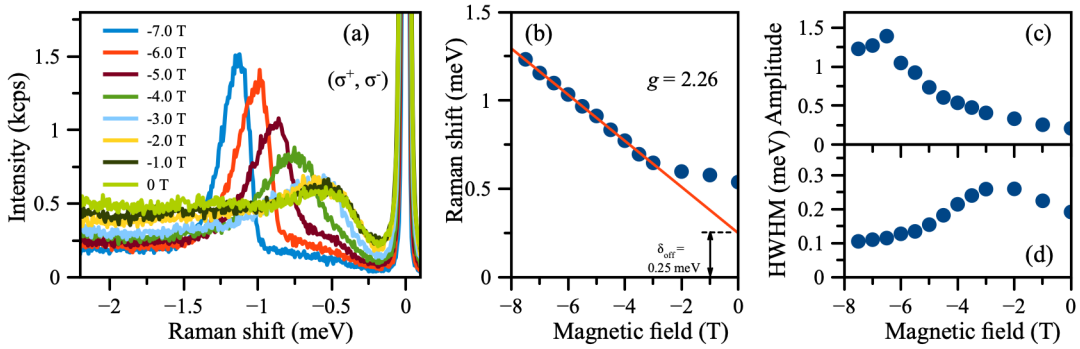

Figure 9.5: (a) Magnetic field dependence of SFRS spectra in (σ^+, σ^-) polarization configuration. The sample is resonantly excited in Faraday geometry from the front side with excitation energy $E_{exc} = 2.090\ eV$, and $T = 1.9$ K. The magnetic field dependence of the corresponding (b) Raman shift, (c) SFRS amplitude, and (d) half width at half maximum (HWHM).

We have mentioned that the two SFRS peaks observed in cross-polarization configurations in the Voigt geometry can be resolved and they are both shifting with the magnetic field as shown in Fig. 9.2(b) and Fig. 9.3(c). As it is shown in Fig. 9.4(b), there seems to be also a second peak in the SFRS spectrum measured in (σ^-, σ^+) configuration with Raman shift around 0.5 meV at $B = -7.5$ T. However, this is actually not a spin-flip peak, since it does not shift with magnetic filed.

Figure 9.5(a) shows the magnetic field dependence of the SFRS spectra in (σ^+, σ^-) polarization configuration at $T = 1.9\ K$ from -7 T to 0 T. The SFRS lines are on top of a background contributed by PL and in the vicinity of the laser line by resonant Rayleigh scattering.[144] At $B = -7$ T, we observed a clear SFRS peak, when ramping the magnetic field down, the SFRS peak shifts close to the laser line. Once reaching $B = -3$ T, the Raman shift becomes very small and keeps nearly constant till 0 T. The magnetic field dependence of the corresponding Raman shift is shown in Fig. 9.5(b), where using the Zeemna equation, we fit the linear dependence part of the data, and by extrapolating to the zero magnetic field, we get an energy offset $\delta_{off} = 0.25$ meV with g-factor 2.26. Note that the Raman shift at $B = 0$ T stays around 0.5 meV. As we have discussed in Fig. 9.3, the angular dependence of SFRS tends to indicate that this peak is related to electrons, however, the energy offset shown here is most probably stemming from the exchange interaction between electron and hole inside the exciton.[248,255]

The SFRS intensity is magnetic field dependent. Figure 9.5(c) shows the magnetic field dependence of the SFRS amplitude, it slightly increases from -7 to -6 T and then decreases continuously. While the half width at half maximum (HWHM) shown in Fig. 9.5(d) slowly increases from -7 to -3 T and then decreases till 0 T.

9.5 Effect of excitation power and temperature

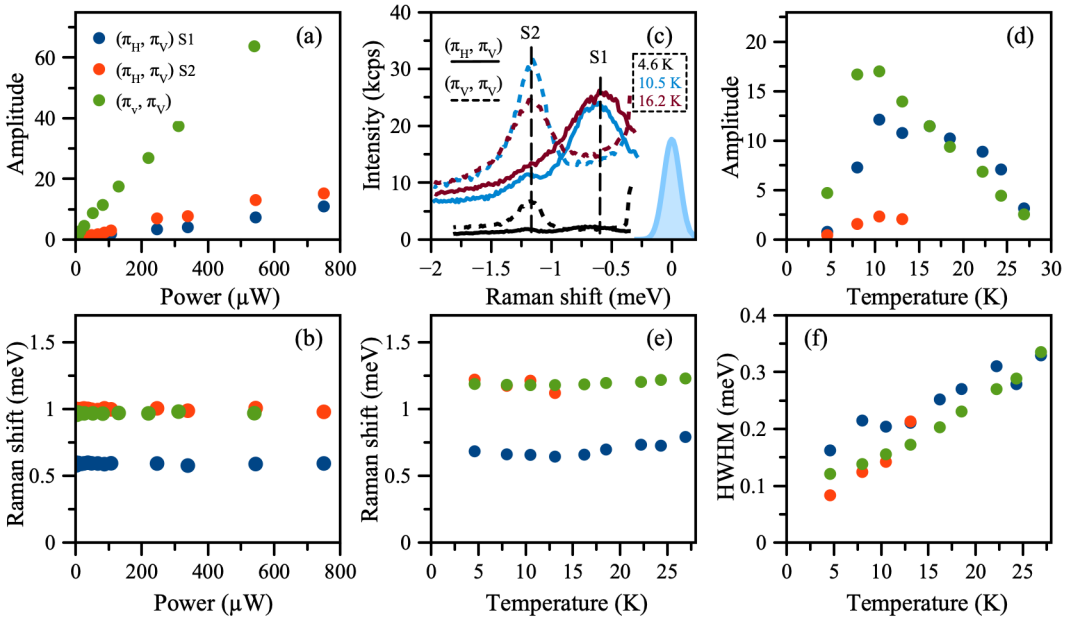

Figure 9.6: Excitation power dependence of (a) SFRS amplitude, (b) Raman shift at $T = 1.9$ K, $B = 6$ T. (c) SFRS spectra measured at $T = 4.6$ K, 10.5 K, 16.2 K with $B = 7.5$ T, the corresponding temperature dependence of SFRS amplitude, Raman shift and half-width at half maximum (HWHM) are shown in (d), (e), (f). All measurements are done in Voigt geometry with polarization configuration (π_H, π_V) or (π_V, π_V), and excitation energy $E_{exc} = 2.049$ eV.

The SFRS process is a particle-type-dependent and temperature sensitive process.[140,144] We conducted the excitation power and temperature dependent measurements at $B = 6$ T as shown in Fig. 9.6, two polarization configurations (π_H, π_V), (π_V, π_V) are considered. It has been reported in CdTe/(Cd,Mg)Te quantum wells that the quasiparticle type can be tuned by laser energy and power, from neutral to positive or negative trions. However, in current excitation power range, the SFRS spectra are the same, therefore, no transformation of the particle happens. The amplitude of the SFRS peak increases linearly with excitation power, and the Raman shift keeps constant as demonstrated in Fig. 9.6(a)-(b).

Phonons are commonly involved in the SFRS proces, consequently the temperature has a strong influence on the SFRS signal. One can see in Fig. 9.6(c) that the SFRS amplitude under (π_V, π_V) configuration increases firstly with temperature, then decreases. The same behavior goes to the $S1$ peak in (π_H, π_V) configuration, on the contrary, the SFRS amplitude from $S2$ peak changes differently. As it is summarized in Fig. 9.6(d), the SFRS amplitude in (π_V, π_V) configuration (green points) and SFRS amplitude for $S1$ peak under (π_H, π_V) (blue points) increases from 5 K up to 10 K, then starts to decrease. For $S2$ peak (red points), the SFRS peak amplitude increases

at the beginning, then it can not be clearly resolved anymore when the temperature is higher than 15 K. The Raman shift of $S2$ peak increases only slightly from 0.68 meV to 0.79 meV when raising the temperature from 4.6 K to 26.9 K. But for the $S1$ peak and signals measured in (π_V, π_V) configuration, no clear Raman shifts are observed. It is worth noting that the half width at half maximum (HWHM) increases linearly in all cases with temperature as shown in Fig. 9.6(f).

9.6 Conclusion

We performed spin flip Raman scattering measurements on $CsPbI_3$ NCs grown in glass matrix. Even though the sample is NCs ensemble with presumably fully random orientation of NCs, we still observed strict selection rules in polarization dependent measurements in both Faraday and Voigt geometries. This is supposed to originate from the cubic nature of the $CsPbI_3$ nanocrystal itself. Analysis of the magnetic field dependence of the Raman shift gives two g-factors, one is about 2.5 and the other one 1.5, and they are excitation energy independent.

Chapter 10

Outlook

We have been witnessing, experiencing and benefiting from the fast development of colloidal semiconductor nanostructures, the good understanding about their properties along with the advanced synthesis technique has lead to the successful application in a broad range of fields, i.e. from laser, LED, solar cell, detector to quantum information and communication systems. Looking forward, several aspects are supposed to be further explored.

The progresses in developing more and more accurate theory have shed light on our road in ahead, from the dark-bright exciton model,[62] to the revised form[100] with further consideration of the long range exchange interaction, the dielectric effect and $1P_{3/2}1S_e$ manifold, we could now have a much better matching between experiments and theory for III-V and II-VI semiconductor nanostructures. However, the effect of high energy levels on the band-edge exciton spin as well as recombination dynamics are rarely reported, this could be checked in further especially from the experiment point of view, since they are closely related with the high temperature, e.g. room temperature, optical performances of the material. The quantum size level structure for narrow-gap semiconductor nanocrystals was also studied by Efros and Rosen long time ago,[256] where they found that coupling of conduction and valence bands is very important and must be considered especially in narrow gap semiconductors band, this is also a good point to check in the magnetic optical experiments, since the band mixing may bring us some new physical phenomena. The theory for the fine structure of perovskite NCs have also been established recently.[101,257] By including the Rashba effect, very interesting triplet bright ground states can be observed. This idea have been checked both theoretically and experimentally. From theory point of view, this is very inspiring and actually has encouraged more people to be involved in this field. However, the first experiment results are highly debated.[63,102,110,111,241,247] Since the Rashba effect is strongly dependent on the structure asymmetry, the modification in energy structure caused by it will vary from sample to sample, which causes disagreements

and contradictions in the literature. So to better understand the fine structure of perovskite NCs, one needs to have a very precise control of the nanocrystal shape, to control the lattice structure of the perovskite NCs at the single nanocrystal level which is extremely difficult and will take time to achieve. Besides that, it is also meaningful to studied the Rashba effect in perovskite bulk single crystal and nanocrystals,[73,120,258] since experimental data are not enough for comprehensive discussion, especially for perovskite NCs. Another interesting topic for pervoskite is the polaron, which has been extensively studied[120,236,259–266] however, the polaronic effect on the spin and exciton fine structure have never been serious discussed from both theory and experiment side, which could be very interesting for future study.

We have known by now that the exciton fine structures in colloidal semiconductor NCs are affected by four intrinsic factors, i.e. the electron-hole exchange interaction, crystal field, nanocrystal shape anisotropy and Rashba effect. Practically, all of them or at least the first three work together in a certain material system, it maybe interesting to study the effect of each of them individually or pair of them in determining the exciton fine structures, especially given to the very well developed synthesis technologies that enable us to have precisely controlled samples.

During the last few decades, the colloidal semiconductor nanostructure research is powered by the progress in synthesis techniques and their application to more and more material systems, it is actually still a good direction to go, for example, new material which is very interesting to try is Cu_2O, it is the mother material of exciton and is still very important for the study of exciton physics.[267,268] The introduction of quantum confinement effect in high quality Cu_2O nanostructures is expected to give us some new physics.[269–271] Other material systems, like TMDCs, are also promising to study.[272,273]

The application of colloidal nanostructures in laser,[38–40] LED,[41–43] solar cell[44,45] and transistors[46] has come to or close to commercial level, but its application in spintronics and scalable quantum information systems is far left behind.[34,47–51] Among the potential applications of colloidal semiconductor NCs in quantum information and communication technologies, the single photon source[130,227,274] is most hopeful to be the first commercial product, due to the flexibility and feasibility of the synthesis technique.

For the study of spin physics in colloidal semiconductor nanostructures, the surface spin is still a very hot topic,[124,125,152] further experiments can be done on nanocrystal with well define surface conditions, which is possible by the current wet-chemical synthesis method. Besides the techniques like FLN,[125] polarization resolved PL spectra,[152] other methods such as SFRS,[143] SQUID can be also tried to detect the surface spin properties. Surface spin study at single dot level can be also put on the schedule, although it is challenging.

Symbols and abbreviations

Symbol	Meaning
$1S_{3/2}$	Hole ground level
$1P_{3/2}$	First excited hole level
$1S_e$	Electron ground level
1PL	First optical phonon-assisted emission
1D	One-dimensional
2D	Two-dimensional
$\|1\rangle$, $\|0\rangle$, $\|-1\rangle$	Bright exciton sublevels
A°	Neutral acceptor
(A°,X), BX	Bound exciton
(A°,M), BM	Bound biexciton
A_{L}	Amplitude of the decay component corresponding to the dark exciton recombination
A_1, A_2, A_3, A_4	Amplitudes from PL decay fitting for CdSe NCs samples
A_{Cu}	Effective electron-phonon interaction parameter relating to copper
A_{Cl}	Effective electron-phonon interaction parameter relating to chloride
A_o	Amplitude of the oscillating part of the Faraday ellipticity signal
A_{no}	Amplitude of the nonoscillating part of the Faraday ellipticity signal
a	crystal radius
a_B	Bohr radius
a_{ex}	Exciton effective radius
a_e	Electron Bohr radius
a_h	Hole Bohr radius
α_e	Rashba coefficient for the electron
α_h	Rashba coefficients for the hole
α	Exchange constant for electron interaction with a single dangling bond spin or Absorption coefficient

Symbol	Meaning
APD	Avalanche photodiode
BS	Beam slitter
β	Ratio of light- to heavy-hole effective mass
B_z,B_+,B_-	Magnetic field components in nanocrystal frame
cw	Continuous-wave mode
CCD	Charge-coupled-device
χ_0	The ratio of the 1PL recombination rate to the ZPL recombination rate at $B = 0$ T
c_{1PL}	Phenomenological parameter determining the increase of the 1PL recombination rate in a magnetic field
χ_{ac}	The ratio of the linearly and circularly polarized recombination rates of the ZPL emission at $B = 0$ T
$^{\circ}C$	Degree of Celsius
$\chi_{1S_{3/2}1S_e}(\beta)$	Dimensionless function
$\delta E_{\pm 2}(B,x)$	Zeeman shifts of the ± 2 dark excitons
ΔT	Time delays of pump-orientation
δt	Time delays of orientation-probe
δE_i	Zeeman energies
$\Delta E^{\pm}_{\max}(B)$	The maximum PL energy shifts in magnetic field
D	The depolarization factor D= $3\varepsilon_o ut/(2\varepsilon_o ut+ \varepsilon_i n)$
DBSs	Dangling bond spins
DBMP	Dangling bond magnetic polaron
D3.3	CdSe NCs with diameter 3.3 nm
D4.1	CdSe NCs with diameter 4.1 nm
D4.9	CdSe NCs with diameter 4.9 nm
D6.1	CdSe NCs with diameter 6.1 nm
d	Dynamical factor
DCP	Degree of circular polarization
Δg	g-factor dispersion
Δ	Net splitting of the hole state
δ_{off}	Energy offset
Δ_{int}	Crystal field induced hole level splitting
Δ_{sh}	Shape anisotropy induced hole level splitting
Δ_{cr}	Bulk crystal field splitting parameter
ΔE_{AF}	Bright-dark splitting
$\|A\rangle$	Bright exciton state
$\|F\rangle$	Dark exciton state
$\|G\rangle$	Crystal ground state
$E_{b,BM}$	Binding energy of bound biexciton
$E_{b,BX}$	Binding energy of bound exciton
$E_{b,M}$	Binding energy of biexciton
$E_{b,T^-(T^+)}$	Binding energy of negative trion (positive trion)

Symbol	Meaning
E_{ex}	Exciton binding energy
E_g	Semiconductor energy gap
$E_v^h(a)$	Confinement energy for hole
$E_v^e(a)$	Confinement energy for electron
$\eta^{SR}_{1S_{3/2}1S_e}$	Short-range electron-hole exchange interaction
$\eta^{LR}_{1S_{3/2}1S_e}$	Long-range electron-hole exchange interaction
$\eta_{1S_{3/2}1S_e}$	Electron-hole exchange constant
η	Exchange interaction
$\eta_{A,F}$	Quantum efficiencies for bright and dark exciton emission
E_p	Kane energy parameter
E_A	Bright exciton energy
E_{ZPL}	Dark exciton energy
E_0	Band gap at zero temperature
$E_{\max}$	PL maximum
E_{LO_i}	Energy of LO_i phonon
$E_p\rho_{db}$	Energy shift due to the formation of dangling bond magnetic polaron
E_z	Zeemann splitting energy
E(σ^-), E(σ^+)	Peak energy of σ^-, σ^+ polarized PL
EP	Electron-phonon interactions
E_{exc}	Excitation laser energy
E_{RS-exc}	Laser energy for resonant excitation
E_p	Dangling bond magnetic polaron binding energy for complete DBS polarization
e	Electron or Elementary charge 1.6022×10^{-19} C
$\vec{e}$	Polarization unit vector
FLN	Fluorescence line narrowing
fs	Femtosecond
FFT	Fast Fourier transform
FWHM	Full width at half maximum
$f_{ZPL}(E)$	Function determining the ZPL related inhomogeneous broadening of the PL spectra due to the NC size dispersion in an ensemble
$f_{1PL}(E)$	Function determining the 1PL related inhomogeneous broadening of the PL spectra due to the NC size dispersion in an ensemble
g	Landé factor
γ_0	Zero-temperature relaxation rate from the bright to the dark exciton state
Γ_A	Recombination rates of the bright exciton
γ_{th}	Thermally-activated relaxation rate from the dark to the bright exciton state

Symbol	Meaning
Γ_{short}	The rate for the short-lasting PL decay
Γ_{long}	The rate for the long-lasting PL decay
$\gamma_{\uparrow}$, $\gamma_{\downarrow}$	Thermal mixing rate between bright and dark states through two-LO-phonon process
g_e	Electron g factor
g_h	Hole g factor
G_X, G_X*, G_{BX}, G_M	CuCl NCs PL Gaussian components referring to the emission from exciton, exciton to high energy defects, bound exciton, biexciton,
GHz	Gigahertz
$\Gamma^{\pm}_{\pm 2,ZPL}(x,B)$	Magnetic field and angular dependent recombination rates contributing to the ZPL emission
γ_{ac}	Linearly polarized recombination rate of the ZPL emission at $B = 0$ T
γ_{ε}	Circularly polarized recombination rate of the ZPL emission at $B = 0$ T
γ_{tot}	The total exciton recombination rate
g_F	Dark exciton g-factor
g	Gram
γ_{LO}	1PL recombination rate at $B = 0$T
h	Hole or Planck constant
$\hbar$	Reduced Planck constant
GTP	Glam-Taylor prism
$\hbar\omega_{ST}$	Short-range exchange splitting
$\hbar\omega_{LT}$	Bulk exciton longitudinal transverse splitting
$H_R^{e(h)}$	Rashba Hamiltonian for electrons (holes)
$\hat{H}$	Hamiltonian
$\widehat{H}^{exch}_{1S_{3/2}1S_e}$	The Hamiltonian of electron-hole exchange interaction
$\widehat{H}^{an}$	Hamiltonian for internal hexagonal crystal field and non-spherical ellipsoidal shape induced hole level splitting
HWHM	Half line width at half maximum
$I(t)$	PL intensity
I	Intensity of the transmitted light with sample
I_0	Intensity of the transmitted light without sample
$I^{\pm}_{i,ZPL}(x,B)$	Intensity of zero-phonon line emission of the dark exciton with σ^+ (σ^-) polarization
$I^{\pm}_{i,1PL}(x,B)$	Intensity of one-LO-phonon line emission of the dark exciton with σ^+ (σ^-) polarization
$I(E,B,0)$	PL intensity at $t = 0$
$I^+(E)$	Intensity for σ^+ circularly polarized PL at energy E
$I^-(E)$	Intensity for σ^- circularly polarized PL at energy E
J	Total angular momentum

Symbol	**Meaning**
$\boldsymbol{J} = [J_x,J_y,J_z]$	Hole spin operator composed from spin 3/2 matrices
κ	The ratio of internal, ε_{in}, to external, ε_{out}, high-frequency dielectric constants
K	The square of the overlap integral between the electron and hole
k_B	Boltzmann constant
kHz	Kilohertz
LO phonon	Longitudinal optical phonon
LO_1, LO_2	longitudinal optical phonons with different energy
LA phonon	Longitudinal acoustic phonon
LOE	Longitudinal orthoexciton
L	Lense
MBE	Molecule beam epitaxy
M	Biexciton
m_e	Electron effective mass
m_h	Hole effective mass
μ	Reduced exciton mass
F_z	Total angular momentum projection on nanocrystal quantization axis
m_0	Free electron mass
μ_B	Bohr magneton
mol.%	Mole percentage
μs	Microsecond
min	Minute
M	Mirror
MS	Mechanical slit
MHz	Megahertz
μ_B	Bohr magneton
μW	Microwatt
μeV	Microelectron volt
NCs	Nanocrystals
n	Refractive index
N_B	Bose-Einstein phonon occupation
N_{LO_i}	Bose-Einstein phonon numbers (i = 1,2)
N	Total number of dangling bond spins at the nanocrystal surface
N_{ex}	Equilibrium population of the excitons
$n_{\pm2}(x,B)$	Boltzmann populations of the ±2 dark exciton states
$n_{j,\overrightarrow{q}}$	Number of phonons at j branch with wave vector of $\overrightarrow{q}$
ω_M	Frequency of biexciton emission
ω_X	Frequency of exciton emission
ω_{OS}	Frequency of spheroidal vibrational mode
ω_{OT}	Frequency of torsional vibrational mode

Symbol	**Meaning**
ω_{OB}	Frequency of breathing vibrational mode
ω	Frequency of emitted light
OC	Optical coupler
OPA	Optical parametric amplifier
OE	Orthoexciton
Ω	Spin precession frequency
ω_L	Angular frequency of Larmor precession
P_c^{int}	Integrated degree of circular polarization
$P_c(t)$	Time resolved degree of circular polarization
PL	Photoluminescence
$\phi_{l,n}$	nth root of the spherical Bessel function of order l, $j_l(\phi_{l,n}) = 0$
$p_{\mathrm{A,F}}$	Occupation number of bright and dark exciton states
p_A	Population of the bright exciton
p_F	Population of the dark exciton
$\Psi_{ex}(r_e,r_h)$	Wave function of a confined exciton
ps	Picosecond
PEM	Photoelastic modulator
PE	Paraexciton
P_c^{eq}	Equilibrium degree of circular polarization
P_c^{sat}	Saturation value of degree of circular polarization
P_{c1}^{eq}, P_{c2}^{eq}	Equilibrium value of degree of circular polarization
ppFR	Pump probe Faraday rotation
ppFE	Pump probe Faraday ellipticity
Ψ	Wave function
P_{oo}	Degree of optical orientation
$P_c^{\sigma^\pm}$	Degree of circular polarization under $\sigma^\pm$ polarized laser excitation
P_{exc}	Excitation laser power
Qubits	Quantum bits
QDs	Quantum dots
$Q_0^{(1)}(\beta)$	Dimensionless function
ρ_{db}	Dangling bond spin polarization degree
R_g	Radius of gyration
r_{lin}	Fraction of the optical phonon-assisted recombination rate via the admixture to the 0^U bright exciton
RP	Resonance profile
SQUID	Superconducting quantum interference device
s_z	Electron spin projection on nanocrystal quantization axis
SAXS	Small angle X-ray scattering
$S_Z^{\sigma,J}$	Z-component of the full electron-hole spin matrix
$\langle S_Z^{\mathrm{ens}} \rangle$	Average exciton spin in the ensemble of wz-CdSe NCs

Symbol	**Meaning**
SF_S, SF_{AS}	Spin-flip at Stokes and antiStokes
σ_{AC}	Exciton-acoustic phonon coupling coefficient
SFRS	Spin-flip Raman scattering
σ_e	Electron Pauli matrix
$\boldsymbol{\sigma} = [\sigma_x,\sigma_y,\sigma_z]$	Electron spin operator composed from Pauli matrices
T_2^*	Dephasing time
τ_{short}	Time constant for fast decay component
τ_{inter}	Time constant for intermediate decay component
τ_{long}	Time constant for long decay component
T	Trion
T^-	Negative trion
T^+	Positive trion
TA phonon	Transverse acoustic phonon
TO phonon	Transverse optical phonon
$1/\tau_{ex}$	Characteristic radiative decay rate of exciton
T	Temperature or Tesla
T_c	Critical temperature for dangling bond magnetic polaron formation
τ_{rd}	Radiative decay time
TCSPC	Time correlated single photon counter
τ_0	Lifetime of the 0^U bright exciton
$\tau_{B=0}$	Lifetime of the dark excitons in zero magnetic field
T_1, T_2, T_3, T_4	Time constants from PL decay fitting for CdSe NCs samples
TOE	Transverse orthoexciton
TE	Triplet exciton
τ	Exciton lifetime
τ_s	Exciton spin relaxation time
τ_{s1}, τ_{s2}	Spin relaxation time
$\Theta(T)$	ZPL linewidth at temperature T
Θ_{LO}	Exciton-longitudinal optical phonon coupling coefficient
TE	Thermal lattice expansion
ε_{in}	Dielectric constant inside the nanostructure
ε_{out}	Dielectric constant of surrounding media
$V_{self(r_{e(h)})}$	Electron (hole) self-energy potential
$V_{pot(r_{e(h)})}$	Spatial confining potential for electron (hole)
$V_{conf(r_{e(h)})}$	Confining potential considering both spatial and dielectric confinement for electron (hole)
v_l	Longitudinal sound velocity
$\|$	8 x 8 unit matrix
v_z	Inversion symmetry-breaking direction along the z axis
ε_R	Exciton Rashba energy

Symbol	**Meaning**
v	Larmor precession frequency
φ_0	Initial phase
$\widehat{E}'_H$	Perturbation matrix
w	Inhomogeneous broadening
w_{Cu}	Energy of an average acoustic, purely Cu-like phonon
w_{Cl}	Energy of an average optic, purely Cl-like phonon
X	Exciton
$\xi_{1S_{3/2}1S_e}(\beta)$	Dimensionless function
X*	Exciton bound to a higher-lying defect state
y_0	Offset of the Faraday ellipticity
ZPL	Zero phonon emission line

List of Figures

List of Tables

Bibliography

[1] M.-L. Chen, X. Sun, H. Liu, H. Wang, Q. Zhu, S. Wang, H. Du, B. Dong, J. Zhang, Y. Sun, et al., *A FinFET with one atomic layer channel*, Nature communications **11**, 1 (2020).

[2] T. N. Theis and H.-S. P. Wong, *The end of moore's law: A new beginning for information technology*, Computing in Science & Engineering **19**, 41 (2017).

[3] I. Žutić, J. Fabian, and S. D. Sarma, *Spintronics: Fundamentals and applications*, Reviews of Modern Physics **76**, 323 (2004).

[4] F. Pulizzi, *The rise of semiconductor spintronics*, Nature Physics **4**, S20 (2008).

[5] R. Pelá and L. Teles, *Spin Transistors vs. Conventional Transistors: What Are the Benefits?*, Journal of superconductivity and novel magnetism **23**, 61 (2010).

[6] A. Rycerz, J. Tworzydło, and C. W. J. Beenakker, *Valley filter and valley valve in graphene*, Nature Physics **3**, 172 (2007).

[7] H. Zeng, J. Dai, W. Yao, D. Xiao, and X. Cui, *Valley polarization in MoS2 monolayers by optical pumping*, Nature Nanotechnology **7**, 490 (2012).

[8] Y. Ye, J. Xiao, H. Wang, Z. Ye, H. Zhu, M. Zhao, Y. Wang, J. Zhao, X. Yin, and X. Zhang, *Electrical generation and control of the valley carriers in a monolayer transition metal dichalcogenide*, Nature Nanotechnology **11**, 598 (2016).

[9] L. Li, L. Shao, X. Liu, A. Gao, H. Wang, B. Zheng, G. Hou, K. Shehzad, L. Yu, F. Miao, Y. Shi, Y. Xu, and X. Wang, *Room-temperature valleytronic transistor*, Nature Nanotechnology **15**, 743 (2020).

[10] S. Wolf, D. Awschalom, R. Buhrman, J. Daughton, v. S. von Molnár, M. Roukes, A. Y. Chtchelkanova, and D. Treger, *Spintronics: a spin-based electronics vision for the future*, science **294**, 1488 (2001).

[11] C. Felser and G. H. Fecher, *Spintronics: from materials to devices*, Springer Science & Business Media (2013).

[12] D. D. Awschalom, D. Loss, and N. Samarth, *Semiconductor spintronics and quantum computation*, Springer Science & Business Media (2013).

[13] B. Hensen, H. Bernien, A. E. Dréau, A. Reiserer, N. Kalb, M. S. Blok, J. Ruitenberg, R. F. Vermeulen, R. N. Schouten, C. Abellán, et al., *Loophole-free Bell inequality violation using electron spins separated by 1.3 kilometres*, Nature **526**, 682 (2015).

[14] S. Wehner, D. Elkouss, and R. Hanson, *Quantum internet: A vision for the road ahead*, Science **362** (2018).

[15] D. Loss and D. P. DiVincenzo, *Quantum computation with quantum dots*, Physical Review A **57**, 120 (1998).

[16] D. P. DiVincenzo, *The physical implementation of quantum computation*, Fortschritte der Physik: Progress of Physics **48**, 771 (2000).

[17] M. Bayer, P. Hawrylak, K. Hinzer, S. Fafard, M. Korkusinski, Z. Wasilewski, O. Stern, and A. Forchel, *Coupling and entangling of quantum states in quantum dot molecules*, Science **291**, 451 (2001).

[18] R. Hanson, L. P. Kouwenhoven, J. R. Petta, S. Tarucha, and L. M. K. Vandersypen, *Spins in few-electron quantum dots*, Reviews of Modern Physics **79**, 1217 (2007).

[19] D. D. Awschalom, L. C. Bassett, A. S. Dzurak, E. L. Hu, and J. R. Petta, *Quantum spintronics: engineering and manipulating atom-like spins in semiconductors*, Science **339**, 1174 (2013).

[20] M. I. Dyakonov and A. Khaetskii, *Spin physics in semiconductors*, vol. 1, Springer (2008).

[21] F. Henneberger and O. Benson, *Semiconductor quantum bits*, CRC Press (2016).

[22] M. M. Glazov, *Electron & nuclear spin dynamics in semiconductor nanostructures*, vol. 23, Oxford University Press (2018).

[23] L. M. Vandersypen and M. A. Eriksson, *Quantum computing with semiconductor spins*, Physics Today **72**, 8 (2019).

[24] G. Scappucci, C. Kloeffel, F. A. Zwanenburg, D. Loss, M. Myronov, J.-J. Zhang, S. De Franceschi, G. Katsaros, and M. Veldhorst, *The germanium quantum information route*, Nature Reviews Materials pp. 1–18 (2020).

[25] N. W. Hendrickx, W. I. Lawrie, M. Russ, F. van Riggelen, S. L. de Snoo, R. N. Schouten, A. Sammak, G. Scappucci, and M. Veldhorst, *A four-qubit germanium quantum processor*, Nature **591**, 580 (2021).

[26] M. Bayer, *Bridging Two Worlds: Colloidal versus Epitaxial Quantum Dots*, Annalen der Physik **531**, 1900039 (2019).

[27] L. Jing, S. V. Kershaw, Y. Li, X. Huang, Y. Li, A. L. Rogach, and M. Gao, *Aqueous based semiconductor nanocrystals*, Chemical reviews **116**, 10623 (2016).

[28] G. Jia, Y. Pang, J. Ning, U. Banin, and B. Ji, *Heavy-Metal-Free Colloidal Semiconductor Nanorods: Recent Advances and Future Perspectives*, Advanced Materials **31**, 1900781 (2019).

[29] J. M. Pietryga, Y.-S. Park, J. Lim, A. F. Fidler, W. K. Bae, S. Brovelli, and V. I. Klimov, *Spectroscopic and device aspects of nanocrystal quantum dots*, Chemical reviews **116**, 10513 (2016).

[30] M. Ouyang and D. D. Awschalom, *Coherent spin transfer between molecularly bridged quantum dots*, Science **301**, 1074 (2003).

[31] R. Beaulac, P. I. Archer, S. T. Ochsenbein, and D. R. Gamelin, *Mn2+-doped CdSe quantum dots: new inorganic materials for spin-electronics and spin-photonics*, Advanced Functional Materials **18**, 3873 (2008).

[32] S. von Kugelgen and D. E. Freedman, *A chemical path to quantum information*, Science **366**, 1070 (2019).

[33] J. H. Olshansky, S. M. Harvey, M. L. Pennel, M. D. Krzyaniak, R. D. Schaller, and M. R. Wasielewski, *Using Photoexcited Core/Shell Quantum Dots To Spin Polarize Appended Radical Qubits*, Journal of the American Chemical Society **142**, 13590 (2020).

[34] C. R. Kagan, L. C. Bassett, C. B. Murray, and S. M. Thompson, *Colloidal Quantum Dots as Platforms for Quantum Information Science*, Chemical Reviews (2020).

[35] M. Bruchez, M. Moronne, P. Gin, S. Weiss, and A. Alivisatos, *Semiconductor Nanocrystals as Fluorescent Biological Labels*, Science **281**, 2013 (1998).

[36] J. H. Yu, S.-H. Kwon, Z. Petrášek, O. K. Park, S. W. Jun, K. Shin, M. Choi, Y. I. Park, K. Park, H. B. Na, et al., *High-resolution three-photon biomedical imaging using doped ZnS nanocrystals*, Nature materials **12**, 359 (2013).

[37] A. L. Efros, J. B. Delehanty, A. L. Huston, I. L. Medintz, M. Barbic, and T. D. Harris, *Evaluating the potential of using quantum dots for monitoring electrical signals in neurons*, Nature Nanotechnology **13**, 278 (2018).

[38] C. Liao, L. Tang, L. Wang, Y. Li, J. Xu, and Y. Jia, *Low-threshold near-infrared lasing at room temperature using low-toxicity Ag 2 Se quantum dots*, Nanoscale **12**, 21879 (2020).

[39] P. Geiregat, D. Van Thourhout, and Z. Hens, *A bright future for colloidal quantum dot lasers*, NPG Asia Materials **11**, 1 (2019).

[40] H. Dong, C. Zhang, X. Liu, J. Yao, and Y. S. Zhao, *Materials chemistry and engineering in metal halide perovskite lasers*, Chemical Society Reviews **49**, 951 (2020).

[41] X. Zhao and Z.-K. Tan, *Large-area near-infrared perovskite light-emitting diodes*, Nature Photonics **14**, 215 (2019).

[42] T. Kim, K.-H. Kim, S. Kim, S.-M. Choi, H. Jang, H.-K. Seo, H. Lee, D.-Y. Chung, and E. Jang, *Efficient and stable blue quantum dot light-emitting diode*, Nature **586**, 385 (2020).

[43] X.-K. Liu, W. Xu, S. Bai, Y. Jin, J. Wang, R. H. Friend, and F. Gao, *Metal halide perovskites for light-emitting diodes*, Nature Materials pp. 1–12 (2020).

[44] G. H. Carey, A. L. Abdelhady, Z. Ning, S. M. Thon, O. M. Bakr, and E. H. Sargent, *Colloidal quantum dot solar cells*, Chemical reviews **115**, 12732 (2015).

[45] X. Zheng, Y. Hou, C. Bao, J. Yin, F. Yuan, Z. Huang, K. Song, J. Liu, J. Troughton, N. Gasparini, C. Zhou, Y. Lin, D.-J. Xue, B. Chen, A. K. Johnston, N. Wei, M. N. Hedhili, M. Wei, A. Y. Alsalloum, P. Maity, B. Turedi, C. Yang, D. Baran, T. D. Anthopoulos, Y. Han, Z.-H. Lu, O. F. Mohammed, F. Gao, E. H. Sargent, and O. M. Bakr, *Managing grains and interfaces via ligand anchoring enables 22.3%-efficiency inverted perovskite solar cells*, Nature Energy **5**, 131 (2020).

[46] D. V. Talapin and C. B. Murray, *PbSe Nanocrystal Solids for n- and p-Channel Thin Film Field-Effect Transistors*, Science **310**, 86 (2005).

[47] C. R. Kagan, E. Lifshitz, E. H. Sargent, and D. V. Talapin, *Building devices from colloidal quantum dots*, Science **353** (2016).

[48] L. N. Quan, B. P. Rand, R. H. Friend, S. G. Mhaisalkar, T.-W. Lee, and E. H. Sargent, *Perovskites for next-generation optical sources*, Chemical reviews **119**, 7444 (2019).

[49] J. Jagielski, S. F. Solari, L. Jordan, D. Scullion, B. Blülle, Y.-T. Li, F. Krumeich, Y.-C. Chiu, B. Ruhstaller, E. J. Santos, et al., *Scalable photonic sources using two-dimensional lead halide perovskite superlattices*, Nature communications **11**, 1 (2020).

[50] S. Morozov, E. L. Pensa, A. H. Khan, A. Polovitsyn, E. Cortés, S. A. Maier, S. Vezzoli, I. Moreels, and R. Sapienza, *Electrical control of single-photon emission in highly charged individual colloidal quantum dots*, Science advances **6**, eabb1821 (2020).

[51] R. K. Yadav, W. Liu, R. Li, T. W. Odom, G. S. Agarwal, and J. K. Basu, *Room-Temperature Coupling of Single Photon Emitting Quantum Dots to Localized and Delocalized Modes in a Plasmonic Nanocavity Array*, ACS Photonics (2021).

[52] A. I. Ekimov and A. A. Onushchenko, *Quantum size effect in three-dimensional microscopic semiconductor crystals*, Jetp Lett **34**, 345 (1981).

[53] A. Ekimov and A. Onushchenko, *Size quantization of the electron energy spectrum in a microscopic semiconductor crystal*, JETP lett **40**, 1136 (1984).

[54] A. I. Ekimov, A. L. Efros, and A. A. Onushchenko, *Quantum size effect in semiconductor microcrystals*, Solid State Communications **56**, 921 (1985).

[55] A. Ekimov, A. Onushchenko, and A. L. Efros, *Quantization of the energy spectrum of holes in the adiabatic potential of the electron*, JETP lett **43**, 376 (1986).

[56] R. Rossetti and L. Brus, *Electron-hole recombination emission as a probe of surface chemistry in aqueous cadmium sulfide colloids*, The Journal of Physical Chemistry **86**, 4470 (1982).

[57] R. Rossetti, S. Nakahara, and L. E. Brus, *Quantum size effects in the redox potentials, resonance Raman spectra, and electronic spectra of CdS crystallites in aqueous solution*, The Journal of Chemical Physics **79**, 1086 (1983).

[58] L. E. Brus, *A simple model for the ionization potential, electron affinity, and aqueous redox potentials of small semiconductor crystallites*, The Journal of chemical physics **79**, 5566 (1983).

[59] L. E. Brus, *Electron–electron and electron-hole interactions in small semiconductor crystallites: The size dependence of the lowest excited electronic state*, The Journal of chemical physics **80**, 4403 (1984).

[60] S. Liu, M. He, X. Di, P. Li, W. Xiang, and X. Liang, *Precipitation and tunable emission of cesium lead halide perovskites (CsPbX3, X= Br, I) QDs in borosilicate glass*, Ceramics International **44**, 4496 (2018).

[61] M. Nirmal, D. J. Norris, M. Kuno, M. G. Bawendi, A. L. Efros, and M. Rosen, *Observation of the "Dark Exciton" in CdSe Quantum Dots*, Physical Review Letters **75**, 3728 (1995).

[62] A. L. Efros, M. Rosen, M. Kuno, M. Nirmal, D. J. Norris, and M. Bawendi, *Band-edge exciton in quantum dots of semiconductors with a degenerate valence band: Dark and bright exciton states*, Physical Review B **54**, 4843 (1996).

[63] L. Chen, B. Li, C. Zhang, X. Huang, X. Wang, and M. Xiao, *Composition-dependent energy splitting between bright and dark excitons in lead halide perovskite nanocrystals*, Nano Letters **18**, 2074 (2018).

[64] D. Canneson, E. V. Shornikova, D. R. Yakovlev, T. Rogge, A. A. Mitioglu, M. V. Ballottin, P. C. Christianen, E. Lhuillier, M. Bayer, and L. Biadala, *Negatively charged and dark excitons in CsPbBr3 perovskite nanocrystals revealed by high magnetic fields*, Nano Letters **17**, 6177 (2017).

[65] P. Tamarat, M. I. Bodnarchuk, J.-B. Trebbia, R. Erni, M. V. Kovalenko, J. Even, and B. Lounis, *The ground exciton state of formamidinium lead bromide perovskite nanocrystals is a singlet dark state*, Nature Materials **18**, 717 (2019).

[66] E. Johnston-Halperin, D. D. Awschalom, S. A. Crooker, A. L. Efros, M. Rosen, X. Peng, and A. P. Alivisatos, *Spin spectroscopy of dark excitons in CdSe quantum dots to 60 T*, Physical Review B **63** (2001).

[67] M. Furis, J. A. Hollingsworth, V. I. Klimov, and S. A. Crooker, *Time-and polarization-resolved optical spectroscopy of colloidal CdSe nanocrystal quantum dots in high magnetic fields*, The Journal of Physical Chemistry B **109**, 15332 (2005).

[68] F. J. P. Wijnen, J. H. Blokland, P. T. K. Chin, P. C. M. Christianen, and J. C. Maan, *Competition between zero-phonon and phonon-assisted luminescence in colloidal CdSe quantum dots*, Physical Review B **78** (2008).

[69] L. Turyanska, J. H. Blokland, U. Elfurawi, O. Makarovsky, P. C. M. Christianen, and A. Patanè, *Photoluminescence of PbS nanocrystals at high magnetic fields up to 30 T*, Physical Review B **82** (2010).

[70] L. Biadala, Y. Louyer, P. Tamarat, and B. Lounis, *Band-Edge Exciton Fine Structure of Single CdSe/ZnS Nanocrystals in External Magnetic Fields*, Physical Review Letters **105** (2010).

[71] M. J. Fernée, C. Sinito, P. Tamarat, and B. Lounis, *State selective pumping reveals spin-relaxation pathways in CdSe quantum dots*, Nano letters **14**, 4480 (2014).

[72] M. Fu, P. Tamarat, H. Huang, J. Even, A. L. Rogach, and B. Lounis, *Neutral and charged exciton fine structure in single lead halide perovskite nanocrystals revealed by magneto-optical spectroscopy*, Nano Letters **17**, 2895 (2017).

[73] M. Isarov, L. Z. Tan, M. I. Bodnarchuk, M. V. Kovalenko, A. M. Rappe, and E. Lifshitz, *Rashba effect in a single colloidal CsPbBr3 perovskite nanocrystal detected by magneto-optical measurements*, Nano Letters **17**, 5020 (2017).

[74] J. Ramade, L. M. Andriambariarijaona, V. Steinmetz, N. Goubet, L. Legrand, T. Barisien, F. Bernardot, C. Testelin, E. Lhuillier, A. Bramati, et al., *Fine structure of excitons and electron–hole exchange energy in polymorphic CsPbBr 3 single nanocrystals*, Nanoscale **10**, 6393 (2018).

[75] M. Furis, H. Htoon, M. A. Petruska, V. I. Klimov, T. Barrick, and S. A. Crooker, *Bright-exciton fine structure and anisotropic exchange in CdSe nanocrystal quantum dots*, Physical Review B **73** (2006).

[76] H. Htoon, S. A. Crooker, M. Furis, S. Jeong, A. L. Efros, and V. I. Klimov, *Anomalous Circular Polarization of Photoluminescence Spectra of Individual CdSe Nanocrystals in an Applied Magnetic Field*, Physical Review Letters **102** (2009).

[77] J. A. Gupta, D. D. Awschalom, A. L. Efros, and A. V. Rodina, *Spin dynamics in semiconductor nanocrystals*, Physical Review B **66** (2002).

[78] R. Hu, D. R. Yakovlev, P. Liang, G. Qiang, C. Chen, T. Jia, Z. Sun, M. Bayer, and D. Feng, *Origin of two Larmor frequencies in the coherent spin dynamics of colloidal CdSe quantum dots revealed by controlled charging*, The journal of physical chemistry letters **10**, 3681 (2019).

[79] Y. You, X.-X. Zhang, T. C. Berkelbach, M. S. Hybertsen, D. R. Reichman, and T. F. Heinz, *Observation of biexcitons in monolayer WSe 2*, Nature Physics **11**, 477 (2015).

[80] A. L. Efros and M. Rosen, *The electronic structure of semiconductor nanocrystals*, Annual Review of Materials Science **30**, 475 (2000).

[81] A. L. Efros and A. L. Efros, *Interband absorption of light in a semiconductor sphere*, Sov. Phys. Semicond. **16**, 772 (1982).

[82] L. Banyai and S. W. Koch, *Semiconductor quantum dots*, vol. 2, World Scientific (1993).

[83] A. L. Efros and M. Rosen, *The electronic structure of semiconductor nanocrystals*, Annual Review of Materials Science **30**, 475 (2000).

[84] L. Keldysh, *Excitons in semiconductor–dielectric nanostructures*, physica status solidi (a) **164**, 3 (1997).

[85] A. V. Rodina and A. L. Efros, *Effect of dielectric confinement on optical properties of colloidal nanostructures*, Journal of Experimental and Theoretical Physics **122**, 554 (2016).

[86] D. Kovalev, M. B. Chorin, J. Diener, F. Koch, A. L. Efros, M. Rosen, N. Gippius, and S. Tikhodeev, *Porous Si anisotropy from photoluminescence polarization*, Applied physics letters **67**, 1585 (1995).

[87] E. A. Muljarov, E. Zhukov, V. Dneprovskii, and Y. Masumoto, *Dielectrically enhanced excitons in semiconductor-insulator quantum wires: Theory and experiment*, Physical Review B **62**, 7420 (2000).

[88] A. Shabaev and A. L. Efros, *1D exciton spectroscopy of semiconductor nanorods*, Nano letters **4**, 1821 (2004).

[89] A. W. Achtstein, A. Schliwa, A. Prudnikau, M. Hardzei, M. V. Artemyev, C. Thomsen, and U. Woggon, *Electronic structure and exciton–phonon interaction in two-dimensional colloidal CdSe nanosheets*, Nano letters **12**, 3151 (2012).

[90] C. Kittel, P. McEuen, and P. McEuen, *Introduction to solid state physics*, vol. 8, Wiley New York (1996).

[91] A. K. Arora, M. Rajalakshmi, and T. Ravindran, *Phonon confinement in nanostructured materials*, in *Encyclopedia of Nanoscience and Nanotechnology*, vol. 8, pp. 499–512, American Scientific Publishers (2004).

[92] H. Lamb, *On the vibrations of an elastic sphere*, Proceedings of the London Mathematical Society **1**, 189 (1881).

[93] S. Okamoto and Y. Masumoto, *Observation of confined acoustic phonons in semiconductor nanocrystals by means of the persistent spectral hole-burning spectroscopy*, Journal of luminescence **64**, 253 (1995).

[94] M. Ikezawa and Y. Masumoto, *Ultranarrow homogeneous broadening of confined excitons in quantum dots: Effect of the surrounding matrix*, Physical Review B **61**, 12662 (2000).

[95] K. Takemoto, B.-R. Hyun, M. Furuya, M. Ikezawa, J. Zhao, and Y. Masumoto, *Universal dephasing mechanism in semiconductor quantum dots embedded in a matrix*, Journal of the Physical Society of Japan **72**, 249 (2003).

[96] K. J. Schnitzenbaumer and G. Dukovic, *Comparison of phonon damping behavior in quantum dots capped with organic and inorganic ligands*, Nano letters **18**, 3667 (2018).

[97] L. Saviot, B. Champagnon, E. Duval, I. Kudriavtsev, and A. Ekimov, *Size dependence of acoustic and optical vibrational modes of CdSe nanocrystals in glasses*, Journal of Non-Crystalline Solids **197**, 238 (1996).

[98] U. Woggon, F. Gindele, O. Wind, and C. Klingshirn, *Exchange interaction and phonon confinement in CdSe quantum dots*, Physical Review B **54**, 1506 (1996).

[99] D. C. Hannah, N. J. Dunn, S. Ithurria, D. V. Talapin, L. X. Chen, M. Pelton, G. C. Schatz, and R. D. Schaller, *Observation of size-dependent thermalization in CdSe nanocrystals using time-resolved photoluminescence spectroscopy*, Physical review letters **107**, 177403 (2011).

[100] P. C. Sercel and A. L. Efros, *Band-Edge Exciton in CdSe and Other II–VI and III–V Compound Semiconductor Nanocrystals- Revisited*, Nano letters **18**, 4061 (2018).

[101] P. C. Sercel, J. L. Lyons, D. Wickramaratne, R. Vaxenburg, N. Bernstein, and A. L. Efros, *Exciton fine structure in perovskite nanocrystals*, Nano letters **19**, 4068 (2019).

[102] M. A. Becker, R. Vaxenburg, G. Nedelcu, P. C. Sercel, A. Shabaev, M. J. Mehl, J. G. Michopoulos, S. G. Lambrakos, N. Bernstein, J. L. Lyons, T. Stöferle, R. F. Mahrt, M. V. Kovalenko, D. J. Norris, G. Rainò, and A. L. Efros, *Bright triplet excitons in caesium lead halide perovskites*, Nature **553**, 189 (2018).

[103] K. Cho, *Unified theory of symmetry-breaking effects on excitons in cubic and wurtzite structures*, Physical Review B **14**, 4463 (1976).

[104] S. Goupalov and E. Ivchenko, *A tight-binding representation of electron-hole exchange interaction in semiconductors*, Physics of the Solid State **43**, 1867 (2001).

[105] T. Takagahara, *Effects of dielectric confinement and electron-hole exchange interaction on excitonic states in semiconductor quantum dots*, Physical Review B **47**, 4569 (1993).

[106] A. I. Ekimov, I. A. Kudryavtsev, A. L. Efros, T. V. Yazeva, F. Hache, M. C. Schanne-Klein, A. V. Rodina, D. Ricard, and C. Flytzanis, *Absorption and intensity-dependent photoluminescence measurements on CdSe quantum dots: assignment of the first electronic transitions*, Journal of the Optical Society of America B **10**, 100 (1993).

[107] T. Richard, P. Lefebvre, H. Mathieu, and J. Allégre, *Effects of finite spin-orbit splitting on optical properties of spherical semiconductor quantum dots*, Physical Review B **53**, 7287 (1996).

[108] O. Labeau, P. Tamarat, and B. Lounis, *Temperature Dependence of the Luminescence Lifetime of Single CdSe/ZnS Quantum Dots*, Physical Review Letters **90** (2003).

[109] E. V. Shornikova, L. Biadala, D. R. Yakovlev, V. F. Sapega, Y. G. Kusrayev, A. A. Mitioglu, M. V. Ballottin, P. C. Christianen, V. V. Belykh, M. V. Kochiev, et al., *Addressing the exciton fine structure in colloidal nanocrystals: the case of CdSe nanoplatelets*, Nanoscale **10**, 646 (2018).

[110] K. Xu, J. F. Vliem, and A. Meijerink, *Long-lived dark exciton emission in Mn-doped CsPbCl3 perovskite nanocrystals*, The Journal of Physical Chemistry C **123**, 979 (2019).

[111] D. Rossi, X. Liu, Y. Lee, M. Khurana, J. Puthenpurayil, K. Kim, A. V. Akimov, J. Cheon, and D. H. Son, *Intense Dark Exciton Emission from Strongly Quantum-Confined CsPbBr3 Nanocrystals*, Nano Letters **20**, 7321 (2020).

[112] J. A. Steele, H. Jin, I. Dovgaliuk, R. F. Berger, T. Braeckevelt, H. Yuan, C. Martin, E. Solano, K. Lejaeghere, S. M. Rogge, et al., *Thermal unequilibrium of strained black CsPbI3 thin films*, Science **365**, 679 (2019).

[113] A. Koliogiorgos, C. S. Garoufalis, I. Galanakis, and S. Baskoutas, *Electronic and Optical Properties of Ultrasmall ABX3 (A= Cs, CH3NH3/B= Ge, Pb, Sn, Ca, Sr/X= Cl, Br, I) Perovskite Quantum Dots*, ACS omega **3**, 18917 (2018).

[114] C. C. Stoumpos and M. G. Kanatzidis, *The renaissance of halide perovskites and their evolution as emerging semiconductors*, Accounts of chemical research **48**, 2791 (2015).

[115] C. C. Stoumpos, C. D. Malliakas, J. A. Peters, Z. Liu, M. Sebastian, J. Im, T. C. Chasapis, A. C. Wibowo, D. Y. Chung, A. J. Freeman, et al., *Crystal growth of the perovskite semiconductor CsPbBr3: a new material for high-energy radiation detection*, Crystal growth & design **13**, 2722 (2013).

[116] A. Swarnkar, A. R. Marshall, E. M. Sanehira, B. D. Chernomordik, D. T. Moore, J. A. Christians, T. Chakrabarti, and J. M. Luther, *Quantum dot–induced phase stabilization of α-CsPbI3 perovskite for high-efficiency photovoltaics*, Science **354**, 92 (2016).

[117] B. Zhao, S.-F. Jin, S. Huang, N. Liu, J.-Y. Ma, D.-J. Xue, Q. Han, J. Ding, Q.-Q. Ge, Y. Feng, et al., *Thermodynamically stable orthorhombic γ-CsPbI3 thin films for high-performance photovoltaics*, Journal of the American Chemical Society **140**, 11716 (2018).

[118] S. B. Todd, D. B. Riley, A. Binai-Motlagh, C. Clegg, A. Ramachandran, S. A. March, J. M. Hoffman, I. G. Hill, C. C. Stoumpos, M. G. Kanatzidis, et al., *Detection of Rashba spin splitting in 2D organic-inorganic perovskite via precessional carrier spin relaxation*, APL Materials **7**, 081116 (2019).

[119] Y. D. Glinka, R. Cai, J. Li, T. He, and X. W. Sun, *Observing dynamic and static Rashba effects in a thin layer of 3D hybrid perovskite nanocrystals using transient absorption spectroscopy*, AIP Advances **10**, 105034 (2020).

[120] H. Choi, Y. H. Shin, C. S. Park, Y. Kim, D. Park, M. S. Jeong, H. Nojiri, Z. Yang, and Y. Kohama, *Combination of Optical Transitions of Polarons with Rashba Effect in MAPbX3 (X= I, Br, and Cl) Under High Magnetic Fields*, arXiv preprint arXiv:2101.07418 (2021).

[121] A. Sahu, M. S. Kang, A. Kompch, C. Notthoff, A. W. Wills, D. Deng, M. Winterer, C. D. Frisbie, and D. J. Norris, *Electronic impurity doping in CdSe nanocrystals*, Nano letters **12**, 2587 (2012).

[122] P. C. Sercel, A. Shabaev, and A. L. Efros, *Photoluminescence enhancement through symmetry breaking induced by defects in nanocrystals*, Nano letters **17**, 4820 (2017).

[123] L. Biadala, Y. Louyer, P. Tamarat, and B. Lounis, *Direct Observation of the Two Lowest Exciton Zero-Phonon Lines in Single CdSe / ZnS Nanocrystals*, Physical Review Letters **103** (2009).

[124] A. Rodina and A. L. Efros, *Magnetic Properties of Nonmagnetic Nanostructures: Dangling Bond Magnetic Polaron in CdSe Nanocrystals*, Nano. Lett. **15**, 4214 (2015).

[125] L. Biadala, E. V. Shornikova, A. V. Rodina, D. R. Yakovlev, B. Siebers, T. Aubert, M. Nasilowski, Z. Hens, B. Dubertret, A. L. Efros, and M. Bayer,

Magnetic polaron on dangling-bond spins in CdSe colloidal nanocrystals, Nature Nanotechnology **12**, 569 (2017).

[126] A. Brodu, M. D. Tessier, D. Canneson, D. Dupont, M. V. Ballottin, P. C. Christianen, C. de Mello Donega, Z. Hens, D. R. Yakovlev, M. Bayer, et al., *Hyperfine Interactions and Slow Spin Dynamics in Quasi-isotropic InP-based Core/Shell Colloidal Nanocrystals*, ACS nano **13**, 10201 (2019).

[127] L. Biadala, F. Liu, M. D. Tessier, D. R. Yakovlev, B. Dubertret, and M. Bayer, *Recombination dynamics of band edge excitons in quasi-two-dimensional CdSe nanoplatelets*, Nano letters **14**, 1134 (2014).

[128] G. Qiang, A. A. Golovatenko, E. V. Shornikova, D. R. Yakovlev, A. V. Rodina, E. A. Zhukov, I. V. Kalitukha, V. F. Sapega, V. K. Kaibyshev, M. A. Prosnikov, P. C. M. Christianen, A. A. Onushchenko, and M. Bayer, *Polarized emission of CdSe nanocrystals in magnetic field: the role of phonon-assisted recombination of the dark exciton*, Nanoscale (2021).

[129] L. Biadala, B. Siebers, Y. Beyazit, M. D. Tessier, D. Dupont, Z. Hens, D. R. Yakovlev, and M. Bayer, *Band-edge exciton fine structure and recombination dynamics in InP/ZnS colloidal nanocrystals*, ACS nano **10**, 3356 (2016).

[130] M. Fu, P. Tamarat, J.-B. Trebbia, M. I. Bodnarchuk, M. V. Kovalenko, J. Even, and B. Lounis, *Unraveling exciton-phonon coupling in individual FAPbI3 nanocrystals emitting near-infrared single photons*, Nature Communications **9** (2018).

[131] M. Bawendi, W. Wilson, L. Rothberg, P. Carroll, T. M. Jedju, M. Steigerwald, and L. Brus, *Electronic structure and photoexcited-carrier dynamics in nanometer-size CdSe clusters*, Physical Review Letters **65**, 1623 (1990).

[132] A. V. Rodina and A. L. Efros, *Radiative recombination from dark excitons in nanocrystals: Activation mechanisms and polarization properties*, Physical Review B **93** (2016).

[133] F. Liu, A. V. Rodina, D. R. Yakovlev, A. A. Golovatenko, A. Greilich, E. D. Vakhtin, A. Susha, A. L. Rogach, Y. G. Kusrayev, and M. Bayer, *Förster energy transfer of dark excitons enhanced by a magnetic field in an ensemble of CdTe colloidal nanocrystals*, Physical Review B **92** (2015).

[134] D. Feng, D. R. Yakovlev, V. V. Pavlov, A. V. Rodina, E. V. Shornikova, J. Mund, and M. Bayer, *Dynamic evolution from negative to positive photocharging in colloidal CdS quantum dots*, Nano Letters **17**, 2844 (2017).

[135] D. Kudlacik, *Characterization of semiconductor nanostructures by spin-flip Raman spectroscopy*, Ph.D. thesis, Universitätsbibliothek Dortmund (2018).

[136] D. Thomas and J. Hopfield, *Spin-flip Raman scattering in cadmium sulfide*, Physical Review **175**, 1021 (1968).

[137] J. Scott and T. Damen, *Anomalous double spin-flip Raman scattering in CdS, and a visible spin-flip laser*, Physical Review Letters **29**, 107 (1972).

[138] V. Sapega, M. Cardona, K. Ploog, E. Ivchenko, and D. Mirlin, *Spin-flip Raman scattering in GaAs/Al x Ga 1- x As multiple quantum wells*, Physical Review B **45**, 4320 (1992).

[139] A. Sirenko, T. Ruf, M. Cardona, D. Yakovlev, W. Ossau, A. Waag, and G. Landwehr, *Electron and hole g factors measured by spin-flip Raman scattering in CdTe/Cd1-xMgxTe single quantum wells*, Physical Review B **56**, 2114 (1997).

[140] J. Debus, D. Dunker, V. Sapega, D. Yakovlev, G. Karczewski, T. Wojtowicz, J. Kossut, and M. Bayer, *Spin-flip Raman scattering of the neutral and charged excitons confined in a CdTe/(Cd, Mg) Te quantum well*, Physical Review B **87**, 205316 (2013).

[141] J. Debus, V. Sapega, D. Dunker, D. Yakovlev, D. Reuter, A. Wieck, and M. Bayer, *Spin-flip Raman scattering of the resident electron in singly charged (In, Ga) As/GaAs quantum dot ensembles*, Physical Review B **90**, 235404 (2014).

[142] J. Debus, T. Shamirzaev, D. Dunker, V. Sapega, E. Ivchenko, D. Yakovlev, A. Toropov, and M. Bayer, *Spin-flip Raman scattering of the* Γ*- X mixed exciton in indirect band gap (In, Al) As/AlAs quantum dots*, Physical Review B **90**, 125431 (2014).

[143] D. Kudlacik, V. F. Sapega, D. R. Yakovlev, I. V. Kalitukha, E. V. Shornikova, A. V. Rodina, E. L. Ivchenko, G. S. Dimitriev, M. Nasilowski, B. Dubertret, et al., *Single and double electron spin-flip Raman scattering in CdSe colloidal nanoplatelets*, Nano Letters **20**, 517 (2019).

[144] A. Sirenko, V. Belitsky, T. Ruf, M. Cardona, A. Ekimov, and C. Trallero-Giner, *Spin-flip and acoustic-phonon Raman scattering in CdS nanocrystals*, Physical Review B **58**, 2077 (1998).

[145] K. Tanaka, T. Takahashi, T. Ban, T. Kondo, K. Uchida, and N. Miura, *Comparative study on the excitons in lead-halide-based perovskite-type crystals CH3NH3PbBr3 CH3NH3PbI3*, Solid state communications **127**, 619 (2003).

[146] V. Golubkov, P. Onushchenko, and A. Onushchenko, *The kinetics of the formation of CdSe nanocrystals in sodium-zinc-silica glass*, Glass Physics and Chemistry **40**, 291 (2014).

[147] A. Guinier, *Diffraction of X-rays of very small angles-application of ultramicroscopic phenomenon*, Ann. Phys. **12**, 161 (1939).

[148] F. Liu, A. V. Rodina, D. R. Yakovlev, A. Greilich, A. A. Golovatenko, A. S. Susha, A. L. Rogach, Y. G. Kusrayev, and M. Bayer, *Exciton spin dynamics of colloidal CdTe nanocrystals in magnetic fields*, Physical Review B **89** (2014).

[149] D. J. Norris and M. G. Bawendi, *Measurement and assignment of the size-dependent optical spectrum in CdSe quantum dots*, Physical Review B **53**, 16338 (1996).

[150] F. Liu, L. Biadala, A. V. Rodina, D. R. Yakovlev, D. Dunker, C. Javaux, J.-P. Hermier, A. L. Efros, B. Dubertret, and M. Bayer, *Spin dynamics of negatively charged excitons in CdSe/CdS colloidal nanocrystals*, Physical Review B **88** (2013).

[151] E. V. Shornikova, D. R. Yakovlev, L. Biadala, S. A. Crooker, V. V. Belykh, M. V. Kochiev, A. Kuntzmann, M. Nasilowski, B. Dubertret, and M. Bayer, *Negatively charged excitons in CdSe nanoplatelets*, Nano Letters **20**, 1370 (2020).

[152] E. V. Shornikova, A. A. Golovatenko, D. R. Yakovlev, A. V. Rodina, L. Biadala, G. Qiang, A. Kuntzmann, M. Nasilowski, B. Dubertret, A. Polovitsyn, I. Moreels, and M. Bayer, *Surface spin magnetism controls the polarized exciton emission from CdSe nanoplatelets*, Nature Nanotechnology **15**, 277 (2020).

[153] M. Chamarro, C. Gourdon, P. Lavallard, O. Lublinskaya, and A. I. Ekimov, *Enhancement of electron-hole exchange interaction in CdSe nanocrystals: A quantum confinement effect*, Physical Review B **53**, 1336 (1996).

[154] A. V. Rodina, A. A. Golovatenko, E. V. Shornikova, and D. R. Yakovlev, *Spin Physics of Excitons in Colloidal Nanocrystals*, Physics of the Solid State **60**, 1537 (2018).

[155] S. V. Goupalov and E. L. Ivchenko, *The fine structure of excitonic levels in CdSe nanocrystals*, Physics of the Solid State **42**, 2030 (2000).

[156] D. Oron, A. Aharoni, C. de Mello Donega, J. Van Rijssel, A. Meijerink, and U. Banin, *Universal role of discrete acoustic phonons in the low-temperature optical emission of colloidal quantum dots*, Physical review letters **102**, 177402 (2009).

[157] A. Tadjine, Y.-M. Niquet, and C. Delerue, *Universal behavior of electron g-factors in semiconductor nanostructures*, Physical Review B **95** (2017).

[158] M. J. Fernee, B. N. Littleton, S. Cooper, H. Rubinsztein-Dunlop, D. E. Gomez, and P. Mulvaney, *Acoustic phonon contributions to the emission spectrum of single CdSe nanocrystals*, The Journal of Physical Chemistry C **112**, 1878 (2008).

[159] S. A. Empedocles, R. Neuhauser, K. Shimizu, and M. G. Bawendi, *Photoluminescence from single semiconductor nanostructures*, Advanced Materials **11**, 1243 (1999).

[160] K. Leung, S. Pokrant, and K. B. Whaley, *Exciton fine structure in CdSe nanoclusters*, Physical Review B **57**, 12291 (1998).

[161] M. Califano, A. Franceschetti, and A. Zunger, *Temperature dependence of excitonic radiative decay in CdSe quantum dots: the role of surface hole traps*, Nano Letters **5**, 2360 (2005).

[162] J. A. Gupta, D. D. Awschalom, X. Peng, and A. P. Alivisatos, *Spin coherence in semiconductor quantum dots*, Physical Review B **59**, R10421 (1999).

[163] Z. Zhang, Z. Jin, H. Ma, Y. Xu, X. Lin, G. Ma, and X. Sun, *Room-temperature spin coherence in zinc blende CdSe quantum dots studied by time-resolved Faraday ellipticity*, Physica E: Low-dimensional Systems and Nanostructures **56**, 85 (2014).

[164] R. Hu, Z. Wu, Y. Zhang, D. R. Yakovlev, P. Liang, G. Qiang, J. Guo, T. Jia, Z. Sun, M. Bayer, et al., *Long-lived negative photocharging in colloidal CdSe quantum dots revealed by coherent electron spin precession*, The Journal of Physical Chemistry Letters **10**, 4994 (2019).

[165] N. P. Stern, M. Poggio, M. H. Bartl, E. L. Hu, G. D. Stucky, and D. D. Awschalom, *Spin dynamics in electrochemically charged CdSe quantum dots*, Physical Review B **72** (2005).

[166] Z. Wu, Y. Zhang, R. Hu, M. Jiang, P. Liang, Q. Yang, L. Deng, T. Jia, Z. Sun, and D. Feng, *Hole-Acceptor-Manipulated Electron Spin Dynamics in CdSe Colloidal Quantum Dots*, The Journal of Physical Chemistry Letters **12**, 2126 (2021).

[167] P. Chen and K. B. Whaley, *Magneto-optical response of CdSe nanostructures*, Physical Review B **70**, 045311 (2004).

[168] A. L. Efros, *Fine structure and polarization properties of band-edge excitons in semiconductor nanocrystals*, Nanocrystal Quantum Dots p. 97 (2010).

[169] S. V. Goupalov, *Anisotropy-induced exchange splitting of exciton radiative doublet in CdSe nanocrystals*, Physical Review B **74** (2006).

[170] X. Li, D. Feng, H. Tong, T. Jia, L. Deng, Z. Sun, and Z. Xu, *Hole surface trapping dynamics directly monitored by electron spin manipulation in CdS nanocrystals*, The journal of physical chemistry letters **5**, 4310 (2014).

[171] S. Crooker, D. Awschalom, J. Baumberg, F. Flack, and N. Samarth, *Optical spin resonance and transverse spin relaxation in magnetic semiconductor quantum wells*, Physical Review B **56**, 7574 (1997).

[172] A. Tartakovskii, M. Makhonin, J. Cahill, D. Whittaker, J. R. Wells, A. Fox, D. Mowbray, M. Skolnick, M. Steer, K. Groom, et al., *Precise measurement of the fraction of charged dots in self-assembled quantum dot ensembles using ultrafast pump-probe techniques*, Applied physics letters **85**, 2226 (2004).

[173] V. I. Klimov, *Semiconductor and metal nanocrystals: synthesis and electronic and optical properties*, CRC Press (2003).

[174] M. Semina, A. Golovatenko, and A. Rodina, *Electron, hole and exciton effective g-factors in semiconductor nanocrystals*, arXiv preprint arXiv:2011.11041 (2020).

[175] M. Combescot and O. Betbeder-Matibet, *Faraday rotation in photoexcited semiconductors: A composite-exciton many-body effect*, Physical Review B **74**, 125316 (2006).

[176] M. Dyakonov, X. Marie, T. Amand, P. Le Jeune, D. Robart, M. Brousseau, and J. Barrau, *Coherent spin dynamics of excitons in quantum wells*, Physical Review B **56**, 10412 (1997).

[177] M. Cardona, *Optical Properties of the Silver and Cuprous Halides*, Phys. Rev **129**, 69 (1963).

[178] M. Khan, *g-Factor and effective mass of electrons in the conduction and the valence bands of CuCl*, Journal of Physics and Chemistry of Solids **31**, 2309 (1970).

[179] A. Goltzene and C. Schwab, *Electron Spin Resonance of Shallow Level Carriers in CuCl*, physica status solidi (b) **71**, K67 (1975).

[180] M. Certier, C. Wecker, and S. Nikitine, *Zeeman effect on the excitonic reflection spectrum of CuCl at very low temperatures*, Physics Letters A **28**, 307 (1968).

[181] W. Staude, *Magneto-Reflectivity Measurements on Exciton Bands in CuCl*, physica status solidi (b) **43**, 367 (1971).

[182] S. Suga, T. Koda, and T. Mitani, *Faraday rotation and the effective g-values of excitons in cuprous halides*, physica status solidi (b) **48**, 753 (1971).

[183] D. Fröhlich, H. Hölscher, and A. Nöthe, *Two-photon magnetoabsorption of exciton polariton in CuCl*, Solid state communications **48**, 217 (1983).

[184] T. Ando, M. Hasuo, and N. Nagasawa, *Magnetic field induced triplet exciton polariton in CuCl*, physica status solidi (b) **179**, 453 (1993).

[185] T. Itoh, Y. Iwabuchi, and M. Kataoka, *Study on the Size and Shape of CuCl Microcrystals Embedded in Alkali-Chloride Matrices and Their Correlation with Exciton Confinement*, physica status solidi (b) **145**, 567 (1988).

[186] S. Nomura, K. Misawa, Y. Segawa, and T. Kobayashi, *Large ¡i¿g¡/i¿ value in CuCl semiconductor microcrystallites*, Physical Review B **47**, 16024 (1993).

[187] M. Ueta, H. Kanzaki, K. Kobayashi, Y. Toyozawa, and E. Hanamura, *Excitonic processes in solids*, vol. 60, Springer Science & Business Media (2012).

[188] S.-H. Wei and A. Zunger, *Role of metal d states in II-VI semiconductors*, Physical Review B **37**, 8958 (1988).

[189] T. Koda, T. Mitani, and T. Murahashi, *Anomalous Exciton Spectra in Uniaxially Deformed CuCl: Experimental Evidence for the Effect of the Stress-Induced k-Linear Term*, Physical Review Letters **25**, 1495 (1970).

[190] A.Glodmann, *Band structure and optical properties of Tetrahedally coordinated Cu- and Ag-Halides*, physica status solidi (b) **81**, 9 (1977).

[191] T. Koda, T. Murahashi, T. Mitani, S. Sakoda, and Y. Onodera, *Effects of uniaxial stress on excitons in CuCl*, Physical Review B **5**, 705 (1972).

[192] D. K. Shuh, R. S. Williams, Y. Segawa, J. ichi Kusano, Y. Aoyagi, and S. Namba, *Line-shape and lifetime studies of exciton luminescence from confined CuCl thin films*, Physical Review B **44**, 5827 (1991).

[193] S. Yano, T. Goto, T. Itoh, and A. Kasuya, *Dynamics of excitons and biexcitons in CuCl nanocrystals embedded in NaCl at 2 K*, Physical Review B **55**, 1667 (1997).

[194] M. Nakayama, H. Ichida, and H. Nishimura, *Bound-biexciton photoluminescence in CuCl thin films grown by vacuum deposition*, Journal of Physics: Condensed Matter **11**, 7653 (1999).

[195] A. Mitra, L. O'Reilly, O. Lucas, G. Natarajan, D. Danieluk, A. Bradley, P. McNally, S. Daniels, D. Cameron, A. Reader, and M. Martinez-Rosas, *Optical properties of CuCl films on silicon substrates*, physica status solidi (b) **245**, 2808 (2008).

[196] M. Certier, C. Wecker, and S. Nikitine, *Zeeman effect of free and bound excitons in CuCl*, Journal of Physics and Chemistry of Solids **30**, 2135 (1969).

[197] M. Sebastian, J. Peters, C. Stoumpos, J. Im, S. Kostina, Z. Liu, M. G. Kanatzidis, A. J. Freeman, and B. Wessels, *Excitonic emissions and above-band-gap luminescence in the single-crystal perovskite semiconductors CsPbB r 3 and CsPbC l 3*, Physical Review B **92**, 235210 (2015).

[198] D. J. Norris, A. L. Efros, M. Rosen, and M. G. Bawendi, *Size dependence of exciton fine structure in CdSe quantum dots*, Physical Review B **53**, 16347 (1996).

[199] C. Zhang, T. N. Do, X. Ong, Y. Chan, and H.-S. Tan, *Understanding the features in the ultrafast transient absorption spectra of CdSe quantum dots*, Chemical Physics **481**, 157 (2016).

[200] V. Babin, P. Fabeni, M. Nikl, G. Pazzi, I. Sildos, N. Zazubovich, and S. Zazubovich, *Polarized luminescence of CsPbBr3 nanocrystals (quantum dots) in CsBr: Pb single crystal*, Chemical physics letters **314**, 31 (1999).

[201] Y. P. Varshni, *Temperature dependence of the energy gap in semiconductors*, physica **34**, 149 (1967).

[202] W. Shan, J. Song, H. Luo, and J. Furdyna, *Determination of the fundamental and split-off band gaps in zinc-blende CdSe by photomodulation spectroscopy*, Physical Review B **50**, 8012 (1994).

[203] K. P. O'Donnell and X. Chen, *Temperature dependence of semiconductor band gaps*, Applied Physics Letters **58**, 2924 (1991).

[204] R. Aceves, V. Babin, M. B. Flores, P. Fabeni, A. Maaroos, M. Nikl, K. Nitsch, G. Pazzi, R. P. Salas, I. Sildos, N. Zazubovich, and S. Zazubovich, *Spectroscopy of CsPbBr3 quantum dots in CsBr: Pb crystals*, Journal of luminescence **93**, 27 (2001).

[205] C. Yu, Z. Chen, J. J. Wang, W. Pfenninger, N. Vockic, J. T. Kenney, and K. Shum, *Temperature dependence of the band gap of perovskite semiconductor compound CsSnI3*, Journal of Applied Physics **110**, 063526 (2011).

[206] A. Shinde, R. Gahlaut, and S. Mahamuni, *Low-temperature photoluminescence studies of CsPbBr3 quantum dots*, The Journal of Physical Chemistry C **121**, 14872 (2017).

[207] B. Wu, H. Yuan, Q. Xu, J. A. Steele, D. Giovanni, P. Puech, J. Fu, Y. F. Ng, N. F. Jamaludin, A. Solanki, S. Mhaisalkar, N. Mathews, M. B. Roeffaers, M. Grätzel, J. Hofkens, and T. C. Sum, *Indirect tail states formation by thermal-induced polar fluctuations in halide perovskites*, Nature communications **10**, 1 (2019).

[208] M. I. Dar, G. Jacopin, S. Meloni, A. Mattoni, N. Arora, A. Boziki, S. M. Zakeeruddin, U. Rothlisberger, and M. Grätzel, *Origin of unusual bandgap shift and dual emission in organic-inorganic lead halide perovskites*, Science advances **2**, e1601156 (2016).

[209] A. Göbel, T. Ruf, M. Cardona, C. T. Lin, J. Wrzesinski, M. Steube, K. Reimann, J.-C. Merle, and M. Joucla, *Effects of the isotopic composition on the fundamental gap of CuCl*, Physical Review B **57**, 15183 (1998).

[210] H. J. Lian, A. Yang, M. L. W. Thewalt, R. Lauck, and M. Cardona, *Effects of sulfur isotopic composition on the band gap of PbS*, Physical Review B **73**, 233202 (2006).

[211] M. Khan, *The Debye-Waller effect on the forbidden gap in cuprous halides*, Philosophical Magazine B **42**, 565 (1980).

[212] A. L. Efros, D. J. Lockwood, and L. Tsybeskov, *Semiconductor Nanocrystals: From Basic Principles to Applications*, Springer Science & Business Media (2013).

[213] S. V. Nair, J. Usukura, and E. Tokunaga, *Accurate modeling of electron-hole binding in CuCl. I. Exciton states*, Physical Review B **102**, 075202 (2020).

[214] G. Sato, T. Akatsu, and K. Miyajima, *Biexciton generation processes for CuCl quantum dot ensembles*, Materials Research Express **3**, 025002 (2016).

[215] T. Ikehara and T. Itoh, *Dynamical behavior of the exciton polariton in CuCl: Coherent propagation and momentum relaxation*, Physical Review B **44**, 9283 (1991).

[216] S. Park, I. Kim, K. Jang, S. Kim, C. Kim, Y. Yee, and G. Jeen, *Photoluminescence properties of CuCl quantum dots and the dependence of biexciton formation rates on quantum dot sizes*, Journal of the Physical Society of Japan **70**, 3723 (2001).

[217] M. Hasuo and N. Nagasawa, *Finding of the radiative decay channel of a biexciton leaving a Z1, 2-1s exciton behind in CuCl*, Journal of luminescence **66**, 410 (1995).

[218] H. L. Wells, *Über die Cäsium-und Kalium-Bleihalogenide*, Zeitschrift für anorganische Chemie **3**, 195 (1893).

[219] C. K. Møller, *Crystal structure and photoconductivity of caesium plumbohalides*, Nature **182**, 1436 (1958).

[220] D. Weber, *CH3NH3PbX3, ein Pb (II)-system mit kubischer perowskitstruktur/CH3NH3PbX3, a Pb (II)-system with cubic perovskite structure*, Zeitschrift für Naturforschung B **33**, 1443 (1978).

[221] Z. Cheng and J. Lin, *Layered organic–inorganic hybrid perovskites: structure, optical properties, film preparation, patterning and templating engineering*, CrystEngComm **12**, 2646 (2010).

[222] A. Kojima, K. Teshima, Y. Shirai, and T. Miyasaka, *Organometal halide perovskites as visible-light sensitizers for photovoltaic cells*, Journal of the American Chemical Society **131**, 6050 (2009).

[223] A. Liu, D. B. Almeida, L. G. Bonato, G. Nagamine, L. F. Zagonel, A. F. Nogueira, L. A. Padilha, and S. Cundiff, *Multidimensional coherent spectroscopy reveals triplet state coherences in cesium lead-halide perovskite nanocrystals*, Science Advances **7**, eabb3594 (2021).

[224] K. Wei, Z. Xu, R. Chen, X. Zheng, X. Cheng, and T. Jiang, *Temperature-dependent excitonic photoluminescence excited by two-photon absorption in perovskite CsPbBr 3 quantum dots*, Optics letters **41**, 3821 (2016).

[225] O. V. Kozlov, R. Singh, B. Ai, J. Zhang, C. Liu, and V. I. Klimov, *Transient Spectroscopy of Glass-Embedded Perovskite Quantum Dots: Novel Structures in an Old Wrapping*, arXiv preprint arXiv:1812.00968 (2018).

[226] G. Morello, M. De Giorgi, S. Kudera, L. Manna, R. Cingolani, and M. Anni, *Temperature and size dependence of nonradiative relaxation and exciton- phonon*

coupling in colloidal CdTe quantum dots, The Journal of Physical Chemistry C **111**, 5846 (2007).

[227] F. Hu, H. Zhang, C. Sun, C. Yin, B. Lv, C. Zhang, W. W. Yu, X. Wang, Y. Zhang, and M. Xiao, *Superior optical properties of perovskite nanocrystals as single photon emitters*, ACS nano **9**, 12410 (2015).

[228] M. Hirasawa, T. Ishihara, T. Goto, K. Uchida, and N. Miura, *Magnetoabsorption of the lowest exciton in perovskite-type compound (CH3NH3) PbI3*, Physica B: Condensed Matter **201**, 427 (1994).

[229] A. Swarnkar, R. Chulliyil, V. K. Ravi, M. Irfanullah, A. Chowdhury, and A. Nag, *Colloidal CsPbBr3 perovskite nanocrystals: luminescence beyond traditional quantum dots*, Angewandte Chemie **127**, 15644 (2015).

[230] Z. Yang, A. Surrente, K. Galkowski, A. Miyata, O. Portugall, R. Sutton, A. Haghighirad, H. Snaith, D. Maude, P. Plochocka, et al., *Impact of the halide cage on the electronic properties of fully inorganic cesium lead halide perovskites*, ACS Energy Letters **2**, 1621 (2017).

[231] H. Chung, S. I. Jung, H. J. Kim, W. Cha, E. Sim, D. Kim, W.-K. Koh, and J. Kim, *Composition-dependent hot carrier relaxation dynamics in cesium lead halide (CsPbX3, X= Br and I) perovskite nanocrystals*, Angewandte Chemie **129**, 4224 (2017).

[232] C. de Weerd, T. Gregorkiewicz, and L. Gomez, *All-Inorganic Perovskite Nanocrystals: Microscopy Insights in Structure and Optical Properties*, Advanced Optical Materials **6**, 1800289 (2018).

[233] J. Navarro-Arenas, I. Suárez, V. S. Chirvony, A. F. Gualdrón-Reyes, I. Mora-Seró, and J. Martínez-Pastor, *Single-Exciton Amplified Spontaneous Emission in Thin Films of CsPbX3 (X= Br, I) Perovskite Nanocrystals*, The journal of physical chemistry letters **10**, 6389 (2019).

[234] R. B. Aich, I. Saidi, S. B. Radhia, K. Boujdaria, T. Barisien, L. Legrand, F. Bernardot, M. Chamarro, and C. Testelin, *Bright-exciton splittings in inorganic cesium lead halide perovskite nanocrystals*, Physical Review Applied **11**, 034042 (2019).

[235] Y. Li, X. Luo, T. Ding, X. Lu, and K. Wu, *Size-and Halide-Dependent Auger Recombination in Lead Halide Perovskite Nanocrystals*, Angewandte Chemie International Edition **59**, 14292 (2020).

[236] M. C. Brennan, A. Forde, M. Zhukovskyi, A. J. Baublis, Y. V. Morozov, S. Zhang, Z. Zhang, D. S. Kilin, and M. K. Kuno, *Universal Size-Dependent Stokes Shifts in Lead Halide Perovskite Nanocrystals*, The Journal of Physical Chemistry Letters **11**, 4937 (2020).

[237] M. Zhou, J. S. Sarmiento, C. Fei, X. Zhang, and H. Wang, *Effect of Composition on the Spin Relaxation of Lead Halide Perovskites*, The Journal of Physical Chemistry Letters **11**, 1502 (2020).

[238] W. Zhao, R. Su, Y. Huang, J. Wu, C. F. Fong, J. Feng, and Q. Xiong, *Transient circular dichroism and exciton spin dynamics in all-inorganic halide perovskites*, Nature Communications **11** (2020).

[239] A. Liu, L. G. Bonato, F. Sessa, D. B. Almeida, E. Isele, G. Nagamine, L. F. Zagonel, A. F. Nogueira, L. A. Padilha, and S. T. Cundiff, *Effect of dimensionality on the optical absorption properties of CsPbI3 perovskite nanocrystals*, The Journal of chemical physics **151**, 191103 (2019).

[240] F. Hu, C. Yin, H. Zhang, C. Sun, W. W. Yu, C. Zhang, X. Wang, Y. Zhang, and M. Xiao, *Slow Auger recombination of charged excitons in nonblinking perovskite nanocrystals without spectral diffusion*, Nano letters **16**, 6425 (2016).

[241] P. Tamarat, L. Hou, J.-B. Trebbia, A. Swarnkar, L. Biadala, Y. Louyer, M. I. Bodnarchuk, M. V. Kovalenko, J. Even, and B. Lounis, *The dark exciton ground state promotes photon-pair emission in individual perovskite nanocrystals*, Nature Communications **11** (2020).

[242] C. Yin, L. Chen, N. Song, Y. Lv, F. Hu, C. Sun, W. W. Yu, C. Zhang, X. Wang, Y. Zhang, and M. Xiao, *Bright-Exciton Fine-Structure Splittings in Single Perovskite Nanocrystals*, Physical Review Letters **119** (2017).

[243] A. Privitera, M. Righetto, F. Cacialli, and M. K. Riede, *Perspectives of Organic and Perovskite-Based Spintronics*, Advanced Optical Materials p. 2100215 (2021).

[244] V. Pinchetti, E. V. Shornikova, G. Qiang, W. K. Bae, F. Meinardi, S. A. Crooker, D. R. Yakovlev, M. Bayer, V. I. Klimov, and S. Brovelli, *Dual-emitting dot-in-bulk CdSe/CdS nanocrystals with highly emissive core-and shell-based trions sharing the same resident electron*, Nano letters **19**, 8846 (2019).

[245] C. Xia, P. Tamarat, L. Hou, S. Busatto, J. D. Meeldijk, C. de Mello Donega, and B. Lounis, *Unraveling the Emission Pathways in Copper Indium Sulfide Quantum Dots*, ACS nano (2021).

[246] N. S. Makarov, S. Guo, O. Isaienko, W. Liu, I. Robel, and V. I. Klimov, *Spectral and dynamical properties of single excitons, biexcitons, and trions in cesium-lead-halide perovskite quantum dots*, Nano letters **16**, 2349 (2016).

[247] D. Rossi, T. Qiao, X. Liu, M. Khurana, A. V. Akimov, J. Cheon, and D. H. Son, *Size-dependent dark exciton properties in cesium lead halide perovskite quantum dots*, The Journal of Chemical Physics **153**, 184703 (2020).

[248] P. Tamarat, L. Hou, J.-B. Trebbia, A. Swarnkar, L. Biadala, Y. Louyer, M. I. Bodnarchuk, M. V. Kovalenko, J. Even, and B. Lounis, *The dark exciton ground*

state promotes photon-pair emission in individual perovskite nanocrystals, Nature communications **11**, 1 (2020).

[249] C. Yin, Y. Lv, X. Zhang, Y. Zhang, W. W. Yu, C. Zhang, Z.-G. Yu, X. Wang, and M. Xiao, *Transition from doublet to triplet excitons in single perovskite nanocrystals*, The Journal of Physical Chemistry Letters **11**, 5750 (2020).

[250] Y. Lv, C. Yin, C. Zhang, X. Wang, Z.-G. Yu, and M. Xiao, *Exciton-acoustic phonon coupling revealed by resonant excitation of single perovskite nanocrystals*, Nature communications **12**, 1 (2021).

[251] Y. Li, X. Luo, Y. Liu, X. Lu, and K. Wu, *Size-and Composition-Dependent Exciton Spin Relaxation in Lead Halide Perovskite Quantum Dots*, ACS Energy Letters **5**, 1701 (2020).

[252] S. Strohmair, A. Dey, Y. Tong, L. Polavarapu, B. J. Bohn, and J. Feldmann, *Spin Polarization Dynamics of Free Charge Carriers in CsPbI3 Nanocrystals*, Nano Letters (2020).

[253] J. Debus, *Spin-flip Raman scattering in low-dimensional semiconductors*, Ph.D. thesis, Universitätsbibliothek Dortmund (2012).

[254] E. Kolobkova, M. Kuznetsova, and N. Nikonorov, *Perovskite CsPbX3 (X= Cl, Br, I) Nanocrystals in fluorophosphate glasses*, Journal of Non-Crystalline Solids **563**, 120811 (2021).

[255] M. Bayer, G. Ortner, O. Stern, A. Kuther, A. Gorbunov, A. Forchel, P. Hawrylak, S. Fafard, K. Hinzer, T. Reinecke, et al., *Fine structure of neutral and charged excitons in self-assembled In (Ga) As/(Al) GaAs quantum dots*, Physical Review B **65**, 195315 (2002).

[256] A. L. Efros and M. Rosen, *Quantum size level structure of narrow-gap semiconductor nanocrystals: Effect of band coupling*, Physical Review B **58**, 7120 (1998).

[257] P. C. Sercel, J. L. Lyons, N. Bernstein, and A. L. Efros, *Quasicubic model for metal halide perovskite nanocrystals*, The Journal of Chemical Physics **151**, 234106 (2019).

[258] M. Sajedi, M. Krivenkov, D. Marchenko, A. Varykhalov, J. Sánchez-Barriga, E. D. L. Rienks, and O. Rader, *Absence of a giant Rashba effect in the valence band of lead halide perovskites*, Physical Review B **102** (2020).

[259] H. Zhu, K. Miyata, Y. Fu, J. Wang, P. P. Joshi, D. Niesner, K. W. Williams, S. Jin, and X.-Y. Zhu, *Screening in crystalline liquids protects energetic carriers in hybrid perovskites*, Science **353**, 1409 (2016).

[260] K. Miyata, T. L. Atallah, and X.-Y. Zhu, *Lead halide perovskites: Crystal-liquid duality, phonon glass electron crystals, and large polaron formation*, Science Advances **3**, e1701469 (2017).

[261] S. A. Bretschneider, I. Ivanov, H. I. Wang, K. Miyata, X. Zhu, and M. Bonn, *Quantifying polaron formation and charge carrier cooling in lead-iodide perovskites*, Advanced Materials **30**, 1707312 (2018).

[262] E. Cinquanta, D. Meggiolaro, S. G. Motti, M. Gandini, M. J. Alcocer, Q. A. Akkerman, C. Vozzi, L. Manna, F. De Angelis, A. Petrozza, et al., *Ultrafast THz probe of photoinduced polarons in lead-halide perovskites*, Physical review letters **122**, 166601 (2019).

[263] A. Forde, T. Inerbaev, and D. Kilin, *Spectral Signatures of Positive and Negative Polarons in Lead-Halide Perovskite Nanocrystals*, The Journal of Physical Chemistry C **124**, 1027 (2019).

[264] G. Kaur, K. J. Babu, and H. N. Ghosh, *Temperature-Dependent Interplay of Polaron Formation and Hot Carrier Cooling Dynamics in CsPbBr3 Nanocrystals: Role of Carrier–Phonon Coupling Strength*, The Journal of Physical Chemistry Letters **11**, 6206 (2020).

[265] M. Puppin, S. Polishchuk, N. Colonna, A. Crepaldi, D. Dirin, O. Nazarenko, R. De Gennaro, G. Gatti, S. Roth, T. Barillot, et al., *Evidence of large polarons in photoemission band mapping of the perovskite semiconductor CsPbBr 3*, Physical Review Letters **124**, 206402 (2020).

[266] J. Zhang, C. Yin, F. Yang, Y. Yao, F. Yuan, H. Chen, R. Wang, S. Bai, G. Tu, and L. Hou, *Highly Luminescent and Stable CsPbI3 Perovskite Nanocrystals with Sodium Dodecyl Sulfate Ligand Passivation for Red-Light-Emitting Diodes*, The Journal of Physical Chemistry Letters **12**, 2437 (2021).

[267] T. Kazimierczuk, D. Fröhlich, S. Scheel, H. Stolz, and M. Bayer, *Giant Rydberg excitons in the copper oxide Cu2O*, Nature **514**, 343 (2014).

[268] A. Farenbruch, D. Fröhlich, D. R. Yakovlev, and M. Bayer, *Rydberg Series of Dark Excitons in Cu2O*, Physical Review Letters **125** (2020).

[269] L.-I. Hung, C.-K. Tsung, W. Huang, and P. Yang, *Room-temperature formation of hollow Cu2O nanoparticles*, Advanced Materials **22**, 1910 (2010).

[270] M. J. Nine, B. Munkhbayar, M. S. Rahman, H. Chung, and H. Jeong, *Highly productive synthesis process of well dispersed Cu2O and Cu/Cu2O nanoparticles and its thermal characterization*, Materials Chemistry and Physics **141**, 636 (2013).

[271] H. Huang, J. Zhang, L. Jiang, and Z. Zang, *Preparation of cubic Cu2O nanoparticles wrapped by reduced graphene oxide for the efficient removal of rhodamine B*, Journal of Alloys and Compounds **718**, 112 (2017).

[272] P. Zhou, I. Tanghe, P. Schiettecatte, D. Van Thourhout, Z. Hens, and P. Geiregat, *Ultrafast carrier dynamics in colloidal WS2 nanosheets obtained through a hot injection synthesis*, The Journal of chemical physics **151**, 164701 (2019).

[273] P. Zhou, P. Schiettecatte, M. Vandichel, A. Rousaki, P. Vandenabeele, Z. Hens, and S. Singh, *Synthesis of Colloidal WSe2 Nanocrystals: Polymorphism Control by Precursor-Ligand Chemistry*, Crystal Growth & Design (2021).

[274] H. Utzat, W. Sun, A. E. Kaplan, F. Krieg, M. Ginterseder, B. Spokoyny, N. D. Klein, K. E. Shulenberger, C. F. Perkinson, M. V. Kovalenko, et al., *Coherent single-photon emission from colloidal lead halide perovskite quantum dots*, Science **363**, 1068 (2019).

List of Publications

Part of this work are or will be published as follows:

(1) E. V. Shornikova, D. R. Yakovlev, N. A. Gippius, **G. Qiang**, M. Nasilowski, B. Dubertret, A. H. Khan, I. Moreels, and M. Bayer. *Exciton binding energy in CdSe colloidal nanoplatelets addressed by one- and two-photon absorption.* Nano letters **21(24)**, 10525-10531 (2021).

(2) **G. Qiang**, A. A. Golovatenko, E. V. Shornikova, D. R. Yakovlev, A. V. Rodina, E. A. Zhukov, I. V. Kalitukha, V. F. Sapega, V. K. Kaibyshev, M. A. Prosnikov, P. C. Christianen, A. A. Onushchenko, and M. Bayer. *Polarized emission of CdSe nanocrystals in magnetic field: the role of phonon-assisted recombination of the dark exciton.* Nanoscale **13**, 790-800 (2021).

(3) E. V. Shornikova, A. A. Golovatenko, D. R. Yakovlev, A. V. Rodina, L. Biadala, **G. Qiang**, A. Kuntzmann, M. Nasilowski, B. Dubertret, A. Polovitsyn, I. Moreels, and M. Bayer. *Surface spin magnetism controls the polarized exciton emission from CdSe nanoplatelets.* Nature nanotechnology **15(4)**, 277-282 (2020).

(4) V. Pinchetti, E. V. Shornikova, **G. Qiang**, W. K. Bae, F. Meinardi, S. A. Crooker, D. R. Yakovlev, M. Bayer, V. I. Klimov and S. Brovelli. *Dual-emitting dot-in-bulk CdSe/CdS nanocrystals with highly emissive core-and shell-based trions sharing the same resident electron.* Nano letters **19(12)**, 8846-8854 (2019).

(5) R. Hu, Z. Wu, Y. Zhang, D. R. Yakovlev, P. Liang, **G. Qiang**, J. Guo, T. Jia, Z. Sun, M. Bayer and D. Feng. *Long-lived negative photocharging in colloidal CdSe quantum dots revealed by coherent electron spin precession.* The journal of physical chemistry letters **10(17)**, 4994-4999 (2019).

(6) R. Hu, D. R. Yakovlev, P. Liang, **G. Qiang**, C. Chen, T. Jia, Z. Sun, M. Bayer and D. Feng. *Origin of two larmor frequencies in the coherent spin dynamics of colloidal CdSe quantum dots revealed by controlled charging.* The journal of physical chemistry letters **10(13)**, 3681-3687 (2019).

(7) D. A. Eurov, D. A. Kurdyukov, E.V. Shornikova, **G. Qiang**, D. R. Yakovlev, M. Bayer and V. G. Golubev.*Monodispersed Spherical Nanoparticles $Gd_xSi_yO_z$: Eu^{3+} for Magnetic Resonance Tomography and Optical Imaging.* Physics of the Solid State **61(4)**, 627-631 (2019).

(8) **G. Qiang**, E. A. Zhukov, E. Evers, D. R. Yakovlev, A. A. Golovatenko, A. V. Rodina, Aleksei A. Onushchenko, and M. Bayer. *Electron spin coherence in CdSe nanocrystals in glass matrix.* In preparation.

(9) **G. Qiang**, D. R. Yakovlev, E. V. Kolobkova, E. V. Shornikova, Danil O. Tolmachev, M. A. Prosnikov, P. C. Christianen, and M. Bayer. *Anomalous polarization and spin dynamics in $CsPbI_3$ perovskite nanocrystals.* In preparation.

(10) **G. Qiang**, D. R. Yakovlev, E. V. Kolobkova, E. V. Shornikova, Danil O. Tolmachev, M. A. Prosnikov, P. C. Christianen, and M. Bayer. *Dark exciton recombination dynamics and polarization properties in $CsPbBr_3$ perovskite nanocrystals in glass matrix.* In preparation.

(11) **G. Qiang**, Dennis Kudlacik, D. R. Yakovlev, A. I. Ekomov, and M. Bayer. *Polarization and spin-flip Raman scattering of Z_3 exciton in CuCl nanocrystals.* In preparation.

(12) **G. Qiang**, Dennis Kudlacik, D. R. Yakovlev, E. V. Kolobkova, and M. Bayer. *Spin-flip Raman scattering in $CsPbI_3$ perovskite nanocrystals in glass matrix.* In preparation.

Acknowledgments

This thesis would not have been completed without the help and support from my supervisors, colleagues, families and friends.

First of all, I would to thank Prof. Dr. Manfred Bayer for giving me the opportunity to visit E2 during my master, and later on to work here for my PhD. Everything happened like a magic.

Thanks to Prof. Dr. Dmitri Yakovlev for giving me the chance to work on colloidal semiconductor nanocrystals projects and the careful and irreplaceable guidance. I also would like to express my gratefulness to Dr. Dennis Kudlacik, Prof. Dr. Evgeny A. Zhukov, Prof. Dr. Donghai Feng, Dr. Elena V. Shornikova, Dr. Danil O. Tolmachev, Dr. Rongrong Hu, Eiko Evers for their comprehensive explanation of the experimental techniques and related working skills. I want to thank especially Prof. Dr. Evgeny A. Zhukov and Prof. Dr. Donghai Feng for teaching me the pump-probe technique.

Special thanks to Dr. Dennis Kudlacik for allowing me to work with him on the spin-flip Raman scattering setup, explaining all the optics and details about the experiments, teaching me Labview and skills for making graphs and writing papers. I benefit greatly from his patience and kindness, and also got a lot of help from him during the preparation of this thesis.

Our researches on colloidal NCs can not moved forward successfully without theoretical supports. I would like to sincerely appreciate Dr. Aleksandr A. Golovatenko and Prof. Dr. Anna V. Rodina for their help with the theory. I always feel excited to discuss questions with them, their great knowledge is so impressive. Without the fascinating collaboration, i could not have completed my thesis as planned. My thanks also go to Dr. Alexey I. Ekimov, Dr. Elena V. Kolobkova and Dr. Aleksei A. Onushchenko for providing us the interesting samples.

I also want to thank the SHG guys, Andreas Farenbruch and Johannes Mund. We have a lot of time working at the same time in the lab, discussing questions and help each other from time to time. That is an amazing part of my lab experience.

I also feel very lucky to meet many great people in the office. I want to thank my officemates, Dr. Pavel Sokolov, Dr.Bernd Berger and Dr. Daniel Schmidt, we have a lot of very pleasant discussions, and i learned a lot of from them. Especially thanks to Pasha who encourages me to study Python which is very useful for processing large batch of data and also in other aspects.

We have a great group because we also have great people behind us. Taking this time, i also want to Lars Wieschollek, Daniel Tüttmann and Klaus Wiegers for the

helium support, especially thanks Lars Wieschollek for helping me with many small but tough problems in the lab. I also want to thank Katharina Sparka and Michaela Wäscher for the effcient admistration work. I want to thanks Lars Klompmaker and Felix Spitzer for the IT support, thanks Alexander Kosarev, Alexandr Kamenski, Andreas Farenbruch, Prof. Dr. Evgeny A. Zhukov for teaching me Russian, thanks Dr. Felix Godejohann for teaching me Deutsch. I want to thank all of my E2 colleagues who provide such a warm and enjoyable atmosphere.

My parents and families are the people who always stay with me no matter where and how i am, without their support, it is impossible for me to have this impressive experience to Dortmund. I love them forever.

Finally, I want to thank all of other people whom I did not mention above. It is the support from all the people that make me able to finish my PhD, thank you all !!